Study of submillimeter-wave antennas and associated technologies

Basem Mohammed Qasem Aqlan

▶ **To cite this version:**

Basem Mohammed Qasem Aqlan. Study of submillimeter-wave antennas and associated technologies. Networking and Internet Architecture [cs.NI]. Université de Rennes; Ǧāmiᶜaï al-Malik Saᶜūd (Riyad), 2022. English. NNT : 2022REN1S095 . tel-04069598

HAL Id: tel-04069598

https://theses.hal.science/tel-04069598

Submitted on 14 Apr 2023

HAL is a multi-disciplinary open access archive for the deposit and dissemination of scientific research documents, whether they are published or not. The documents may come from teaching and research institutions in France or abroad, or from public or private research centers.

L'archive ouverte pluridisciplinaire **HAL**, est destinée au dépôt et à la diffusion de documents scientifiques de niveau recherche, publiés ou non, émanant des établissements d'enseignement et de recherche français ou étrangers, des laboratoires publics ou privés.

UNIVERSITÉ DE RENNES 1

THESE DE DOCTORAT DE

L'UNIVERSITE DE RENNES 1

ECOLE DOCTORALE N° 601
Mathématiques et Sciences et Technologies de l'Information et de la Communication
Spécialité : **Traitement du Signal et Télécommunications**

Par
Basem M. Q. AQLAN

Study of Submillimeter-Wave Antennas and Associated Technologies

Thèse présentée et soutenue à Rennes, le
Unité de recherche : IETR, UMR CNRS 6164, Institut d'Electronique et des Technologies du numéRique

Rapporteurs avant soutenance :

Aurelian CRUNTEANU STANESCU	Directeur de Recherche Xlim Limoges
Jean-Marc Ribero	Professeur, Université Côte d'Azur

Composition du Jury :

Examinateurs :	CAMILLA KÄRNFELT	INGENIEUR IMT-ATLANTIQUE BREST
	OLIVIER WEITTEN	INGENIEUR AIR LIQUIDE GRENOBLE
	OLIVIER LAFOND	Professeur, Université de Rennes 1
	Elodie RICHALOT	Professeur - Université Gustave Eiffel
	Aurelian CRUNTEANU STANESCU	Directeur de Recherche Xlim Limoges
	Jean-Marc RIBERO	Professeur, Université Côte d'Azur
Dir. de thèse :	Mohamed HIMDI	Professeur, Université de Rennes 1
Co-dir. de thèse :	Hamsakutty VETTIKALLADI	Associate Professor, King Saud University

ACKNOWLEDGMENT

Write your acknowledgment here.

TABLE OF CONTENTS

LIST OF FIGURES

LIST OF TABLES

ABBREVIATION

6G	6G Sixth-generation
AR	Axial ratio
AUT	Antenna under test
Az.	Azimuth
BW	Bandwidth
CATR	Compact antenna test range
CNC	Computer numerical control
CP	circularly polarized
DFSS	Double-fan shaped-slot
DRIE	Deep reactive ion etching
DR-WG	double ridge waveguide
EDM	Electrical Discharge Machining
Ele.	Elevation
EM	Electromagnetic
FPC	Fabry-Perot Cavity
FSS	Frequency selective surface
GRIN	gradient refractive index
HPBW	half-power beam width
LHCP	Light-hand circularly polarized
LTCC	Low-Temperature Co-fired Ceramic
MBAs	Multi beam antennas

MTS	Metasurface
PBG	Photonic bandgap
PG	Peak gain
PPW	parallel-plate waveguide
PRS	Partially reflective surface
RCA	Resonant cavity antenna
RHCP	right-hand circularly polarized
SIW	substrate integrated waveguide
SLL	Side lobe level
SPPs	Surface Plasmon polaritons
SPs	Surface plasmons
Tbps.	Terabit per seconds
THz	Terahertz
TM	Transverse magnetic
VDI	Virginia Diodes Inc.
VNA	Vector network analyzer
XPD	Cross polarization discrimination

Chapter 1 Introduction

1.1 Terahertz Spectrum: Applications and Usage Scenarios

Recently, the global wireless data traffic has been exponentially increasing along with the growth of applications that require data rates of several tens of Gbps. The increase in the data rate provided by every new generation of cellular networks is insufficient for the annual growth of demand. The significant rapid growth of wireless utilization has driven researchers to investigate appropriate regions in the radio spectrum to fulfill this demand [1].

Terahertz (THz) spectrum spans the frequency range from 0.1 to 10 THz between infrared and microwave radiation in the electromagnetic spectrum as shown in Figure 1.1, has been highly valued in different fields such as wireless cognition, imaging, spectroscopy, sensing, super-high precision positioning and future wireless communications [2].

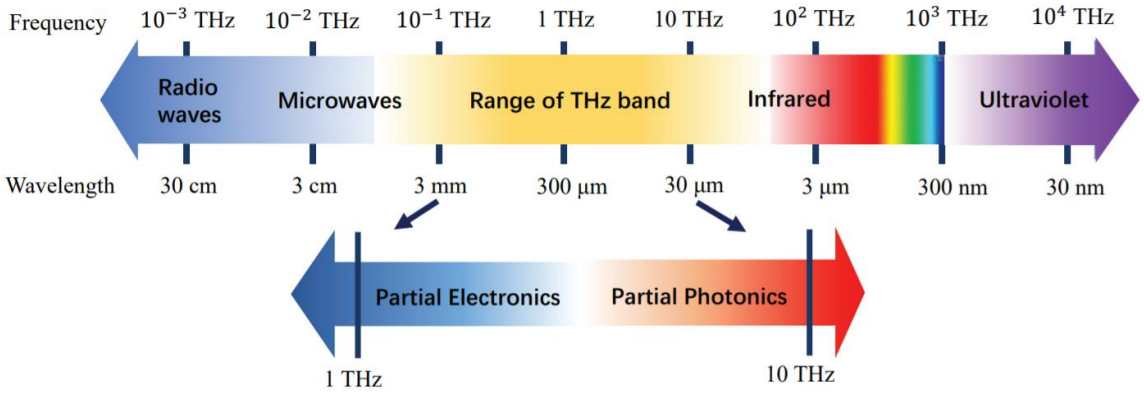

Figure 1.1: The range of THz band in the electromagnetic spectrum.

Sub-THz frequency (0.1 – 1 THz) band, which has not been allocated for specific uses yet, has an extremely broad atmospheric transmission window (~ 100 GHz bandwidth) with manageable losses will be ideal for building a wireless link with ultra-high data rates up to 1Tbps with super-reliable and minimum latency communication, which is an enabler for beyond fifth-generation (5G) wireless mobile communications in the future. In the following, some of the wireless ultra-high data rate scenarios depicted in Figure 1.2 are presented.

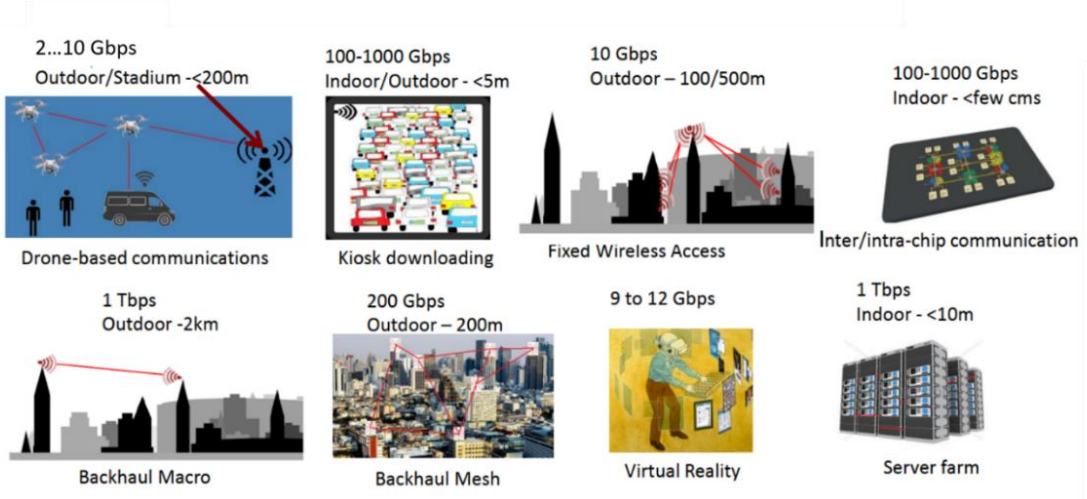

Figure 1.2: Beyond 5G scenarios with Tbps data rate requirements [3].

Finally, it is worth mentioning that sub-THz and real THz bands are being investigated for other types of applications in addition to the communication due to the small-wavelength characteristics, the ultra-wide bandwidth, and narrow-beam widths at THz frequencies. For instance, the THz wireless systems are also promising for novel sensing, smart healthcare, imaging, and positioning capabilities to enhance automated machinery, autonomous cars, intra-body THz communications with nanotechnology THz transceivers, and new human interfaces [2, 4].

1.2 THz Waves: Propagation, Advantages, and Disadvantages

In this section, the major THz band limitations and hardware challenges are presented.

1.2.1 Interaction of THz Waves

The atmosphere has absorption bands mainly due to two components: water vapor (H_2O) and oxygen (O_2). The atmospheric attenuation from 30 GHz to 3 THz, is shown in Figure 1.3 [5]. If the atmospheric attenuation is less than 10 dB, the effect is relatively small. On the other hand, if the atmospheric attenuation exceeds 10 dB at 1 km, for example, kilometer-class communication becomes difficult. Such frequencies are 60, 183, 325, and 351 GHz and above. Thus, to limit the effects of distortions/losses in future THz radio communication systems on these frequency ranges, the future channels will have to use a bandwidth free of strong absorption lines, and in this perspective, the 200–320 GHz band looks promising, and the frequencies beyond 275 GHz are still free. This may be one of the reasons why the 300 GHz band is attracting attention for communication applications.

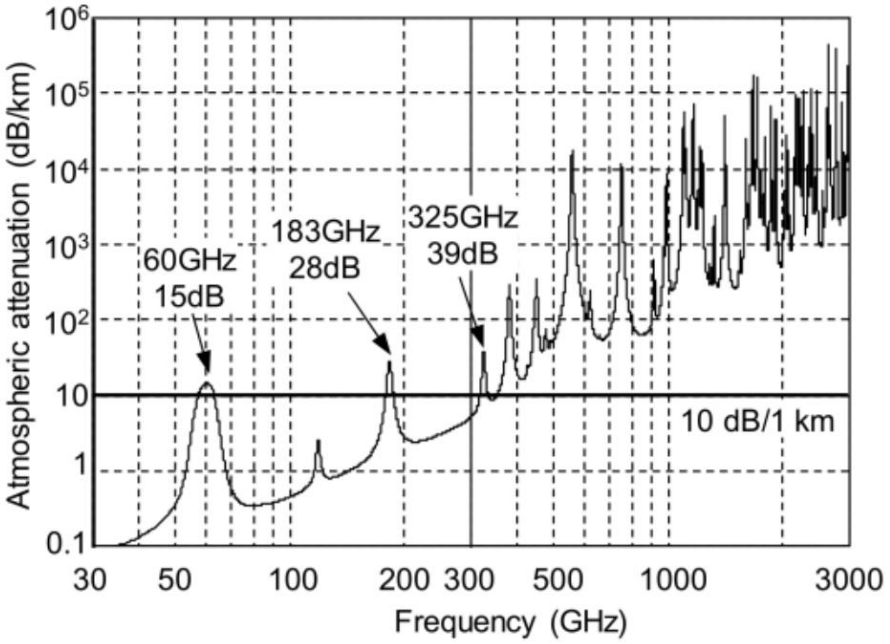

Figure 1.3: Atmospheric attenuation of radio waves from 30 GHz to 3 THz [6, 7].

Thus, the long-distance THz wireless communication is a real challenge with these high propagation losses, and the low sub-THz bands below 300 GHz have more opportunities for these applications. However, a high-gain directional antenna is necessary to deal with the overall propagation losses for outdoor long-distance scenarios such as backhaul and fixed wireless access. Besides, MIMO technology with beamforming can help to counteract these losses and achieve ultra-high data rates. Note that these propagation losses are negligible and irrelevant for the short-range indoor sub-THz/THz communication. Nevertheless, these scenarios are still facing important losses from the surrounding environment and furniture details.

Besides, the sub-THz/THz wireless communication is more exposed to severe blockage and penetration losses than the 60 GHz mmWave losses, as shown in [2, 8] and references therein. But it is worth mentioning that these attenuations, molecular/gas absorption, propagation losses as well as reflections, scattering, and diffraction phenomena, have much more contribution to the THz bands. Thus, the efficient communication link will be most likely in Line of Sight (LOS) and/or with a possible few existing Non-Line of Sight (NLoS) paths.

1.2.2 THz Challenges and Limitations: Hardware Technology

The RF front-end is all the components between the antenna and the baseband system of a transceiver, namely mixer or modulator, phase shifter, filters, data converters, and power amplifier (PA). The schematic in Figure 1.4 shows a simplified block representation of a transmitter (Tx) and receiver (Rx) RF frontend.

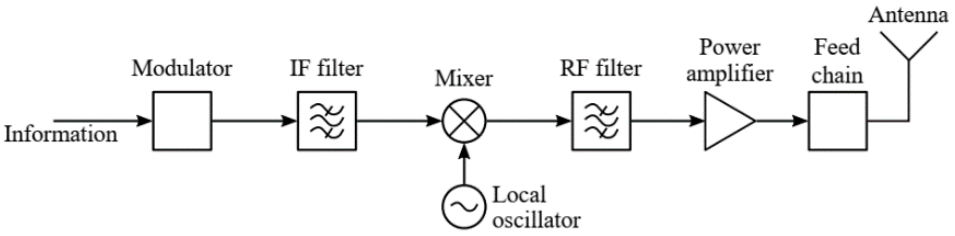

(a)

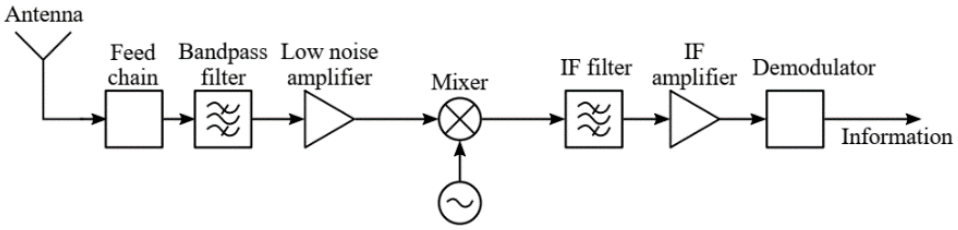

(b)

Figure 1.4: Block diagram of a basic RF system. (a) Transmitter, and (b) receiver.

Note that the THz hardware components exist for decades for radio astronomy and satellite applications, but the available components do not suit the emerging sub-THz communication scenarios since the latter has more stringent hardware constraints and requirements such as transceiver dimension, heat dissipation, processing power, operating temperature, and cost. Thus, nowadays, technology is still not mature enough for sub-THz frequencies, even though significant efforts have been made in the last years. For instance, electronics technology is the most convenient for massive low-cost production and business interest for such Tbps scenarios.

The RF systems operating at Sub-THz frequencies and above suffer from strong atmospheric attenuation, see Figure 1.3. This issue could be solved, in theory, by increasing the transmitted power. However, the RF power that THz sources can deliver is low, being one of the most significant challenges for the implementation of many systems in this frequency range.

The active components used to generate or detect the THz waves play a central role in the emergence of these technologies. Figure 1.5 gives an overview of the current performance of THz sources [9]. For electronic components (transistors, diodes), there is a significant drop in power with frequency (about $1/f^3$). In the sub-THz range of 0.1 to 1 THz, powers of the order of 1 to 100 mW are possible in the solid state and at room temperature, which makes it possible to consider communication systems in this range.

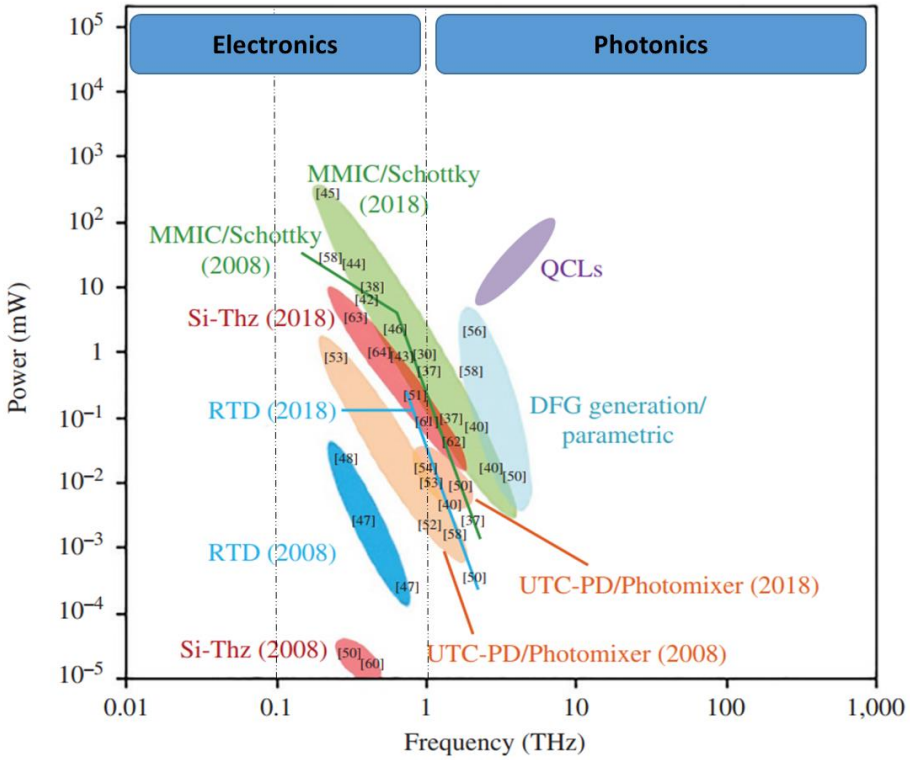

Figure 1.5: State of the art of THz sources [9] (references in the graph from [9]). microwave monolithic integrated circuits (MMIC), resonant tunneling diode (RTD), and difference frequency generation (DFG).

For optoelectronic components (quantum cascade lasers; QCLs), the reverse trend is observed. Nevertheless, the latter must be cooled to cryogenic temperatures and, if one takes into account the atmospheric absorption and the powers generated, it seems uncertain that communications at frequencies above 1 THz will emerge soon. Resonant tunneling diodes (RTDs) also have an interesting compactness or performance ratio at room temperature. Finally, the optoelectronic components; uni-traveling-carrier photodiodes (UTC-PDs) or photoconductor-type (photomixers) have a fairly wide operating range, allowing an optical-to-THz conversion interesting for spectroscopy or communications.

1.3 Motivation

Antennas are indispensable components for generating and recurving THz signals, so the development and implementation of THz antennas are critical to the wireless system performance. Currently, there are limited options for antenna designs for the THz band, and their performance is also inadequate for certain potential applications. Indeed, for wireless communications, the free space path loss at THz frequencies is sufficiently large, and thus high-directivity wideband antennas are required to compensate for the loss. In terms of antenna

fabrication, more efforts are needed to design antennas with lower cost and complexity but with the same or better performance. At high frequencies, the electromagnetic wave suffers from more severe free-space loss and blockage, which substantially degrades the signal-to-interference-plus-noise ratio (SINR) [10]. To cope with this shortcoming, high-gain antennas with a directional beam can be deployed (possibly at both transmitting and receiving ends), which greatly enhances the SINR, mitigates the Doppler effect, and improves the data security, thus have been widely used in long-range millimeter-wave (MMW) point-to-point communications with a line-of-sight (LOS) link [11, 12]. However, the narrow beam provides only limited spatial coverage, making it not amenable to multiuser mobile streaming. In addition, for non-LOS communications, the single-directional beam needs to be steered either electronically or mechanically in order to find a reliable substitute link. Alternatively, the multi-beam antennas (MBAs) [13], which are capable of generating a number of simultaneous but independent directive beams with a high gain value to cover a predefined angular range, provide a solution to overcome the above shortcomings of antennas at WM-864 frequency bands (220- 330 GHz), with a single-directive beam. Therefore, in this thesis, all-metal sub-THz antenna structures and multi-beam antenna for future high-speed wireless communication systems that overcome the aforementioned limitations are developed.

This Chapter firstly discusses the emerging B5G scenarios and gives a general background about the sub-THz bands including their channel characteristics, challenges, and limitations.

One approach to compensate for the high atmospheric attenuation and low available power in the THz range is to use a high-gain antenna with the rest of the components in the RF frontend. Therefore, the development of a suitable and low-cost fabrication technique for sub- terahertz antennas is, nowadays, the main challenge for the passive part of the RF frontend, and it would contribute to the realization of the broad spectrum of potential applications for THz systems. This thesis aims to add to this development by the design and fabrication of several sub-THz antenna structures through the use of different fabrication techniques.

1.4 Outlines

The thesis is organized as follows:

Chapter 2 reviews the available fabrication antenna technologies at the sub-THz band (0.1 to 1 THz). It also covers reviews of the Luneburg lens antenna based on dielectric and artificial electromagnetic materials. In this chapter, different antenna fabrication technologies are presented. Computer numerical control (CNC) machining and electro-erosion technology are thoroughly discussed. Technologies utilized in high frequencies such as silicon micromachining are introduced in different discussed research papers. Different types of passive multi-beam antennas such as dielectric electromagnetic material and artificial

electromagnetic material are discussed with their relative resonance frequencies, bandwidths, fabrication processes, and efficiencies.

In the next chapters, some of these technologies are used to build high gain wideband antennas in the sub-terahertz frequency bands.

In chapter 3, a circularly polarized horn conical antenna is designed and fabricated at 300 GHz using wire-cutting electro-erosion technology. The fabricated prototype represents the first compact, broadband, and high-gain antenna in the sub-THz frequency range.

In chapter 4, a laser-cutting technology on brass has been applied for the first time in literature to fabricate a low-cost, compact, and high gain Fabry–Perot cavity (FPC) antennas at 300 GHz with linear and circular polarization characterization. The detail of the fabrication methodology is discussed in the chapter.

In chapter 5, a Bull's-Eye (BE) antenna with circular polarization characterization based on crossed-slot and double-fan shaped-slot elements is designed and fabricated with the aim of silicon micromachining technology and CNC milling at 300 GHz.

In chapter 6, a metallic Luneburg lens based on a parallel-plate waveguide (PPW) loaded with variable posts is designed. A high-gain beam scanning antenna at 300 GHz is thoroughly discussed. The followed methodology is discussed in detail.

In chapter 7, metallic Luneburg Lens Based on Parallel-Plate Loaded with uniform Posts is designed and fabricated to reduce the costs and the complexity of fabrication at 300 GHz. In addition, a dielectric Luneburg lens with different thicknesses have been developed and fabricated at 300 GHz with linear and circular polarization characterization.

In chapter 8, the overall conclusions of sub-THz antenna prototypes and multi-beam antenna based on the PPW Luneburg lens are dedicated. Some directions to the future expression of this research are suggested as well.

Chapter 2 Literature Review of Antenna Fabrication Technologies at Sub-THz band

There are many technologies used to realize antennas and multibeam at millimeter/sub-millimeter frequency bands. Different technologies and fabrication techniques are discussed for efficient antennas at the sub-THz band. In the following, we focus more on all metal antenna fabrication technologies as they have the lowest losses. Also, low-temperature cofired ceramics (LTCC) and 3D printing are added to this literature as a way to compare all-metal and substrate-based antennas.

2.1 Computerized Numerical Control (CNC) Machining

2.1.1 CNC Drilling

Some prototype corrugated horns for the 1.25–1.57 THz band have been designed and fabricated by direct machining in a single block of aluminum. Figure 2.1 shows, that two different kinds of corrugated horns with similar performance have been considered: long conical-profile corrugated horns and shorter profiled corrugated horns. Notice that the profiled horn is much shorter than the conical horn [14].

Figure 2.1: Photographs of prototype corrugated horns. The horn on the left is the conical corrugated horn, and the one on the right is the profiled corrugated horn. The latter is much shorter as can be seen in the above photograph.[14]

Smooth-walled multiple flare-angle horns have been designed and manufactured very rapidly and cheaply in large numbers, by repeated direct drilling into a single plate of aluminum using a shaped machine tool (Figure 2.2). A constructed a 230 GHz focal-plane array comprising 37 smooth-walled horns fabricated by direct drilling (Figure 2.3).

The measured beam patterns for a large sample of these horns across the array demonstrate the suitability of their manufacturing techniques for large format arrays [15].

Figure 2.2: The high-speed steel machine tool used for the fabrication of the 230 GHz drilled horn prototype [15].

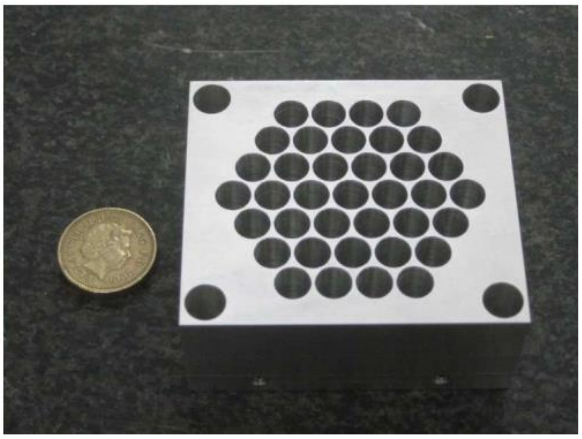

Figure 2.3: The 37-horn array prototype, made by repeated drilling into a single block of aluminum [15].

2.1.2 CNC Milling

A multi-flare angle horn antenna has been optimized to demonstrate low cross-polarization, low side-lobe level, good return loss, and excellent beam circularity over the 1700–2100-GHz frequency range [16] (Figure 2.4). A prototype with directivity of 31.7 dBi and a cross-polarization level below 22 dBi was measured at 1.9 THz with excellent agreement with the calculation. The proposed antenna is machined out of a single metallic block of oxygen-free copper (Figure 2.4) using an end-mill that is shaped under the multi flare angle horn contour. This tool enables the rapid and inexpensive manufacture of the horn, which is perfectly suited for the fabrication of large focal-plane arrays. This technique offers an alternative to conventional electroformed horn arrays which are time-consuming and expensive.

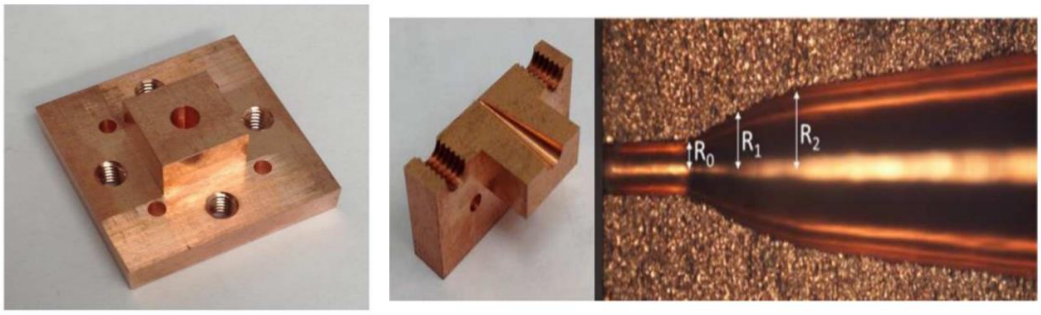

(a) (b)

Figure 2.4: (a) Photograph of a fabricated 1.9-THz multiflare angle horn which was machined on a copper block drilled (b) Horn cut in half for dimension inspection [16].

A high gain quasi-planar reflector antenna for 325–500 GHz applications is investigated. The antenna is composed of four parts: a feeding horn, quasi-planar reflectors, choke slots, and an E-plane flared horn [17]. All parts are highly integrated inside a metal block for obtaining a compact size. The low-cost conventional milling process is used for fabrication. Two opposite halves are fabricated and integrated by using alignment pins and screws, and their surfaces are electroplated with a 2.5-μm gold layer. The UG387 flanges are used for the feeding horns. Measured results show that the fabricated prototype achieves a wide impedance bandwidth of 43.75% from 325 to 500 GHz with a reflection coefficient below -20 dB. The maximum gain is 32 dBi at 500 GHz and the gain is higher than 26.5 dBi over the whole operating band.

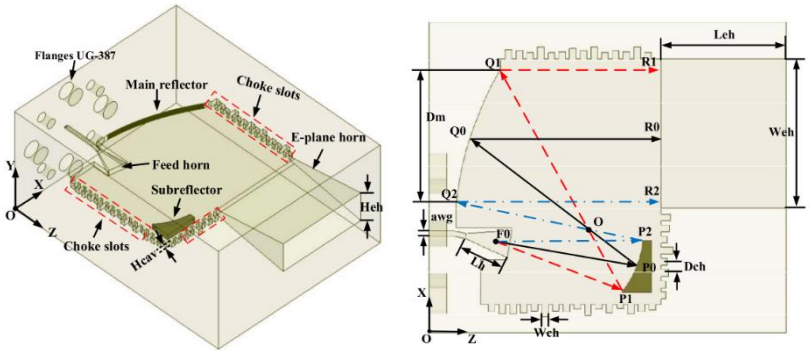

(a) (b)

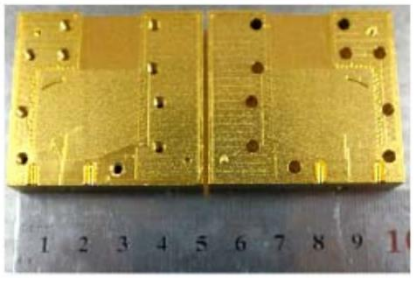

(c)

Figure 2.5: Configuration of the quasi-planar reflector THz antenna. (a) 3-D view, (b) top view, and (c) photograph of the fabricated THz prototypes.

2.2 Diffusion Bonding Technology

Diffusion bonding is a solid-state welding technique to bond plane surfaces together by applying heat and force to the materials, using the diffusion of atoms. Diffusion bonding of multiple thin metal plates is a commercially available fabrication process that can fabricate feed horns above 100 GHz. In recent years, the development of the corporate-feed waveguide slot array antenna through diffusion bonding has been demonstrated as a relatively low-cost and simple manufacturing process.

In [18], a 4 ×4-element corporate-feed waveguide slot array antenna is proposed using the diffusion bonding technique in the 120 GHz band, as shown in Figure 2.6 (Left). This bonding technique is based on the atomic diffusion of elements at the joining interface. Thin platelets containing patterns of etched holes or slots can be sandwiched together in a stack of many layers to form the final antenna structure. Though it offers a relatively high performance possibly up to 1 THz, the constituting multiple layers still need to be laser cut or CNC machined, which leads to additional fabrication complexity. Cavity structures are introduced into the corporate-fed slot array and provide mutual coupling adjustment and a broadband characteristic. The presented array has a maximum gain and efficiency of 21.1 dBi and 80.0%, respectively. Moreover, the 1 dB-down gain bandwidth is 17.6 %, which is a very promising feature.

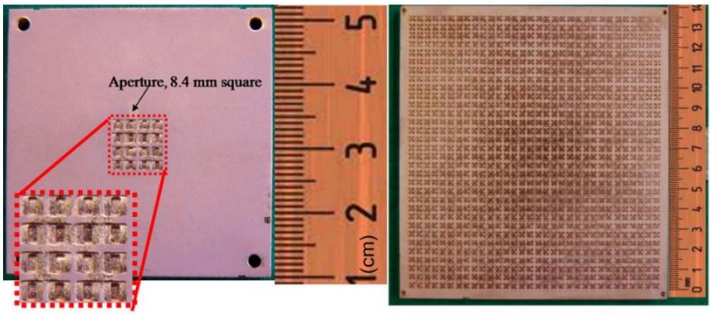

Figure 2.6: 4×4 and 32×32-element waveguide slot array [18, 19].

A 32×32-element and a 64 ×64-element array in the 120 GHz band are presented in [19] with increased efficiency and bandwidth as shown in Figure 2.6 (Right). But the measured results of the two arrays show more than 38 dBi gain can be achieved in the frequency band of interest.

2.3 Metal Forming Techniques

2.3.1 Electroforming Process

At higher frequencies the manufacturing process is critical. Classical milling is still a good candidate and can be used up to 350 GHz for corrugated horns. For the rectangular to the circular junction, spark erosion is a good candidate for direct machining. As a drawback, the surface roughness is not as good as classical milling. The electroforming process becomes necessary as the horn dimensions decrease, the mandrel being easier to manufacture and control. The other advantage is that the horn is manufactured in one piece.

The horn realized by the electroforming process is presented in Figure 2.7 and has shown the best results in cross-polarization [20]. In order to verify the wide-band characteristics of the horn, the RF pattern has been measured from 76.56 to 109.10 GHz.

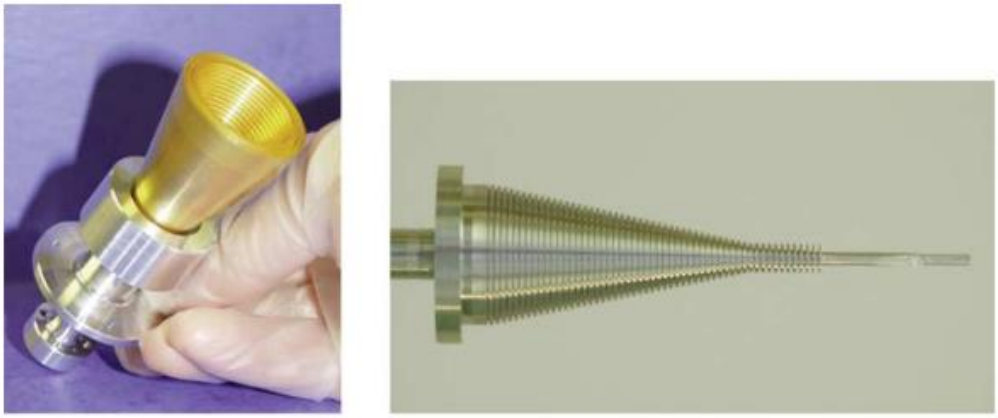

Figure 2.7: Horn manufactured by electroforming process (right figure: the mandrel)[20].

2.3.2 Electro-erosion Process

Electrical Discharge Machining (EDM) is a machining method primarily used for hard metals or those that would be impossible to machine with traditional techniques. One critical limitation, however, is that EDM only works with electrically conductive materials. EDM is especially well-suited for cutting intricate contours or delicate cavities that would be difficult to produce with a grinder, an end mill, or other cutting tools. Metals that can be machined with EDM include Hastelloy, hardened tool-steel, titanium, carbide, Inconel, and Kovar.

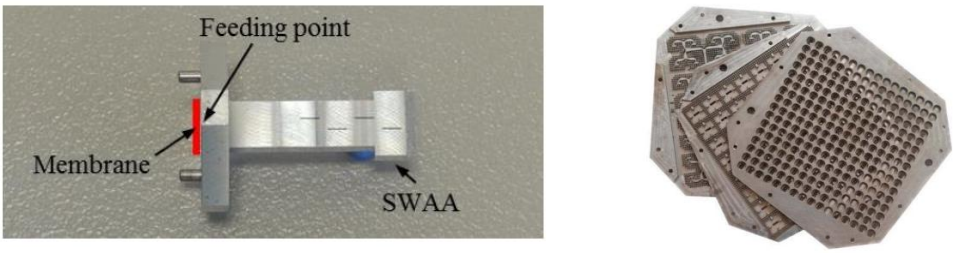

(a) (b)

Figure 2.8: Photograph of the array antenna fabricated by (a) wire EDM and (b) die-sink EDM [21, 22].

Recently, progress in wire-cut and die-sink EDM in terms of accuracy and very precise control of the machining tools has made possible the fabrication of very delicate components such as antennas at millimeter-wave frequency.

In [21] slotted waveguide antenna array was made in aluminum by wire EDM technique and a milling technique as shown in Figure 2.8(a). A −10 dB bandwidth of 3.54 GHz was achieved while the antenna exhibits a measured realized gain of 10.7 dBi at a resonance frequency of 58.8 GHz, with a high total efficiency of 95%. Authors in [22], fabricated of 16×16 slot array antenna by using die-sink EDM [22] as shown in Figure 2.8(b). The measured impedance bandwidth was 18% with a reflection coefficient better than -10 dB, and the radiation patterns satisfy over the 56-67 GHz frequency band. The measured total aperture efficiency was over most of the frequency band better than 80%.

2.4 Low-Temperature Cofired Ceramic (LTCC) Technology

In recent years, LTCC technology has shown its potential to offer stable and low-loss performance for millimeter-wave/THz integrated circuits. A typical LTCC structure allows printing low-loss conductors on multi-layer ceramic substrates where large quantities of components can be embedded. The proven reliability of the multi-layering LTCC technique permits high-level circuit integration and relative ease of manufacture.

The authors in [23] proposed a 270 GHz linearly polarized radial line slot array (RLSA) using the LTCC process. Based on the classic RLSA at microwave frequency, the presented work introduces an integrated feeding transition and strip loading to improve impedance bandwidth. Figure 2.9 shows the fabricated antenna prototype. The measured -10 dB S11 is from 261.3 GHz to 282.2 GHz, and the measured gain is higher than 24.6 dBi over 271.2– 281 GHz with a peak gain of 27.6 dBi at 275.2 GHz. Due to the non-uniform illumination and asymmetrical feeding, the antenna aperture efficiency is less than 40%.

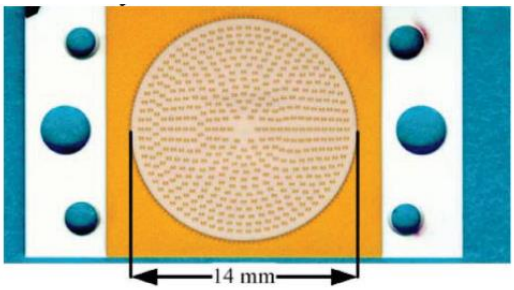

Figure 2.9: Fabricated 270 GHz LTCC RLSA antenna [23].

Authors in [24] reported a TE_{20}-mode substrate integrated waveguide (SIW) fed slot antenna array working at 140 GHz. Figure 2.10 shows the proposed 8×8 slot array consists of eleven substrate layers and six metal layers. The dielectric-loaded radiating slots are excited with a feeding network comprising a power divider and E-plane coupler. The measured results show a maximum boresight gain of 21.3 dBi at 140.6 GHz and a good impedance matching between 129.2 and 146 GHz. It is noted that there is a large reduction in the measured efficiency which is from the fabrication tolerances and variation of the material properties.

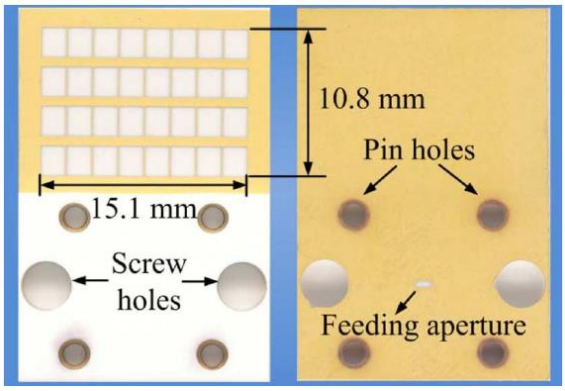

Figure 2.10: Fabricated prototype of the 140 GHz LTCC slot antenna array [24].

Apart from waveguide slot arrays, the LTCC technique can also be used to design 300-GHz step-profiled corrugated horn antennas [25]. As can be seen from Figure 2.11, the horn structure is subtly formed by a hollow multilayer LTCC substrate and metal vias. The air cavity reduces the loss of the antenna which is beneficial to impedance matching.

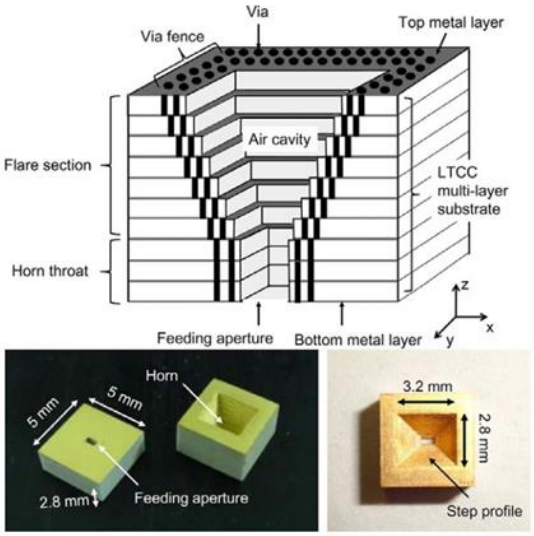

Figure 2.11: Schematics of the 300 GHz LTCC horn antenna [25].

To verify the design concept, an LTCC hollow waveguide was fabricated and measured with an insertion loss of less than 0.6 dB/mm. The resultant LTCC horn antenna has a size of 5 mm × 5 mm × 2.8 mm. The measurement shows the frequency range of more than 10 dB return loss is from 230 to 330 GHz. The antenna has a peak gain of 18 dBi with the 3-dB gain bandwidth from 248 to 320 GHz.

2.5 3D Printing Technology

As an emerging technique, 3D printing offers high flexibility and precision as well as a potential fast turnaround, which enables a lot of new electromagnetic component designs including 3D printed THz antennas. The authors in [26] describe a 3D printed all-dielectric THz horn antenna based on a hollow-core electromagnetic crystal (EMXT) structure. Polymer-jetting prototyping technique is adopted to fabricate the dielectric horn antenna. To measure the radiation pattern of the fabricated horn in Figure 2.12, THz time-domain spectroscopy (THz-TDS) system is used as the horn cannot be fed by a conventional metal waveguide. The measured gain has large differences from 5 dBi to 23 dBi in the frequency range of 80 - 190 GHz because of the passbands of the EMXT waveguide structure. However, the reflection coefficient of the antenna cannot be measured through the simulated one presented.

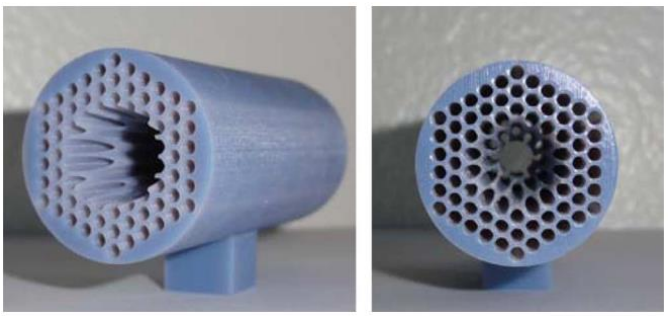

Figure 2.12: Fabricated THz EMXT horn antenna [26].

The authors in [27] present three different dielectric reflectarrays operating at 100 GHz. Figure 2.13 presents the reflectarrays fabricated by polymer-jetting 3-D printing technology. The material loss and dielectric constant at 100 –600 GHz are first observed using the THz time-domain spectrometer system. Then reflectarrays with different aperture phase distributions are studied to quantify the fabrication limits. The measured gain of the three prototypes at 100 GHz is 22.5, 22.9, and 18.9 dB, respectively. The proposed design is expected to be readily scalable to higher THz bands.

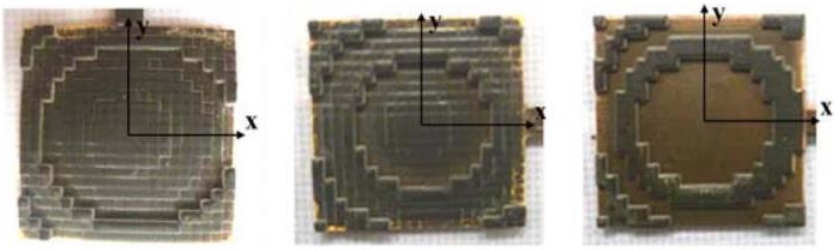

Figure 2.13: Three 3D printed reflectarrays [27].

The researchers at the City University of Hong Kong report a fixed frequency scanning transmitarray using 3D printed dielectric material in the frequency range of 225-325 GHz for the first time [28]. According to the presented measured results, a maximum gain of 27.5 dBi and a scanning range of 14.3° can be achieved. Figure 2.14 shows the fabricated dielectric lens antennas.

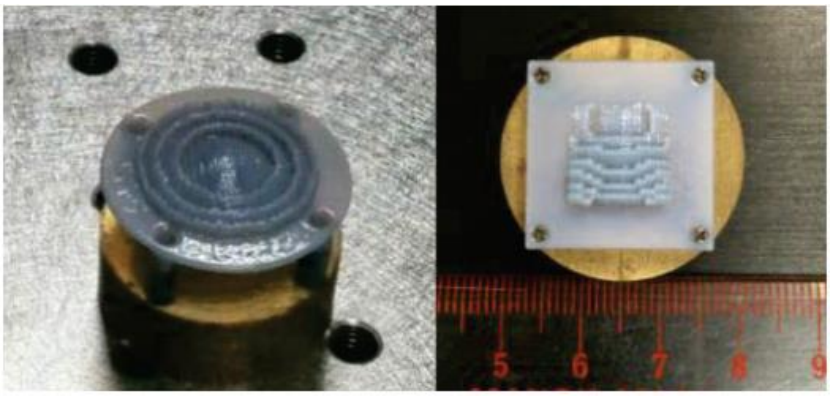

Figure 2.14: Fabricated THz lens antennas [28].

2.6 Micromachining Technology

The last technique we need to highlight is micromachining technology, which shows potential at THz frequencies with permanent thick-resists, thick-resist electroforming, and deep reactive ion etching (DRIE) of silicon micromachining. These techniques use photolithographic techniques to produce features accurate to 3 μm or less.

2.6.1 PolyStrata Microfabrication

The PolyStrata microfabrication process is a thick-resist electroforming micromachining technique, that involves sequential deposition of copper and photoresist on a carrier substrate. Multilayer structures can be realized by fusing a dozen or more layers with a layer thickness from 10 μm to 100 μm. At the end of the process, the unwanted photoresist is removed chemically, leaving air-filled free-standing metal and dielectric structures.

Reference [29] presents a waveguide slotted array fabricated using the PolyStrata process. The measured results show the S11 of the antenna shown in Figure 2.15 is below -10 dB over the 275 to 295 GHz frequency range and the gain of the antenna at 280 GHz is 20 dBi.

Figure 2.15: Fabricated array installed in a brass test fixture with two WR-3 waveguide [29].

The slot-waveguide array can also be used for frequency scanning as long as the slots are arranged to conform to a Chebyshev or a Taylor distribution. At the low THz band, this concept is demonstrated in [30], where 10 and 20-element slot arrays were fabricated using the PolyStrata sequential copper deposition process and subsequently gold-plated, as shown in Figure 2.16. A Standard WR-05 waveguide is used to feed the two waveguide arrays. Both the fabricated antennas have good impedance mating over the entire frequency band from 130 to 180 GHz. The measured gain is 15.5 dBi for a 10-element array at 150 GHz, and 18.9 dBi for a 20-element array at 150 GHz, and the scan range is around 32.5° over the frequency range.

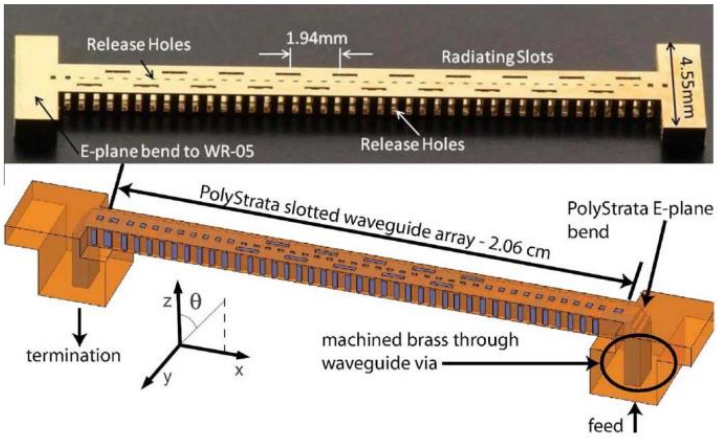

Figure 2.16: Details of the 20- element slot array [30].

2.6.2 DRIE-based Silicon Micromachining

Deep reactive ion etching (DRIE) micromachining is a dry etching technique, that relies on plasma etching of bulk silicon, which has been successfully applied to mmW and THz advanced packing. To etch holes and trenches in Si wafers, high-density plasma is generated by efficient RF power coupling.

The main steps of the fabrication micromachined process for standard WR-3.4 waveguide are illustrated in Figure 2.17 [31]. The device layer (DL) of the silicon-on-insulator (SOI) wafer is etched using DRIE with a three-step Bosch process Figure 2.17(b). The buried oxide (BOX) layer of the SOI wafer acts as an etch stop during DRIE, ensuring that the resulting etch profile is free from curvature and is subsequently removed by plasma etching. Both the SOI wafer and the silicon cap wafer are then metalized with 1.0 μm of gold (waveguide top and bottom) using sputter deposition Figure 2.17(c), resulting in a thickness of 0.3 μm on the waveguide sidewalls. Finally, the individual chips are bonded using thermo-compression bonding at 200 ℃, Figure 2.17 (d).

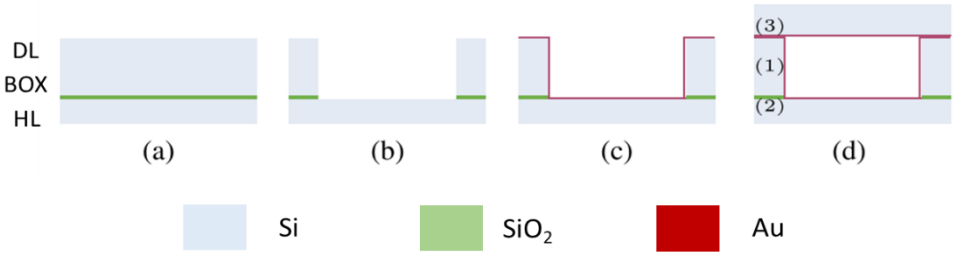

Figure 2.17: Fabrication process: (a) Initial SOI wafer, (b) waveguide structure after DRIE silicon etch and subsequent removal of the BOX layer, (c) metallization using sputtering, and (d) final waveguide after thermo-compression bonding.[31]

The proposed antenna in [32] is fabricated on a high resistivity Si (HR-Si) wafer using DRIE. As can be seen from Figure 2.18, the H-plane dielectric horn antenna is fed by a dielectric ridge waveguide (DRW) and is compatible with the planar circuit integration. Since the antenna feed waveguide dimensions are smaller than those of a standard WR-01 waveguide (254 μm×127 μm), the authors propose a noncontact measurement approach to measure the antenna gain. The measured gain of the antenna is around 8 -12 dBi at the band of (750 – 1000) GHz but the reflection coefficient cannot be measured using this method. Also, due to the limitation of the method, the E-plane radiation pattern could not be measured.

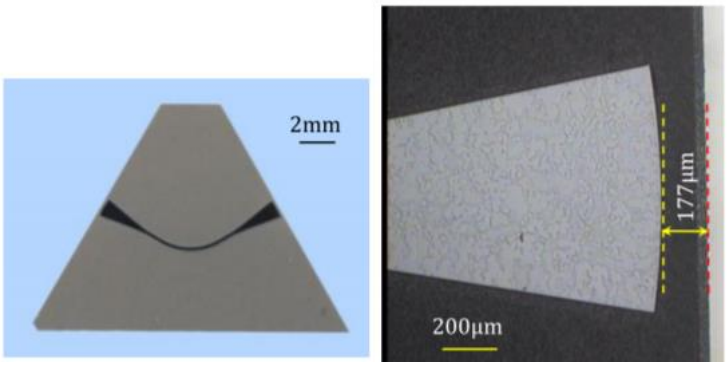

Figure 2.18: Fabricated H-plane dielectric horn in [32].

A corporate-feed slotted waveguide array antenna in the 350-GHz band is proposed as shown in Figure 2.19. The fabrication process of the laminated plates is made with silicon wafers and etched by the DRIE process. Five thin metallic laminated plates of 200 μm thickness have been used for the fabrication. These are gold-plated and then bonded with the diffusion bonding process.

A 16×16 element array antenna has been designed and fabricated in the 350-GHz band with the same proposed silicon process (Figure 2.19 (b)[33]. The broadband characteristic in terms of the antenna gain is demonstrated by measurement in this frequency band. The 3dB-down

gain bandwidth is 50.8 GHz in simulation and is 44.6 GHz in measurement. The top and lateral views of the antenna prototype are shown in Figure 2.19(b).

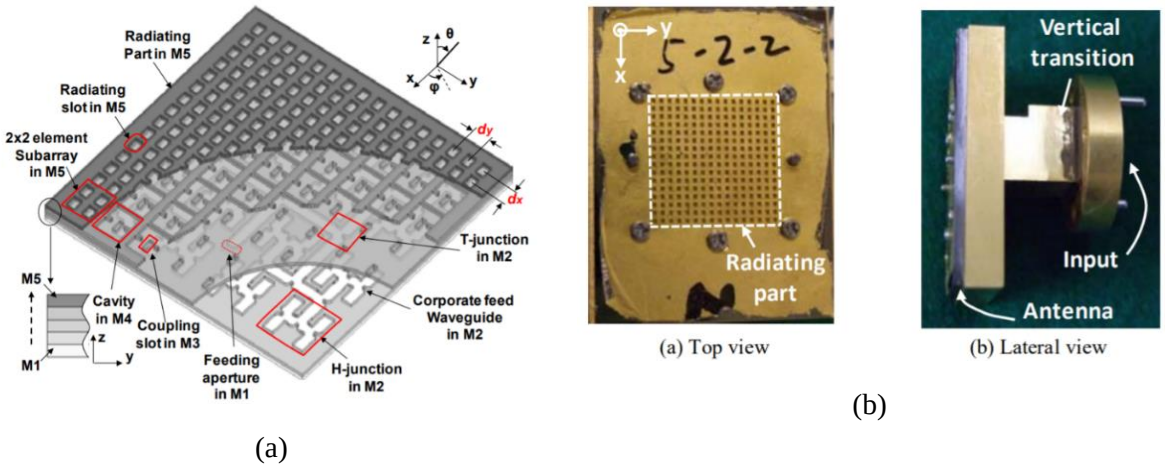

Figure 2.19: (a) 3D view of corporate-feed slotted waveguide array antenna, (b) 16×16 element array antenna prototype [33].

Corrugated horn antennas have been demonstrated and fabricated at 560 GHz with the DRIE process on silicon as shown in Figure 2.20. The measurement of two of the (2×2) 560 GHz array antennas has shown that the return loss and directivity are 13 dB and 22 dB, respectively. All of the measured antennas had below -25 dB of the cross-polarization and symmetrical beam patterns [34].

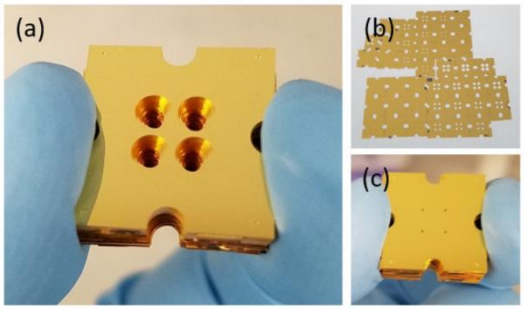

Figure 2.20: (a) Assembled (2×2) silicon corrugated horn antennas including the transition. (b) 38 platelets coated with gold metal before being assembled. (c) WR 1.5 (191 μm × 381 μm) waveguides on the backside of the stacked antenna [34].

Two high-gain flat array antenna designs operating in the 320 – 400 GHz frequency range are reported as shown in Figure 2.21. The two antennas show measured gains of 32.8 dBi and 38 dBi and consist of a 16 × 16 element array and a 32 × 32 element array, respectively, which are fed by a corporate H-tree beamforming network [35]. The measured operation bandwidth for both antennas is 80 GHz (22% fractional bandwidth), and the total measured efficiency is

above -2.5 dB and above -3.5 dB for the two designs in the whole bandwidth. The low measured loss and large bandwidth are enabled by optimizing the designs to the process requirements of the SOI micromachining technology used in that work.

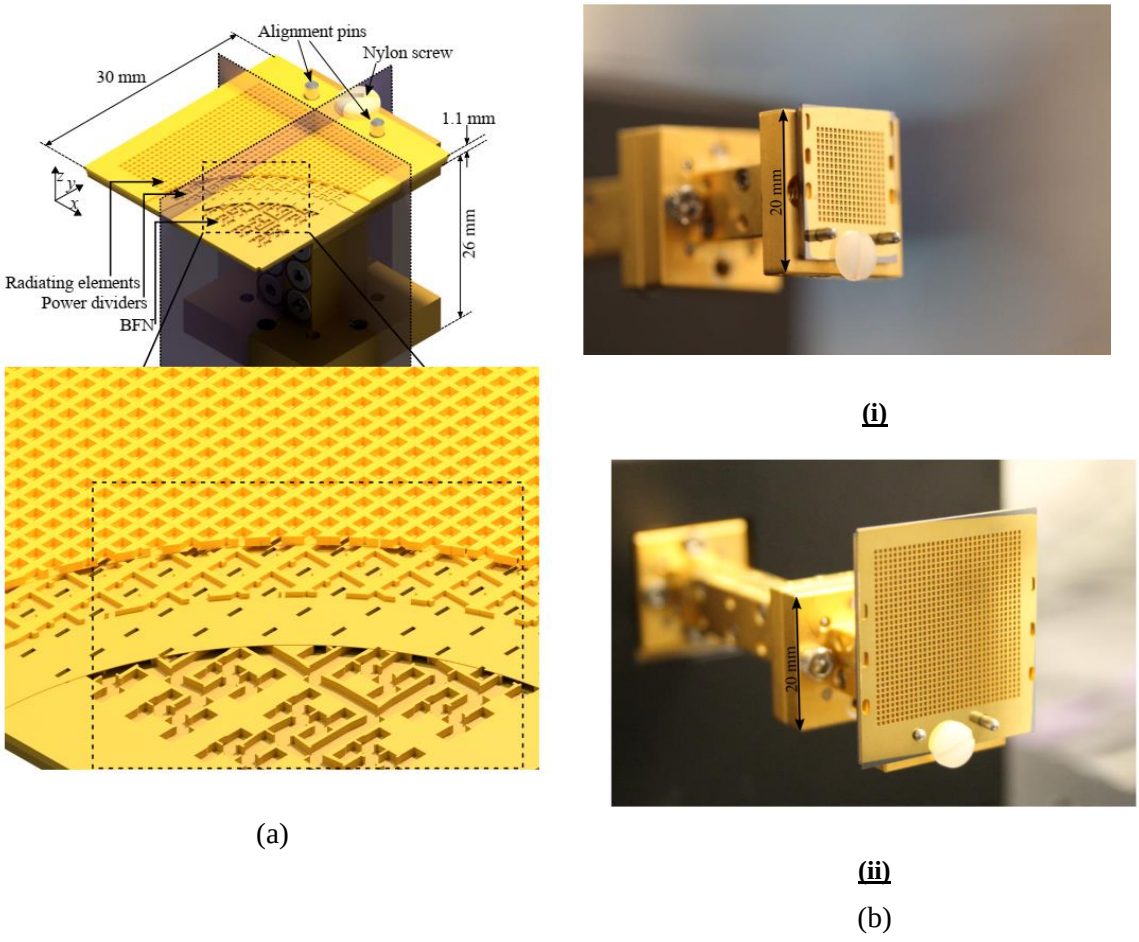

(a)

(i)

(ii)

(b)

Figure 2.21: (a) CAD model of the 32 × 32 element array mounted on a standard WM-570 waveguide piece (b) pictures of the manufactured antennas mounted on a standard WM-570 waveguide flange. The antenna in (i) is the 16 × 16 element array and the antenna in (ii) is the 32 × 32 element array. The standard flange size is 20 mm × 20 mm [35].

2.7 Conclusion

To conclude the technologies briefly discussed in terms of their pros and cons, Table 1.1 offers a comparison between them as a summary.

Table 1.1: Comparison between different fabrication technologies in literature.

Tech.	LTCC	Diffusion bonding	3D Printing	Electro-erosion	Micromachining
Frequency	Up to 300 GHz	Up to 300 GHz	Up to 300 GHz	Up to 100 GHz	Up to 300 GHz
Material	Substrate-based	Air-based	dielectric-based	Air-based	Air-based [36]
Material Losses	Moderate	Very low	High	Very low	Very low
Radiation losses	Very low	Very low	High	Very low	Very low
Allowed number of stacked layers	High	High	Moderate	Moderate	High (with increased complexity)
Electrical contact between metallic layer	Excellent	Excellent	Impossible	Excellent	Excellent
Accuracy	High	High (±10 µm)	High	Moderate	Very high

2.8 Multi-beam Antennas (MBAs)

An overview of the existing multi-beam antenna technologies, which include passive multibeam antennas (MBAs) based on quasi-optics beamforming, beamforming circuits, multi-beam phased-array antennas enabled by various phase-shifting methods, and digital MBAs with different system architectures.

The passive MBAs are a class of MBAs that achieve the desired beamforming in the RF domain without using any active components [13, 37]. In general, the passive MBAs contain a finite number of well-isolated input ports. Each port controls a single narrow beam pointing in a predefined direction. Multiple beams can thus be simultaneously emitted from a shared

aperture of a certain physical size for covering a prescribed angular range. The resolution is limited by the beamwidth, while the number of beams determines the range of coverage. Typically, the performance of the passive MBAs is characterized by the scanning range, polarization, gain, sidelobe level, bandwidth, port isolation, and efficiency. According to the system architecture and principle of operation, the passive MBAs can be divided into three categories:1) passive MBAs based on reflectors; 2) passive MBAs based on lenses; 3) passive MBAs based on beamforming circuits. We will focus on our work on the passive MBAs based on the lens.

2.8.1 Passive MBAs Based on Lenses

The lens-based beamforming components are transmitting devices that provide the targeted multibeam radiation. One side of the lens is illuminated by the input waves emitted from the feeding antennas, while the other side of the lens serves as the radiating aperture [38].

Luneburg lenses are quasi-optics beamforming, which is a spherically symmetric lens with a gradient refractive index (GRIN). The Luneburg lens [39] is a well-known device that focuses radiation emitted from a point source located on its perimeter, as shown in Figure 2.22, to a plane wave emanating from the diametrically opposite side of the lens (or vice versa), using a refractive index profile that decreases radially from its center. Such devices have been experimentally realized as a series of concentric rings, where the refractive index is varied in steps rather than as a smooth function of radius. A perfect Luneburg lens is isotropic and could support full angular coverage by moving the feeding point. At high frequencies, this kind of lens can be a feasible steerable antenna since arrays and phase shifters are complex and not even available in the market [40].

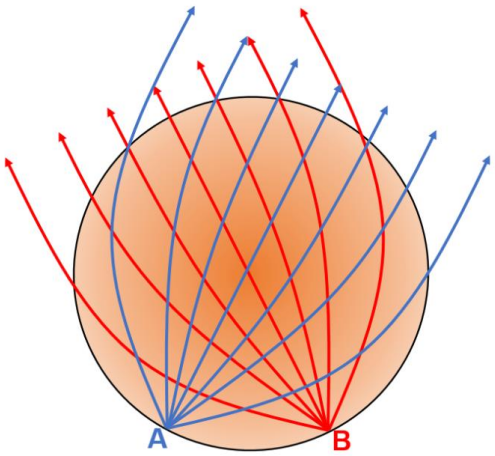

Figure 2.22: Cross-section of a standard Luneburg lens.

A Luneburg lens follows the relation between refractive index and radial position given in equation (2.1). In this equation, ‘‘ρ’’ stands for the current radius while ‘‘R” represents the out-most radius of the Luneburg lens. It can be seen from Figure 2.23 that the refractive index ‘‘n’’ falls from $\sqrt{2}$ to 1 from center to surface, while the relative permittivity ‘’ε_r’’ varies from 2 to 1. If a Luneburg lens is placed in air, there will be no reflections at the lens-air interface since the refractive index at the lens surface is the same as that of air. This solves the problem of reflection with conventional lenses.

$$n = \sqrt{\varepsilon_r} = \sqrt{2 - \left(\frac{\rho}{R}\right)^2} \tag{2.1}$$

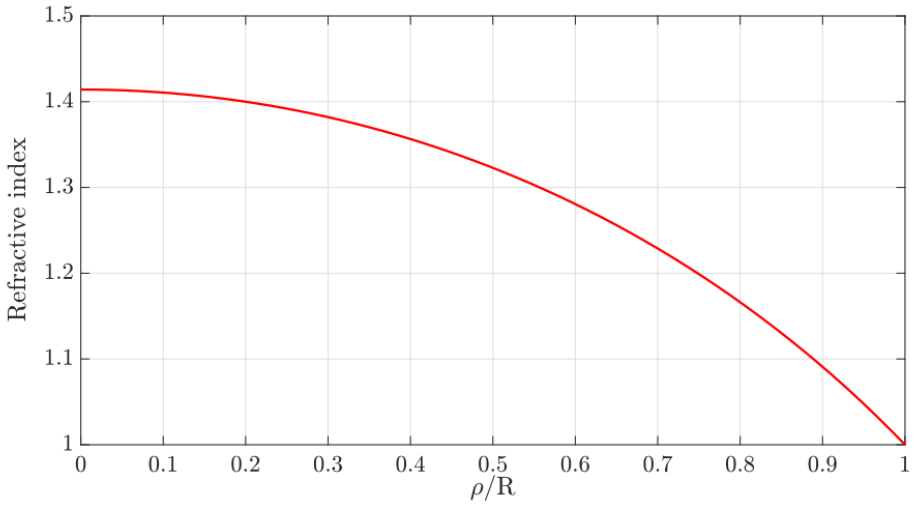

Figure 2.23: Refractive index variation of a standard Luneburg lens.

To design the Luneburg lens practically, from literature we found two types of materials have been used as shown in the following section.

2.8.1.1 Dielectric Electromagnetic Material

Since Rudolf Luneburg proposed the simple solution to generate two special foci with the gradient-index lens, different methods have been investigated to manufacture and implement it in microwave antenna applications. Authors in [41], showed that 10-discrete layers of dielectric were sufficient to provide Luneburg lens behavior instead of continuously varying refractive index materials. Their lens had 18 inches’ diameter and was aimed to be used at X band. They adopted equal ‘ε_r’ increment method for the 10 layers instead of equal ‘n’ increment, as relative permittivity is usually more directly measured than the refractive index. The focusing effect of multi-layer dielectric Luneburg lens with frequencies is explored in [42]. The authors simulated a 10-layer lens with a 200 mm diameter with a frequency varying from

2.45 GHz to 10 GHz. They showed that splitting the 3D lens model into a 1/4 sphere is enough to get the correct radiation pattern in simulation due to E-field symmetry and H-field symmetry. In [43], also built a 2D Luneburg lens operating in TE_{10} mode with an almost-parallel plate waveguide filled with polystyrene. The authors tuned the refractive index by changing the thickness of polystyrene.

In [44-46], the method of controlling permittivity changed to drilling small holes in dielectric disks instead of varying the height of the dielectric as shown in Figure 2.24. Adding air holes can decrease the equivalent dielectric constant by having less material per unit volume, and the density of holes determines the resulting refractive index. However, all these lenses have quite complex manufacturing procedures, like binding dielectric layers, contouring dielectrics, or drilling numerous holes.

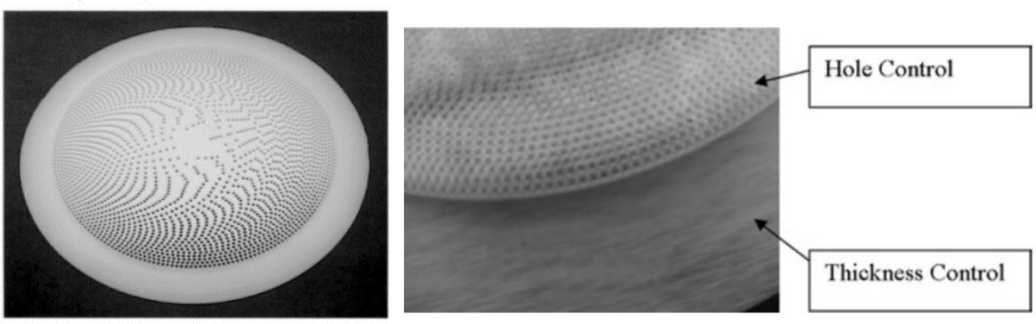

Figure 2.24: Luneburg lens by hole density method [44-46]

To achieve easier fabrication, a 2D metasurface Luneburg lens with a printed circuit board technique was designed [40]. As can be seen from Figure 2.25, the authors etched crossed microstrip lines over a copper-clad substrate and controlled the refractive index by meandering the transmission lines and varying line widths on each unit cell. Their lens operated at 13 GHz in TEM mode, with a tapered transmission line feed and a flare. The scanning angle was from -45° to $+45^{\circ}$ with a -3 dB cross-over level. The author in [47] also made use of the etching technique to fabricate a Luneburg lens with I-shaped unit cells at around 10 GHz. In 2010, authors presented another way to achieve a 2D Luneburg lens refractive index profile using Fakir's bed of nails substrate inside a parallel plate waveguide [48]. They modified the pin height to achieve the needed local refractive index at 10 GHz [49].

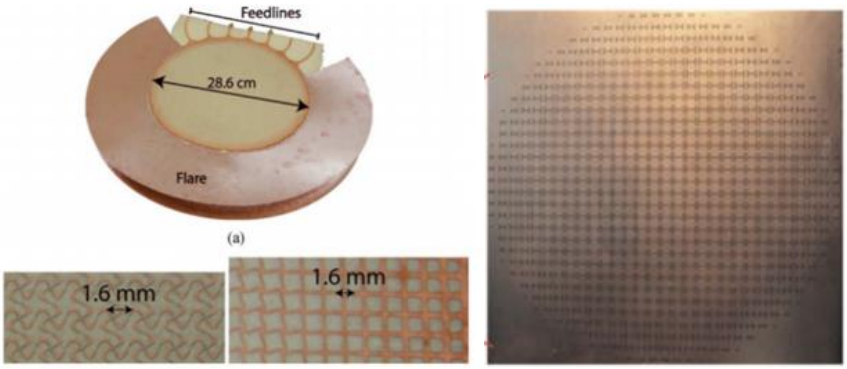

Figure 2.25: Metasurface Luneburg lens with printed circuit board [40], [47]

In 2012, a circular patch array with varying patch sizes on a dielectric substrate was applied and achieved Luneburg lens behavior inside a parallel plate waveguide [50]. The center frequency of their design is 13 GHz and the dielectric had a permittivity of 10.2. The authors also suggested two different flare structures match the impedance of thin waveguide and free space. However, since most of the energy was confined inside the substrate, the effect of flares was limited. In [51], a similar configuration was proposed.

2.8.1.2 Artificial Electromagnetic Material

Although huge progress has been made in fabricating methods, all these Luneburg lenses contain dielectric. At high frequencies, electromagnetic waves propagating along the surface of the dielectric substrate will extend many wavelengths into dielectric, causing relatively high dielectric loss. Moreover, some of them do not support TEM waves, which leads to intrinsically limited bandwidth [52]. In a contrast, metals are good conductors with large and imaginary dielectric constants at microwave frequencies. Electromagnetic waves are almost all screened out due to the high conductivity of the metal, stopping fields to propagate inward [52].

In [53], it is theoretically demonstrated and experimentally validated that a periodic and regular vertical metal posts array on a ground plane, as shown in Figure 2.26, can act as an isotropic artificial dielectric material, and therefore can be operated as a lens. The post's size, spacing, and height controls the refractive index. It is important to note that there is no upper ground plane on the top of the metal posts The authors proposed an approximate analysis of the index based on a transverse resonance method (TRM) which gives an analytical formula to derive 'n_{eff} ' from the physical parameters of the metal post structure.

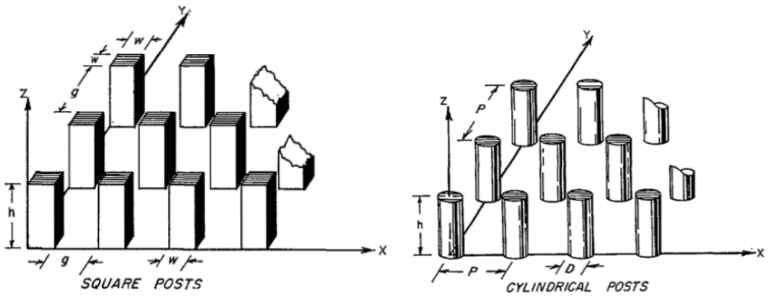

Figure 2.26: Metal posts as a surface-wave structure [53].

In [54], a photonic bandgap (PBG) structure, based on periodic and regular metal posts in a parallel-plate waveguide (PPW), is proposed to guide surface waves as shown in Figure 2.27. It has been demonstrated that periodic metal posts have arbitrary surface impedances and guide surface waves. In Figure 2.27 (b), the cross-sectional view of the PBG structure and its transverse resonance equivalent circuit are presented. Using the transmission-line theory and considering post dimensions, the surface impedance is derived as

$$Z_{TM} = jW\eta_1 \tan(k_1 t) \tag{2.2}$$

where $\eta_1 = \sqrt{\mu_0/\varepsilon_0\varepsilon_1}$,$k_1 = 2\pi/\lambda$, and $W = (P - D)/P$ is the ratio of the length unfilled by the post to the period.

The relation between the required refraction index 'n' and metal post height $'t'$ is obtained using the TRM. From the transverse resonance condition, the sum of two impedances $\vec{Z}_{x=t^+}$, and $\overleftarrow{Z}_{x=t^-}$ in Figure 2.27 should be zero on the resonance line, i.e., $\vec{Z}_{x=t^+} + \overleftarrow{Z}_{x=t^-} = 0$, which is written as

$$\sqrt{n(r)^2 - \varepsilon_{r2}}\ \tanh\left(k_0\sqrt{n(r)^2 - \varepsilon_{r2}}\,(h-t)\right) = \frac{\varepsilon_{r2}}{\sqrt{\varepsilon_{r1}}}\, W \tan(k_1\, t) \tag{2.3}$$

This equation is numerically solved for the desired metal post heights 't'. The concept is applied to design and fabricate a PPW Luneburg lens at 76.5 GHz for radar application. Contrary to [53], there is an upper plate on the top of the metal posts, and it can be noted that the PPW spacing is constant.

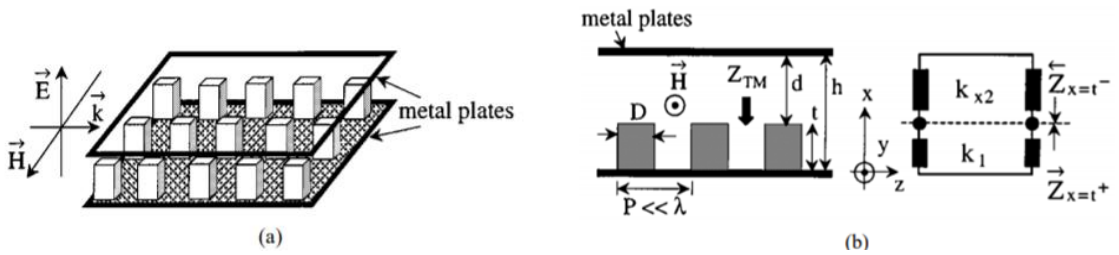

Figure 2.27: Geometry of the PBG structure. (a) periodic and regular metal posts in a PPW. (b) cross-sectional view and transverse resonance equivalent circuit of the structure [54].

In [55], the influence of lattices and metal post shapes at millimeter-wave frequencies, on the performances of an asymmetric parallel-plate waveguide Luneburg lens (APWLL) is studied. Square, hexagonal, and circular metal post shapes were considered, and also square and hexagonal lattices, as shown in Figure 2.28(a) and Figure 2.28(b), respectively. It was found that hexagonal lattice with circular-shaped metal posts is best as an actual isotropic homogeneous artificial material with angular independence.

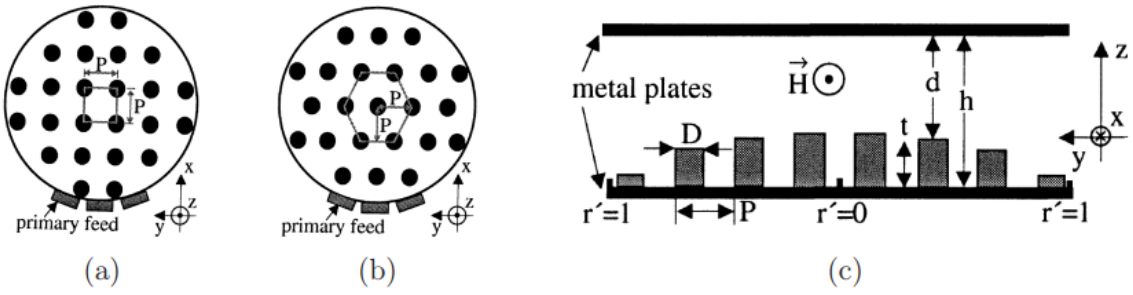

Figure 2.28: Top view of two APWLLs with circular posts: (a) square lattice, (b) hexagonal lattice, and (c) cross-sectional view of the APWLLs [55].

Recently, a full metal metasurface with 2-layers of glide-symmetric configurations was proposed [56]. It has a higher effective refractive index and ultra-wideband, resulting in a flat Luneburg lens operating from 4 to 18 GHz. In order to implement this technology at 60 GHz frequency, a different unit cell for the Luneburg lens was proposed in [57]. Some other applications of glide symmetry technology can be found in [58-60].

PART I: HIGH-GAIN ANTENNAS FOR SUB-THZ WIRELESS COMMUNICATIONS

Chapter 3 Circularly Polarized Nonplanar Antenna

3.1 Introduction

Recently, the terahertz (THz) frequency spectrum spanning from 0.1 THz to 10 THz has been highly valued in different fields such as wireless cognition, imaging, spectroscopy, sensing, super-high precision positioning, and future wireless communications [1]. Sub -THz frequency (100 GHz - 1 THz) band, which has not been allocated for specific uses yet, has an extremely broad atmospheric transmission window (~100 GHz bandwidth), with manageable losses, and will be ideal for building wireless links with ultra-high data rates up to a terabit per second (Tbps) with super-reliability and minimal latency communications. All of these properties make the sub-THz spectrum ideal for sixth-generation (6G) wireless mobile communications [2].

At THz frequencies, the need for high gain antennas is very important in order to overcome high atmospheric absorption, and high path loss at these frequencies, which will affect the budget of the wireless link. The need for directive antennas for 6G wireless fronthaul/backhaul for cellular mobile radio networks is increased in the case of applying point-to-point high data rate wireless links according to fixed radio systems [61]. Moreover, circularly polarized (CP) antennas are required for any modern wireless communication system due to their ability to avoid multipath fading and polarization mismatch between the antennas and enhance the channel capacity of the communication link. Therefore, it is important to develop front-end components focusing on CP THz antennas. For sub-THz frequencies (i.e. 300 GHz), manufacturing errors become crucial concerning antenna characteristics, so a simple structure, such as a horn, is preferred. Horn antennas have been proposed at THz frequencies [16, 25, 26, 34, 62, 63] with good radiation performance but no one has designed CP horn antennas at Sub-THz frequencies.

Recently, progress in Wire-cutting and die-sink Electrical Discharge Machining (EDM) technique in terms of accuracy and very precise control of the machining tools has made possible the fabrication of very delicate components needed for antennas at the millimeter-wave frequency [21, 22, 64]. A directive and low loss antennas obeying the THz-wireless communication requirements can be obtained. Compared to a conical corrugated horn antenna with 24 gold-coated silicon platelets at 330 GHz manufactured by using a deep reactive-ion etching (DRIE) process of silicon micromachining [65], our structure is very simple with three main components of brass and made economically by using a metal cutting Wire EDM.

In this chapter, we numerically and experimentally investigate a circularly polarized conical horn antenna for the WM-864 frequency (220 GHz-330 GHz) band, which has been fabricated

by direct Wire EDM machining in a single block of metal. The rest of the paper is organized as follows. Section 3.2 describes the basic concept of conical horn antenna design in terms of parametric study and its design factors for improving the antenna characteristics. Section 3.3 presents a fabricated prototype of the Sub-THz CP horn antenna. Finally, the measured reflection coefficient (S11), antenna directivity, axial ratio (AR), 2D radiation patterns in both principle planes, 2D AR, and the radiation pattern at different frequencies, confirm the simulations are provided in 3.4 To the best of our knowledge, this is the first time a 300 GHz CP conical horn antenna has been successfully manufactured by direct machined using Wire EDM in one block of metal. In comparison with the CP horn antenna proposed in [66] using EDM technology at 110 GHz, which is comprised of a series of hexagonal and transition waveguides, our proposed structure is considered to be much easier for design and fabrication at 300 GHz.

3.2 Antenna Design and Configuration

The geometry of a conical horn antenna is shown in Figure 3.1. To design a conical horn for a desired gain ‘‘G’’ of 20 dBi at a 300 GHz design frequency (free space wavelength $\lambda_0 = 1$ mm), we use the following procedure [67]:

$$a_i = \frac{3\lambda}{2\pi} \tag{3.1}$$

$$a_o = \frac{\lambda}{2\pi}\sqrt{10^{(G_{dBi}+2.91)/10}} \tag{3.2}$$

$$R = \frac{4a_o^2}{3\lambda} \tag{3.3}$$

$$\theta = \sin^{-1}\left(\frac{a_o}{R}\right) \tag{3.4}$$

$$L = \frac{a_o - a_i}{\tan\theta} \tag{3.5}$$

where “a_i” is the radius of the throat horn, “a_o” is the radius of aperture horn, “R” is the slant length, “θ” is the flare angle, and “L” length of the conical horn.

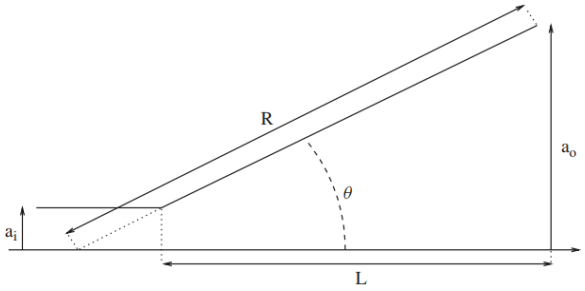

Figure 3.1: Conical horn geometry.

Figure 3.2 illustrates the 3D geometrical view of the proposed antenna structure. The antenna consists of three components, which are waveguide feed, circular polarizer disk, and conical horn respectively. The waveguide feed is a standard WR-03 rectangular waveguide that works in a WM-864 frequency band. This component, the rectangular waveguide, works as feeding for the whole structure without using a transformer section from the rectangular waveguide WR-03 to the circular waveguide in the input of the conical horn.

The conical horn element is a smooth-walled conical horn antenna that is easier to manufacture at high frequencies (i.e. 300 GHz) compared to a corrugated walled which becomes complicated in terms of the manufacturing process. For our desired gain of 20 dBi, the dimensions of the conical horn antenna were calculated by using (1-5). We found the optimum dimensions for the radius of the horn throat is $a_i = 0.4$ mm, the radius of the horn aperture $a_o = 1.9$ mm ,and the conical horn axial length $L = 4$ mm.

The aperture "a_o" and throat "a_i" radii of the conical horn play a very important role in the performance of the antenna such as directivity. We studied the effects of different dimensions of a conical horn antenna in terms of directivity with respect to frequency as shown in Figure 3.3. As the flare angle increases (in our study i.e. a_o), the directivity for an assumed horn length ($L = 4$ mm) increases until it reaches a maximum, beyond which it begins to decrease. The decrease is a result of the dominance of the quadratic phase error at the aperture. From Figure 3.3 it's clear that the radius of the horn aperture $a_o = 1.9$ mm and radius of horn throat $a_i = 0.4$ mm gives the highest directivity, which cover the desired bandwidth from 270 GHz to 330 GHz.

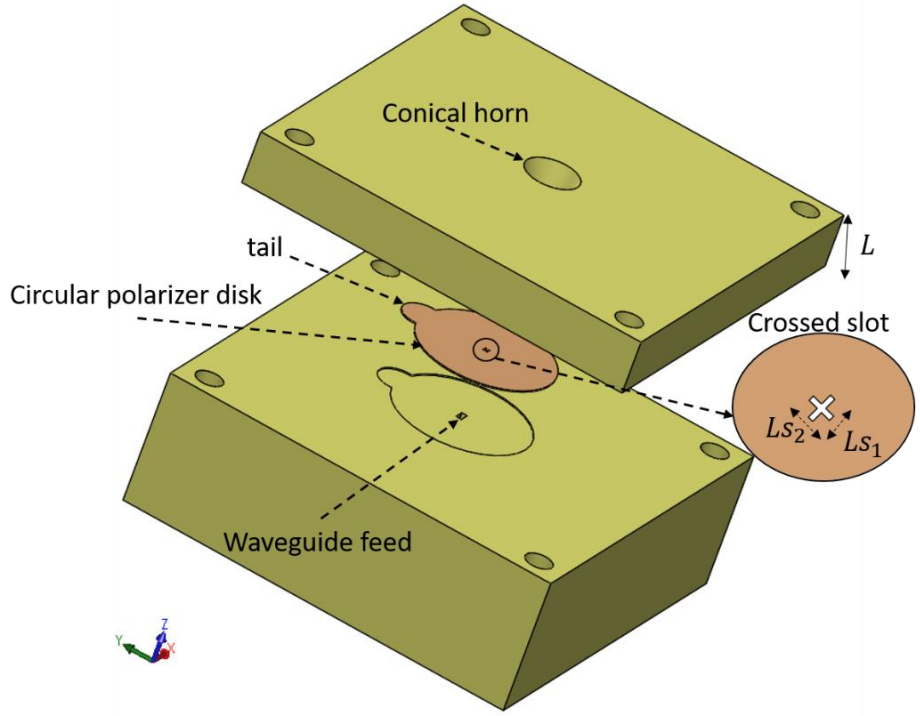

(a)

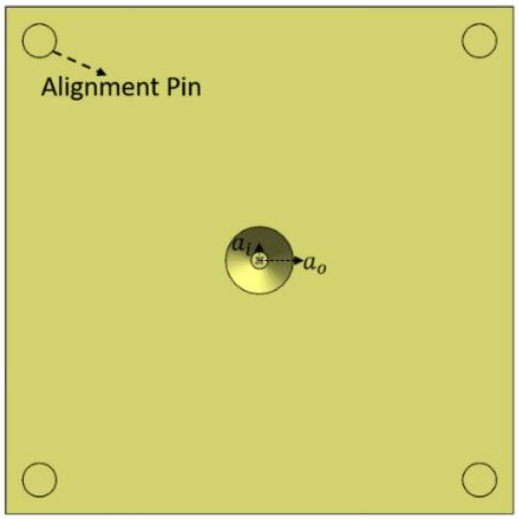

(b)

Figure 3.2: Structure of the proposed antenna (a) 3-D exploded view, (b) top view.

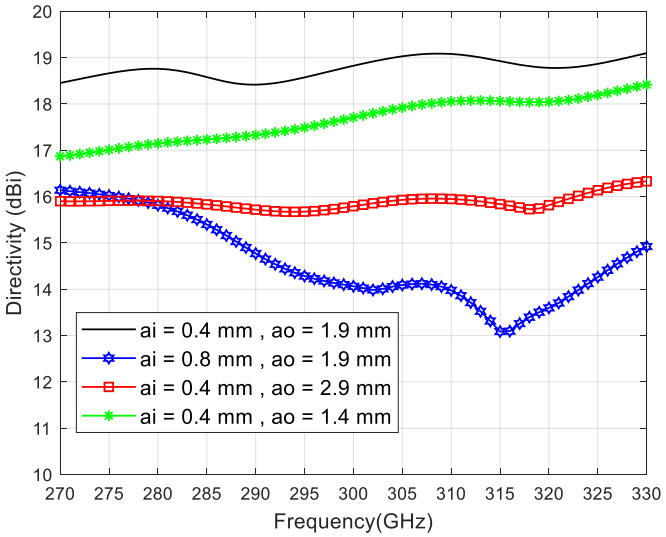

Figure 3.3: The directivity versus frequency for different dimensions of the conical horn antenna.

We noticed that the length of the crossed slot of the circular polarizer disk has a large impact on the AR as shown in Figure 3.4. We fixed the length of slot 1 as ($Ls_1 = 0.51$ mm) and change the length of slot 2 "Ls_2'' by a fixed value of ''s'' with respect to Ls_1 (i.e. $Ls_2 = Ls_1 - s$). It is clear from Figure 3.4 that a change in the small value of ''s'' (20 μm) shifts the AR below 3 dB in frequency from 305 GHz to 312 GHz.

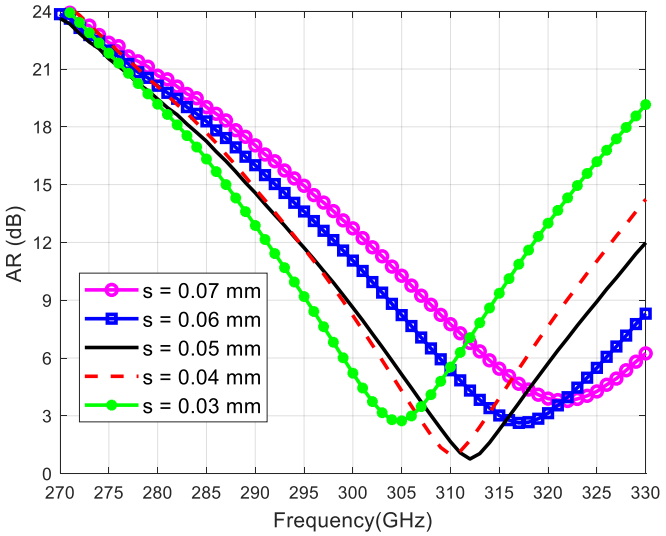

Figure 3.4: The axial ratio (AR) versus frequency for different lengths of crossed-slot antenna.

The AR in the azimuth plane is kept below 3dB on a range of angle theta ''$\boldsymbol{\theta}$'' up to $\sim \pm 10^{\circ}$ which covers the half-power beamwidth (HPBW) equal to 18.5°, as defined in Figure 3.5(a). Also, it is noted that in the elevation plane shown in Figure 3.5(b), the AR is less than 3dB over

the whole main lobe, except for the highest value of frequency at 315 GHz. The maximum gain of the radiation pattern is equal to 18.4 dBic in both planes at the broadside direction.

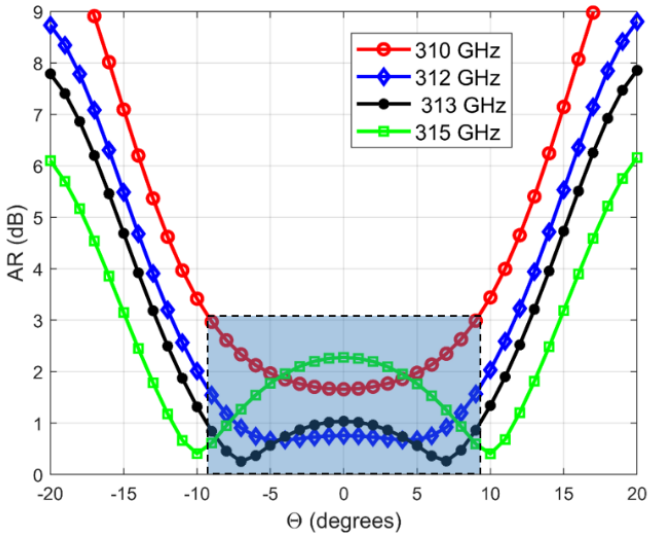

(a)

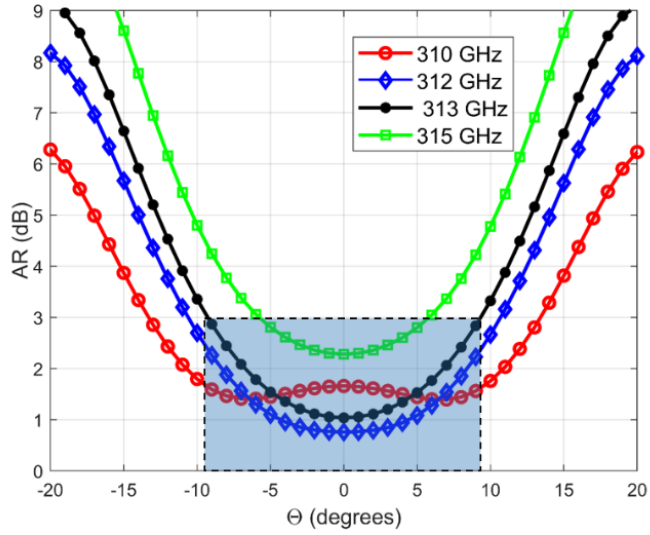

(b)

Figure 3.5: The simulated AR vs theta angle in (a) Azimuth-Plane, and (b) Elevation-Plane at different frequencies 310 GHz,312 GHz,313 GHz, and 315 GHz.

Figure 3.6 illustrates the simulated realized gain, radiation, and total efficiencies of the proposed antenna. The total efficiency is around 87.5%, the radiation efficiency is 99%, and the realized gain is 18.5 dBic at 312 GHz.

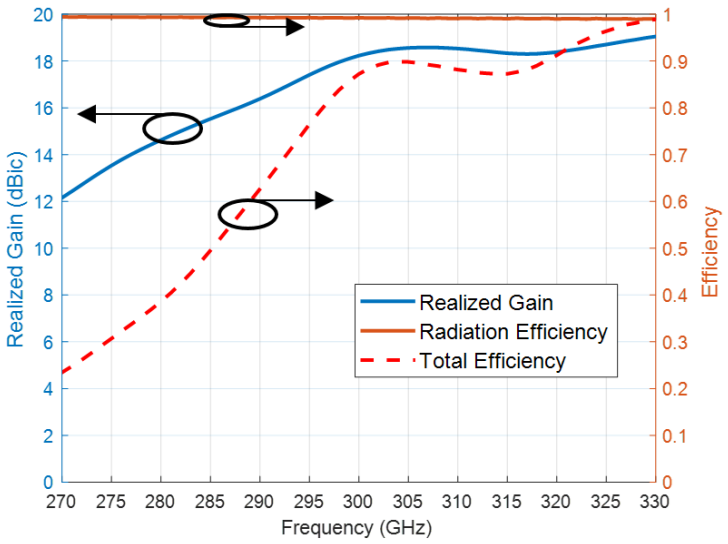

Figure 3.6: The simulated realized gain, radiation efficiency, and total efficiency versus frequency of the proposed antenna.

3.3 Fabrication Process

There are three modern manufacturing technologies used to produce the antenna structure with very delicate components. These are Wire-cutting EDM, mechanical drilling, and laser-cutting. Wire-cutting EDM is a thermo-electrical process that uses a continuously moving metal wire (usually brass) used as an electrode (tool) to remove material by a series of sparks produced between the workpiece and the electrode as shown in Figure 3.7. A stream of dielectric fluid (deionized water) continuously flowing in the machining zone, is used to wash away tiny particles being eroded, regulate the discharge, and keep the wire and workpiece cool. The wire and workpiece must be electrically conductive [68, 69].

The waveguide feed and the conical horn were manufactured by wire-cutting EDM technique in a brass block with an electrical conductivity $\sigma = 35.86 \times 10^6$ Sm^{-1}. This Wire-cutting EDM is direct machining and has features of simplicity and mechanical robustness since the geometry of the proposed antenna is directly engraved onto the block of metal.

Figure 3.7: Sinker electrical discharge machining (EDM).

We used mechanical drilling technology for a novel footprint disk of a circular polarizer with a thickness of 100 μm and four-hole alignments parts for the whole structure. Also in order to avoid the movement crossed slot in the circular polarizer disk a small tail is provided as shown in Figure 3.2(a). A laser etching technique has been used to create crossed slot of circular polarizer disk in the proposed antenna as narrower as 100 µm (value of slot width) by using (LPKF ProtoLaser S 124102 laser machine). The infrared laser beam (λ= 1080 nm) is focused on the footprint disk of the circular polarizer with a thickness of 100 μm with the appropriate settings, such as laser scan speed (400 mm/s), laser spot size (25 µm × 25 µm) and fluency (10 W/spot). The final prototype of the fabricated proposed antenna is shown in Figure 3.8. The circular polarizer disk with a crossed slot can be easily replaced by another disk with a longitudinal slot; in this case, the antenna will be linearly polarized.

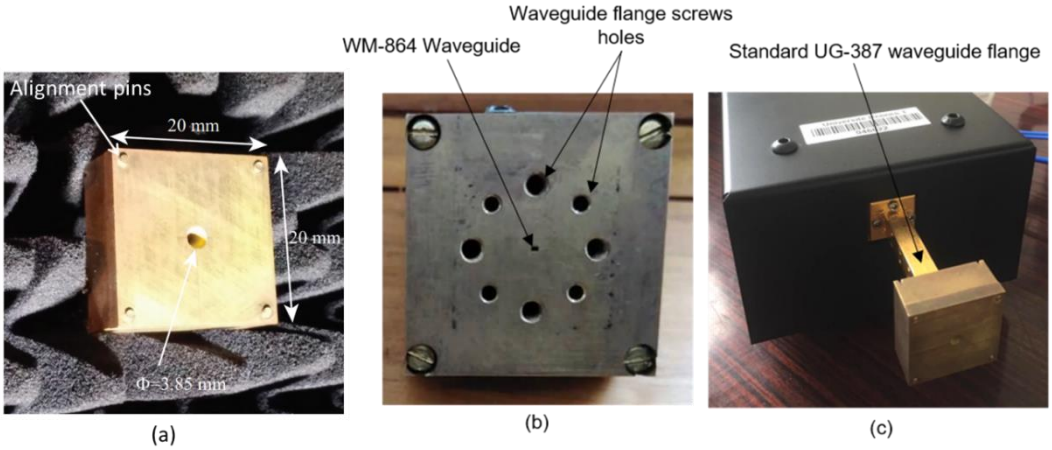

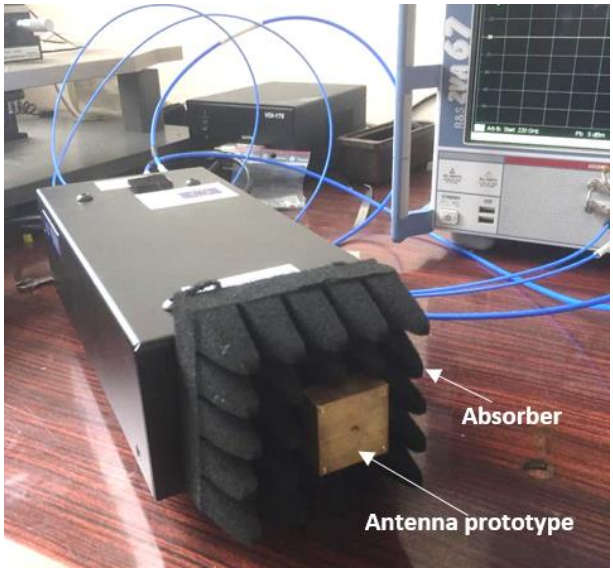

(d)

Figure 3.8: Pictures of the 300 GHz CP conical horn prototype fabricated by Wire-cutting EDM (a) Antenna prototype (top view) (b) feeding of antenna prototype (bottom view), and (c) Antenna prototype with absorber mounted on a standard UG-387 waveguide flange.

3.4 Experimental Results and Discussion

The measurement setup for impedance matching characterization can be seen in Figure 3.9, where (a) is a Vector Network Analyser (Rohde & Schwarz ZVA-67) connected to, (b) a local oscillator frequency (Rohde & Schwarz SMB 100A). The local oscillator frequency is coupled to Virginia Diodes Inc. (VDI) frequency extender constructed for 220 − 330 GHz (c) where WR-3.4 flanges (d) is connected to the antenna under test (e).

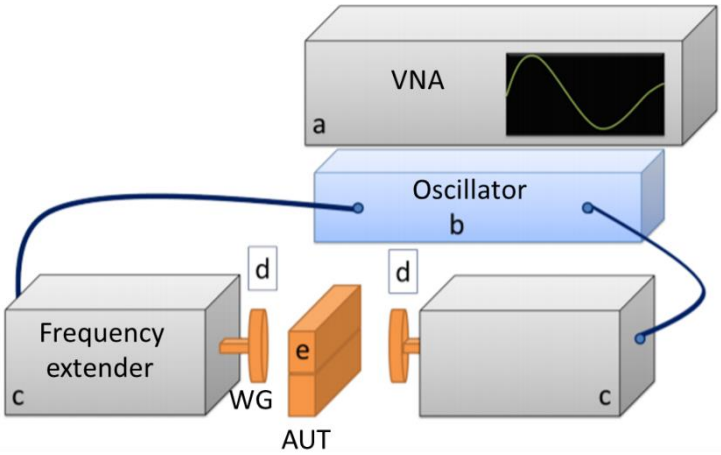

Figure 3.9: Measurement setup of S- parameter. a) network analyzer (Rohde & Schwarz ZVA-67), b) local oscillator frequency (Rohde & Schwarz SMB 100A), c) VDI frequency extender, d) WR-3.4 flange, e) antenna under test (AUT).

The measurement of the 300 GHz CP conical horn antenna showed that the reflection coefficient (S_{11}) less than -15 dB in the range of interest from 270 GHz to 330 GHz is as shown in Figure 3.10. The measured RHCP realized gain is 18.2 dBic at 303 GHz and total directivity is 18.3 dBic at 312 GHz.

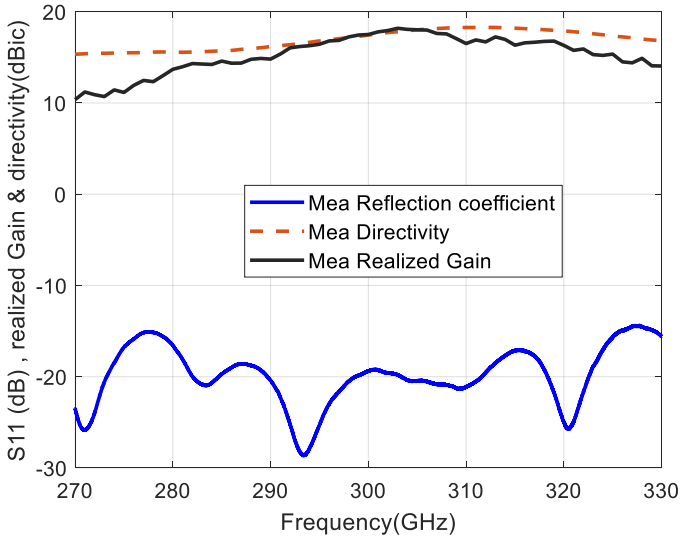

Figure 3.10: Measured reflection coefficient (S11), realized gain, and directivity for the prototype of the 300 GHz CP horn antenna.

The far-field measurement setup based on a compact range of millimeter-wave anechoic chamber facilities used at IETR is shown in Figure 3.11.

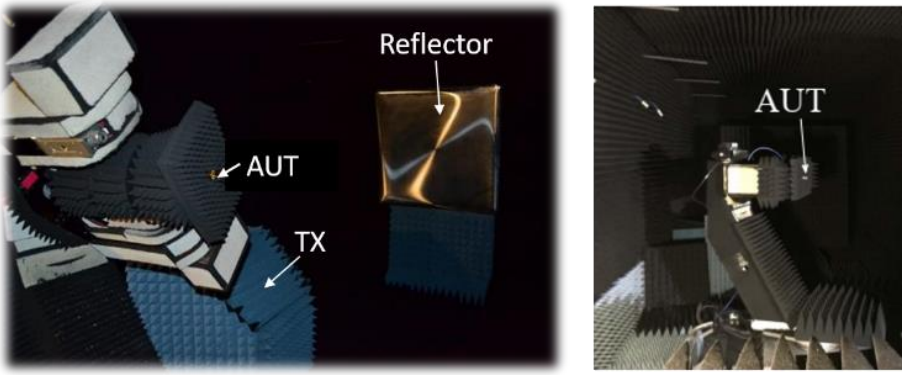

Figure 3.11: Antenna radiation pattern far-field measurement setup at IETR.

The simulated and measured AR of the proposed antenna is shown in Figure 3.12. The minimum measured AR at 312 GHz is 1.15 dB with the measured 3-dB AR bandwidth of 7 GHz between 309 GHz to 316 GHz being 2.3%. This frequency shift is due to the

manufacturing tolerance. There is a good agreement between the simulated and measured results.

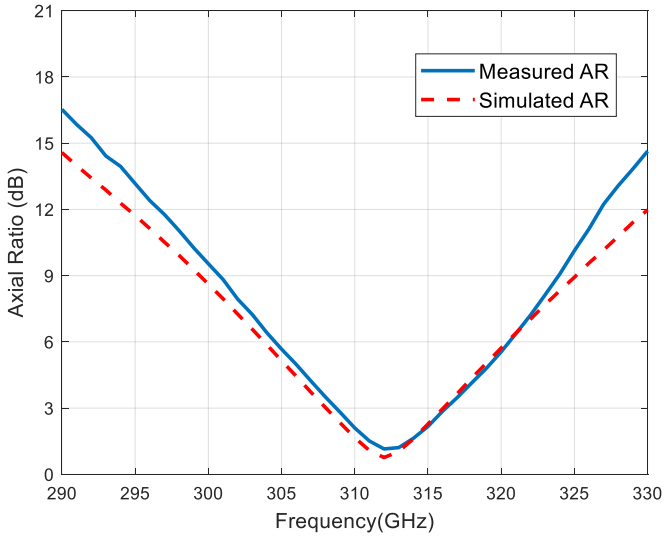

Figure 3.12: Axial ratio (simulated and measured) of 300 GHz CP conical horn antenna.

The measured directivity of the proposed antenna is given in Figure 3.13, which is obtained by integrating the 3D measured radiation pattern of the antenna under test (AUT) over the upper hemisphere. The measured broadside RHCP directivity reaches 18.3 dBic at 312GHz, while the simulated directivity is nearly 19 dBic. Also, note that there is a good agreement between the simulated and measured results of the proposed antenna.

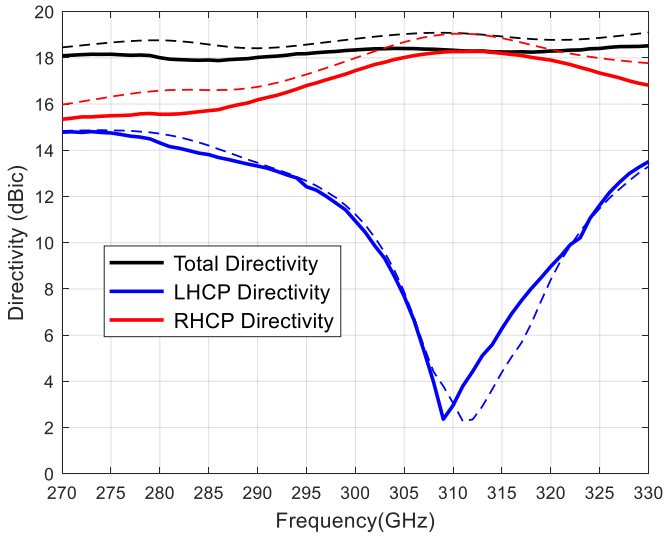

Figure 3.13: Measured (solid lines) and simulated (dashed lines) of the total, RHCP, and LHCP directivities.

Figure 3.14 shows the 2D measured far-field pattern of the proposed antenna in both principal planes (azimuth, and elevation), varying as a 2D plot with each point colored according to its normalized gain value in dB for the RHCP radiation pattern, and left-hand circular polarized (LHCP) radiation pattern for different frequencies 309 GHz, 312 GHz, 313 GHz, and 316 GHz. It is noted that the antenna works as RHCP radiation pattern which is the co-polarization and LHCP radiation pattern which is cross-polarization. It's clear from Figure 3.14 that the measured normalized gain occurs at the broadside direction, which is equivalent to azimuth ($az = 0^{\circ}$) and elevation ($ele = 0^{\circ}$).

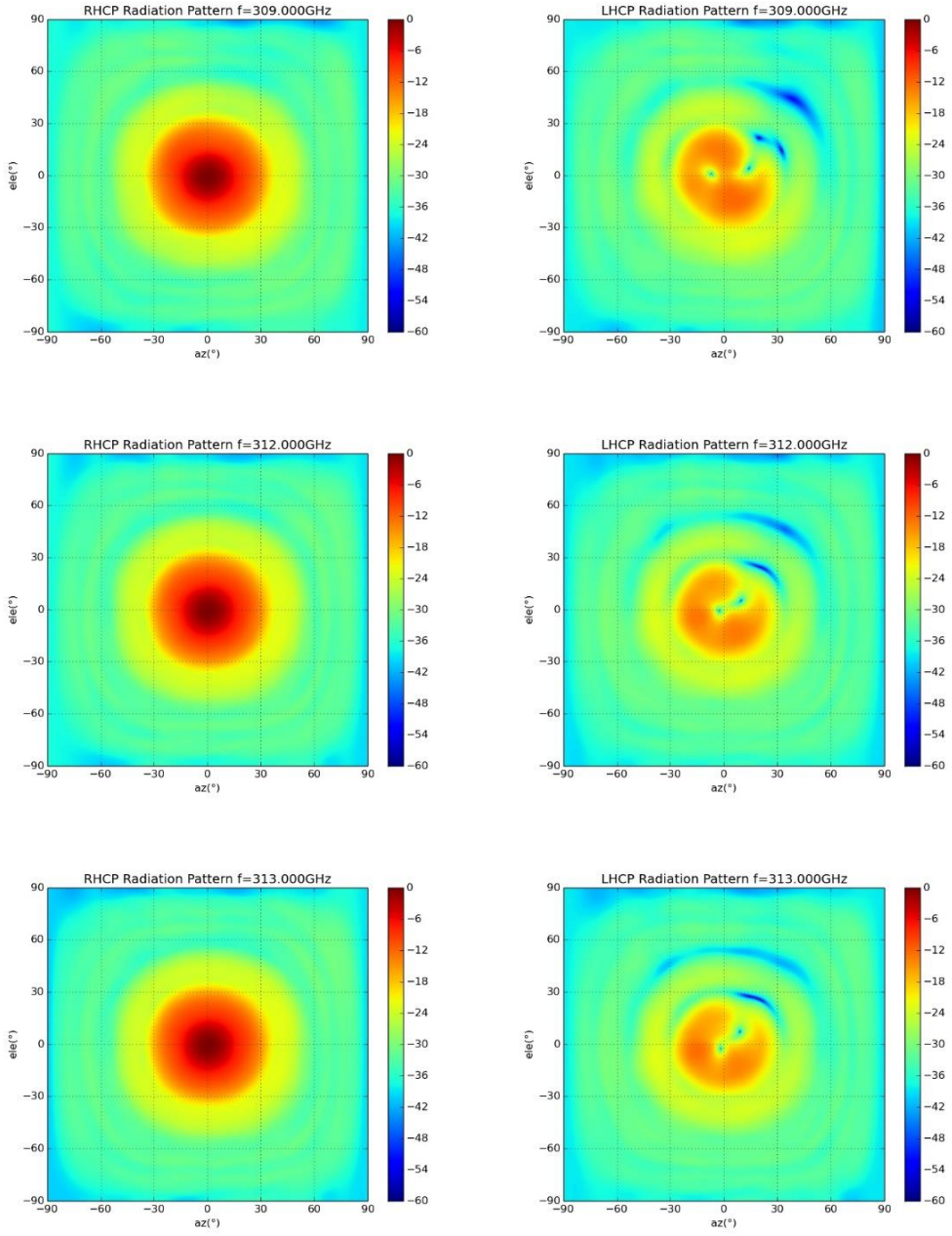

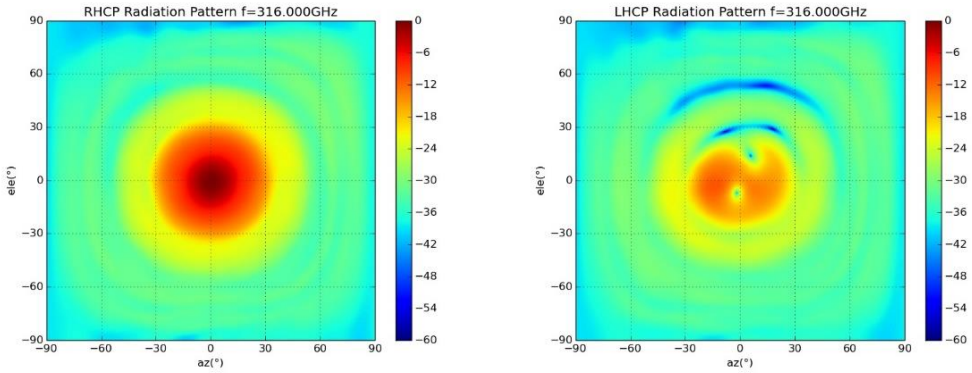

Figure 3.14: Measured normalized 2D co-polarization (RHCP), and cross-polarization (LHCP) radiation patterns of the proposed antenna at 309 GHz, 312 GHz, 313 GHz, and 316 GHz.

Figure 3.15 illustrates the 2D measured AR plots of the proposed antenna at 309 GHz, 312 GHz, 313 GHz, and 316 GHz. The AR is kept below 3 dB within the scope of the main beam between -10° to 10° at broadside direction for frequencies shown here in this figure (309 GHz, 312 GHz, 313 GHz, and 316 GHz, respectively). The AR reaches a lower value near 1 dB at 312 GHz, and 313 GHz as shown in the figure by the black color in the bar right of the plot.

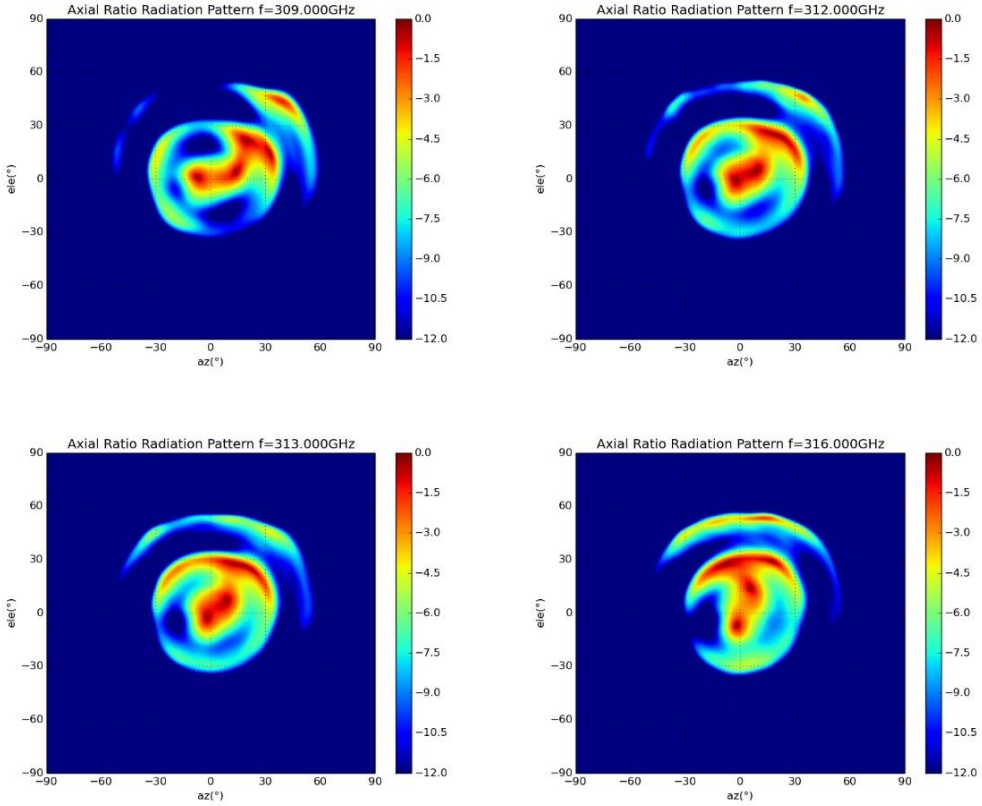

Figure 3.15: Measured normalized 2D axial ratio plots at 309 GHz, 312 GHz, 313 GHz, and 316 GHz.

The measured and simulated normalized RHCP radiation patterns of the proposed antenna in both the azimuth plane and elevation plane at 300 GHz, 309 GHz, 312 GHz, 313 GHz, and 316 GHz are given in Figure 3.16 It can be seen that, because of the symmetry of the antenna, measured radiation patterns of both planes are similar, and agree well with the simulated results. The normalized cross-polarization pattern plots (LHCP) of the proposed antenna are also given in Figure 3.16. The maximum isolation between the co-polarization RHCP and its cross-polarization LHCP is more than 10 dB except at 300 GHz. The measured cross-polarization levels are better than 20 dB below the main beam at the broadside direction at 312 GHz, and 313 GHz. The first sidelobe levels of the normalized RHCP radiation pattern are below -20 dB at the measured frequency.

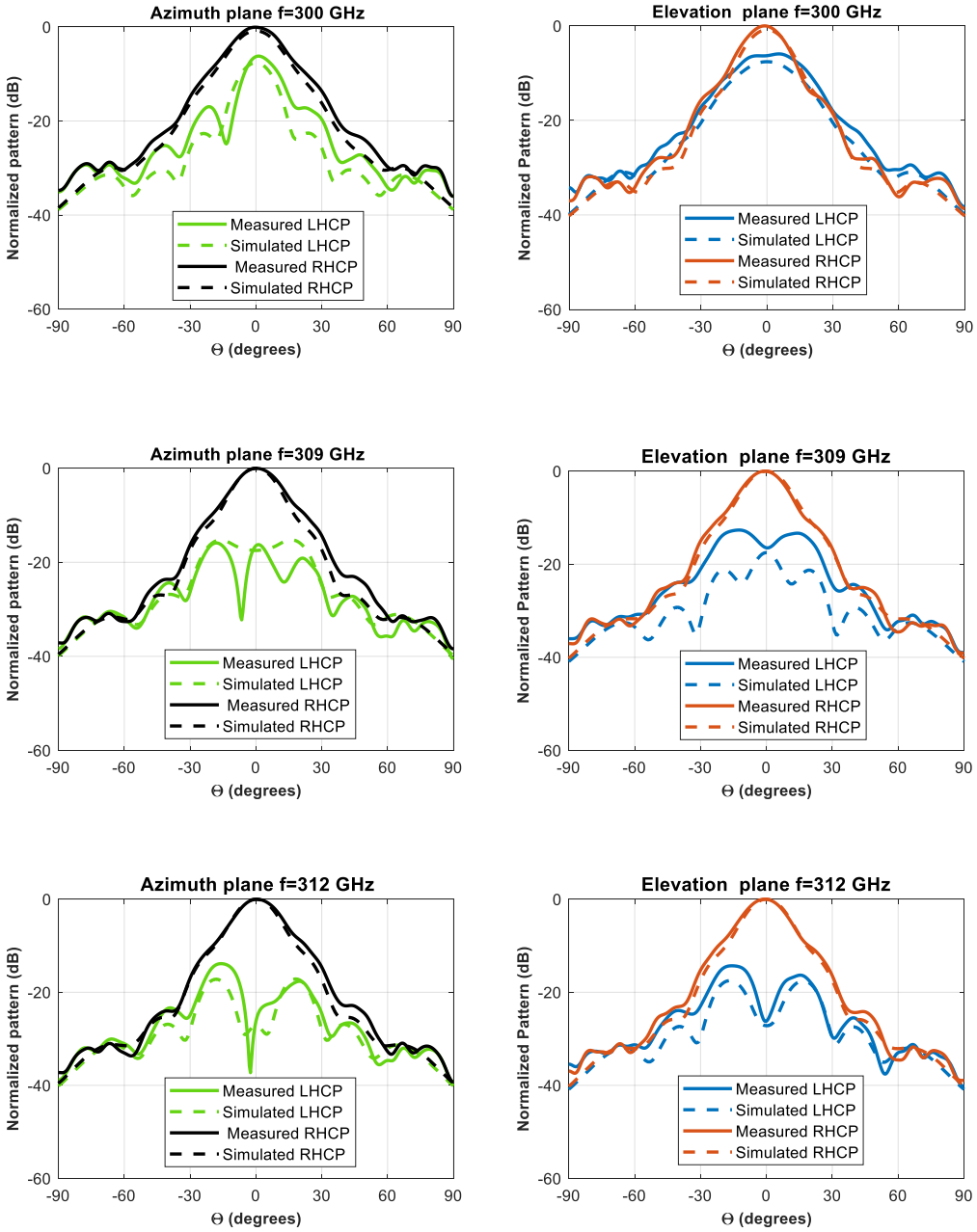

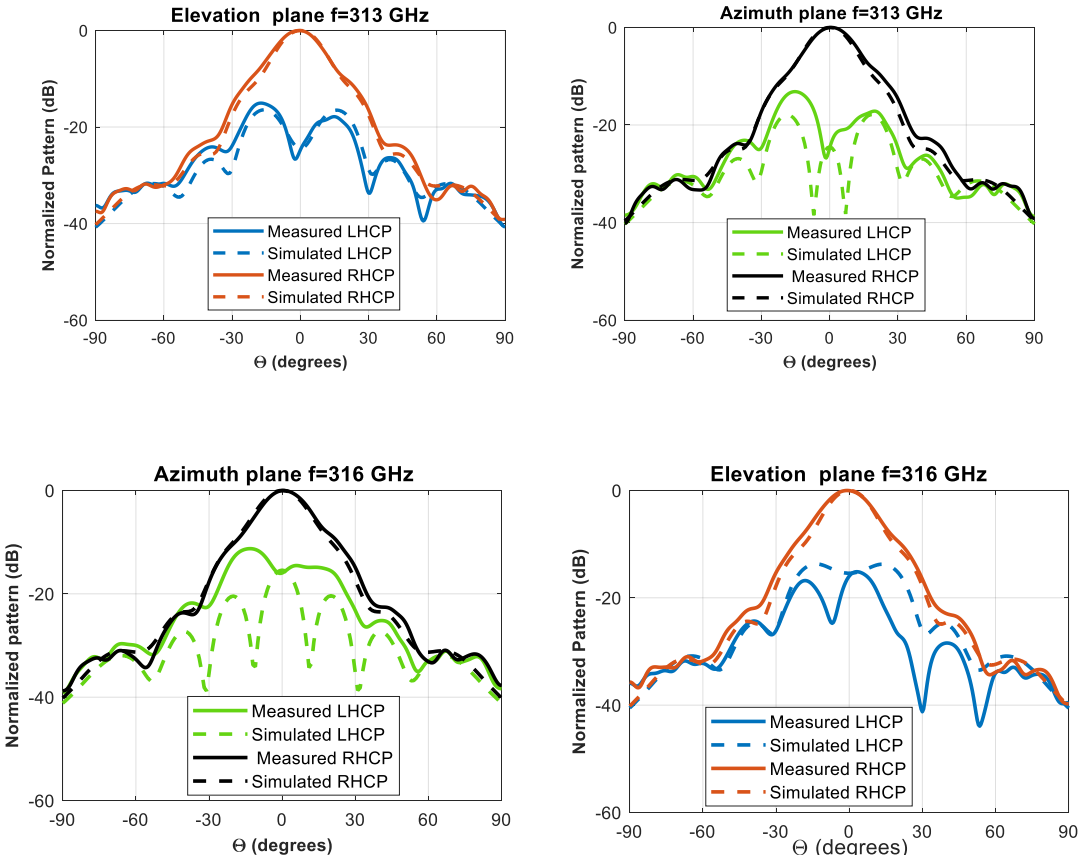

Figure 3.16: Measured and simulated normalized radiation patterns of the proposed antenna of the principal planes at different frequencies: f = 300 GHz, f = 309 GHz, f = 312 GHz, f = 313 GHz, and f = 316 GHz.

The measured normalized radiation patterns at 312 GHz of the proposed antenna over a wide range of cut-plane observation angles at 0 ˚, -45 ˚, -90 ˚, and -135 ˚ are shown in Figure 3.17. There is a good agreement of radiation patterns at different cut-planes of varied φ angles, which suggests that the proposed antenna has good CP radiations. The radiation pattern exhibits excellent stability with respect to the azimuthal angle φ (0˚, -45˚, -90˚, and -135˚), and good symmetry is also observed in the elevation planes. Similar results were also observed between 309 GHz to 316 GHz and the AR is below 3 dB. For brevity, not all plots have been included.

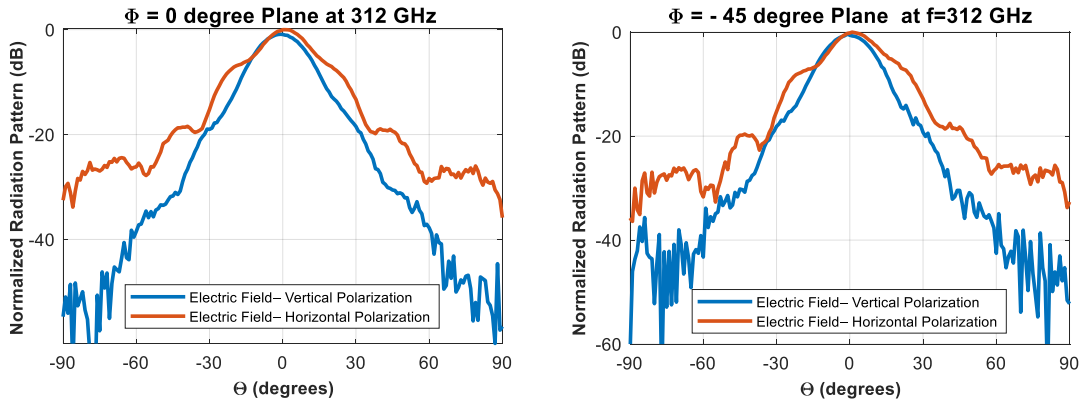

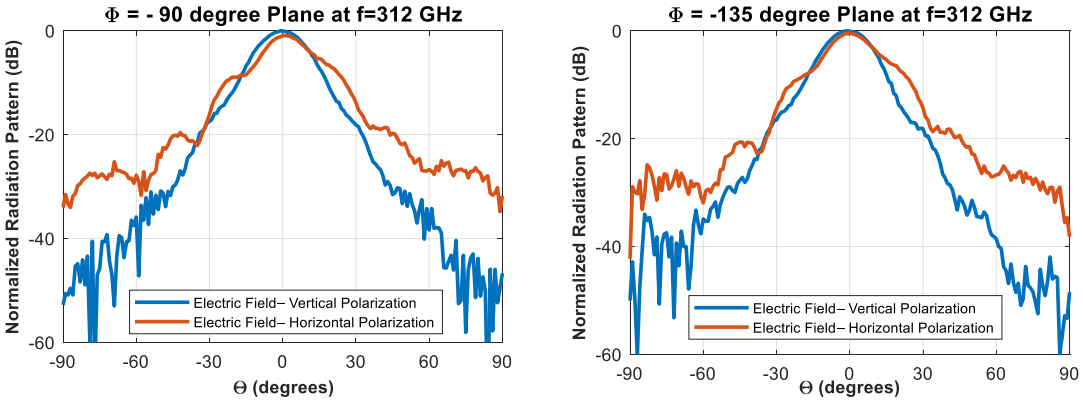

Figure 3.17: Measured normalized radiation patterns of the proposed antenna at different angles of 0, -45, -90, and -135 degrees at 312 GHz.

2D Orthographic (UV) plots the far-field as a 2D colormap plot using an orthographic projection of the unit sphere from the z-axis onto the x-y-plane. The projected x-y- coordinates are named u and v respectively. They have the following relation to the spherical angles: $u = \cos\phi \sin\theta$ and $v = \sin\phi \sin\theta$. Note that this orthographic projection always limits the view to the upper hemisphere ($\theta \leq 90^{\circ}$).

To have a better understanding of the 3D patterns of the antenna, the 2D color-map in the reciprocal (u-v) spectral plane of the CP horn antenna at 300 GHz is plotted in the u-v spectral plane in Figure 3.18 for the broadside. It can be easily noticed that a very good pattern symmetry is obtained for the CP horn antenna.

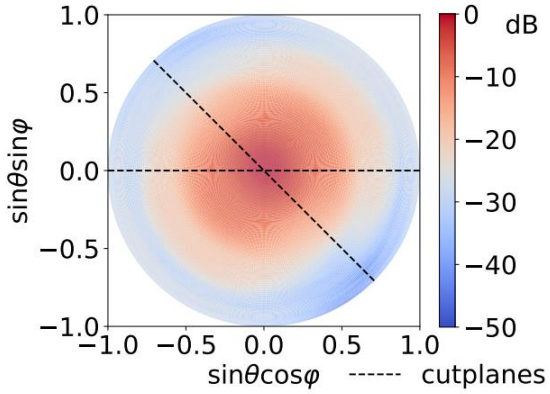

Figure 3.18: 2D far-field radiation patterns of the CP horn antennas measured at 300 GHz.

Table 3.1 gives a comparison among different CP antennas in the sub-THz band. Some key parameters are listed, including working frequency band, 3dB AR bandwidth, maximum gain, and technology of fabrication. The results show that our antenna is currently the first antenna, which is achieved with a very simple all-metal structure with compact size in the sub-THz band

using wire EDM techniques. The measured results proved that manufacturing parts have high precision.

Table 3.1: Comparison between the proposed CP horn antenna with other latest CP sub-THz antenna.

Ref.	Antenna type	Freq (GHz)	3dB AR BW %	Max Gain (dBic)	Fabrication Technique	Remarks
[70]	Antipodal curvedly tapered slot	500	4	12.2	Silicon micromachining	Low gain
[71]	Double-fan-shaped slot	500	2	12.5	Silicon micromachining	Low gain
[66]	Hexagonal waveguide based horn antennas	110	40	18	Wire EDM	Complex structure
[72]	Discrete dielectric lens	300	18.33	30.8	3D printing	Large size
This work	The proposed antenna	300	2.33	18.4	Wire EDM	Simple structure

3.5 Conclusion

A sub-THz CP conical horn antenna fabricated by direct machining in one block of metal using the Wire- EDM technique operating at 300 GHz was presented. Circular polarization was achieved by exiting two orthogonal modes through the crossed slot of the circular polarizer disk of the proposed antenna. The antenna yields a measured impedance bandwidth of 60 GHz from 270 GHz to 330 GHz. The measured directivity of 18.3 dBic at broadside direction at 312 GHz. The measured 3-dB AR bandwidth of 7 GHz from 309 GHz to 316 GHz. Radiation patterns of the fabricated Sub-THz CP conical horn antenna have been measured and the results agree well with the simulations. This antenna finds potential application in Tbps wireless communication at the sub-THz frequency band.

Chapter 4 Low-profile Planar Antennas

4.1 Introduction

High transmission data rates, low latency, high reliability, and interference-free operation are the most needed features today for applications ranging from communications to infotainment and positioning to healthcare. The demand is the driving force behind recent remarkable developments in wireless networks in new frequencies [73]. This leads to making the terahertz (THz) (0.1 to 10 THz) band the key candidate for future wireless networks. Successful deployment of wireless networks relies heavily on antenna design, and future wireless networks are no exception. Recently, a new IEEE standard (Std.802.15.3d-2017) has been established around 300 GHz, and data rates transmissions up to 100 Gb/s have already been demonstrated [74]. The sub-THz band (0.1 to 1 THz) around 300 GHz could be a key enabler as strong candidate technology to realize sixth-generation (6G) wireless communication speeds up to 1Tpbs [73, 75]. Moving up to sub-THz range frequency means a drastic increase in free-space path-loss and atmospheric absorption (i.e., absorption by molecules in air). Consequently, unprecedentedly high gain antennas are necessary to compensate for the path loss. Antenna arrays with complex feeding networks can provide better directivity and gain but have narrow bandwidth and high loss, especially at high THz frequencies due to feeding, and substrate materials losses, which has a great influence on the performance of antennas resulting in a significant decrease in antenna radiation efficiency. Horn antennas [76, 77] and reflector antennas [17] have been reported with good radiation patterns, low cross-polarization, and wide-band operation, but have the shortcoming of bulky size, which makes them difficult to assemble with planar circuits. Lens antennas have also been proposed at higher THz frequencies as good directivity and high gain antennas for broadside radiation [78-80]. The antenna-based lens normally has a profile of several wavelengths, which is increased even more if a higher gain value is desired, and can be challenging at the sub-THz band (i.e. 300 GHz) in terms of compact integrated systems. Another serious weakness of dielectric lens antennas is the surface wave effect and dielectric loss, and it is necessary to optimize its material and geometry in the future. Contrarily, Fabry–Perot cavity (FPC) antennas featuring high radiating performance and low profile and low cost, and low complexity of fabrication, have attracted broad interest from research in recent years. However, most FPC antennas reported to date have been extensively investigated in the microwave range [81-83] and recently in the millimeter-wave (MMW) band by applying single-layer frequency selective surface (FSS) as a partially reflective surface (PRS) [84, 85]. Authors in [86, 87] have successfully proposed the FPC antenna designs at the THz band. Nevertheless, due to the limitation of fabrication technologies, the first steps toward experimental validation of FPC antennas have already been taken in [88] by using a SU-8 photoresist micromachining technology at 284 GHz. Although

this design has been fabricated, it cannot provide a wide bandwidth (~ 4.5 GHz) and the measured results of radiation patterns are not up to the mark.

In this chapter, we firstly introduce a fully metallic FPC antenna design that operates at 300 GHz and is fabricated with laser-cutting brass technology with good accuracy at such high frequency. Circularly polarized (CP) antennas are required for wireless communication systems because of their ability to avoid multipath fading, mismatch the polarization (alignment issue), and enhance the channel capacity. Therefore, developing front-end components with a focus on CP sub-THz antennas is important. We secondly present the first fully metallic CP-FPC antenna enabled by laser-cutting in the sub-THz range. Using laser-cutting metal brass, we present the simplified technology procedure at 300 GHz; with a low-cost fabrication process. This laser cutting technology works by directly cutting the brass metal layers, without the need of a mask and a metallization process, which ease the fabrication. All brass metal layers are simply stacked by using four plastic screws. This direct-mount procedure is easier than alternative setups of silicon-micromachining which needs a bonding alignment method [89] and is expensive. These antennas find potential applications in future 6G wireless communication systems.

4.2 Linearly Polarized FPC Antenna

4.2.1 Aperture-FSS Unit Cell

In [84], a PRS is placed at a half-wavelength height above the ground plane to form a one-dimensional cavity, leading to a high directive beam radiation, which is generally explained by the ray-tracing or leaky-wave approach [90, 91]. A primary radiator such as a radiating slot is used to excite the cavity. In our proposed antenna, the aperture FSS layer works as PRS, where a square aperture element has been chosen for the design. The geometry of the aperture FSS unit cell is shown in Figure 4.1. The optimized dimensions of each aperture '$\boldsymbol{a}$' are 0.42 $\boldsymbol{\lambda_0}$× 0.42 $\boldsymbol{\lambda_0}$ and the periodicity '$\boldsymbol{p}$' is 0.5 $\boldsymbol{\lambda_0}$ as shown in Figure 4.1. The thickness of the FSS layer is 0.1 $\boldsymbol{\lambda_0}$.

The initial simulations were performed on the unit-cell structure with periodic boundary conditions for computational efficiency. The simulated reflection characteristics (magnitude and phase) of the aperture FSS unit cell are shown in Figure 4.1. High values for the reflection coefficient magnitude are achieved for the unit cell with dimensions inset in Figure 4.1, indicating high antenna directivity. The aperture FSS unit cell exhibited a positive reflection phase gradient over frequency, which resulted in improved antenna bandwidth [84, 92].

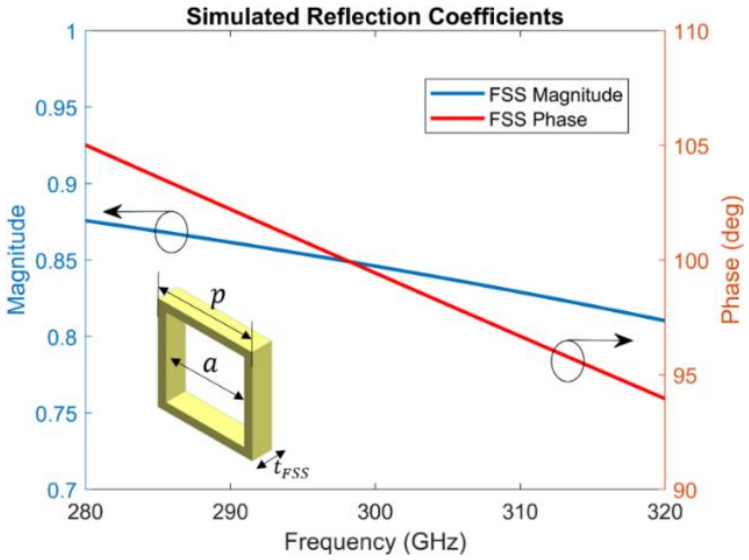

Figure 4.1: Simulated complex reflection coefficient of the proposed aperture FSS unit cell (dimensions is inset).

4.2.2 FPC Antenna Configuration with Aperture-FSS Layer

The configuration of the proposed sub-THz linear polarized FPC antenna is illustrated in Figure 4.2. It consists of seven metallic layers, namely a ground layer, an integrated stepped horn element (three layers), a coupling layer, a cavity layer, and an aperture-FSS layer, from the bottom to the top. The ground layer (layer A), a slot antenna that works as a primary radiator with broadside radiation, has a dimension of $\boldsymbol{L_s = 0.48\ \lambda_0}$ and $\boldsymbol{W_s = 0.1\ \lambda_0}$ and thickness of $\boldsymbol{t_1 = 0.1\ \lambda_0}$; where $\boldsymbol{\lambda_0}$ is the free space wavelength at 300 GHz. A slot-fed waveguide has been used as the primary radiator for the whole antenna structure. The waveguide is a standard WM-864 rectangular one with a UG-387/U flange and works from 220 GHz to 330 GHz.

Maintaining high gain over a wide bandwidth is a big challenge for such an FPC antenna design, and as a result, the horn element is integrated. The three layers (B, C, and D) are employed to construct the integrated step-profiled horn element as shown in Figure 4.2(b). The rectangular apertures shape of the horn element has dimensions, as illustrated in Table 1. This stepped horn antenna is used to improve the impedance matching performance of the whole antenna structure [93]. The coupling layer (layer E), comprises two slots that are excited with equal phase and amplitude by the WM-864 waveguide through a ground layer and a stepped horn antenna element. The distance between two coupling slots along the *y*-direction is 'd_{cs}', which is equal to 0.97 λ_0.

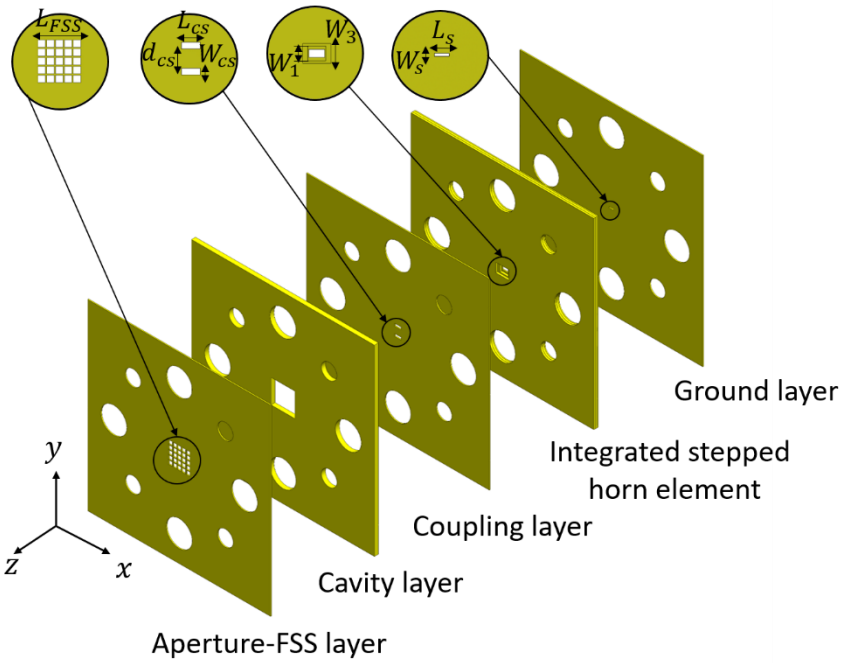

(a)

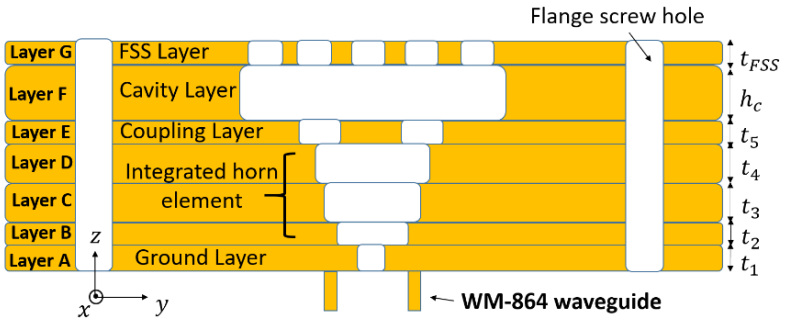

(b)

Figure 4.2: Configuration of the proposed 300 GHz FPC antenna with holes of standard WM-860 waveguide flange. (a) 3D-explosive structure (b) and sectional side-view.

The cavity layer (layer F), which is supported by a metallic plate shown in Figure 4.2(a), determines the resonant height 'h_c' between the coupling layer and aperture-FSS layer, which could be calculated by the equation (4.1). The length, width, and thickness of this square cavity are L_c, W_c, and h_c, respectively shown in Table 4.1. The aperture-FSS layer (layer G), consisting of an array of the aperture with a periodicity of 'p' between each aperture element. The geometrical parameters of the square apertures in the FSS layer are adjusted to alter the magnitude and phase of incident electromagnetic fields, to achieve highly directivity radiation

patterns performance as explained in the above section. The aperture-FSS layer works in a standing-wave environment (i.e., inside a resonant cavity). Fabry-Perot (FP) resonance condition [84] must be satisfied and is determined by the following equation:

$$\varphi_{FSS} + \varphi_{Co} - \frac{4\pi h_c}{\lambda_0} = 2\pi N \,. \quad N = 0.1.2 \ldots \tag{4.1}$$

where φ_{FSS} and φ_{Co} are the reflection phases of aperture-FSS and coupling layers, respectively. h_c is resonant cavity height, and N represents the resonance mode number of the FP resonant cavity. Only the zeroth-order mode (N= 0) of the FP cavity is considered to keep the low profile of the antenna. When the resonant condition is satisfied, the maximum directivity at the broadside is obtained [94].

Table 4.1: Antenna design parameters (Units: mm)

Layers	Parameters	value	Parameters	value	Parameters	value
Ground	t_1	0.1	L_s	0.48	w_s	0.1
Integrated horn element	t_2	0.1	L_1	0.8	w_1	0.4
	t_3	0.2	L_2	1	w_2	0.75
	t_4	0.2	L_3	1.42	w_3	1
Coupling	t_5	0.1	L_{cs}	0.7	w_{cs}	0.25
Cavity	h_c	0.44	L_c	2.6	w_c	2.6
Aperture-FSS	t_{FSS}	0.1	L_{FSS}	2.3	w_{FSS}	2.3

4.2.3 Simulation Results

In order to analyze the performance of the FPC antenna based on the aperture-FSS layer, keeping all other parameters fixed, realized gains of the proposed antenna with different aperture-FSS configurations are shown in Figure 4.3.

As can be observed in the figure, when there is no aperture-FSS layer above the cavity, the antenna gain is around 7.5 dBi. By introducing the proposed aperture-FSS layer, the antenna gain can be improved significantly when compared without the FSS layer. The optimum lateral size of the FSS layer was 2.32 λ_0 ×2.32 λ_0 at 300 GHz, which equates to 5 x 5 aperture-FSS unit cells. This size was chosen to give the best moderate size in terms of fabrication with stability gain over desired bandwidth. The peak realized gain of 17.2 dBi is obtained around 300 GHz. It increases as expected by increasing the FSS area. The effect of the FSS area on the return loss (S11) performance was found to be negligible.

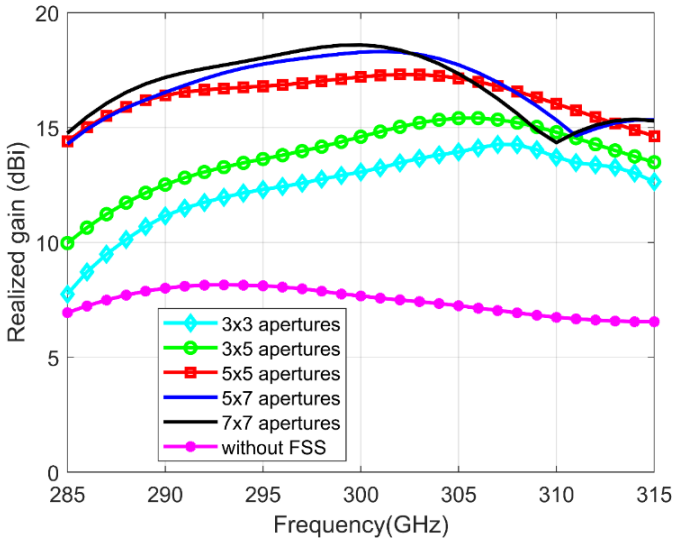

Figure 4.3: Realized gains of the 300 GHz FPC antenna with different aperture-FSS configurations.

Figure 4.4 illustrates the performances of the linearly polarized sub-THz FPC antenna with a standard UG-387/U waveguide flange. As can be seen, the impedance bandwidth covers from 287 to 305.5 GHz with a bandwidth of 18.5 GHz for the reflection coefficient (S11) ≤ -10 dB. The simulated maximum directivity obtained for the proposed aperture-FSS FPC antenna at the broadside is 17.87 dBi (i.e., 61.24).

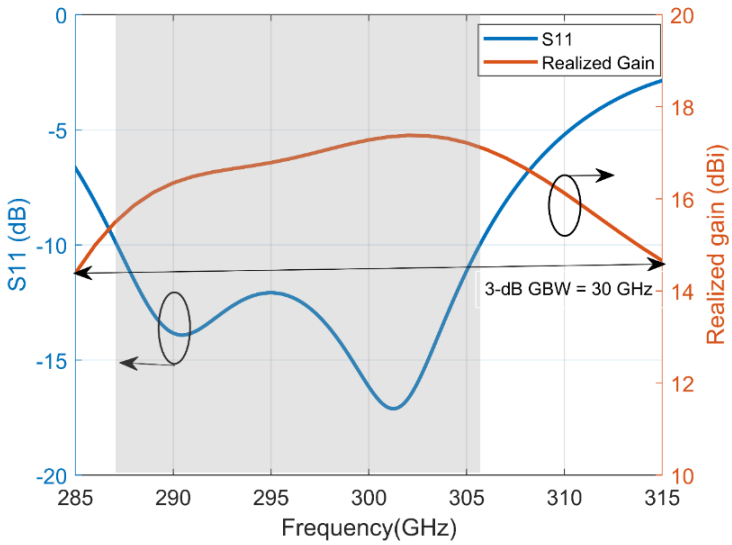

Figure 4.4: Simulated reflection coefficient (S11) and realized gain of the proposed antenna.

The 3-dB gain bandwidth (3-dB GBW) calculated from the results in Figure 4.4 is 30 GHz (10%). Based on these results, a figure of merit for the proposed sub-THz FPC antenna defined by the product of maximum directivity and the 3-dB broadside gain bandwidth is (61.24) ×

(0.1) = 6.124, which is close to the value of 7.11 for a thick PRS [95] reported at 60 GHz. The directivity-bandwidth figure of merit is 2.48 times larger than the best obtainable with planar and thin PRS structures (i.e. 2.47) [81].

Figure 4.5 gives the E-field distributions of the whole antenna with an aperture-FSS layer including holes of alignments pins and fixated screws for standard UG-387/U rectangular flange at 300GHz. We note that; the EM energy converges along the boresight direction.

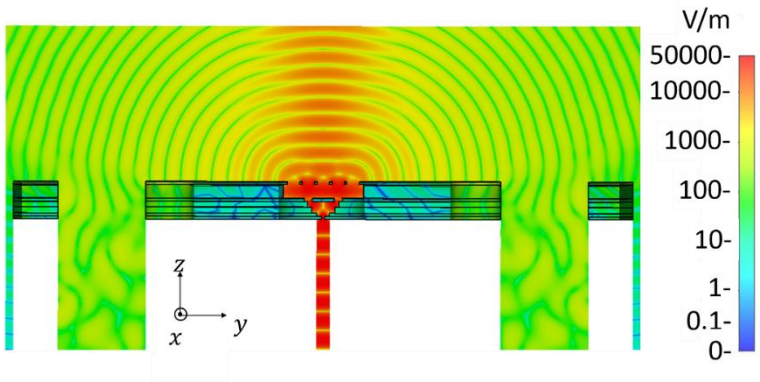

Figure 4.5: Simulated E-field distributions of the proposed antenna with standard UG-387/U rectangular flange holes at 300 GHz.

4.2.4 Fabrication Technology

To achieve ease of fabrication, a laser cutting technology has been used for each brass metal layer in the proposed antenna using the LPKF ProtoLaser U4 laser machine as shown in Figure 4.6, with technical support from Manufacturing Measurement Analysis of Radiating Systems (M^2ARS) at IETR. The seven brass metal layers needed for one antenna assembly, having different thicknesses as shown in Table 4.1, have been used to manufacture the proposed 300 GHz FPC antenna are shown in Figure 4.7. This brass is often used as a laser-cut metal, which is a highly reflective material with an electrical conductivity of $\sigma = 35.86 \times 10^6$ Sm^{-1}. All brass metal layers are fixed by using four plastic screws as shown in Figure 4.7.

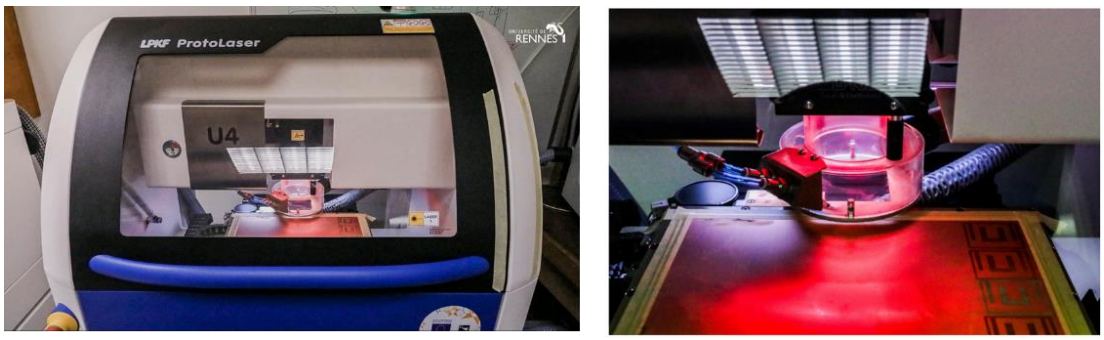

Figure 4.6: LPKF ProtoLaser U4 laser machine

The ultraviolet (UV) laser beam wavelength (λ= 355 nm in the UV spectrum), is focused on each brass metal layer individually having a different thickness to obtain the desired dimension, with the appropriate settings, such as a laser cutting speed of 200 mm/s, and a laser spot size of 20 µm; which is the fabrication tolerance. The proposed antenna with aperture-FSS layer is fabricated and assembled, which is shown in Figure 4.7. The complete antenna comprises a feed antenna part (A-F layers), a 5×5 metallic aperture-FSS part (G layer), and a standard WM-864 rectangular waveguide with a UG-387/U flange. The metal layers contain holes for the alignment dowel pins and screws, which enable a direct connection to the standard UG-387 waveguide flange without any additional test fixtures or interfaces. This direct-mount technique is superior to alternative setups using silicon-micromachining without bonding the alignment method [89]. We can notice that the laser cutting technology uses only brass metal layers, without the need for a metallization process. But silicon micromachining uses a dielectric substrate and it is metalized, the thickness of metallization must be more than two or three times the skin depth in order to reduce the ohmic losses at higher frequencies. Another significant point is the need for a mask and clean room for silicon micromachining which is more expensive but not the case for laser-cutting technology. On the other hand, silicon micromachining provides more accuracy. Also, for silicon micromachining, we are limited to a thickness of 400 μm accuracy but for laser-cutting we succeeded to reach 800 μm thickness accuracy.

4.2.5 Experimental Results and Discussion

The reflection coefficient characterization (S11) is measured using a Rohde &Schwarz ZVA67 vector network analyzer (VNA) and a Virginia Diodes Inc. (VDI) frequency extender module (220 – 330 GHz) with a WM-864 waveguide flange interface. Figure 4.7(b) shows a microscope image of the aperture-type FSS layer, where the actual sidewall width was found to be 80 μm. Figure 4.7(c) shows the manufactured antenna mounted in a standard WM-864 waveguide flange.

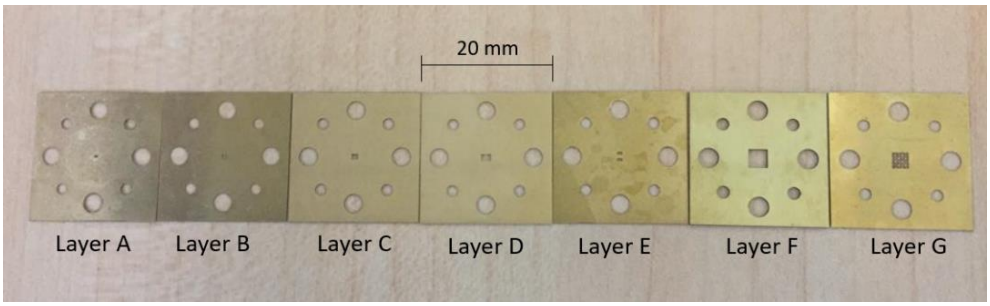

(a)

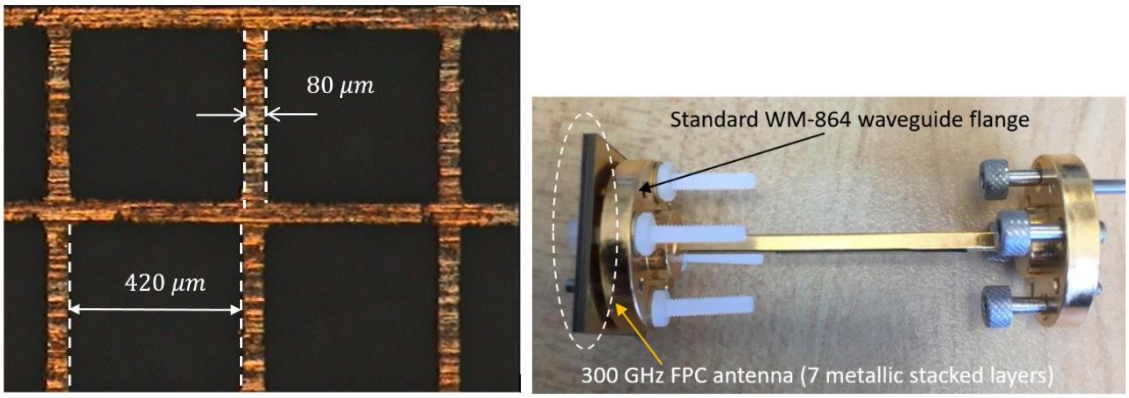

(b) (c)

Figure 4.7: Photographs (a) 7 brass metal layers required to assemble one antenna, (b) microscope image of the aperture-type FSS layer, and, (c) the manufactured antenna mounted on a standard WM- 864 waveguide flange. The antenna is aligned using two standard alignment pins and fixated with four plastic screws. The standard flange size is 20 mm x 20 mm.

The measured reflection coefficient (S11) is below -10 dB at the working band from 282 to 304 GHz with a bandwidth of 22 GHz as shown in Figure 4.8. Figure 4.8 also indicates the measured realized gain of the antenna, and it shows that the gain ranges from 14.4 dBi to 17.7 dBi in the frequency band of 285 to 310 GHz. There is some divergence between the measured and simulated realized gain; this may be because of assembling and fabrication tolerances that are normal in the 300 GHz band. The measured and simulated directivities of the proposed antenna are also presented in Figure 4.8.

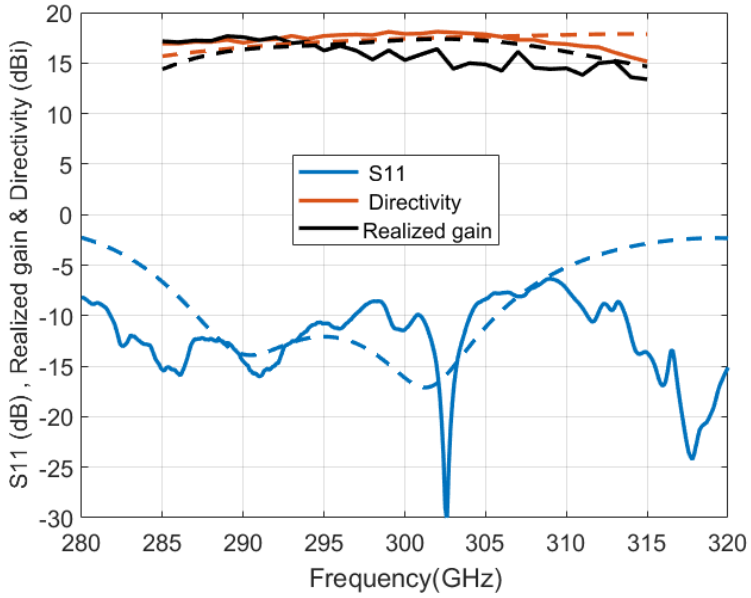

Figure 4.8: Measured (solid lines) and simulated (dashed lines) of (S11), directivity, and realized gain for 300 GHz FPC antenna prototype.

To demonstrate the characteristics of the proposed antenna, such as the radiation patterns, are measured in a compact antenna test range (CATR) chamber at IETR (funded by the European Union through the European Regional Development Fund, through the CPER Projects 2015–2020 SOPHIE/STIC and Ondes) as shown in Figure 4.9.

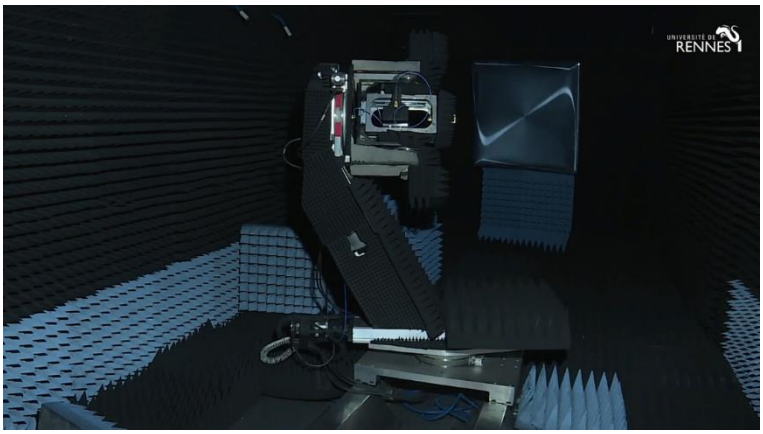

Figure 4.9: Compact Antenna Test Range (CATR) chamber.

The measured elevation (Ele.)-plane and azimuth (Az.)-plane radiation patterns, shown in Figure 4.10, are in acceptable agreement with the simulation results. In the measured elevation-plane cuts, the main beam is a broadside direction. Some minor discrepancies have to be noticed on the sidelobe level (SLL), and the SLL is kept below 15 dB as designed, except at higher frequency (i.e., 305 GHz). The measured main beam in azimuth-plane cuts is a slight shift from the broadside direction; this is because the flange used has a small tilt (the long waveguide section in the photo, Figure 4.7(c), the SLL is kept below 15 dB as designed.

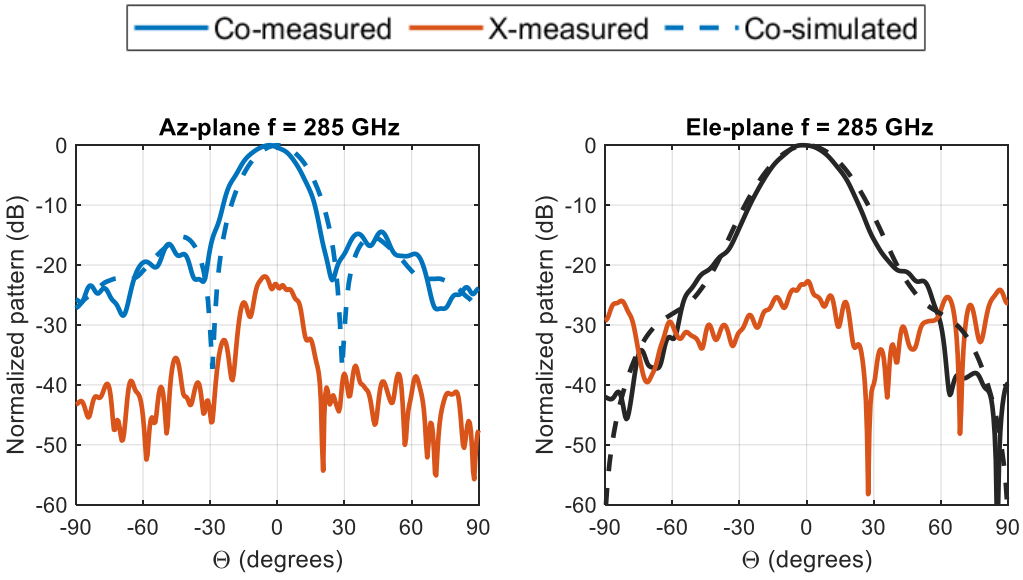

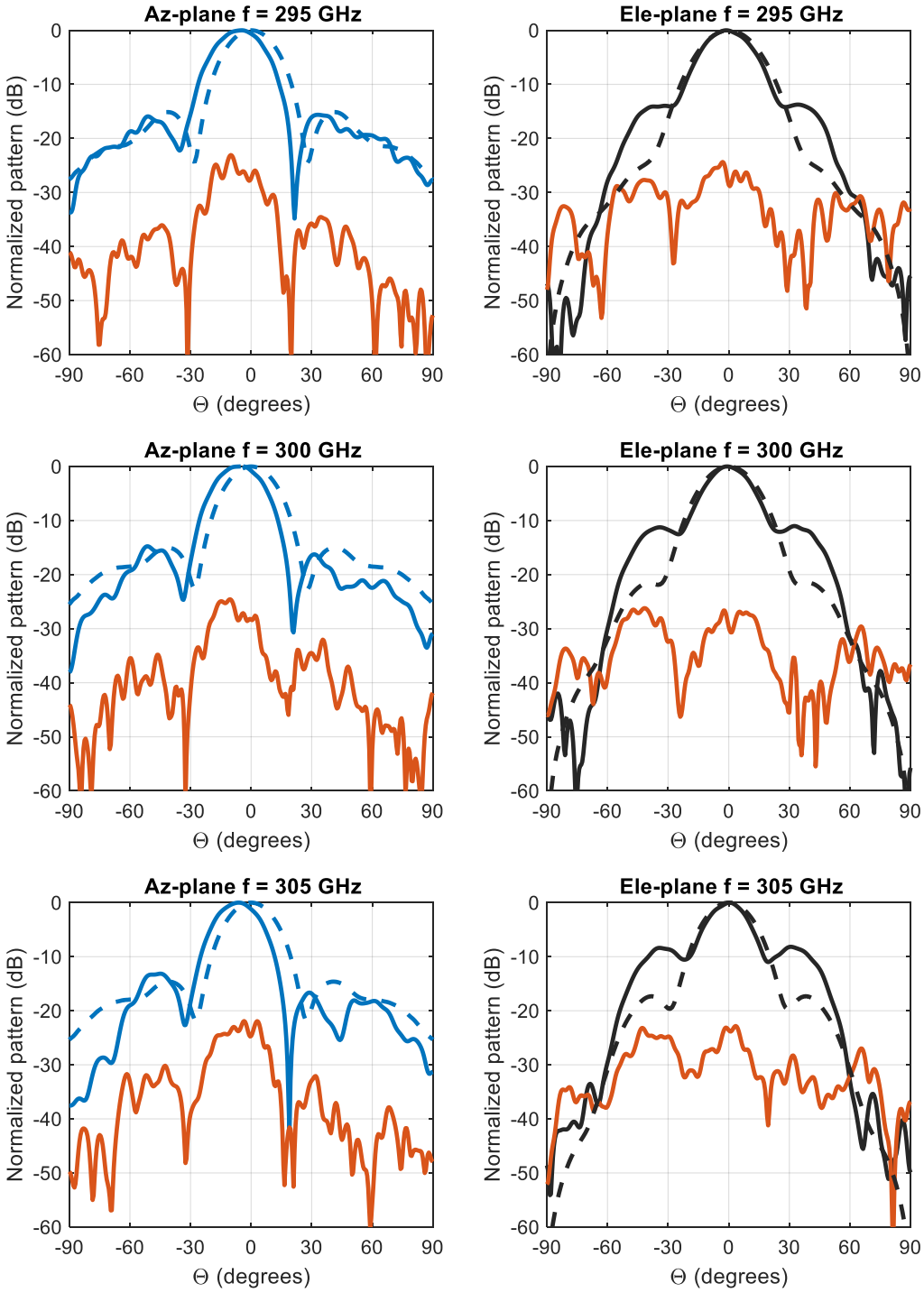

Figure 4.10: Measured (solid lines) and simulated (dashed lines) normalized radiation patterns of the proposed antenna of the azimuth (Az.) and elevation (Ele.) planes at different frequencies.

The measured cross-polarization levels are more than 25 dB at these frequencies. The simulated cross-polarization in both principal planes is more than 93 dB over the entire bandwidth of interest. The cross-polarization radiation pattern for one of the frequencies at 300 GHz is

presented in Figure 4.11(a). The maximum cross-polarization level at the broadside direction is less than –93 dB over the whole desired band as shown in Figure 4.11(b).

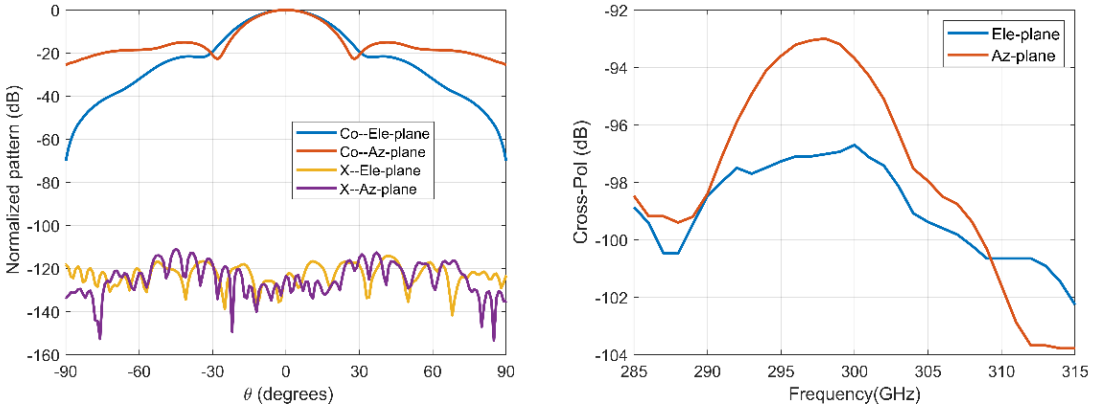

(a) (b)

Figure 4.11: Simulated (a) normalized co,cross-pol radiation patterns at 300 GHz and (b) cross-pol level of the FPC antenna prototype.

Figure 4.12 shows the measured 2D normalized radiation patterns of the proposed FPC antenna in the u-v plane coordinate system ($u = \sin\theta\cos\phi$, and $v = \sin\theta\sin\phi$) at different frequencies, to verify the results and investigate the radiation characteristics outside the two principal planes, where the advantage of transformation to the u-v plane is evident as well. The measured radiation pattern shows a highly directive pattern in all plane cuts, which coincides with the simulation results.

Table 4.2 compares the performances of the proposed fully metallic FPC antenna at 300 GHz with different sub-THz reported prototypes in the literature. It can be seen that the proposed antenna has a low-profile planar structure using the Fabry-Perot resonant cavity without any dielectric materials. The proposed antenna is fabricated using low-cost laser cutting technology, and also achieves higher gain and good wide bandwidth as compared to those using different high-cost technologies. These facts indicate that the proposed antenna structure is a good candidate for sub-THz applications.

Table 4.2: key factor comparison of the measurement of this work and other published works.

Reference	Antenna type	Manufacturing process	Center frequency (GHz)	Bandwidth (GHz)	Gain (dBi)	Size (mm3)	Fabrication complexity
[25]	Profiled corrugated horn	LTCC	300	100	18	5×5×2.8	High
[88]	Fabry–Perot cavity	Micromachining	284	~ 4.5	15.9	11.8 ×11.8 × 8.45	Low
[17]	Quasi-planar reflectors	Metallic milling	400	175	> 26.5	16 ×16 × 5.5	High
This work	Fabry–Perot cavity	Laser cutting brass	300	22	17.7	2.6 × 2.6 × 1.24	Low

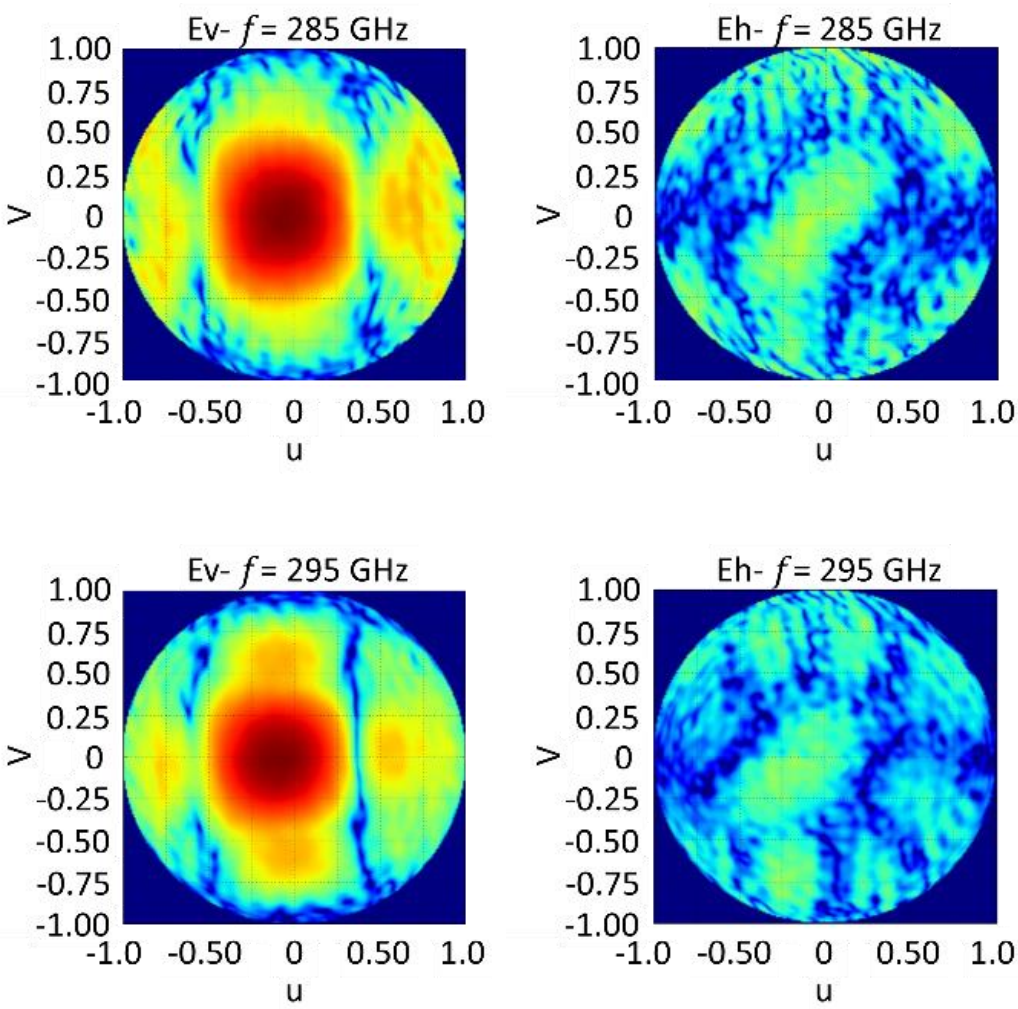

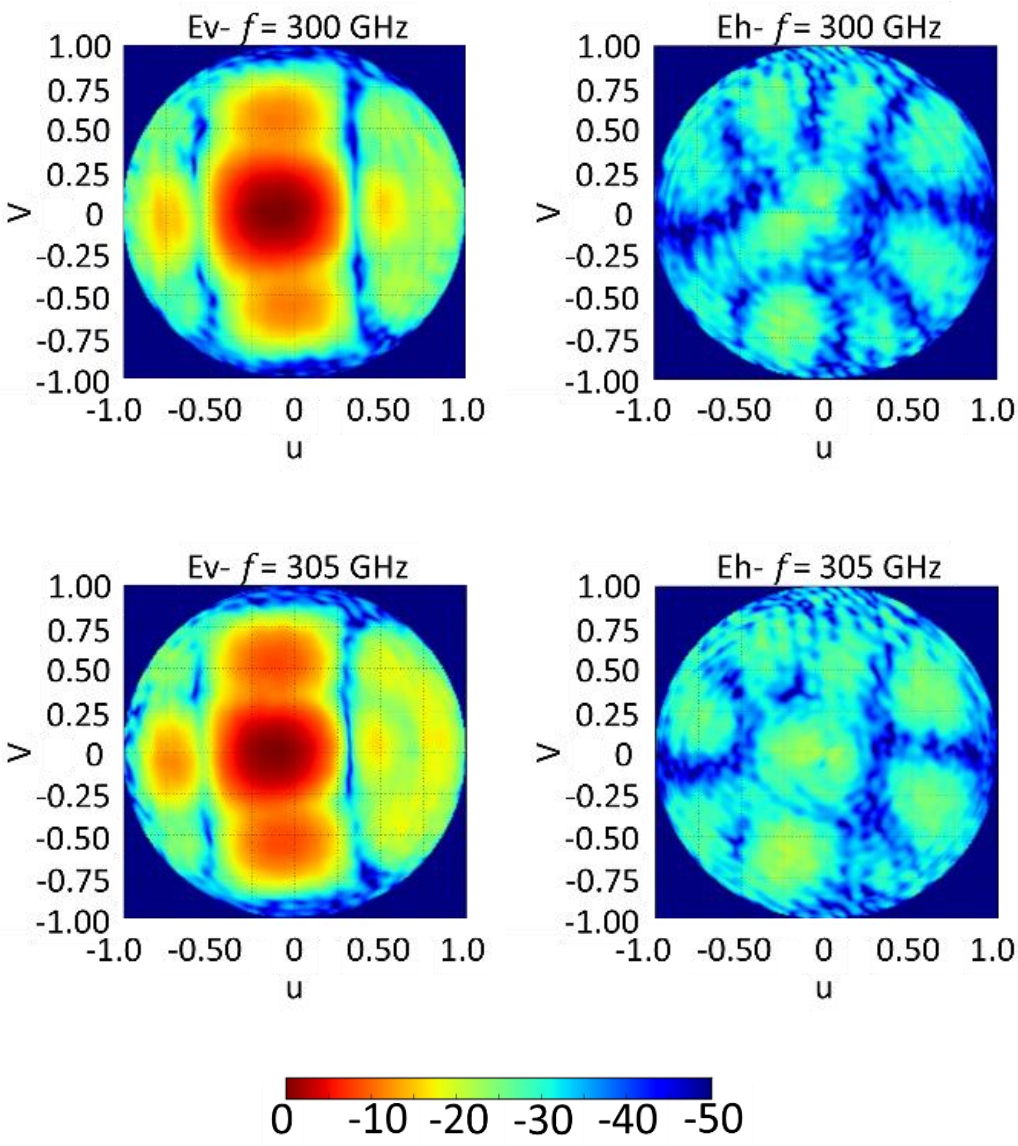

Figure 4.12: Measured 2D color-maps of the proposed FPC antenna (Co 'Ev' & Cross 'Eh'- polarization components), in the u-v spectral plane at different frequencies. The color bar is on the dB scale.

4.2.6 Conclusion

A linearly polarized sub-THz FPC antenna with high gain and low cross-polarization has been presented. The proposed antenna has been designed with a standard WM-864 rectangular waveguide flange, and it has been fabricated in brass metal using low-cost laser-cutting technology. This laser cutting brass technique has been shown to provide the fabrication of complicated details of the design with high precision. The 300 GHz FPC antenna has been measured using facilities at IETR, and the results obtained are in good agreement with simulation results.

4.3 Circularly Polarized FPC Antenna

4.3.1 Unit Cell Model (Hexagonal Aperture Element)

The design model of a unit cell for aperture type-FSS layer is studied using periodic analysis since this model assumes the transverse extent of hexagonal radiating aperture unit cell structure and is theoretically infinite. Periodic boundary analysis is performed using the frequency-domain solver of CST Microwave Studio. Furthermore, this model assumes that the FSS layer is illuminated by a normally incident plane wave, i.e., that the propagation vector is normal to the plane of the FSS layer. We can achieve a high gain antenna when the reflection coefficient magnitude of the unit cell is high [96]. Furthermore, to improve the antenna bandwidth the reflection coefficient phase of the unit cell should vary slowly with frequency. Thus, the proposed unit cell of hexagonal radiating apertures FSS layer achieves its requirements. The hexagonal aperture is used to excite two orthogonal modes with an equal magnitude and a 90° phase difference between them, thus inducing CP current and radiating CP waves.

The aperture-type FSS acts as a partially reflective surface (PRS), which functions as high-gain antennas [90, 96], where a hexagonal aperture element has been chosen as the FSS unit cell for the design. The aperture-FSS layer is placed at a half-wavelength height above the ground plane to form a one-dimensional cavity, leading to a high directive beam radiation, which is generally explained by the ray-tracing or leaky-wave approach [90, 91].
Figure 4.13 demonstrates the geometry of the proposed hexagonal radiating aperture unit cell. It is found that the periodicity of the unit cell $p = 0.48\,\lambda_0$, the unit cell has two symmetrically isosceles triangle chamfers, $c_t = 0.14\,\lambda_0$, and the thickness of radiating aperture, $t_{FSS} = 0.1\,\lambda_0$, where λ_0 is the operation frequency at 300 GHz.

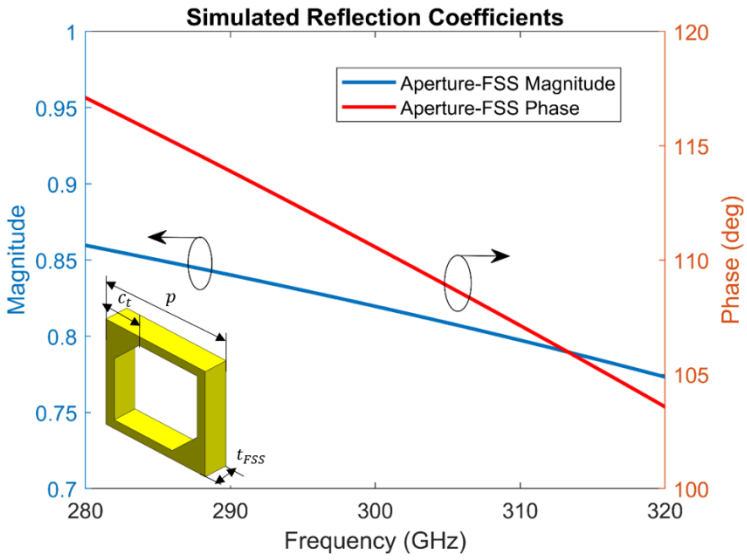

Figure 4.13: Simulated complex reflection coefficient of the proposed aperture–FSS unit cell.

4.3.2 Circularly Polarized Fabry-Perot Cavity Antenna

Figure 4.14(a) shows the 3D view of the FPC antenna with aperture type-FSS layer at 300 GHz. The proposed antenna comprises seven metallic layers: ground layer, integrated stepped horn layers (three layers), coupling layer, cavity layer, and FSS layer. A slot antenna is engraved on the ground layer (layer A) with a thickness of $t_1 = 0.1\ \lambda_0$.

The standard WM-864 rectangular waveguide (864 µm × 432 µm) feed is directly connected to layer A at the backside. The length of the slot is usually chosen to be a half-wavelength. This single waveguide-fed slot acts as the primary feed antenna. Layer A is the coupling slot element widely used; however, the resonant element may restrict the realization of the wideband impedance matching. Inspired by the conventional broadband horn antenna, the coupling slot size can progressively increase (B, C, and D layers) and realize the wideband impedance matching from the exciting source. The conventional horn antenna design is transformed into an integrated step-profiled horn. To construct the integrated step-profiled horn element, we used layers B, C, and D, as shown in Figure 4.14(b), formed by three rectangular aperture shapes of metallic layers. To improve the antenna impedance matching, we used the horn element.

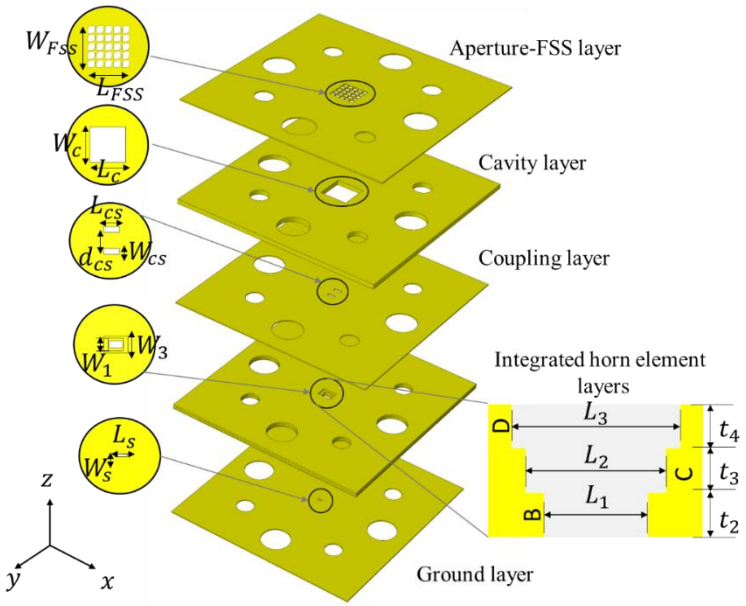

(a)

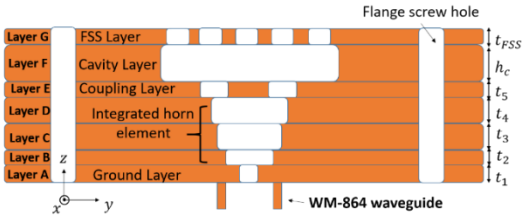

(b)

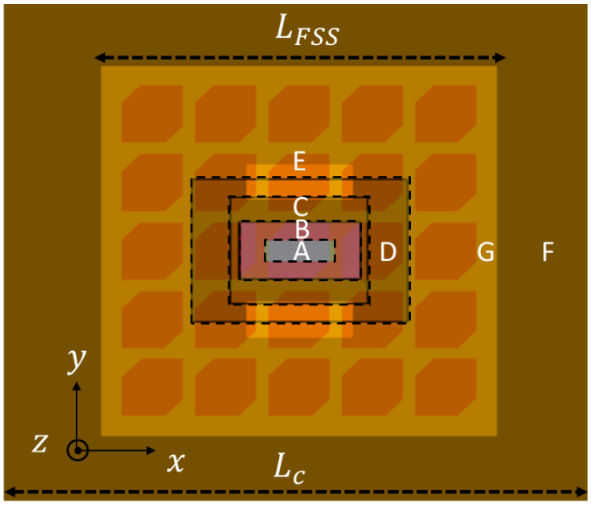

(c)

Figure 4.14: Configuration: (a) exploded view of the proposed antenna, (b) cross-section view, and (c) top view.

A coupling layer (layer E) consisting of two parallel slots is used to broaden the single-slot feed's impedance matching bandwidth in the ground layer as shown in Figure 4.15.

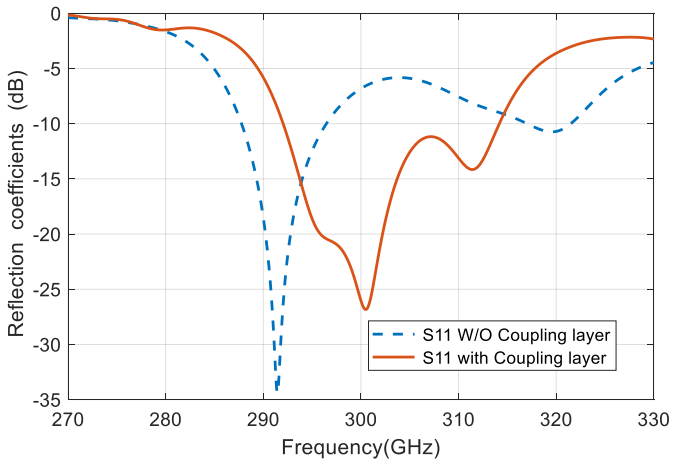

Figure 4.15: The impedance matching bandwidth (s11) with and without the coupling layer.

The cavity layer (layer F) is used to support the FSS layer, which is the distance to achieve the resonance condition of Fabry–Pérot by using Equation (4.3). The FSS layer is realized by perforated grids of hexagonal radiating apertures made by cutting through a metallic layer of finite thickness of 0.1 mm, supported by a metallic cavity layer, forming an air cavity with the metallic coupling layer.

For fabrication, we integrate the standard UG-387/U waveguide flange into the antenna design. The side view of the FPC antenna with aperture type-FSS layer is shown in Figure 4.14(b). There is a coupling between the base antenna (A–E layers) and the FSS layer that affects the antenna's performance in terms of S11, gain, and efficiency. The EM waves radiated from the base antenna impinge on the FSS layer, which forces the distribution of EM waves in space and controls the phase. The apertures of the FSS get excited, and multiple reflections and transmissions happen inside the cavity layer; finally, the wave leakage outside of the cavity from the FSS layer and this coherent wave leakage makes the antenna structure become high-gain, affecting the performance of the antenna. The reflection coefficient phase of the whole proposed antenna in Figure 4.14(a) is $\boldsymbol{2\pi N}$ as explained in equation (4.2) , which is calculated by using the simple well-known ray-tracing formula [96, 97].

$$\varphi_{FSS}(f_0) + \varphi_{Co}(f_0) - 2\beta h_c = 2\pi N; \qquad N = 0.1.2. \ldots \tag{4.2}$$

where N is the order of resonant mode, $\varphi_{FSS}(f_0)$ and $\varphi_{Co}(f_0)$ are the reflection phases of the FSS and the coupling layers, respectively, β is the propagation constant, and h_c is the cavity thickness. The resonance condition takes place at the boresight angle ($\theta = 0^{\circ}$), and the resonance frequency f_0 can be obtained from the following equation:

$$h_c = \frac{c}{4\pi f_0}[\varphi_{FSS}(f_0) + \varphi_{Co}(f_0) - 2\pi N] \tag{4.3}$$

From the above analysis, it is clear that the order of resonant mode N usually is equal to zero ($N = 0$) to realize low-profile performance. For a perfect metallic coupling layer and FSS layer, their reflection phase $\varphi_{Co}(f_0)$ and $\varphi_{FSS}(f_0)$ are a multiple of π, provided that the resonance height h_c is approximately $\lambda_0/2$. The 2D top view of the 5×5 element subarray of the hexagonal radiating apertures truncated the corners is depicted in Figure 4.14 (c). The FSS layer, consisting of an array of hexagonal radiating apertures, is designed for the self-generation of CP waves. The optimized design parameters of the proposed CP-FPC antenna are shown in Table 4.3.

Table 4.3: Antenna Designs Parameters (mm)

Layers	Param.	Value	Param.	Value	Param.	Value
Ground	t_1	0.1	L_s	0.46	w_s	0.1
Integrated horn element	t_2	0.1	L_1	0.8	w_1	0.4
	t_3	0.2	L_2	0.9	w_2	0.75
	t_4	0.2	L_3	1.42	w_3	1
Coupling	t_5	0.1	L_{cs}	0.7	w_{cs}	0.25
Cavity	h_c	0.44	L_c	2.6	w_c	2.6
Aperture-FSS	t_{FSS}	0.1	L_{FSS}	2.32	w_{FSS}	2.32

4.3.3 Simulation Results

The simulated realized gain between the antenna with and without the FSS layer is shown in Figure 4.16. As can be seen, after adding the FSS layer, the gain is significantly increased by an average of 7 dB over the whole frequency band, the largest gain difference of 9.3 dB occurs at 290 GHz. Moreover, the antenna gain is again increased by approximately 0.4-2 dB, by the addition of the cavity layer, as shown in Figure 4.16.

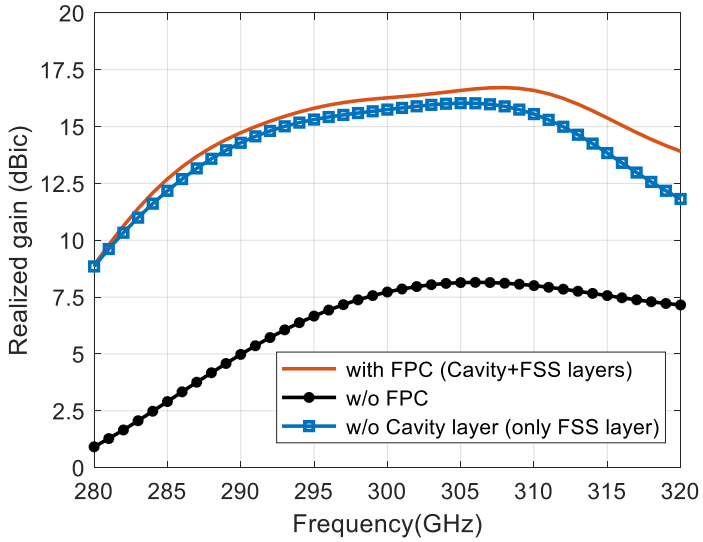

Figure 4.16: Simulated antenna gains with a different configuration.

Figure 4.17 illustrates optimization in terms of axial ratio (AR) and gain performances of five different apertures–FSS sizes, keeping the same periodicity and dimensions of the aperture unit-cell (due to the reasons explained in Section 4.3.1). The optimum aperture-FSS size in terms of the AR and gain is 5 x 5, which corresponds to a lateral size of 2.32 λ_0 × 2.32 λ_0 at 300 GHz. This size was chosen to give the best AR value of 0.51 dB, obtained at 296 GHz. The peak realized gain of 16.7 dBic is obtained at 307 GHz.

Figure 4.18 shows the simulated right-hand circular polarized (RHCP) realized-gain radiation patterns of the antenna at 296 GHz in four azimuthal cut planes. They are approximately identical, with sidelobes lower than 16 dB. The maximum RHCP gain of 16 dBic is predicted with a 3-dB radiation beamwidth of 26.4° at 296 GHz.

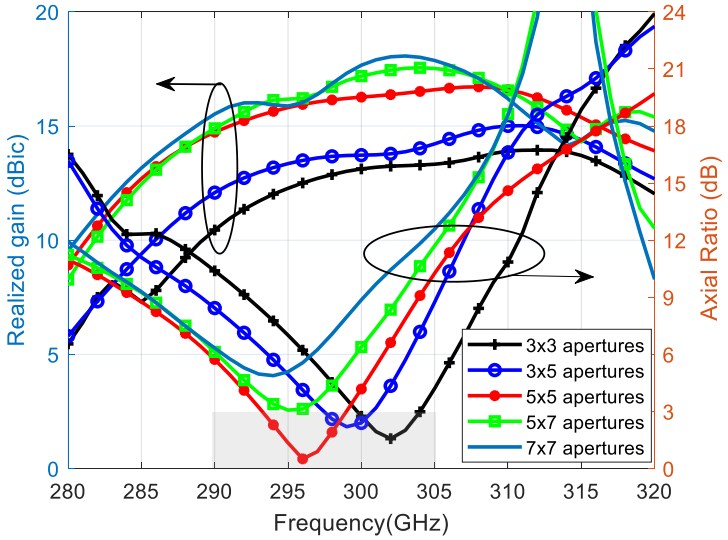

Figure 4.17: Simulated axial ratio, and realized gain versus frequency.

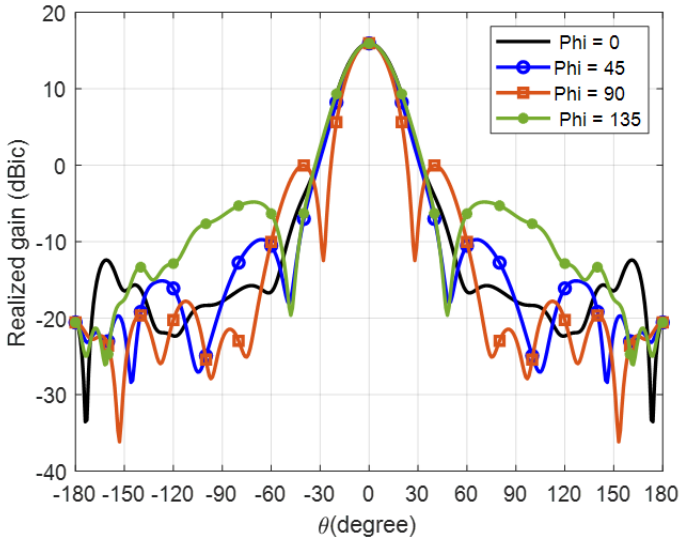

Figure 4.18: Simulated radiation patterns at 296 GHz.

Figure 4.19 shows the antenna polarization performance: AR versus the elevation angle (θ) at the frequency of 296 GHz. The best AR is 0.51 dB at the broadside direction and the predicted 3-dB AR beamwidth is more than ±17.3°, within the 3-dB radiated beamwidth of 26.4°, indicating that the antenna is indeed radiating most of the energy in circular polarization.

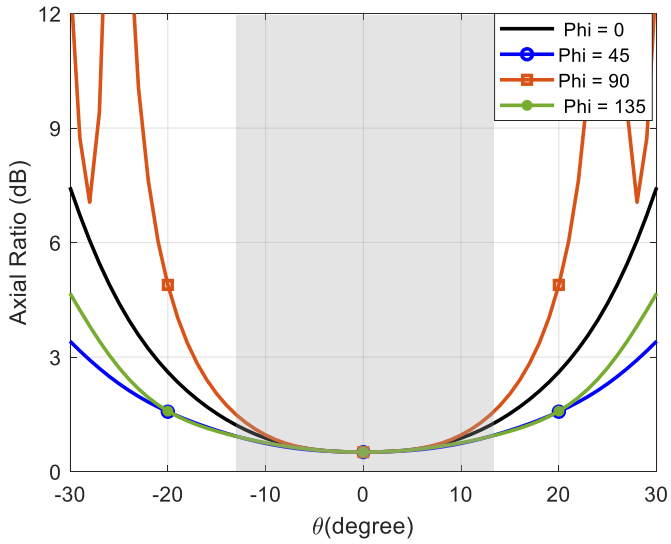

Figure 4.19: Simulated angular variation of axial ratio at 296 GHz.

Figure 4.20 shows the electric-field distributions in the E-plane cut inside the proposed CP-FPC antenna at 296 GHz, which displays the procedure of the slot coupling EM energies from feed standard WM-864 waveguide to free space.

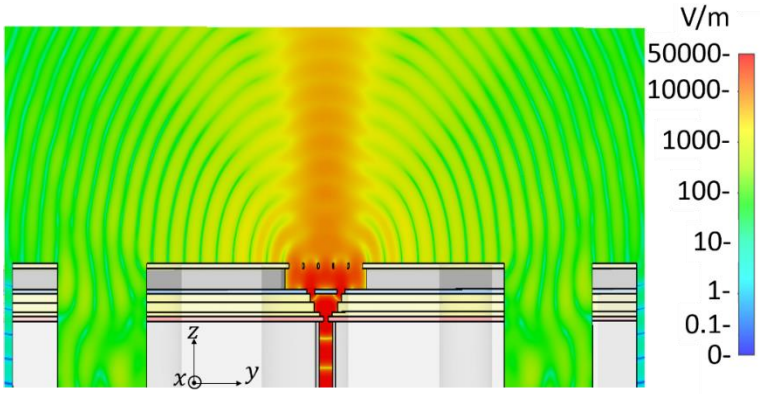

Figure 4.20: The E-field distribution in the E-plane cut inside the proposed antenna at 296 GHz.

Figure 4.21 illustrates the simulated reflection coefficient (S11) and the realized RHCP gain of the proposed antenna. The reflection coefficient impedance bandwidth <−10 dB is 22.3 GHz covering from 292.2 to 314.5 GHz. The simulated 3-dB RHCP gain bandwidth is 9.7% (from 287 to 316 GHz) of the center frequency with a maximum RHCP gain of 16.1 dBic at 298 GHz.

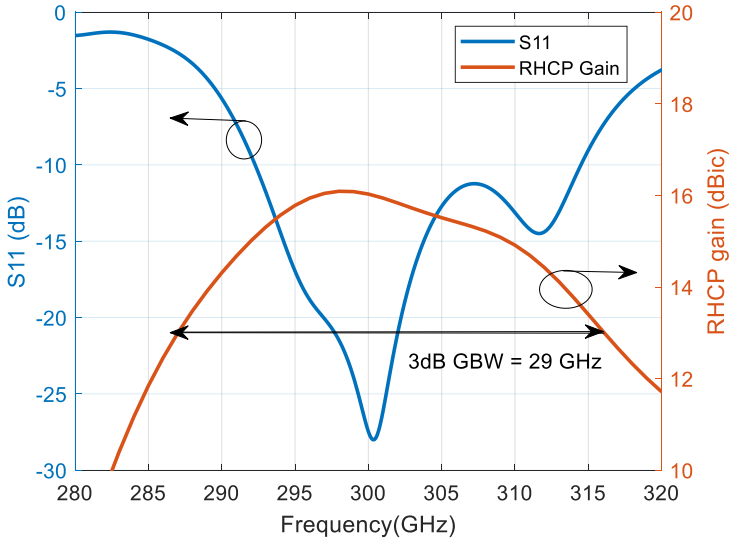

Figure 4.21: The simulated reflection coefficient (S11) and the realized RHCP gain versus frequency of the proposed antenna.

4.3.4 Fabrication Process

The seven brass metal layers needed for the 300 GHz CP-FPC antenna, having different thicknesses in Table 4.3, fabricated using laser-cutting technology as explained in section (4.2.4), have been used as shown in Figure 4.22(a). Using a metallic layer to form a CP-FPC antenna is advantageous in simplifying its fabrication process based on which the aperture–FSS layer and feeding antenna layers can be fabricated separately and then assembled at a later fabrication stage. This reduces the fabrication complexity and cost.

Figure 4.22(b) shows a microscopic image of the CP aperture-type FSS layer, where the actual sidewall width was found to be 50 μm . The proposed antenna with periodic aperture–FSS layer is fabricated and assembled, as shown in Figure 4.22 (c). The complete antenna is composed of feeding antenna parts (A–F layers), 5 × 5 metallic apertures–FSS CP part, and a standard WM-864 rectangular waveguide with UG-387/U flange.

This technology is attractive in terms of low cost and less complexity compared with silicon micromachining technology.

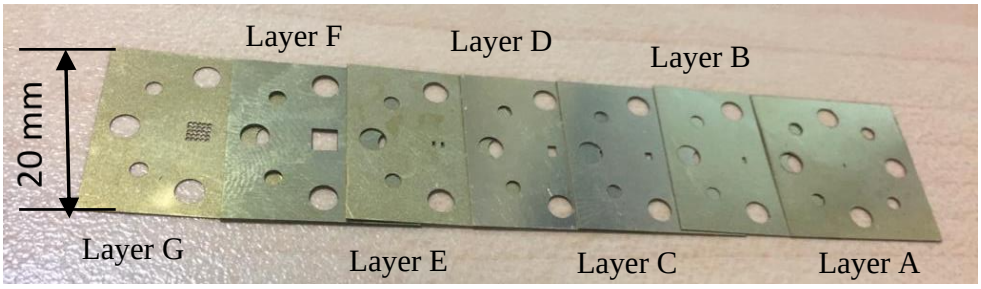

(a)

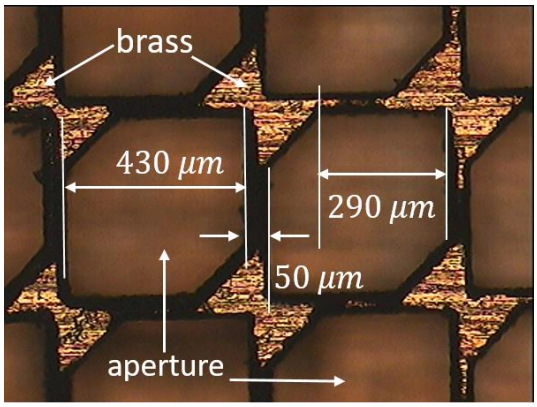

(b)

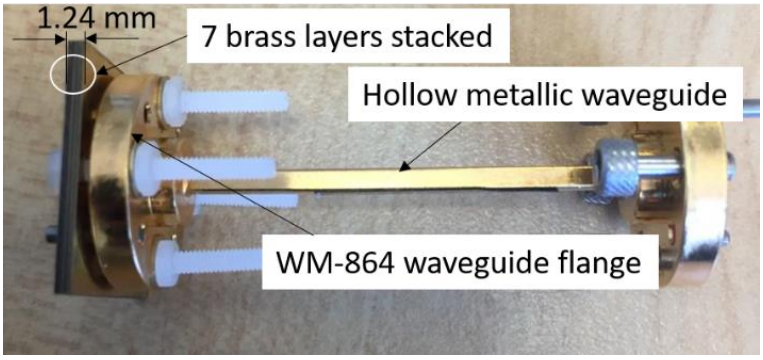

(c)

Figure 4.22: Photographs of (a) 7 brass metal layers required to assemble one antenna, (b) microscopic image of the aperture-type FSS layer, and (c) the manufactured assembled antenna mounted on a standard WM-864 waveguide flange. The antenna is aligned using two standard alignment dowel pins and fixated with four plastic screws. The standard flange size is 20 mm × 20 mm.

4.3.5 Experimental Results and Discussion

In this section, we present the measurements of the fabricated prototype. The reflection coefficient (S11) is measured based on a setup shown in Figure 4.23. The basic components of

the setup consist of a Rohde & Schwarz ZVA67 vector network analyzer (VNA) and a Virginia Diodes Inc. (VDI) frequency extender module (220 – 330 GHz) with a WM-864 waveguide flange interface.

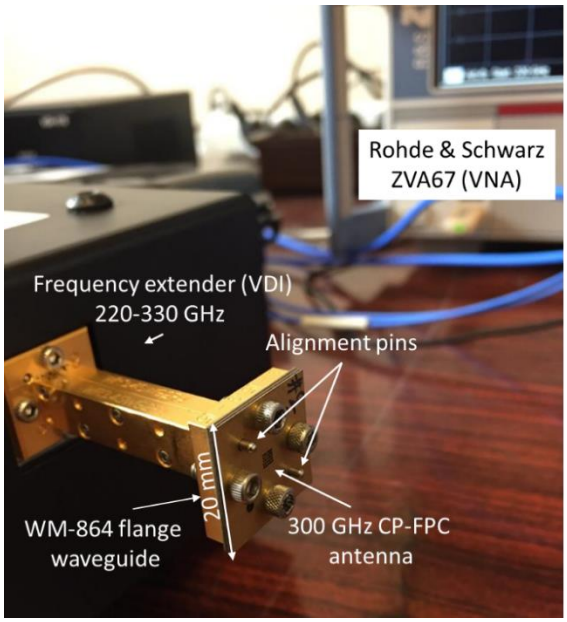

Figure 4.23: Impedance matching measurement setup, where antenna prototype mounted on a standard WM-864 waveguide flange using two alignment pins and four screws.

The measured reflection coefficient (S11<-10 dB) is at a working band from 281 to 305 GHz with a bandwidth of 24 GHz, as shown in Figure 4.24.

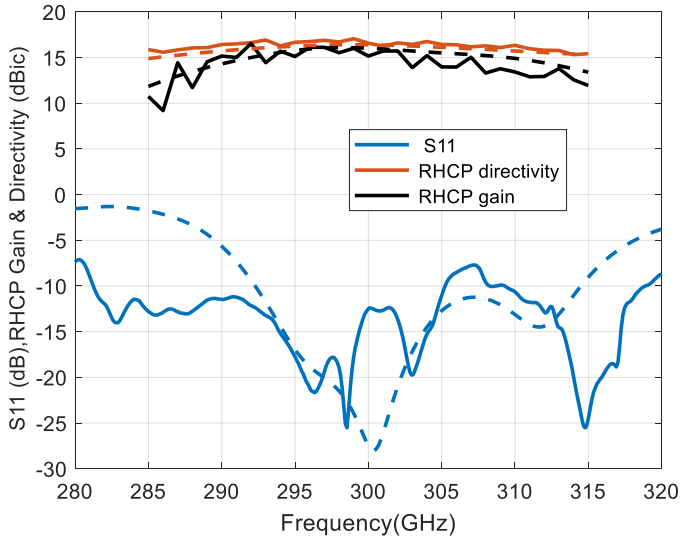

Figure 4.24: Measured (solid lines) and simulated (dashed lines) reflection coefficient (S11), RHCP realized gain, and RHCP directivity for the 300 GHz CP-FPC antenna prototype.

Figure 4.24 also indicates the measured RCHP gain and RHCP directivity of the CP-FPC antenna and it shows that the RCHP gain of the antenna is 13.4 to 16.5 dBic from 290 to 310 GHz. The antenna yields a maximum measured RHCP gain of 16.5 dBic and a measured RHCP directivity of 16.7 dBic at 292 GHz. There is some divergence between the measured RHCP realized gain and simulated results; this may be because of assembling and fabrication tolerances that are acceptable in the 300 GHz band.

To demonstrate the proposed antenna's characteristics, such as the axial ratio, realized gain, directivity, and half-power beamwidth (HPBW), radiation patterns are measured in a compact antenna test range (CATR) chamber at IETR (funded by the European Union through the European Regional Development Fund, through the CPER Projects 2015–2020 SOPHIE/STIC and Ondes). The measurement setup consists of a transmit antenna, a reflector, a positioner, and the antenna under test (AUT). A picture of the setup is shown in Figure 4.25.

The CATR is based on a corner-fed rolled edge reflector of approximately 1200 mm x 1200 mm, producing a cylindrical quiet zone of 600 mm diameter and 600 mm depth. The approximate distances from the feed to a reflector and the reflector to the AUT are respectively 2.3 m and 3.8 m. But as the spillover (i.e. radiation from the feed that falls outside the edge of the reflector) is low, the distance between the reflector and the AUT is not the key point for the dynamic range budget. The CATR feed is a 13 dBi linear CATR feed horn designed and manufactured by Thomas Keating Ltd.

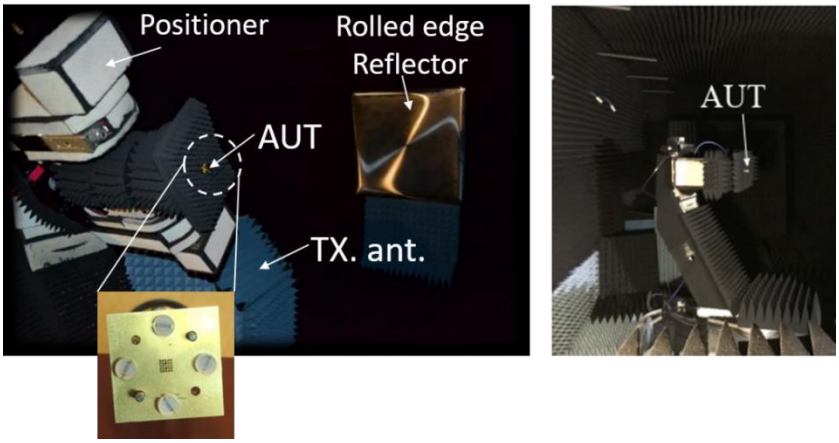

Figure 4.25: The far-field radiation patterns measurement setup at IETR.

The AUT is placed on a roll-over slide over the azimuth positioner. The CATR feed orientations are obtained using a high precision rotation axis. The whole system is settled in a temperature-controlled anechoic chamber of 3.5 m × 3.0 m ×11 m.

The RF measurement system architecture is very classical and is based on VDI WR3 TxRef and high dynamic Rx modules, highlighting a minimum dynamic range of 120 dB. The

dynamic range of the whole system is sufficient to have a dataset eligible for the specific calibration procedure developed by IETR [98]. With such calibration, classical computation of the AR using two orthogonal orientations of linear polarization feed is possible. This calibration enables to estimate and compensation of phase error introduced by the positioning system, limiting the phase error to the contributions of the RF measurement system dynamic range.

The AR is computed using a classical procedure based on a complex measurement of the electrical field received by the AUT when two orthogonal orientations of the linearly polarized feed. This computation is possible thanks to our specific calibration procedure of the CATR, enabling as well 3D measurement with Ludwig 3 representation without polarization tracking, and knowledge of the electrical field ellipse of polarization for each sampling point.

The measured 3-dB AR bandwidth obtained is 5.12 GHz (292.8–297.92 GHz), whereas the simulated one is 5.17 GHz (293.8–298.97 GHz) and is presented in Figure 4.26.

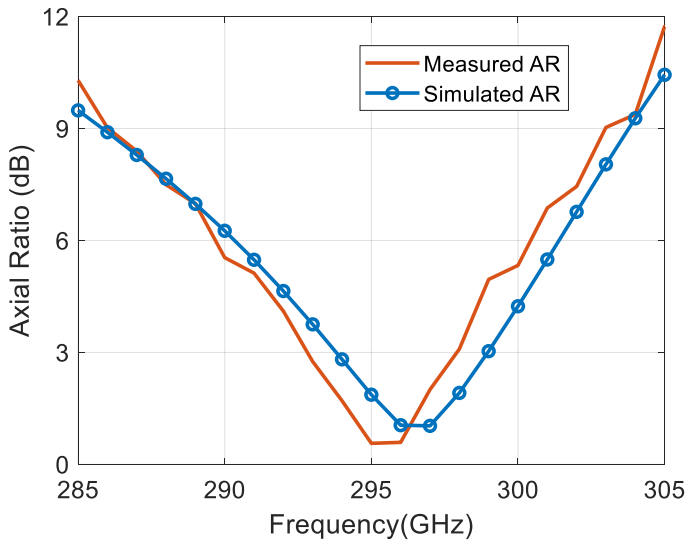

Figure 4.26: Axial ratio (AR) (measured and simulated) of the proposed antenna.

The proposed CP-FPC antenna has a measured RHCP directivity of 16 dBic and a 3-dB RHCP directivity bandwidth of 10% (285–315 GHz) over the desired band. The measured 3-dB AR bandwidth is 5.12 GHz (292.8–297.92 GHz), as shown in Figure 4.26. The measurement of directivity of the antenna is computed using a spherical harmonic expansion tool [98-100], which is applied to reconstruct the 3D radiation pattern at any point as it gives access to an exact interpolation of the complex EM electrical field.

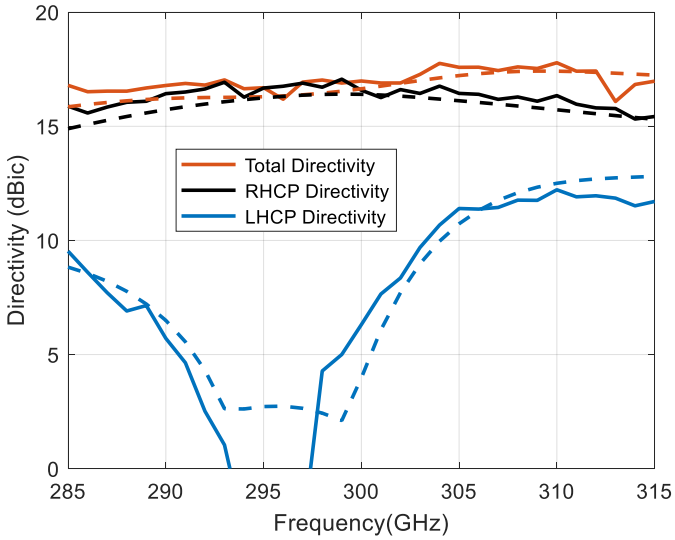

Figure 4.27: Measured (solid lines) and simulated (dashed lines) of the total, RHCP, and LHCP directivities.

The measured 2D-radiation pattern of the proposed antenna for both co-polarization (RHCP) and cross-polarization (LHCP) at different frequencies is presented in Figure 4.28. The fabricated prototype works as the RHCP antenna from 292 to 297 GHz, confirming the proposed simulated antenna results. It is clear from Figure 4.28 that the measured normalized patterns occur at the broadside direction, which is equivalent to azimuth ($az = 0^{\circ}$) and elevation ($ele = 0^{\circ}$).

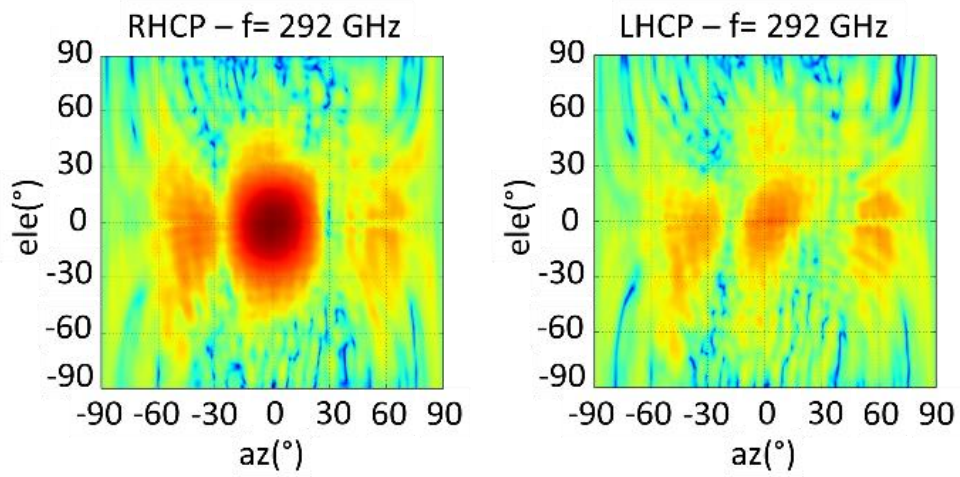

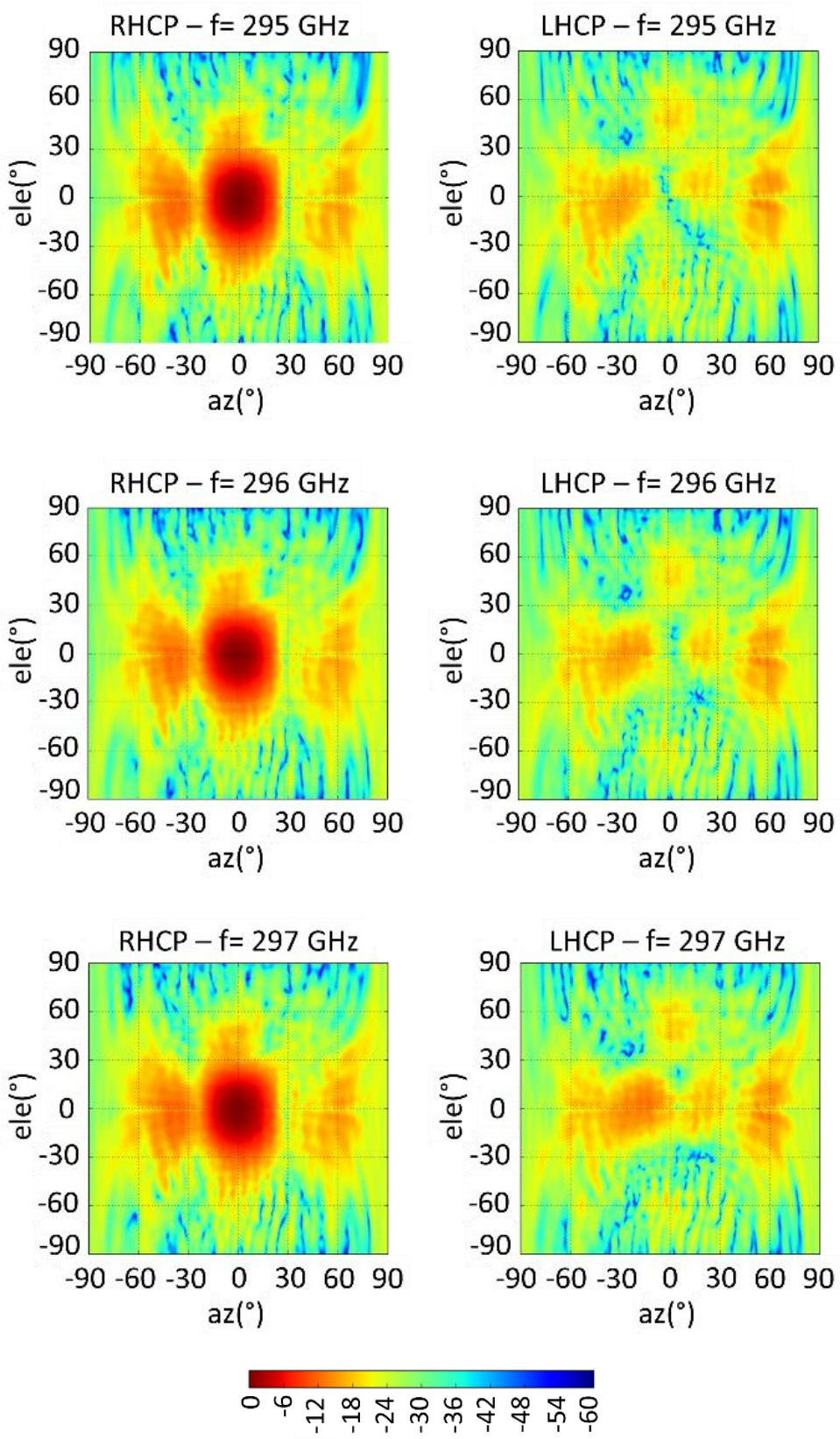

Figure 4.28: Measured normalized 2D co-polarization (RHCP) and cross-polarization (LHCP) radiation patterns of the proposed antenna at different frequencies. The color bar is on the dB scale.

Figure 4.29 shows the 2D measured AR plots of the proposed antenna at 292, 295, 296, and 297 GHz respectively. The AR is kept below 3 dB within the scope of the main beam between -13.2° and 13.2° at broadside direction for the frequencies shown in this figure. The AR reaches a lower value near 0.51 dB at 295 and 296 GHz, as shown in the figure by the black color in the bar on the dB scale.

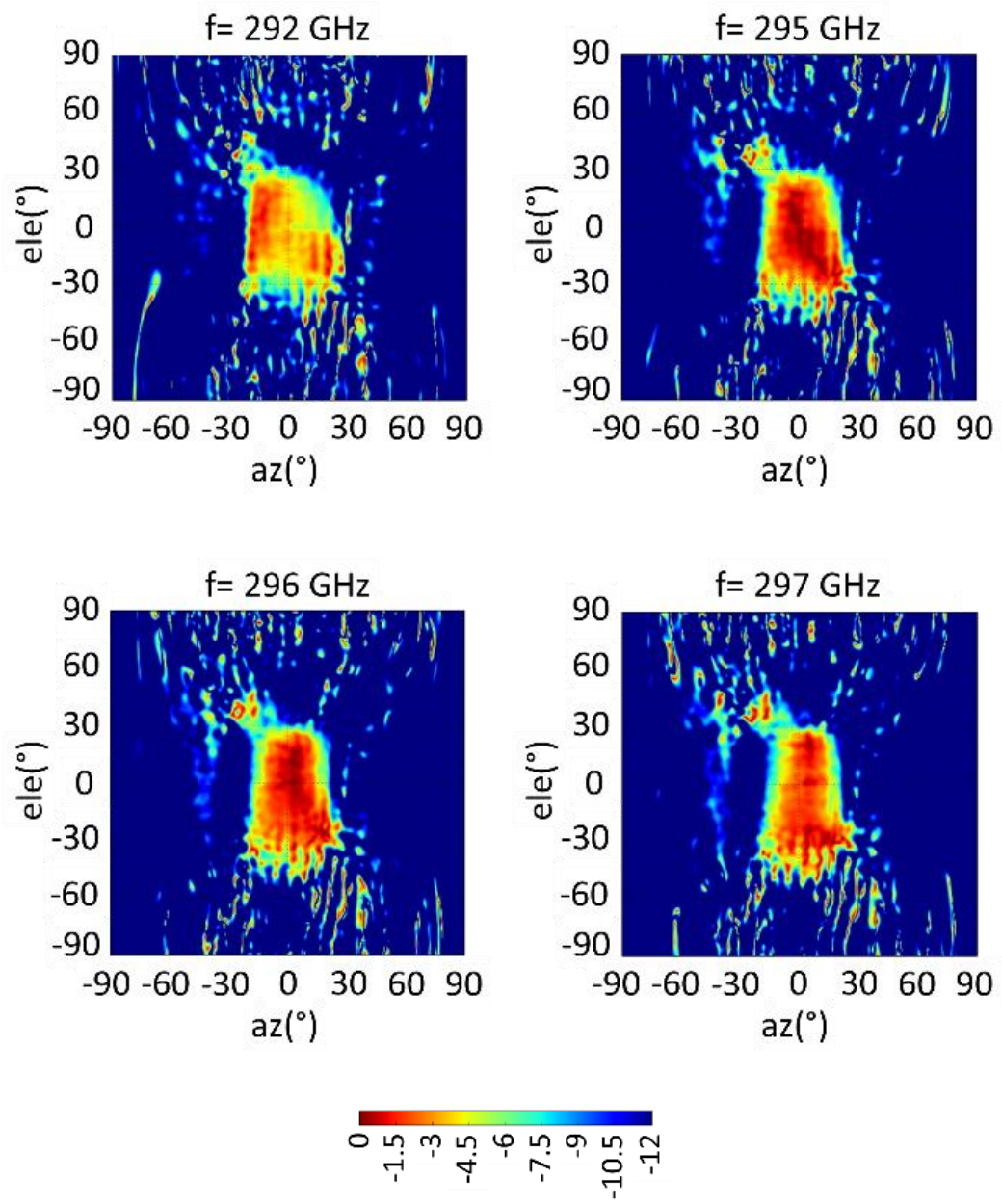

Figure 4.29: Measured normalized 2D axial ratio plots at 292, 295, 296, and 297 GHz. The color bar is on the dB scale.

The normalized measured RHCP (co-pol) and LHCP (cross-pol) radiation patterns of the fabricated antenna in both azimuth-plane and elevation-plane cuts, at four frequency points (292, 295, 296, and 297 GHz), are shown in Figure 4.30. There is a good agreement between

all simulations and measurement results. Also, there is approximately a 20-dB difference between the co-pol and cross-pol measured gain values (i.e., cross-polarization discrimination (XPD) = 20 dB) at 295 and 296 GHz, similar to the simulated ones.

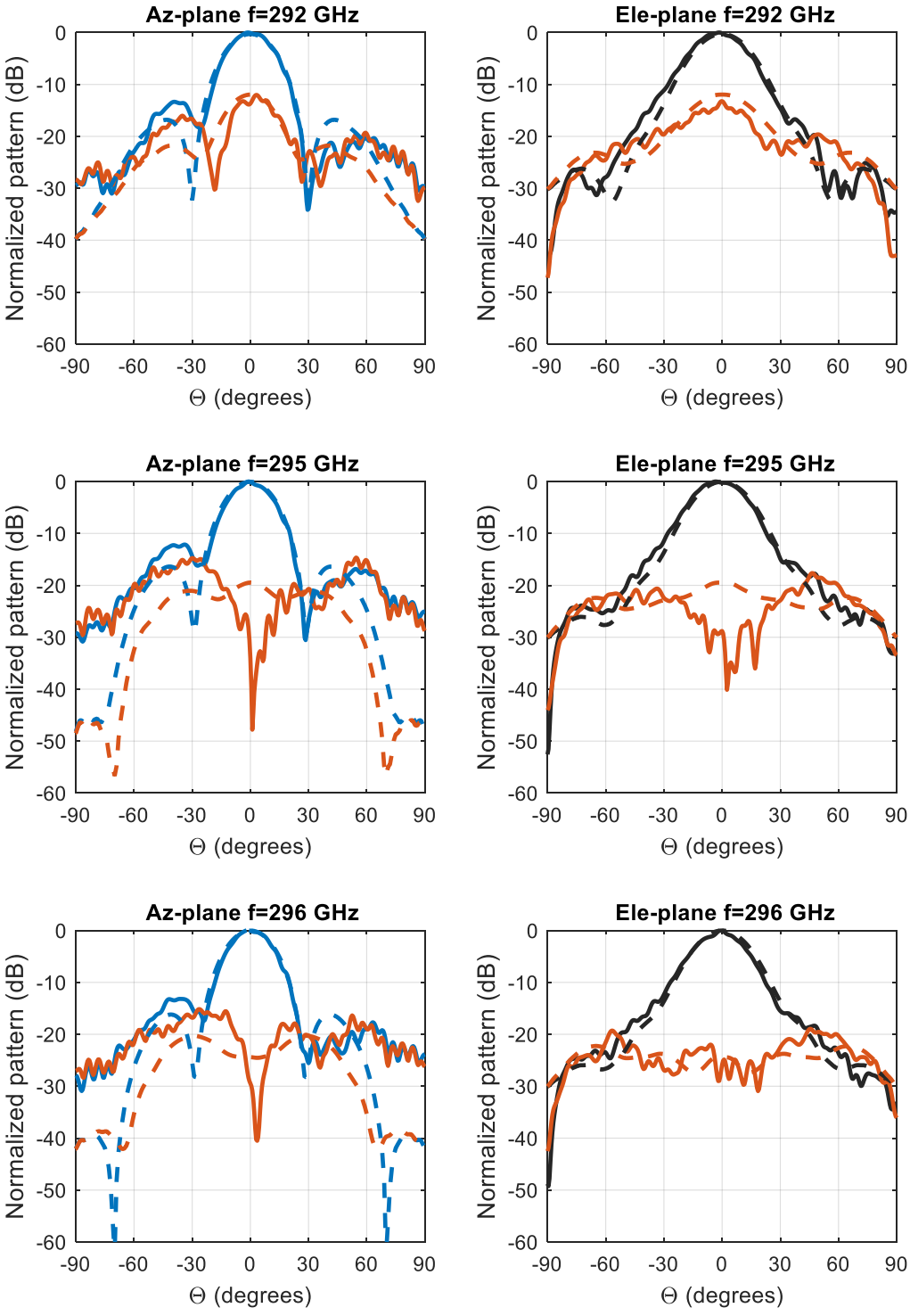

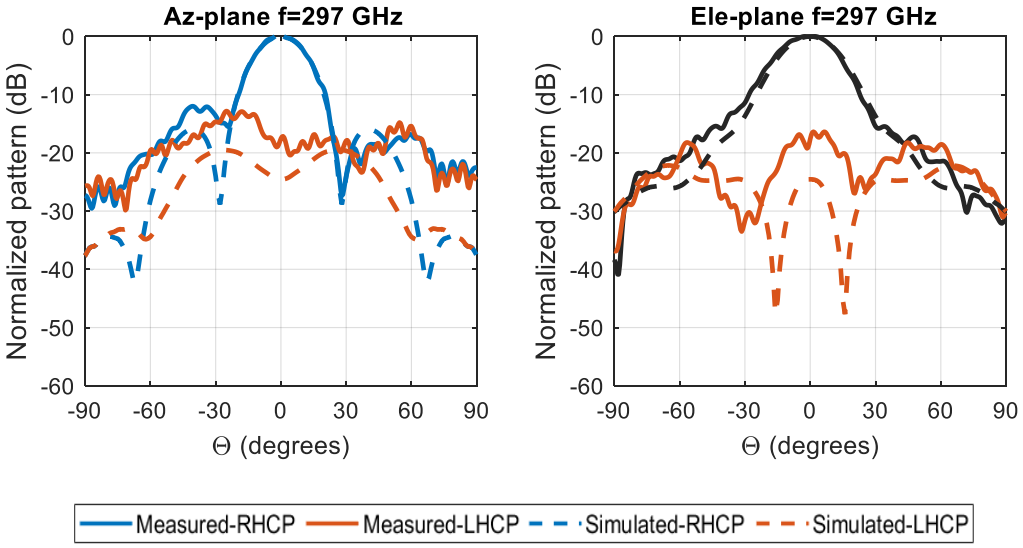

Figure 4.30: Measured (solid lines) and simulated (dashed lines) broadside radiation patterns of the designed antenna in both principle planes at different frequencies.

The CP-FPC antenna has an average measured HPBW in both Ele-plane and Az-plane. The simulated and measured data are shown in Figure 4.31, which are acceptable.

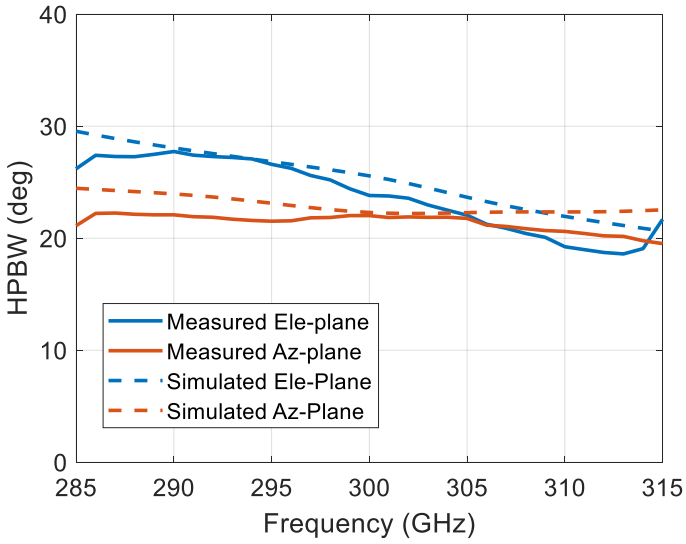

Figure 4.31: Measured (solid lines) and simulated (dashed lines) HPBW for the Ele-plane, and Az-plane cuts.

To verify the results and investigate the radiation characteristics outside the two principal planes (Az-plane and Ele-plane), we measured the upper hemisphere far-field in the UV-plane for the CP-FPC antenna. The results plotted in Figure 4.32, show a wide-radiation pattern in the v-plane ($v = \sin\theta \sin\phi$), and a narrow-radiation pattern in the u-plane ($u = \sin\theta \cos\phi$).

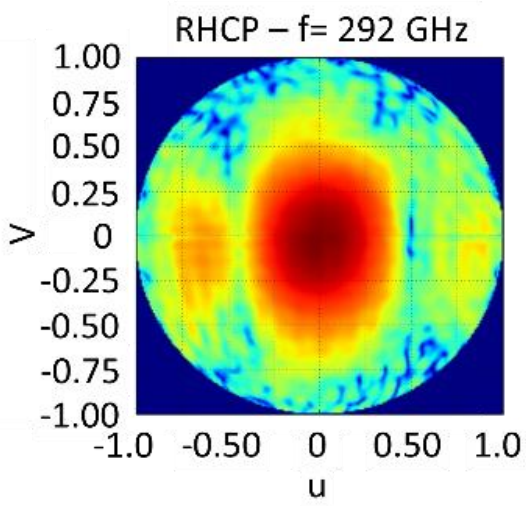
RHCP – f= 292 GHz
1.00
0.75
0.50
0.25
0
-0.25
-0.50
-0.75
-1.00
V
-1.0
-0.50
0
0.50
1.0
u

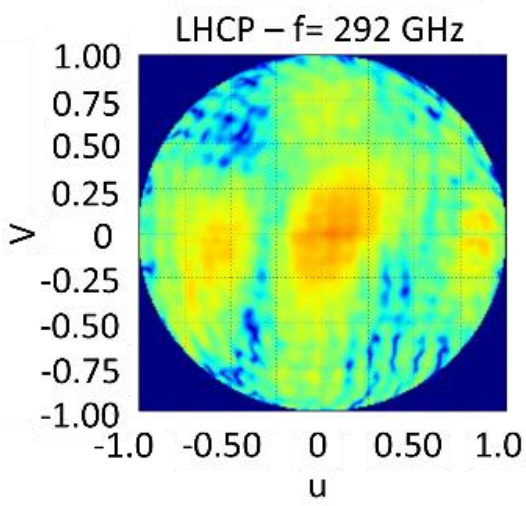
LHCP – f= 292 GHz
1.00
0.75
0.50
0.25
0
-0.25
-0.50
-0.75
-1.00
V
-1.0
-0.50
0
0.50
1.0
u

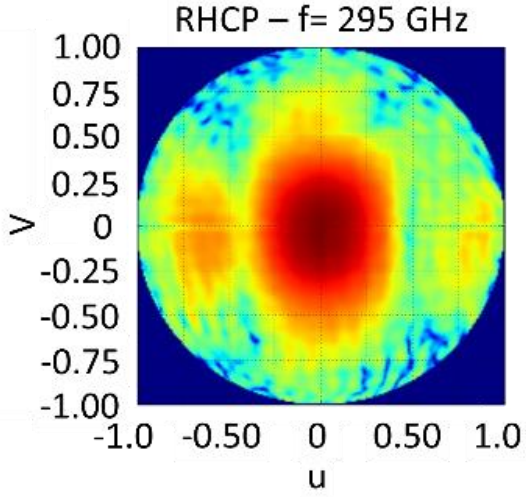
RHCP – f= 295 GHz
1.00
0.75
0.50
0.25
0
-0.25
-0.50
-0.75
-1.00
V
-1.0
-0.50
0
0.50
1.0
u

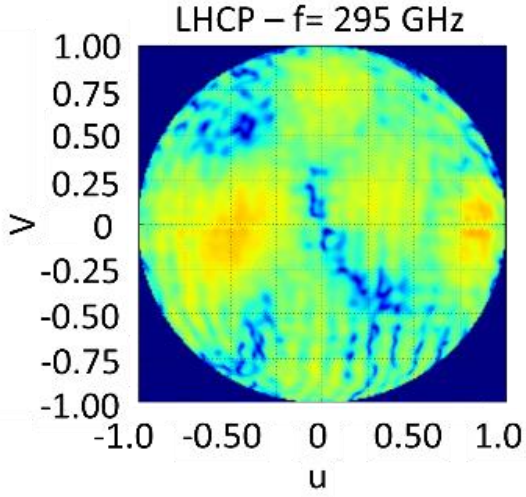
LHCP – f= 295 GHz
1.00
0.75
0.50
0.25
0
-0.25
-0.50
-0.75
-1.00
V
-1.0
-0.50
0
0.50
1.0
u

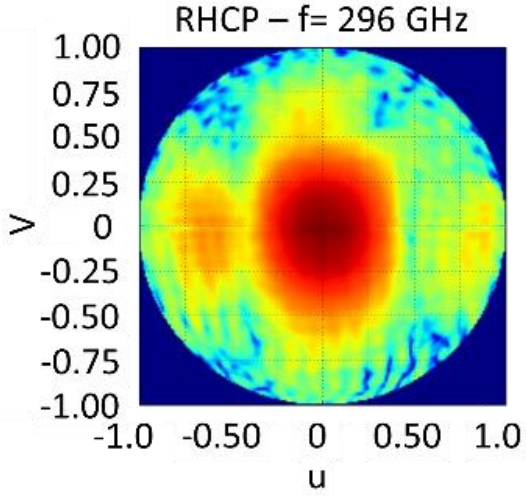
RHCP – f= 296 GHz
1.00
0.75
0.50
0.25
0
-0.25
-0.50
-0.75
-1.00
V
-1.0
-0.50
0
0.50
1.0
u

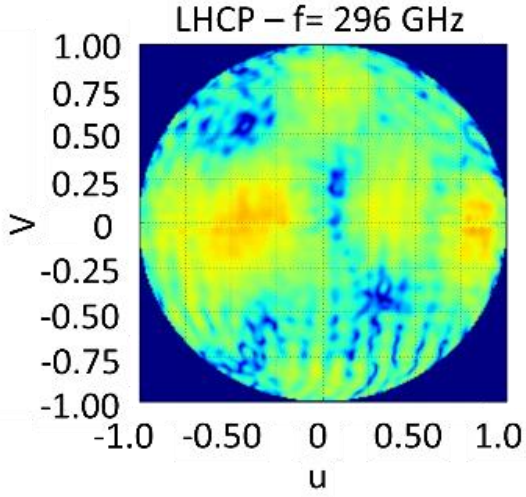
LHCP – f= 296 GHz
1.00
0.75
0.50
0.25
0
-0.25
-0.50
-0.75
-1.00
V
-1.0
-0.50
0
0.50
1.0
u

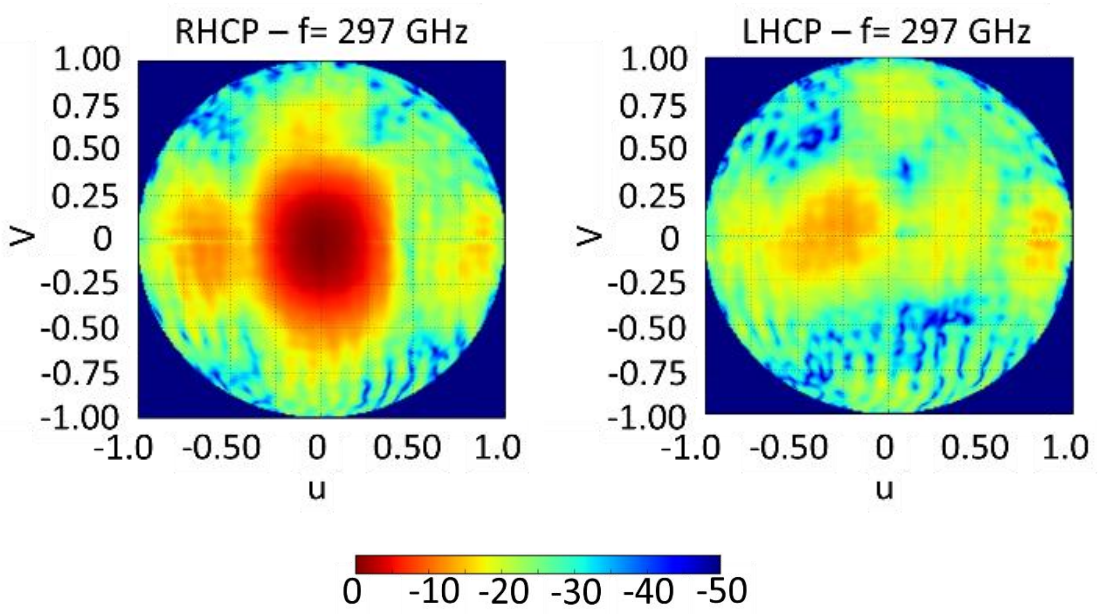

Figure 4.32: Measured 2D-colormpas far-field of the proposed CP-fpc antenna in u–v spectral plane at different frequencies. The color bar is on the dB scale.

It is noticed that the proposed antenna radiates RHCP radiation. The LHCP radiation FPC antenna will be generated easily by rotating the aperture–FSS layer by 90°, as shown in Figure 4.33. The LHCP antenna's simulation results are the same as those for the proposed antenna due to their completely symmetric structure, except that the new antenna radiates LHCP waves. This indicates that both RHCP and LHCP FPC antennas can be designed with the proposed hexagonal aperture–FSS layer.

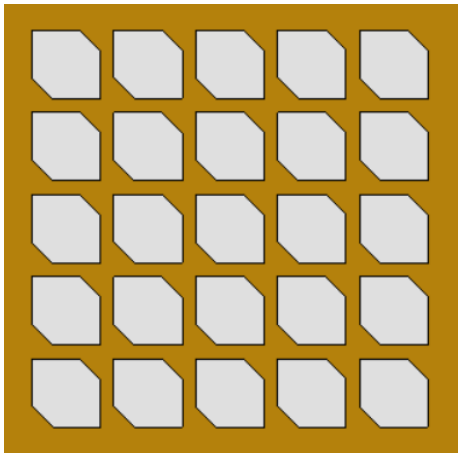

Figure 4.33: Rotation of the hexagonal aperture–FSS layer for LHCP-FPC antenna.

The brass plates are attached directly using two dowel pin alignments of waveguide flange with four plastic screws. The tolerance of fabrication is 20 µm (laser spot size of 20 µm) as mentioned in fabrication technology. The effect of 20 µm tolerance on the AR bandwidth for

aperture-FSS unit cells of the proposed antenna is shown in Figure 4.34. As we notify in Figure 4.34 below that, the scale factor (cutting the CP-aperture unit cell) is more sensitive which can produce shifting in AR bandwidth.

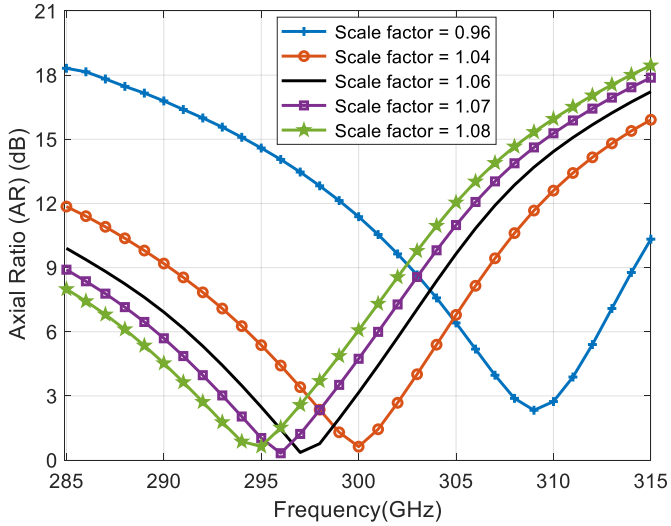

Figure 4.34: The effect of cutting CP aperture laser beam on AR bandwidth

The block structure's size, which does not greatly influence the characteristics of the proposed antenna, is set as 20 mm × 20 mm according to the standard WM-864 waveguide flange size, including alignment and screws holes.

The claim of small size is validated as shown below with the simulated current distributions, radiation patterns, antenna gain, and the AR versus frequency, which are unaltered with and without waveguide flange.

The proposed CP-FPC antenna's performance is compared with other recently reported sub-THz CP antennas, which are summarized in Table II. Some key parameters are listed, including frequency design, 3dB AR bandwidth, realized gain, and fabrication technology. Table II indicates that our proposed antenna delivers a high-gain, low-cost, and low-profile structure compared to the others.

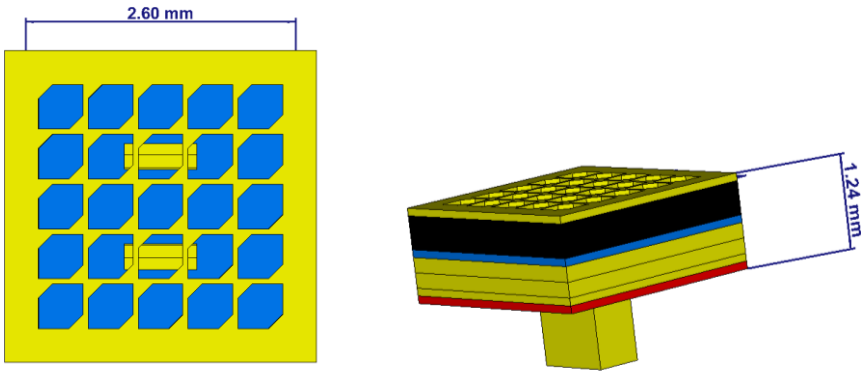

(a)

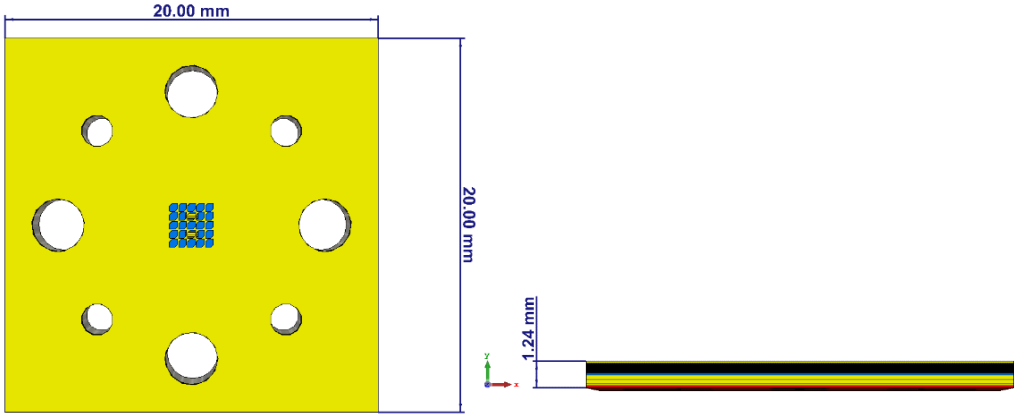

(b)

Figure 4.35: The CP-FPC structure (a) without and (b) with the waveguide flange holes(alignment and screws).

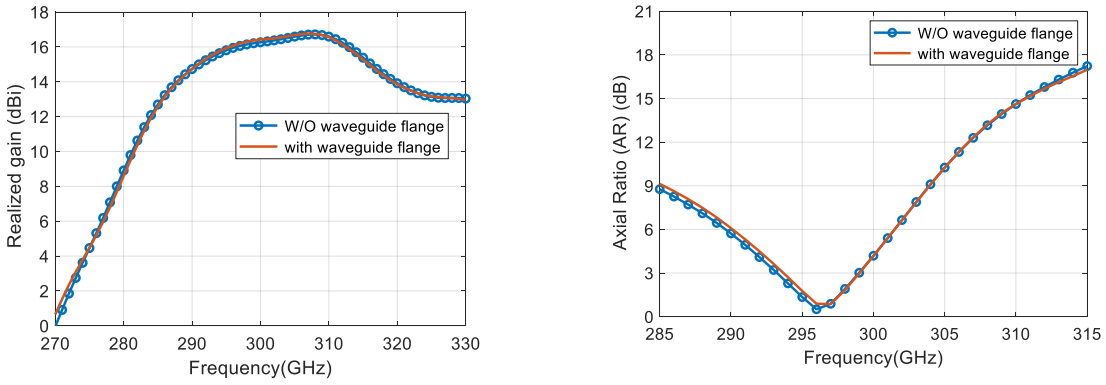

(a) (b)

Figure 4.36: The CP FPC antenna (a) antenna gains and (b)the AR versus frequency

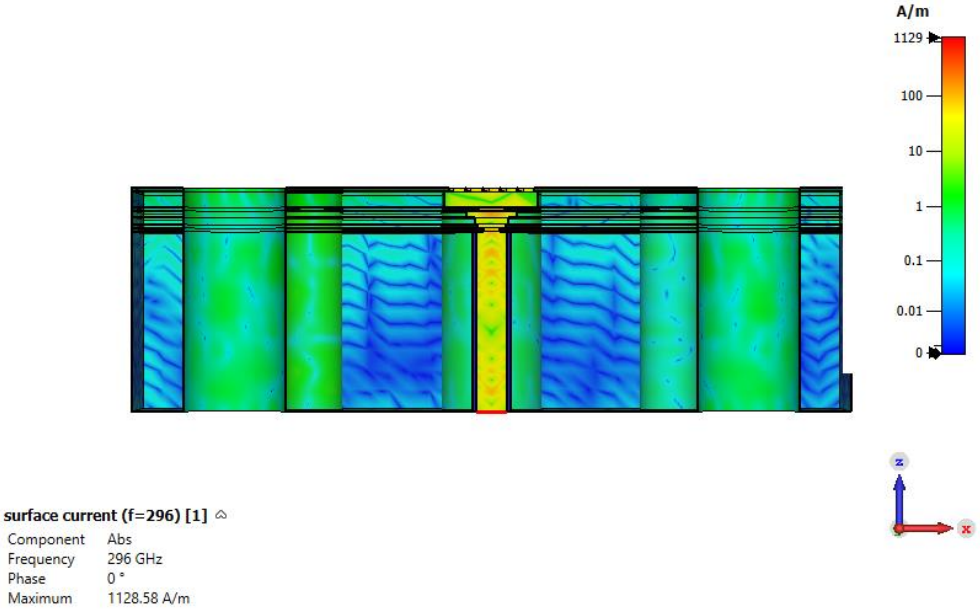

(a)

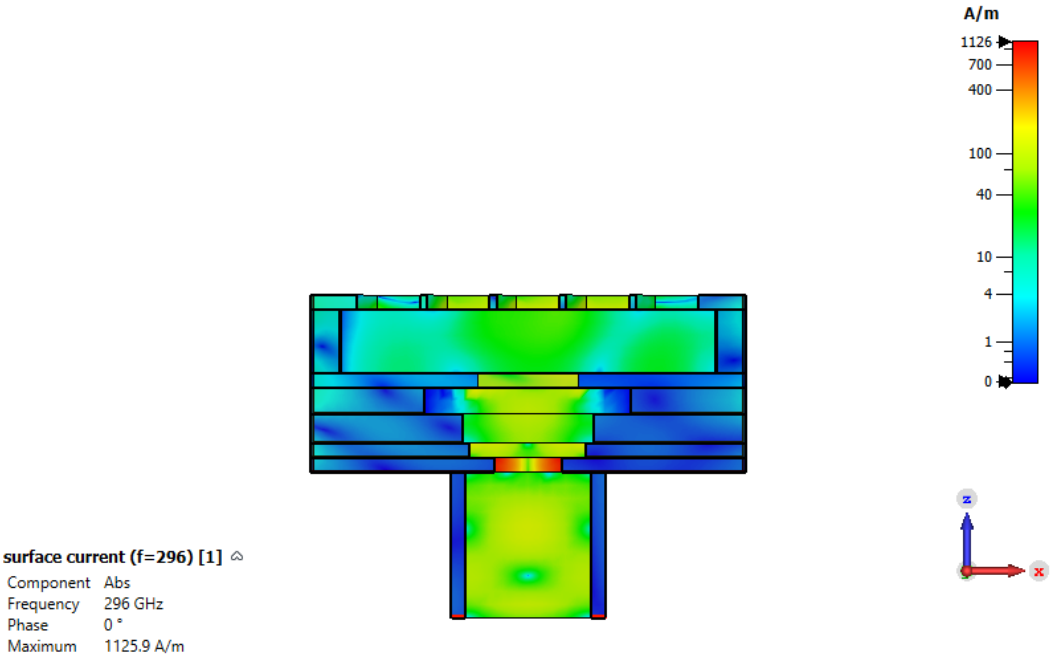

(b)

Figure 4.37: The simulated current distributions (a) with and (b) without the waveguide flange holes(alignment and screws).

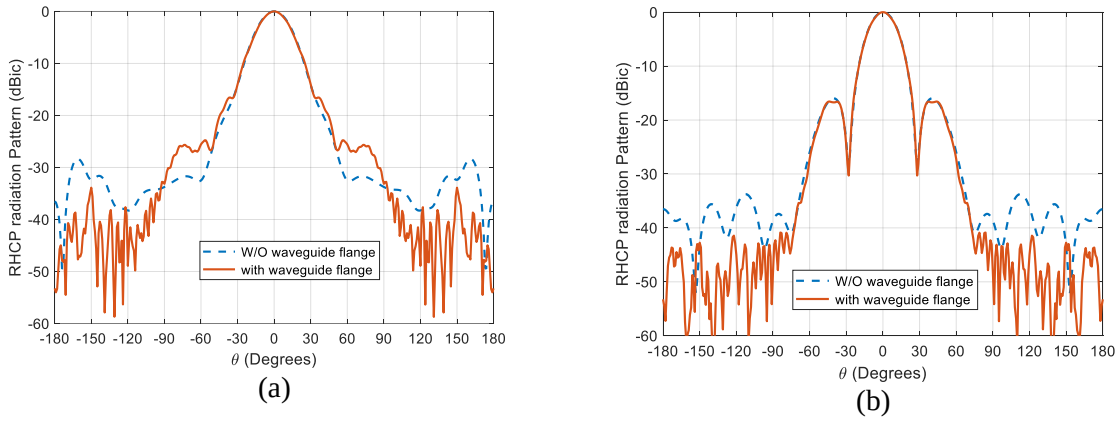

Figure 4.38: The simulated radiation patterns (a) Phi = 0 and (b) Phi= 90.

Table 4.4: Comparison between the proposed work with other latest CP sub-THz antenna

Ref	Antenna type	Freq (GHz)	3dB-AR BW (%)	Max gain (dBic)	Matching BW (%)	3-dB gain BW (%)	Fabrication process	Fabrication complexity	Size
[71]	Double-fan-shaped slot	495	2	12.5	2	NA	Silicon micromachining	Moderate	$13.3\lambda_0 \times 13.3\lambda_0 \times 1.3\lambda_0$
[72]	Dielectric lens	300	~18.3	30.8	NA	26.66	3D printing	High	$20\lambda_0 \times 20\lambda_0 \times 4.2\lambda_0$
[77]	Conical horn	300	2.33	18.4	20	NA	Wire EDM	Moderate	$4\lambda_0 \times 4\lambda_0 \times 4.1\lambda_0$
[101]	Deflection pyramidal horn	300	33.33	10.4	33.33	13.3	CNC	High	$10\lambda_0 \times 1.5\lambda_0 \times 6.7\lambda_0$
This work	Fabry-Perot cavity	300	1.73	16.5	8	6.66	Laser cutting	Low	$2.6\lambda_0 \times 2.6\lambda_0 \times 1.24\lambda_0$

4.3.6 Conclusion

A CP-FPC antenna working in the sub-THz band has been presented. The proposed antenna has been designed with the standard WM-864 waveguide flange dimensions, and it has been fabricated in brass metal using laser cutting technology. The metallic aperture–FSS layer was working as a polarizer to convert LP waves into CP waves. The 300 GHz CP-FPC antenna has been characterized using a millimeter-wave compact range anechoic chamber, obtaining radiation patterns characteristics between the frequency from 285 to 315 GHz. A 3 dB measured AR bandwidth of approximately 1.73 % (5.12 GHz) with a central frequency of 296 GHz is achieved. Finally, it has a low profile of 2.6 λ_0×2.6 λ_0×1.24 λ_0, which can be applied to future terahertz wireless communication systems in the sub-THz band.

4.4 Circularly Polarized Antenna Based on Metasurface Superstrate

The 3-D exploded view of the proposed antenna is shown in Figure 4.39(a). The antenna is fed by a standard WM-864 rectangular waveguide (864 μm ×432 μm). The waveguide is coupled to a ground layer. The ground layer (Layer A) is a slot antenna with a 100 $\boldsymbol{\mu}$m thickness of metal brass. Layers B, C, and D are integrated-stepped horn elements (three layers) with different thicknesses of metal brass as shown in Table 4.5, which have been used as multistage to improve the impedance matching bandwidth. The coupling layer (Layer E) consisting of two-parallel slots is used to broaden matching impedance, which is in phase with the ground layer and integrated horn element. Cavity layer (Layer F) is supported metal plate to Metasurface (MTS) superstrate layer, having a thickness to achieve resonance condition of Fabry-Perot, which is normally equal to a half-wavelength at the resonant frequency of 300 GHz. The basis mathematical analysis used for choosing the dimensions of the proposed antenna structures can be found in [84, 85, 97], which are calculated by using the simple well-known ray-tracing formula.

The MTS layer is realized by perforated grids of hexagonal and octagonal-shaped radiating apertures made by cutting through a metallic brass layer of finite thickness of 100 μm as presented in Figure 4.39(b). The 5 x 5 array consists of a combination of circularly polarized (CP) elements and linearly polarized (LP) elements. The CP elements are LHCP hexagonal radiating apertures and the LP elements are octagonal-shaped aperture radiators; which are obtained by superimposing one LHCP aperture radiator and one RHCP aperture radiator as shown in Figure 4.39(c).

For fabrication, we integrate the standard UG-387/U waveguide flange (i.e. alignments and screws holes) into the antenna design. The design parameters detail of layers (units in millimeters) is reported in Table 4.5.

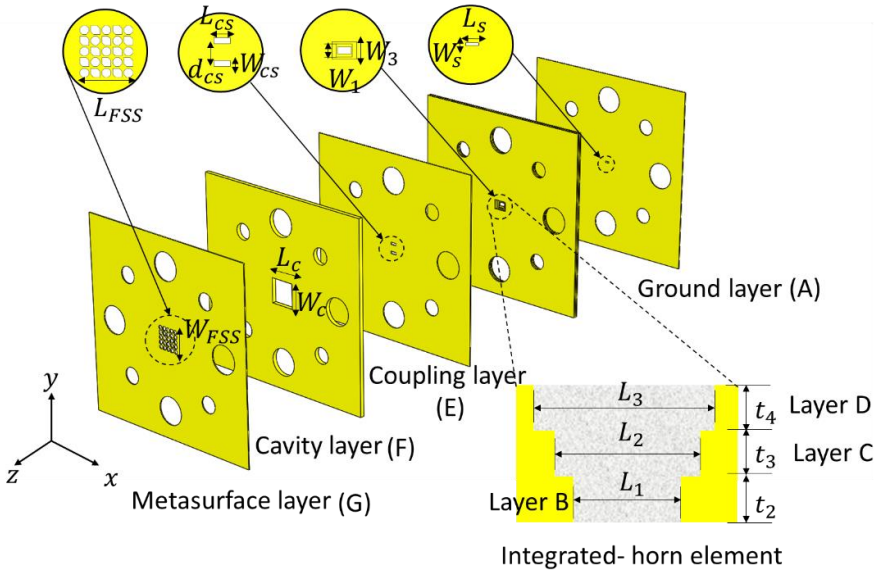

(a)

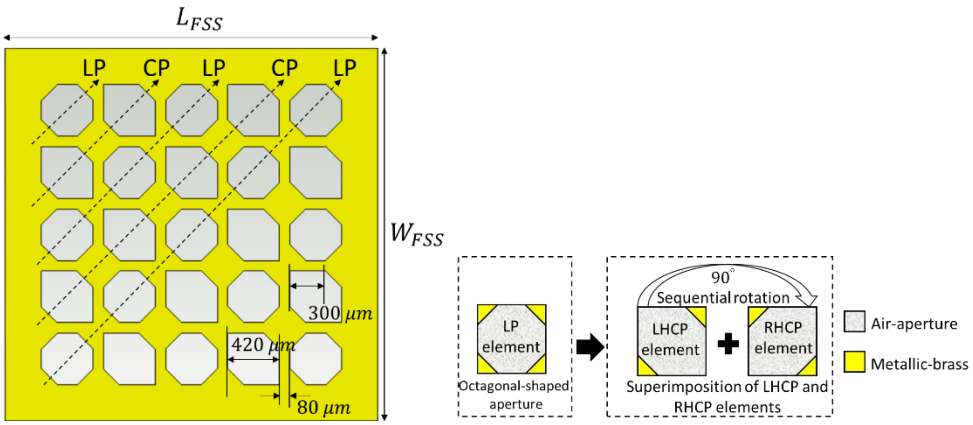

(b) (c)

Figure 4.39: 300 GHz CP-RCA:(a) exploded model view of 7-layered-structures (brass used for all layers) [102], (b) top view of metasurface layer (dimensions is inset), and (c) graphical demonstration of the working principle of the proposed LP octagonal-shaped aperture.

Table 4.5: Design parameters dimensions (units: mm)

Layers	Param.	Value	Param.	Value	Param.	Value
Ground	t_1	0.1	L_s	0.46	w_s	0.1
Integrated	t_2	0.1	L_1	0.8	w_1	0.4
horn	t_3	0.2	L_2	1	w_2	0.75
element	t_4	0.2	L_3	1.42	w_3	1
Coupling	t_5	0.1	L_{cs}	0.7	w_{cs}	0.25
Cavity	h_c	0.44	L_c	2.6	w_c	2.6
MTS	t_{FSS}	0.1	L_{FSS}	2.32	w_{FSS}	2.32

4.4.1 Experimental Results and Discussion

To achieve simplicity in fabrication, each metal layer in the proposed antenna is manufactured by using laser cutting brass technology as explained in section (4.2.4). There are seven brass metal layers for one antenna assembly, with different thicknesses as shown in Table 4.5, and have been used to manufacture the proposed 300 GHz CP-RCA are shown in Figure 4.40 (a).

Using a metallic layer to form a CP-RCA is advantageous in simplifying its fabrication process based on which the MTS superstrate layer and feeding antenna layers can be fabricated separately and then assembled at a later fabrication stage. This reduces the fabrication complexity and cost.

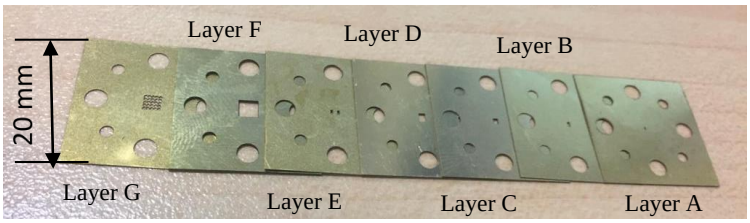

(a)

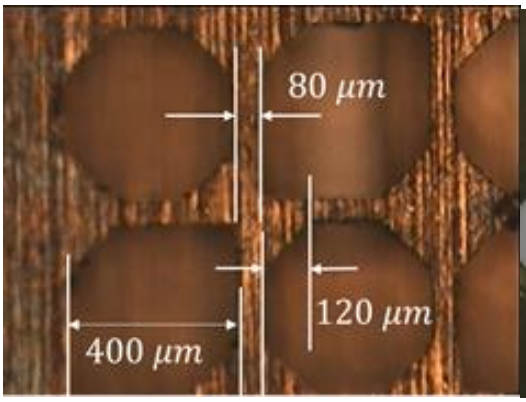

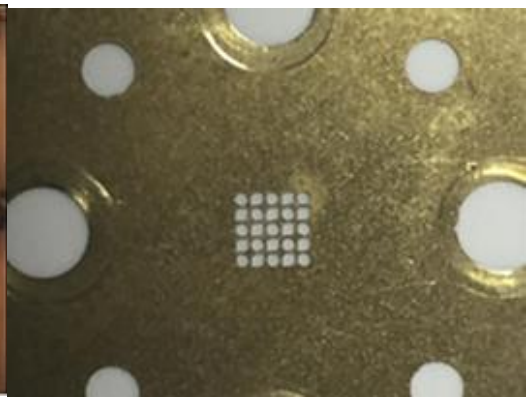

(b) (c)

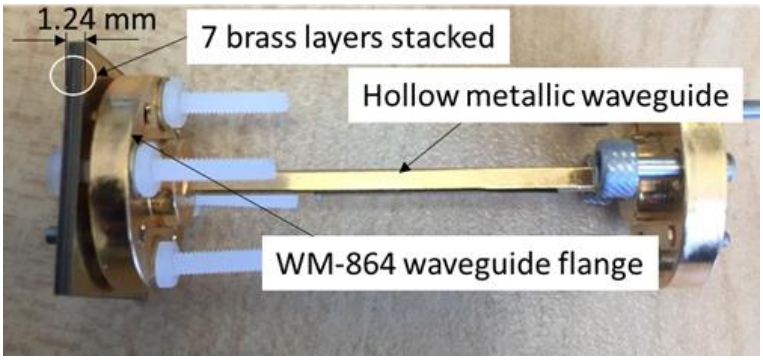

(d)

Figure 4.40: Photographs of manufactured CP-RCA at 300 GHz (a) seven metal brass fabricated layers (b) microscope image of MTS layer, (c) enlarged image of CP-MTS layer, and (d). fabricated prototype connected to standard UG-387/U waveguide flange [102].

Figure 4.40 (b) demonstrates a microscope image of the geometry of the novel proposed radiating hexagonal and octagonal-shaped aperture unit cells. It is found that the periodicity of the unit cells $p = 0.48\,\lambda_0$, the unit cell of LHCP unit cell has two symmetrically isosceles triangle chamfers, of $0.12\,\lambda_0$,where λ_0 is the operation frequency at 300 GHz. Figure 4.40(c) shows an enlarged image of the CP MTS superstrate layer (layer G). For measurements, the proposed antenna must be connected to a standard UG-387/U waveguide flange as shown in Figure 4.40 (d).

The measured and simulated reflection coefficients (S11) of the proposed CP-RCA are shown in Figure 4.41. The measured impedance bandwidth for reflection coefficient < -10 dB is 10 %, covering from 275 to 305 GHz. There is a discrepancy between the simulated and measured results, which can be attributed to the fabrication tolerances.

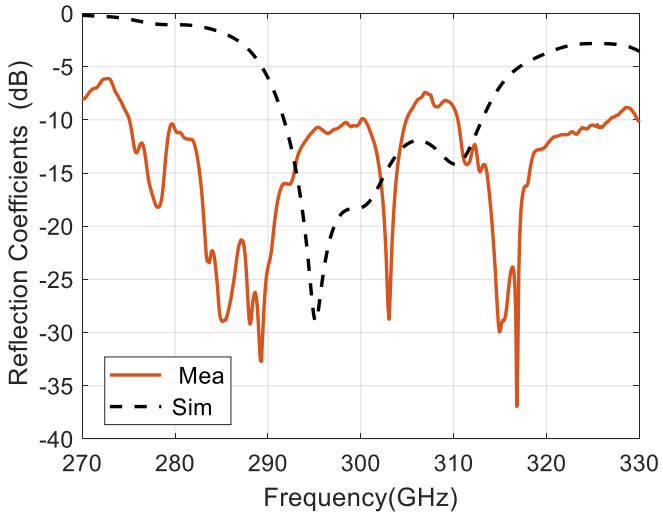

Figure 4.41: Measured and simulated the reflection coefficients (S11) of the CP-RCA.

Figure 4.42 illustrates the measured LHCP directivity, realized gain, and radiation efficiency of the proposed antenna. The maximum LHCP directivity is 16.8 dBic and the maximum LHCP realized gain is 16.2 dBic. The measured overall radiation efficiency is more than 65 % from 290 to 310 GHz.

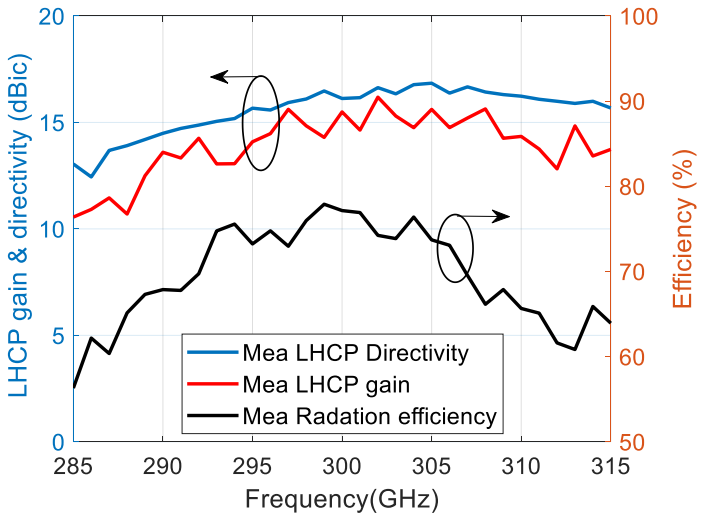

Figure 4.42: Measured LHCP directivity, realized gain, and radiation efficiency of the proposed antenna.

The proposed CP-RCA has a measured LHCP directivity of 16.8 dBic and 3-dB LHCP directivity bandwidth of 10% (285–315 GHz) over the desired band, as shown in Figure 4.43.

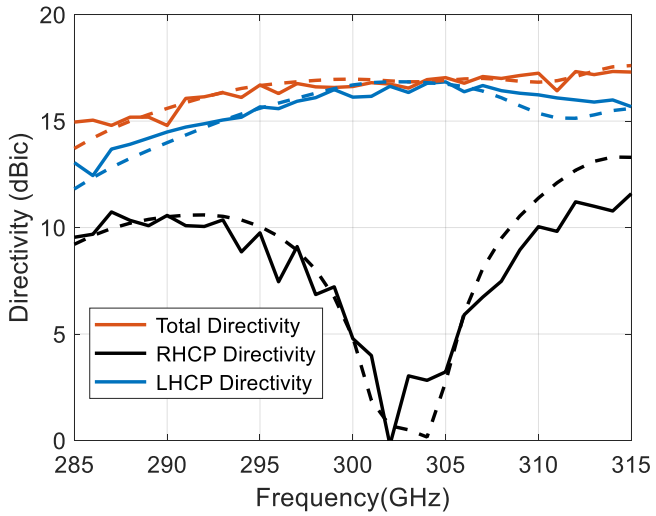

Figure 4.43: The measured (solid lines) and simulated (dashed lines) of the total, LHCP, and RHCP directivities for the proposed antenna.

It is noted in Figure 4.44 that, the measured 3-dB AR bandwidth obtained is 4.24 GHz (301.3–305.54 GHz) with a deviation from the broadside direction by 5 degrees in both principal planes due to slight variation in the dimension (the long-side section of hollow waveguide flange, Figure 4.40 (d)), whereas the simulated one is 3.6 GHz (301.1– 304.7 GHz).

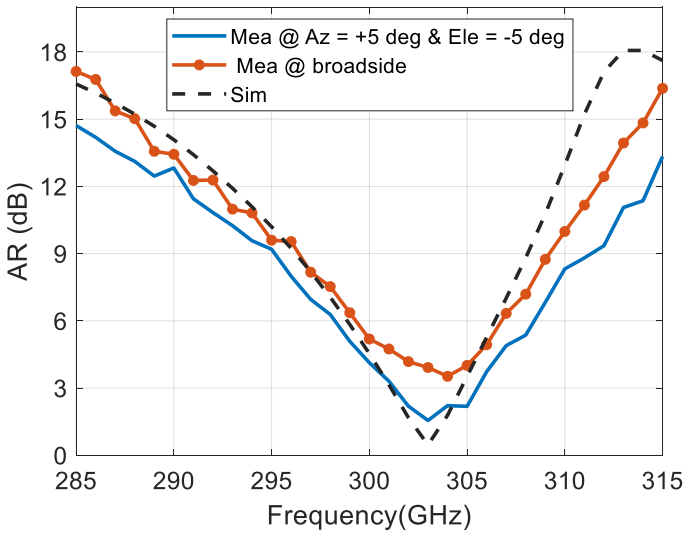

Figure 4.44: Measured and simulated axial ratio (AR) of the proposed antenna.

Figure 4.45 shows the 2D measured AR plots of the proposed antenna at 300, 302, 303, and 305 GHz. The bend of the long-side section of the hollow waveguide flange (WM-864 waveguide) is the one that affects the broadside direction.

Figure 4.46 shows the measured normalized radiation patterns in a compact antenna test range (CATR) chamber at IETR [98] (funded by the European Union through the European Regional Development Fund, through the CPER Projects 2015–2020 SOPHIE/STIC and Ondes) at 300 GHz, 302 GHz, 303 GHz, and 305 GHz respectively for the CP-RCA.

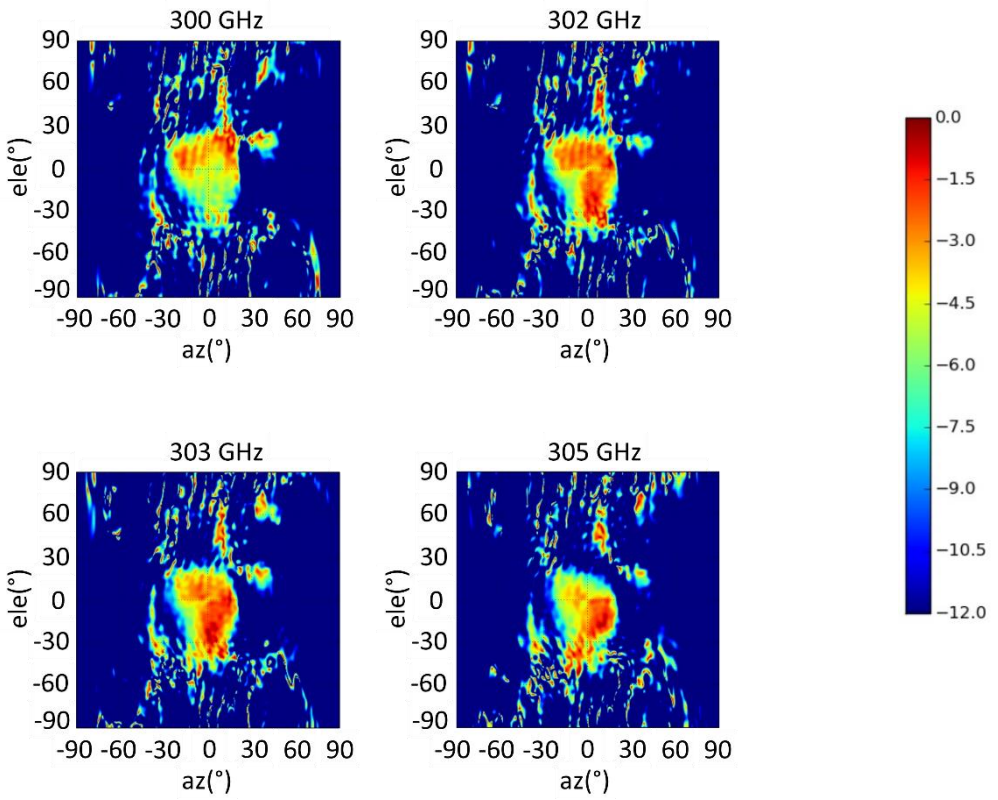

Figure 4.45: Measured 2D AR of the proposed antenna at different frequencies.

A good agreement is obtained between the measured and simulated far-fields as shown in Figure 4.46. At higher frequencies (i.e. 300 GHz), the physical dimensions are very tiny, and hence a slight variation in the dimension (the long-side section of hollow waveguide flange Figure 4.40 d) has a noticeable effect on the radiation characteristics. The measured results have some deviation in the azimuth plane. However, it would be acceptable for such low-cost prototyping fabrication.

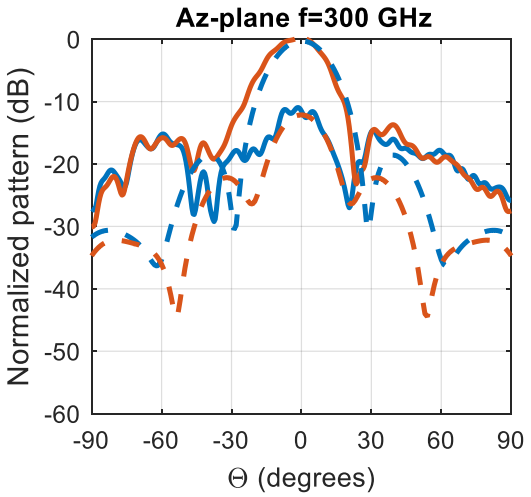
Az-plane f=300 GHz
Normalized pattern (dB)
0
-10
-20
-30
-40
-50
-60
-90 -60 -30 0 30 60 90
Θ (degrees)

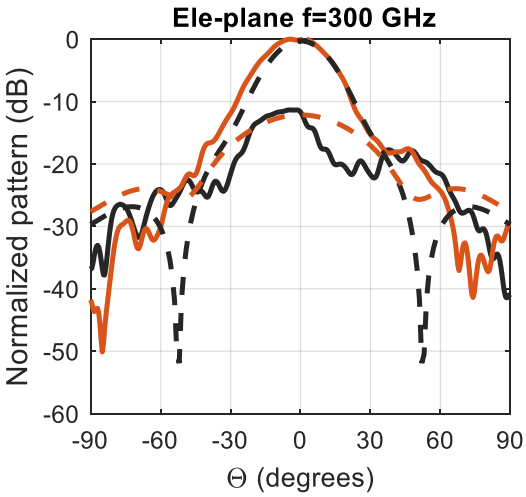
Ele-plane f=300 GHz
Normalized pattern (dB)
0
-10
-20
-30
-40
-50
-60
-90 -60 -30 0 30 60 90
Θ (degrees)

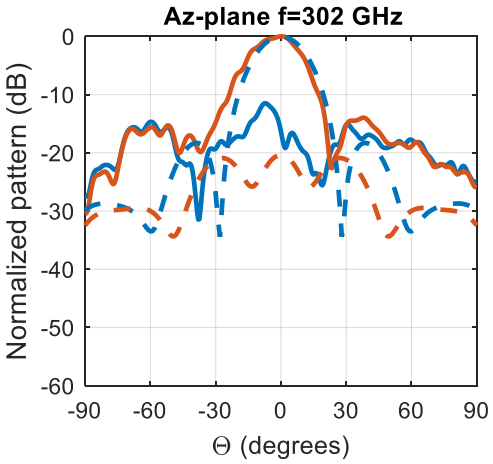
Az-plane f=302 GHz
Normalized pattern (dB)
0
-10
-20
-30
-40
-50
-60
-90 -60 -30 0 30 60 90
Θ (degrees)

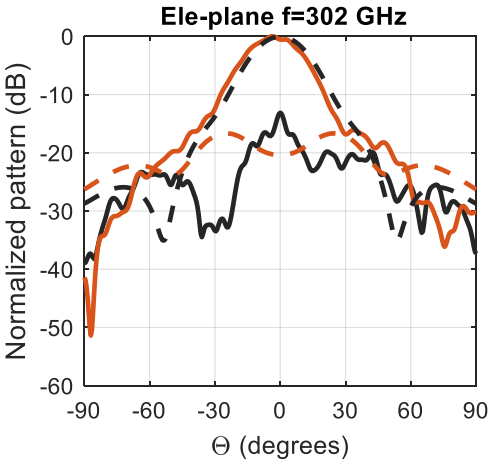
Ele-plane f=302 GHz
Normalized pattern (dB)
0
-10
-20
-30
-40
-50
-60
-90 -60 -30 0 30 60 90
Θ (degrees)

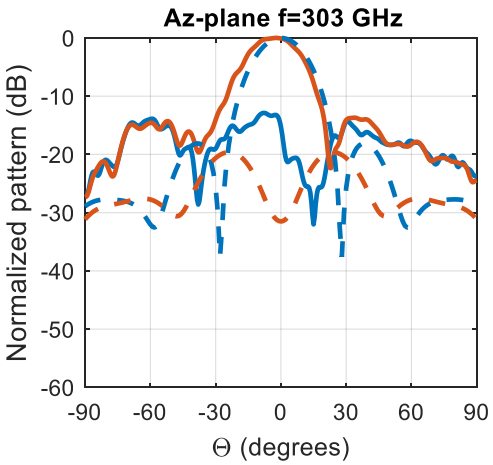
Az-plane f=303 GHz
Normalized pattern (dB)
0
-10
-20
-30
-40
-50
-60
-90 -60 -30 0 30 60 90
Θ (degrees)

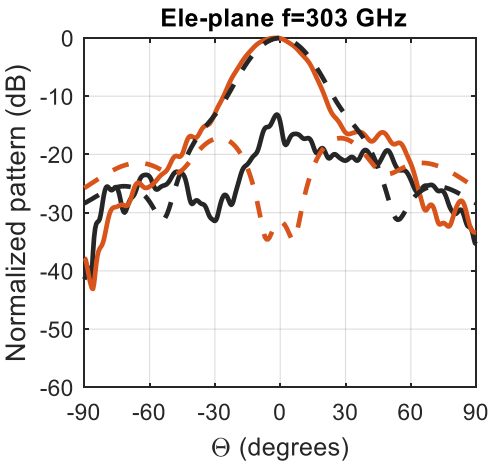
Ele-plane f=303 GHz
Normalized pattern (dB)
0
-10
-20
-30
-40
-50
-60
-90 -60 -30 0 30 60 90
Θ (degrees)

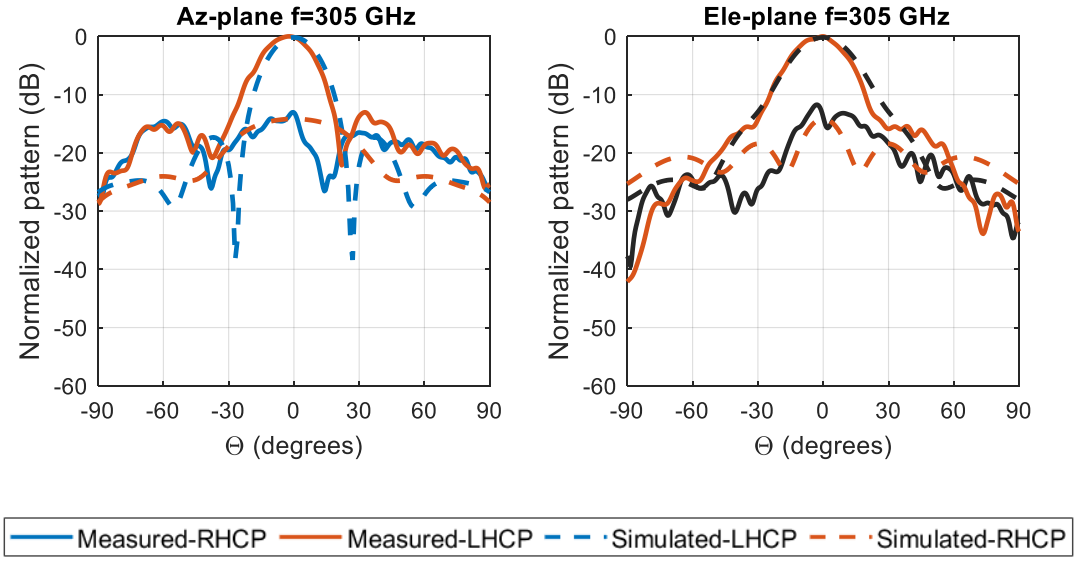

Figure 4.46: Measured (solid lines) and simulated (dashed lines) radiation pattern of the CP-FPC antenna at 300, 302, 303, and 305 GHz for Azimuth (Az.), and Elevation (Ele.)-Plane cuts.

For completeness, the upper hemisphere far-field radiation patterns in the UV-plane at 300, 302, 303, and 305 GHz frequencies, are also plotted in Figure 4.47. As seen, acceptable sidelobe levels (SLLs) of $\leq$ -15 dB is maintained in other azimuthal planes.

Table 4.6 gives a comparison among different antenna CP in the sub-THz band. A detailed comparison of antenna type, working frequency band, 3dB AR bandwidth (BW), peak gain (PG), and technology of fabrication is illustrated in Table 2. The results show that our antenna is currently the first one with a fully metallic CP high-gain planar structure, which is achieved using simplified laser-cutting brass technology at 300 GHz The measured results proved that manufacturing parts have high accuracy.

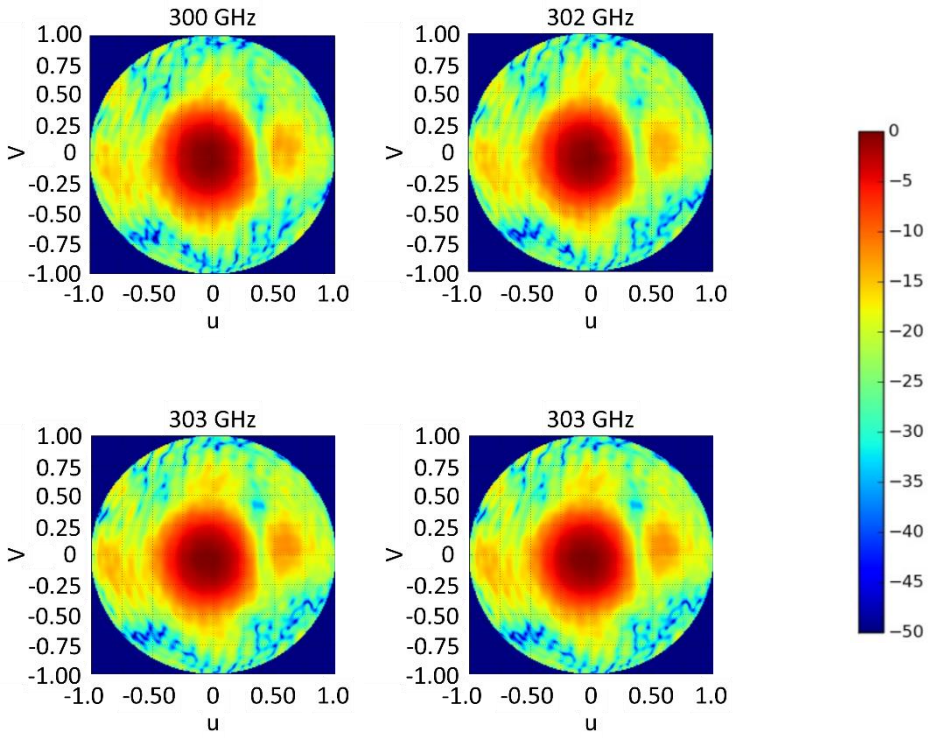

Figure 4.47: Measured LHCP components of the directivity for the CP-RCA antenna in u–v spectral plane at different frequencies. The color bar is on the dB scale.

Table 4.6: Comparison between the proposed work with other latest CP sub-THz antenna.

* The simulated results, NA (not available).

Ref.	Antenna type	Freq band	3-dB AR BW (%)	PG (dBic)	Fabrication Technique	Advantage/ disadvantage Structure
[103]	On-chip antenna with SIW	270 GHz	3.29 *	-0.5 *	CMOS 65 nm	Integrated with receiver /Low-gain
[71]	Double-fan-shaped slot	500 GHz	2	12.5	Silicon micromachining	Planar/ low-gain
[104]	4 x 4 Slot array	350 GHz	NA	18.4	Microfabrication	High-gain/ no measured results
[72]	Discrete dielectric lens	300 GHz	18.3	30.8	3D printing	High-gain/ bulky
[77]	Conical horn	300 GHz	2.33	18.4	Wire EDM	High-gain/ bulky
This work	Resonant cavity –loaded MTS	300 GHz	1.41	16.2	Laser-cutting	Planar and high-gain

4.4.2 Conclusions

A CP-RCA working prototype at the 300 GHz band has been presented in this communication. The proposed antenna was designed with the standard WM-864 waveguide flange dimensions, and a laser cutting brass technology is used for the fabrication of different layers in the design. This direct-mount technique is easier than alternative setups of silicon-micromachining which needs the bonding alignment method and is expensive. On the other hand, silicon micromachining provides more accuracy.

The proposed antenna yields a measured LHCP gain of 16.2 dBic with a directivity of 16.7 dBic at 302 GHz. A 3 dB measured AR bandwidth of approximately 1.41% (4.24 GHz) with a central frequency of 296 GHz is achieved. The antenna performance is compared to other state-of-art designs. This compact $2.6\lambda_0 \times 2.6\lambda_0 \times 1.24\lambda_0$ the antenna can find application in future sub-THz wireless communication systems.

Moreover, it is noted that the above-mentioned RCA radiates LHCP radiation. The RHCP radiation RCA will be generated easily by rotating the MTS superstrate layer by 90°. The new antenna's simulation results are the same as those for the proposed antenna due to their completely symmetric structure, except that the new antenna radiates RHCP waves. This indicates that both RHCP and LHCP RCAs can be designed with the proposed MTS superstrate layer.

Chapter 5 Planar Periodic Corrugated Metallic Antennas

5.1 Introduction

Sub-terahertz (0.1 THz - 1 THz) frequency bands represent a promising solution to encourage the development of new wireless communication technologies. The sub-THz band includes an enormous amount of available bandwidth, which will enable extremely wideband channels with tens of GHz-wide bandwidth required for front- and back-hauling in beyond 5G systems, ultra-high-definition multimedia streaming, and data centers. This could potentially provide a means to meet the 6th generation (6G) requirement of terabits per second (Tbps) data rate. Recently, a new IEEE standard (802.15.3d-2017) has been established around 300 GHz and data rates transmissions up to 100 Gb/s have already been demonstrated [74]. Generally, the antenna is the most essential and significant element of any terahertz wireless communication system along with active elements and associate technologies. Moving up to sub-THz range frequency means a drastic increase in free-space path-loss and atmospheric absorption (i.e., absorption by molecules in air). Consequently, unprecedentedly high gain antennas are necessary to compensate for the path loss. Metallic corrugated antenna structures have recently been demonstrated as an alternative solution to classical high-volume antennas such as horns [105, 106], since they offered better radiation characteristics and, at the same time, presented lower profiles and lighter weights.

Circularly polarized (CP) antennas are more important for any modern wireless communication system due to their features such as robustness against environmental interference, not being sensitive to the orientation of the transmitting and receiving antennas, and being more capable of mitigating polarization mismatch. There are a few publications on CP high gain-antennas sub-THz frequencies known in the literature [72, 77, 107]. The proposal of a 300 GHz modified Fresnel lens [107], and discrete dielectric Lens [72] antennas were manufactured by 3D printing technique. The volume of lens antennas is oversized as a result both of them had large profiles resulting in difficulty to process in terms of integration and miniaturization. Another CP sub-THz antenna with a conical horn element having a 270-330 GHz bandwidth was fabricated and tested using the wire electrical discharge machining (EDM) technique [77]. The directivity of the antenna was measured, the achieved directivity was 18.3 dBic at 312 GHz. The measured 3 dB axial ratio of the fabricated antenna prototype has a bandwidth of 7 GHz from 309 GHz to 316 GHz.

In this chapter, we introduce a leaky-wave antenna based on bull's eye structure in the sub-THz band. Cavity-backed crossed slot and double-fan-shaped slot elements are applied to generate the circular polarization characterization at the 300 GHz frequency. The first design

has a measured impedance bandwidth (279.2 - 314 GHz) with a simulated LCHP realized gain of more than 16.13 dBic. The second one has a measured impedance bandwidth of 110 GHz.

This chapter is organized as follows. In Sections 5.2 and 5.3, the theoretical concept of leaky-wave antenna such as bull's eye structure is presented. In Section 5.4, the crossed-slot antenna element design and its simulated results are reported. In Section 5.5, we show another design with a double-fan-shaped slot, and its simulated results are discussed. Two prototypes for the design have been fabricated and their experimental results are reported in Sections 5.4.2 and 5.5.2.

5.2 Planar Corrugated Structure

Planar corrugated structure is very suitable for forming such a low-profile antenna with high performance. In the next section, the Bull's Eye antenna concept and its geometry and design are presented. The results for a sub-terahertz CP bull's eye antenna illuminated by the WM-864 waveguide are shown as well, being both optimized to maximize the realized gain over the whole frequency band.

5.2.1 Bull's Eye Antenna Concept

Spoof surface plasmon (SP) are electromagnetic waves propagating along the periodically planar corrugated metal surface, whose properties are analogous to surface plasmon polaritons (SPPs) in the optical frequencies [108-110]. The highly confined surface waves or spoof SP can be sustained and guided on the metallic corrugated grooves structure with transversal magnetic (TM) polarized surface waves. By implementing corrugation on the metal surface, a series of concentric annular grooves or straight slits can be incorporated on the surface to convert surface waves into a collimated or Bessel beam.

The spoof SP wave propagating along the metallic surface (X-axis) will be decomposed into a series of plane wave components and radiated to the free space as shown in Figure 5.1, which satisfies the grating equation [111] :

$$k_0 \sin\theta = k_{sp} + k_g \qquad (5.1)$$

where k_0, k_{sp}, k_g are the wavenumbers of free-space propagation, the surface plasmon, and the grating, respectively. Here, k_{sp} is determined from the groove geometry D_g,W_g, and W_r in relation to the frequency, and k_g is determined by the period 'p'of the gratings, or $k_g = 2\pi/p$. Since the beaming angle θ determines the shape of the Bessel beam, equation (5.1) relates the surface structure to the beam shape.

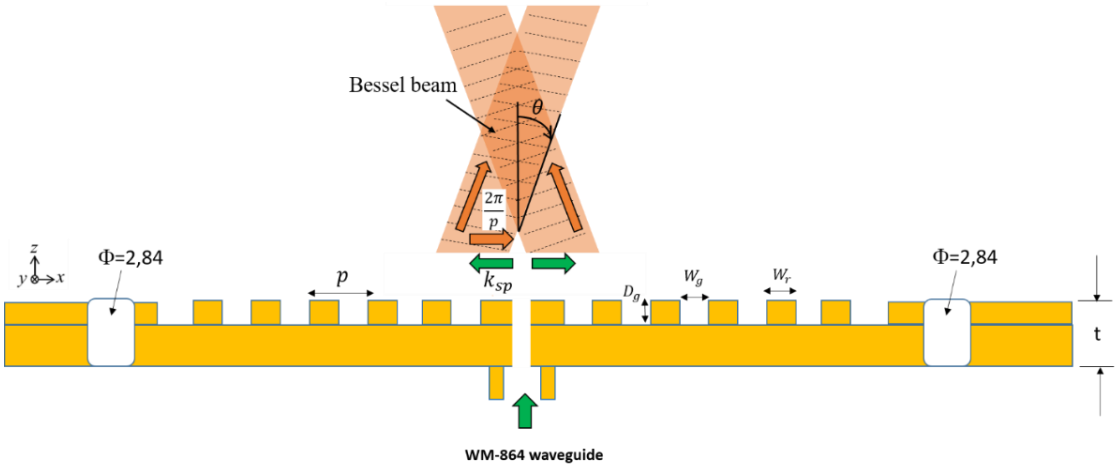

Figure 5.1: Schematic of the Bessel beam generation mechanism. (Insets) Detailed views of the CP proposed antenna.

5.3 Crossed-Slot Antenna Element

An illustration of proposed the flat metallic plate Bull's-Eye antenna is shown in Figure 5.2. The low-profile proposed antenna consists of central sub-wavelength crossed-waveguide apertures surrounded by concentric periodic annular grooves (i.e. corrugations) drilled in a flat metallic plate that has a thickness of $t = \lambda_0$, where λ_0 is the wavelength operation working at 300 GHz. According to the authors [112], among the possible surface plasmons (SPs) structures, subwavelength apertures in metallic plates have advantages such as high contrast and extraordinary transmission (i.e. enhanced transmission and beaming are achieved). The standard WM-864 waveguide feeds the crossed-waveguide apertures, the depth of which, determines the resonant frequency of the proposed antenna. The lower resonance is determined by the crossed-aperture width. For narrow crossed-apertures on a flat plane, the power coupled across the aperture is nearly isotropically radiated. The grooves change the field pattern dramatically, resulting in a more directed beam. The width of the grooves and width of the ridges control the angle where constructive interference takes place. For the proposed fabrication, we integrate the standard UG-387/UM waveguide flange into the antenna design.

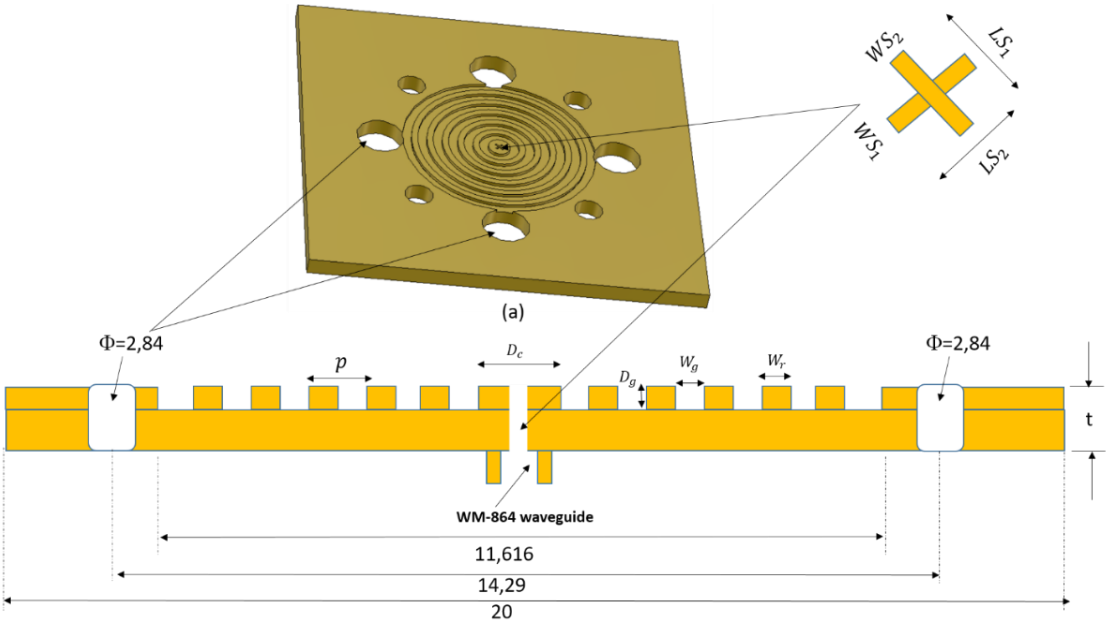

Figure 5.2: Diagram of a Sub-THz CP Bull's-Eye antenna (a) Perspective view with waveguide-864 flange screws (b) Cross-section with design details.

A crossed-waveguide aperture is used as an excitation in the middle of the metallic plate, and it is fed by a standard WM-864 waveguide at the bottom of the plate. The antenna consists of 6 concentric corrugated rings surrounding a crossed-waveguide aperture on a metallic plate. A radiating crossed-waveguide apertures with unequal sub-wavelengths of *Ls*1 = 0.58 mm, *Ls*2 = 0.54 mm and a width of *ws1* = *ws2* = 0.1 mm are drilled in flat metallic plane. The crossed-waveguide apertures are used to excite the two orthogonal modes in the antenna, with equal amplitudes and a 90∘ phase shift between them; thus, CP radiation can be achieved. Figure 5.2 shows both the side view and exploded view of the proposed antenna. By making the length of slot 1 (Ls1) longer than the length of slot 2 (Ls2), right-hand circular polarization (RHCP) radiation can be obtained; if the Ls1 is shorter than the Ls2, the antenna radiates left-hand circular polarization (LHCP) waves.

The power coupling is done through subwavelength crossed-apertures resonance determined by the length of the aperture. Hence, the aperture length is $\approx \lambda_0/2$. Meanwhile, the aperture width mainly fixes the operation bandwidth. In order to obtain a moderately high-quality factor, the slot width must be Ws $\ll \lambda_0$. The most critical parameter for broadside radiation is the periodicity of the groove, which must be taken as approximately equal to the operation wavelength, $p \approx \lambda_0$. The grooves' width, Wg, and depth, Dg, fix principally the attenuation constant and were obtained utilizing an optimization routine. The optimized dimensions are as follows, the diameter of the central circular raised region Dc is 1.326 mm. The period of the corrugated structure p is 0.923mm, with the width of grooves W_g = 0.55 mm and the width of the ridge $W_r = 0.373$ mm. The depth of the groves rings is 0.185 mm.

The initial design parameters of the proposed antenna are given in equation (5.2), obtained from [113].

$$W_g \approx \lambda_0/2$$

$$\frac{D_g}{W_g} \approx 0.4$$

$$t \approx \lambda_0 \qquad (5.2)$$

$$p \approx \lambda_0$$

To generate the CP, the crossed slot is composed of two orthogonal slots of different lengths. From the dimensions shown in Table 5.1, it can be observed that the length difference of the slots is 0.4 mm, which corresponds approximately to λ0/4, where λ0 = 1 mm is the wavelength at the operation frequency, f_0 = 300 GHz. This guarantees that the phase difference between both slots is close to 90º.

Table 5.1: Design parameters of bull's eye antenna

Groove width, Wg	0.55
Groove depth, Dg	0.185
Groove periodicity, 'p'	0.923
Ridge width, Wr	0.373
The thickness of metal plate, t	1
Number of grooves	6
Slot length 1, Ls1	0.58
Slot length 2, Ls2	0.54
Diameter of the central circular, Dc	1.326
slot width , Ws1=Ws2	0.1

Two orthogonal modes could be excited as explained by the field distribution shown in Figure 5.3. It is also evident that the E-filed distribution follows a circular shape describing that the proposed antenna exhibits a left-handed CP (LHCP) pattern in the broad-side direction.

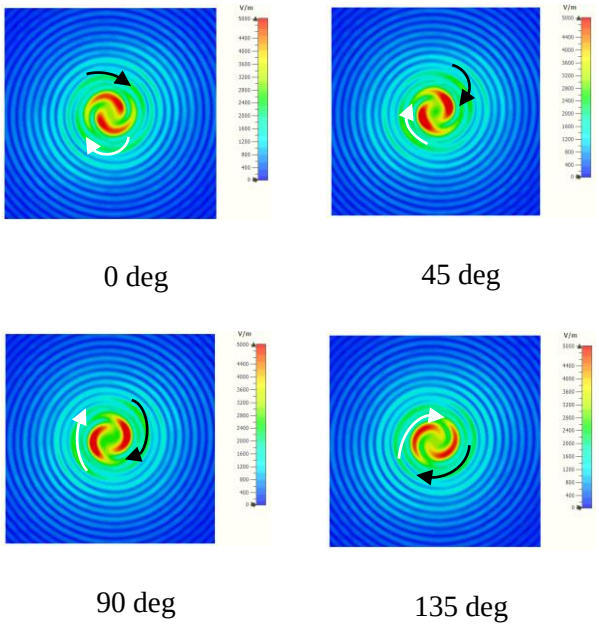

Figure 5.3: Upper view of the E-field variations on the Bull's Eye antenna for different phase values at 300 GHz and four different snap.

5.3.1 Simulated Systems

The simulated gain of the corrugated structure (with 6 grooves) at 300 GHz is about 16.3 dBi, while the simulated gain of the flat structure (without grooves) is about 4.8 dBi as shown in Figure 5.4. The gain enhancement is approximately 11.5 dBi at 300 GHz, which means the corrugated metallic structure shaped the beams from the crossed-apertures to broadside radiation.

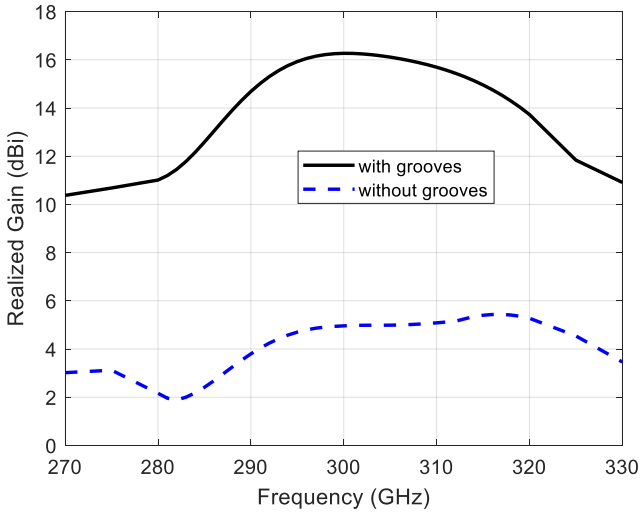

Figure 5.4: Simulated broadside realized gain for the proposed antenna with grooves (solid black) and no grooves (solid blue line).

The simulated E-plane and H-plane radiation patterns of the corrugated metallic structure and flat metal plate without corrugation at the desired frequency of 300 GHz are illustrated in Figure 5.5, from which we observe broadside radiation in both planes. In both planes, the narrow 3dB beamwidth is about 9.7° and the sidelobe levels (SLLs) are lower than -41 dB, which demonstrates the radiation patterns are symmetric.

A study was carried out in order to find the optimum number of grooves for maximum realized gain while maintaining a low antenna profile. A remarkable enhancement in realized gain is observed for a number of rings up to 6, as shown in Figure 5.6. After this number, the realized gain does not much improve, while the antenna profile gets large. The effect of the number of grooves on the return loss (S11) axial ratio (AR) performance was not found.

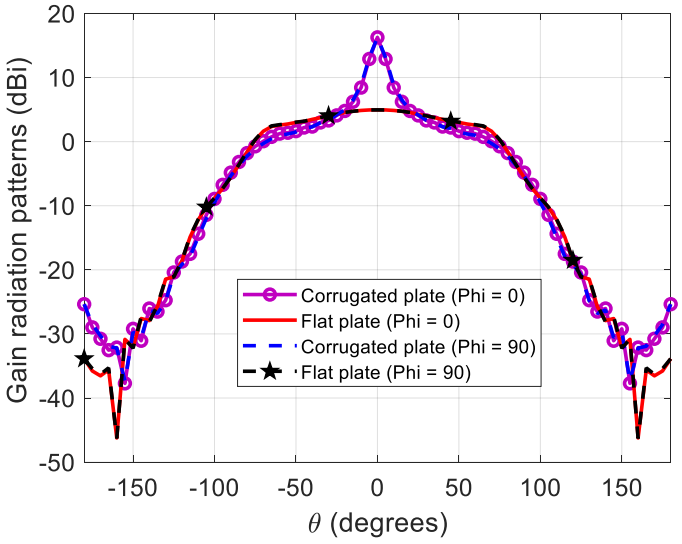

Figure 5.5: Gain at 300 GHz in E-plane and H-plane for the proposed antennas with grooves, and no grooves.

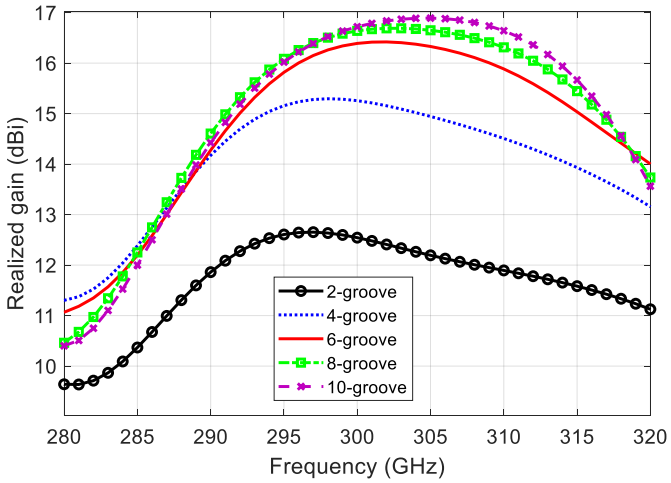

Figure 5.6: Maximum realized gain versus the number of grooves for the bull's eye antenna.

Figure 5.7(a) shows the return loss (S11) performance for four different thicknesses of the metallic plate, keeping all other parameters fixed. The optimum thickness of the metallic plate was 1 mm (1 λ_0). This thickness was chosen to give the best axial ratio values in desired bandwidth band. The effect of metallic plate thickness on the realized gain performance was found to be negligible.

A study was done fixing the slots length difference to $\lambda_0/25$; see Figure 5.7(b). Now the best AR is achieved with $h = 1$ mm (1 λ_0). These results suggest that the plate height has some non-trivial effect on the phase difference achieved between orthogonal linear components. Nevertheless, an in-depth study of this phenomenon is beyond the scope of this thesis.

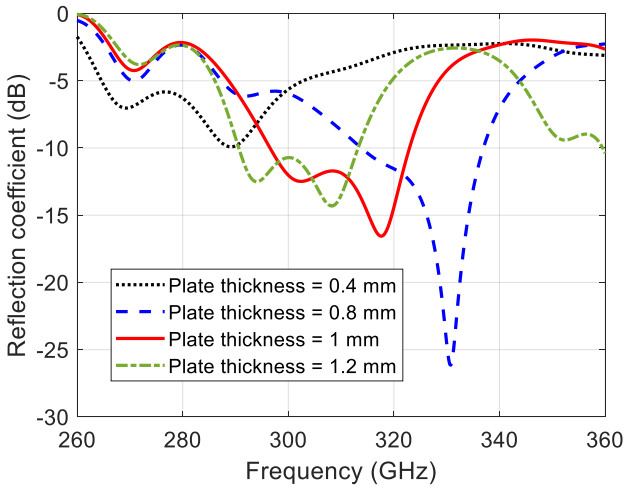

(a)

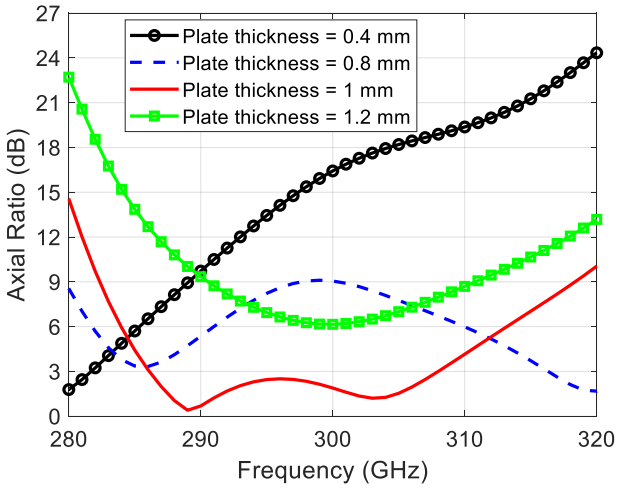

(b)

Figure 5.7: Numerical study of the height of the metallic plate 't' is varied between 0.4 and 1.2 mm: (a) Reflection coefficient and (b) Axial ratio versus frequency.

Figure 5.8 illustrates the simulated LHCP realized gain, total directivity, and efficiency of the CP bull's eye antenna with the crossed-slot element. The maximum LHCP realized gain is 16.13 dBic, and total directivity is 16.44 dBic, at 300 GHz. The total efficiency is more than 80%, between 295- 325 GHz.

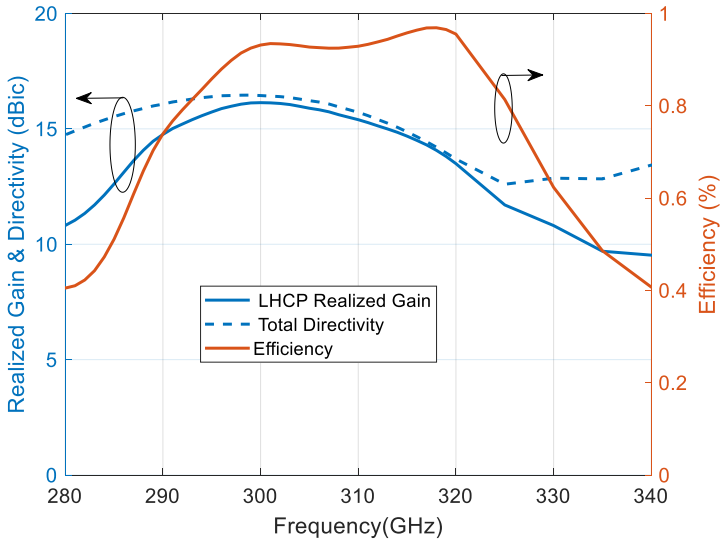

Figure 5.8: The simulated LHCP realized gain, total directivity, and efficiency versus frequency of the CP bull's eye antenna with the crossed-slot element.

The simulated AR of the proposed antenna is shown in Figure 5.9. The minimum measured AR at 290 GHz is 0.675 dB with the 3-dB AR bandwidth of 21 GHz between 287 GHz to 308 GHz being 7 %.

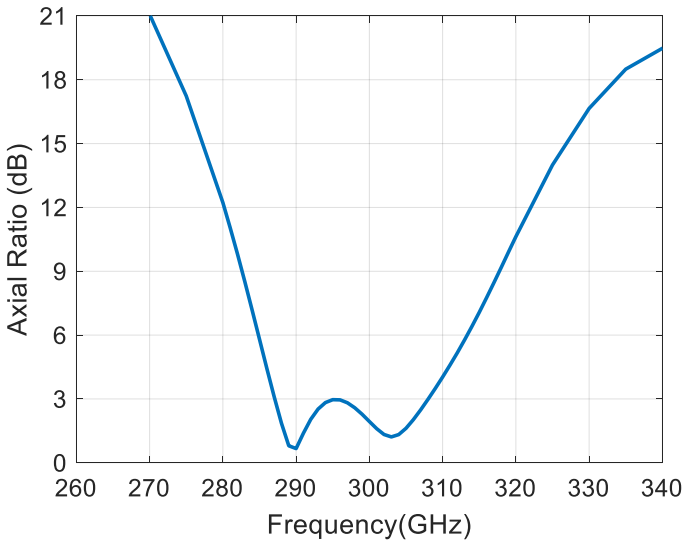

Figure 5.9: The simulated axial ratio of CP bull's eye antenna with the crossed-slot element.

The AR in the azimuth plane is kept below 3dB on a range of angle theta ‘‘θ’’ up to $\sim \pm 4^{\circ}$ except for the value of frequency at 295 GHz, with the average half-power beamwidth (HPBW) equal to 10.25°, as defined in Figure 5.10(a). Also, it is noted that in the elevation plane shown in Figure 5.10 (b), the AR is less than 3dB on a range of angle theta ‘‘θ’’ up to $\sim \pm 3^{\circ}$ except for the value of frequency at 295 GHz. The maximum gain of the radiation pattern at 300 GHz, is equal to 16.13 dBic in both planes at the broadside direction.

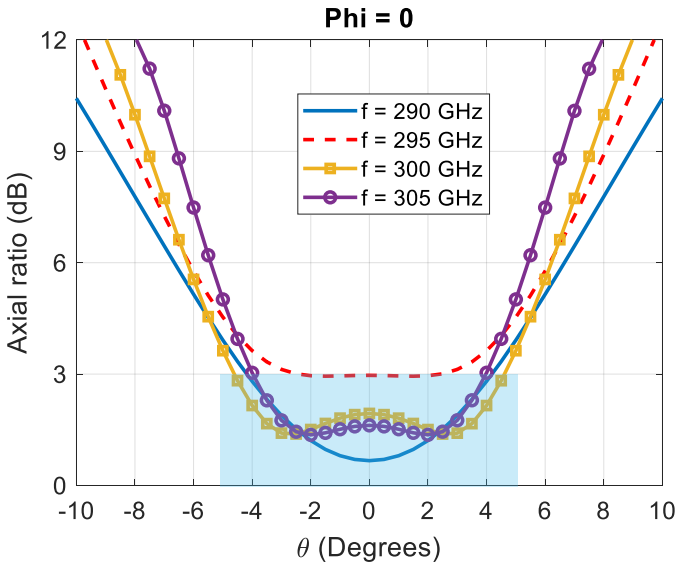

(a)

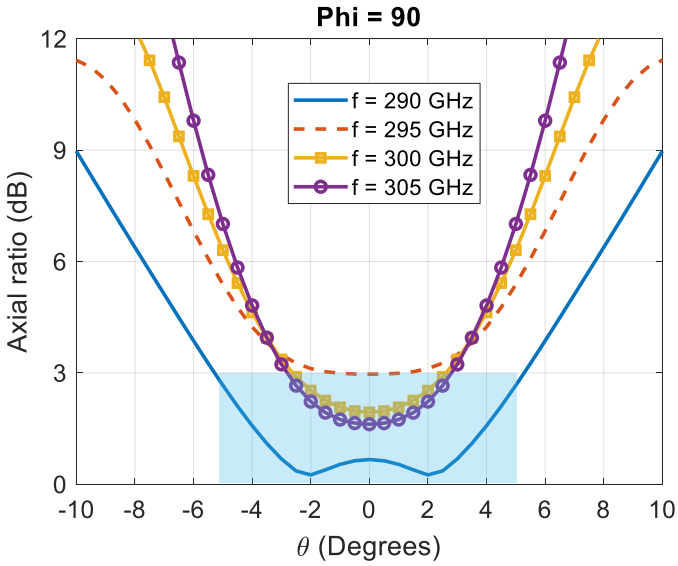

(b)

Figure 5.10: The simulated AR vs theta angle in (a) Azimuth-Plane, and (b) Elevation-Plane at different frequencies.

The simulated radiation patterns of the proposed antenna in both the azimuth plane and elevation plane at 290 GHz, 295 GHz, 300 GHz, 305 GHz, 310 GHz, and 320 GHz are given in Figure 5.11. It can be seen that, because of the symmetry of the antenna, simulated radiation patterns of both planes are similar. The sidelobe levels of the radiation pattern are below -20 dB at desired frequencies.

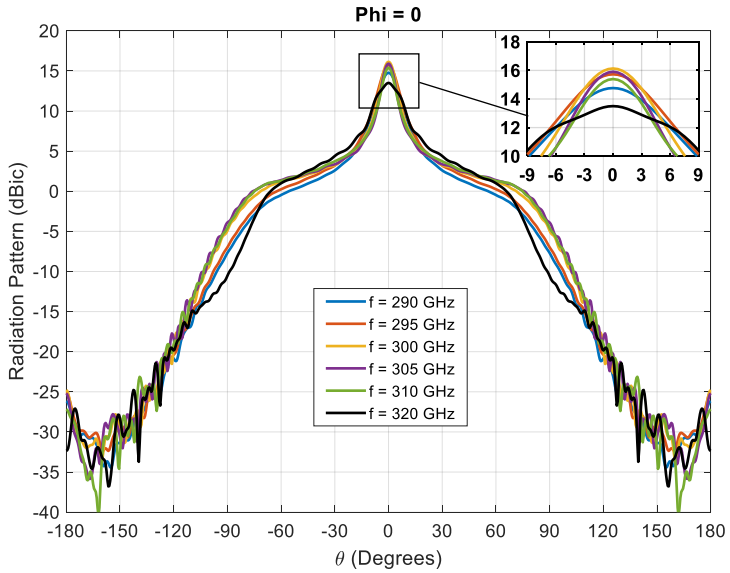

(a)

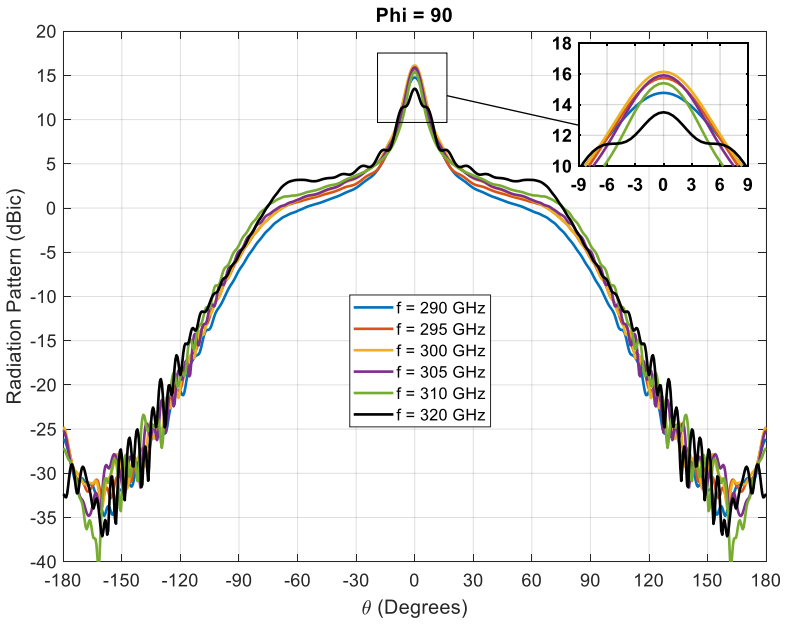

(b)

Figure 5.11: Simulated radiation patterns of the CP bull's eye antenna of the principal planes at different frequencies.

In terms of leaky waves, the radiation process is easily explained. As illustrated in Figure 5.12(a), the wave produced by the crossed- aperture has a diffractive pattern, with no favored direction in the upper plane, when no groves around the central crossed apertures are included. In comparison, when six periodic annular grooves are added, radiation is preferred at the broadside, as seen in Figure 5.12 (b). Alternatively, the process can also be understood: only the direct wave radiated from the aperture does exist without surface grooves, Figure 5.12(a). Through the grooves, part of the energy passing through the central aperture is coupled to support and guide spoof surface plasmon (SSP) propagating along with the subwavelength groove structures, and then the SSP is modulated periodically to radiate, as shown in Figure 5.12 (b).

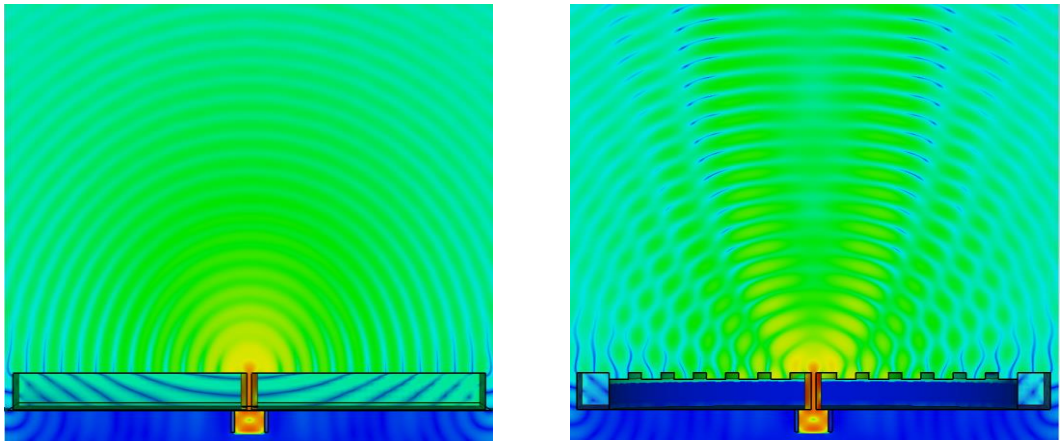

(a) (b)

Figure 5.12: Cross-sectional view of the H-field (a) without and (b) with corrugations at 300 GHz.

5.3.2 Fabrication and Experimental Results

The bull's eye antenna was manufactured and measured. As sub-THz CP bull's eye antenna demand high precision manufacturing, silicon micromachining technology was selected to manufacture all the pieces.

Figure 5.13 shows the main simulation and measurement results. As shown in the solid blue curve of Figure 5.13, good matching is obtained with S11 < -10 dB from 279.2 to 314 GHz, which represents a fractional BW of 11.6 %. There is a shift between measurement and simulation results due to fabrication tolerance.

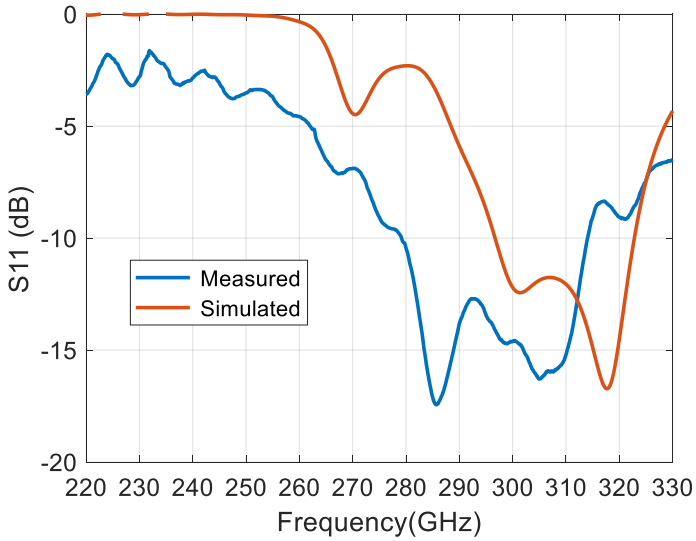

Figure 5.13: The reflection coefficient (s11) for CP bull's eye antenna with the crossed-slot element.

To comprehensively verify the design results, the crossed-slot antenna element exhibiting LHCP is fabricated and measured. The fabricated antenna is shown in Figure 5.14. It consists of three silicon layers with a thickness of 200-µm, and two of 400-µm. The feeding WM-864 waveguide is drilled in the bottom wafer.

The crossed-slot and the six-ring slots are drilled in a wafer of the thickness of 200-µm. After sputtering gold, the three silicon wafers are bonded together by gold–gold thermocompression. We scribed the wafers to get the proposed antenna with a dimension of $20 \times 20 \times 1$ mm^3.

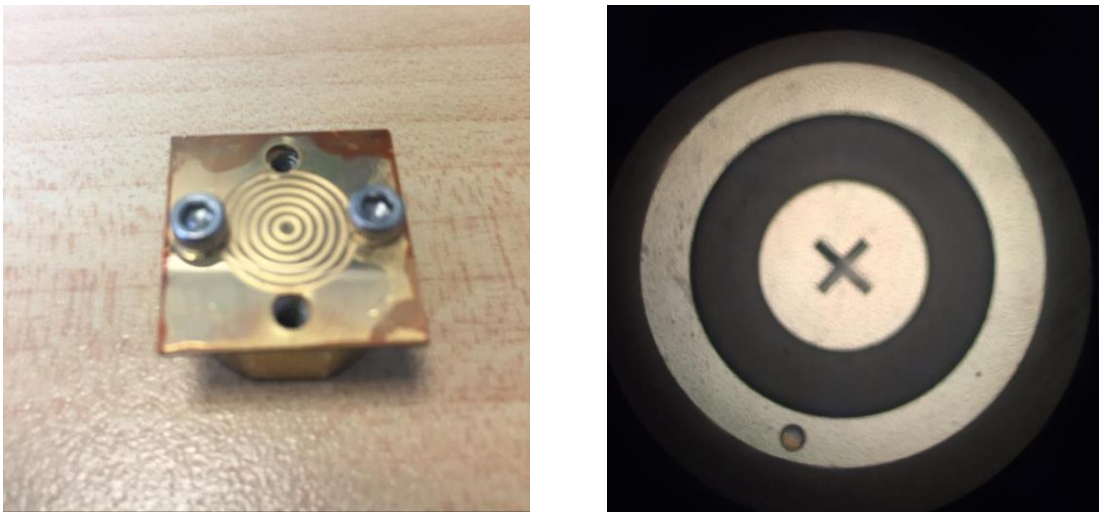

(a) (b)

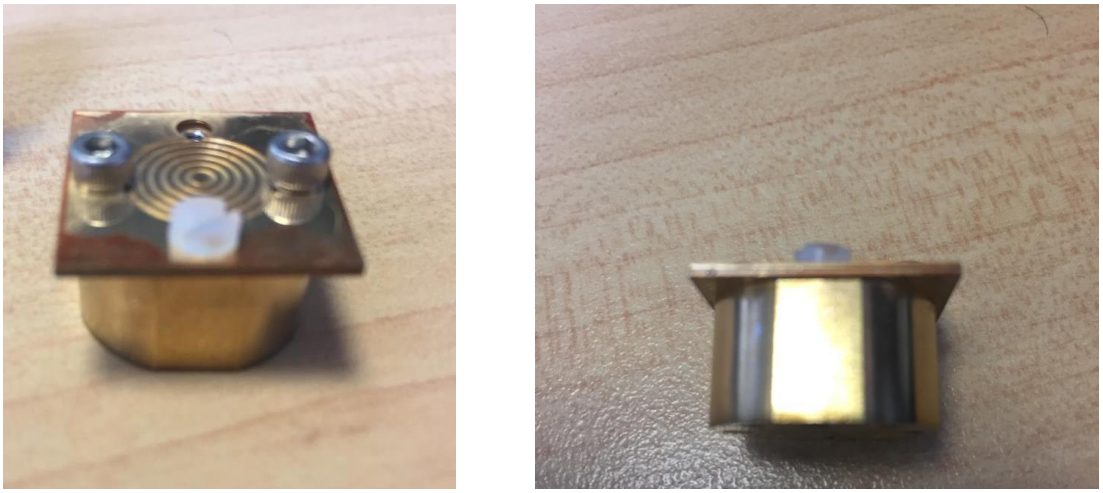

(c) (d)

Figure 5.14: Photographs showing the fabricated bull's eye antenna. (a) Top view of concentric periodic corrugations around the crossed-shaped slot. (b) microscope image of crossed-slot element (c) side view of WM-864 waveguide connection.

5.4 Double-fan Shaped-slot Antenna Element

5.4.1 Simulated Systems

The double-fan-shaped slot (DFSS) antenna plays two important roles: radiator and polarizer. The shape of the double-fan-shaped slot is determined by two interlocked fan shapes. The two fans are of the same size and symmetrical to the center. As we know, the TE_{10} mode electric field is linearly polarized (E_x) in the waveguide. However, to create circular polarization, an orthogonal electric field component (E_y) of the same amplitude as E_x and simultaneously 90° phase distinctive is needed. An orthogonal polarization component can be generated by controlling the double-fan-shaped slot.

Here, the rotation angle 'θ' is assumed for the position of the fan in respective to the origin during its rotation in clockwise or counterclockwise directions. By adjusting the parameters θ of the slot, the design can be further optimized to achieve proper amplitude and phase for producing a left-handed or right-handed circular polarization.

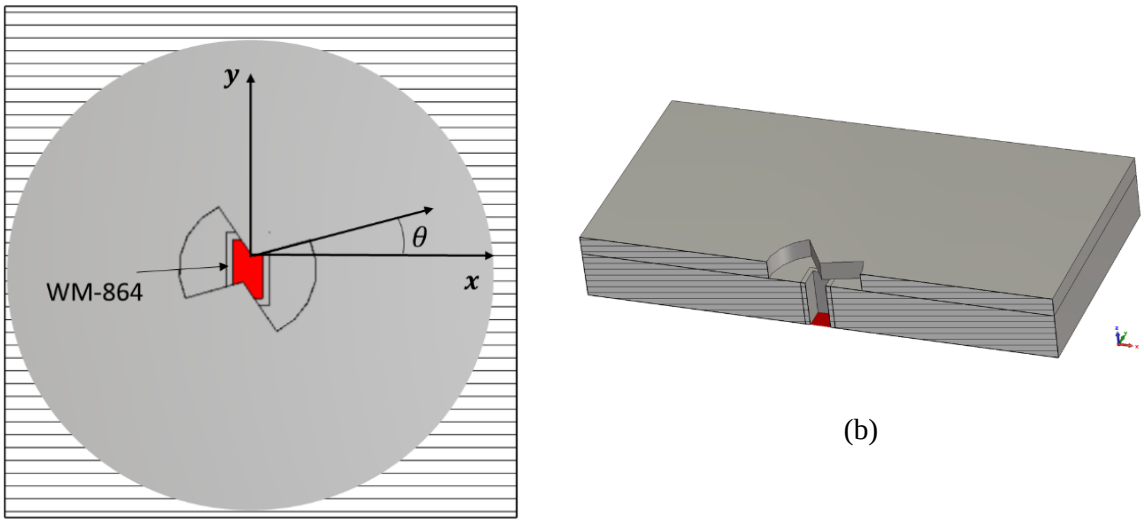

(a) (b)

Figure 5.15: Schematic diagram of the proposed Double-fan shaped-slot antenna.

The proposed circular polarization (CP) bull's eye antenna is composed of a standard rectangular waveguide, a double-fan-shaped slot, and six grooves as shown in Figure 5.16, the radiation structure. The geometry and dimensional parameters of the proposed grooves are similar to that in the previous section. The antenna is directly fed by the standard WM-864 waveguide with a cross-section of 864 × 432 μm^2. The polarizer has the shape of two quasi-circular sector parts which are centrally symmetrical with respect to the origin.

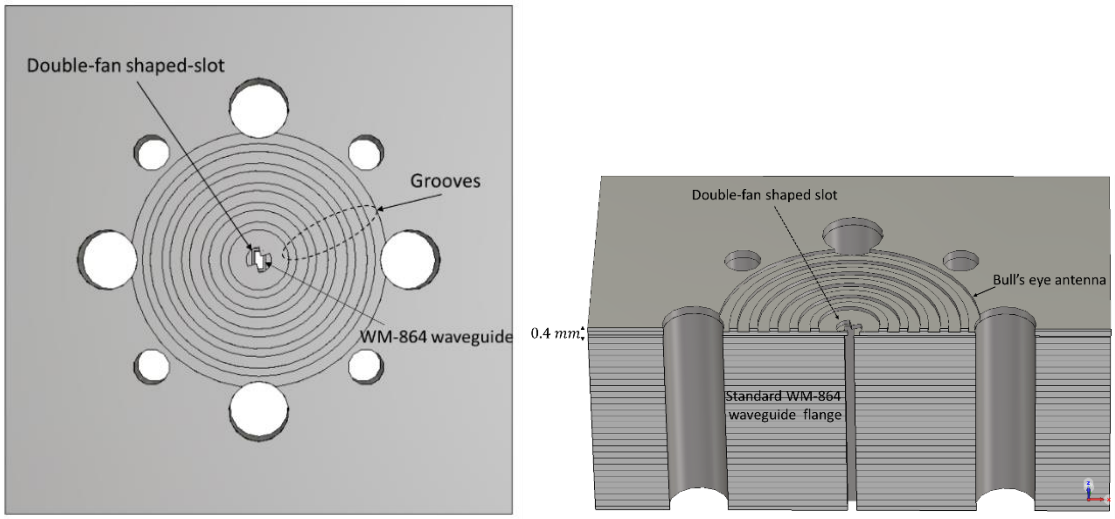

(a) (b)

Figure 5.16: The bull's eye feed by CP DFSS (a) top view and (b) cutting-side view.

Figure 5.17 illustrates the simulated RHCP realized gain, total directivity, and efficiency of the CP bull's eye antenna with the double-fan shaped-slot element. The maximum RHCP realized gain is 16.37 dBic, and total directivity is 16.61 dBic, at 325 GHz. The total efficiency is more than 88%, between 260 - 360 GHz.

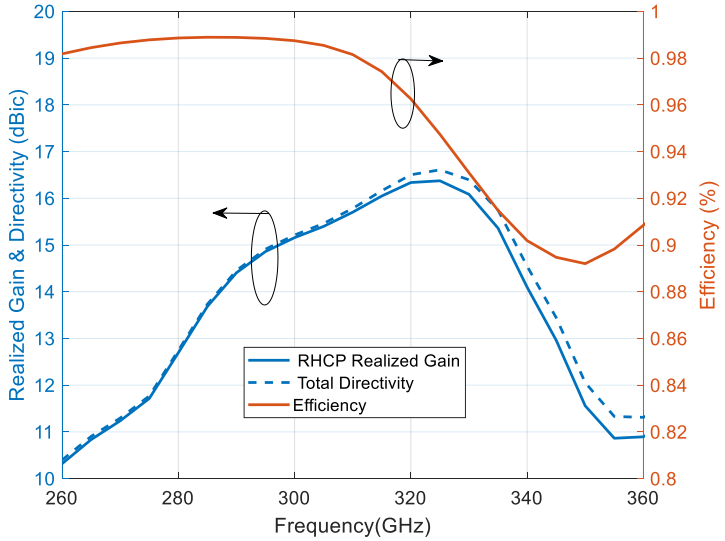

Figure 5.17: The simulated RHCP realized gain, total directivity, and efficiency versus frequency of the CP bull's eye antenna with the double-fan shaped-slot element.

The simulated AR of the proposed antenna is shown in Figure 5.18. The minimum measured AR at 300 GHz is 0.12 dB with the 3-dB AR bandwidth of 32.39 GHz between 280.77 GHz to 313.16 GHz being 10.8 %.

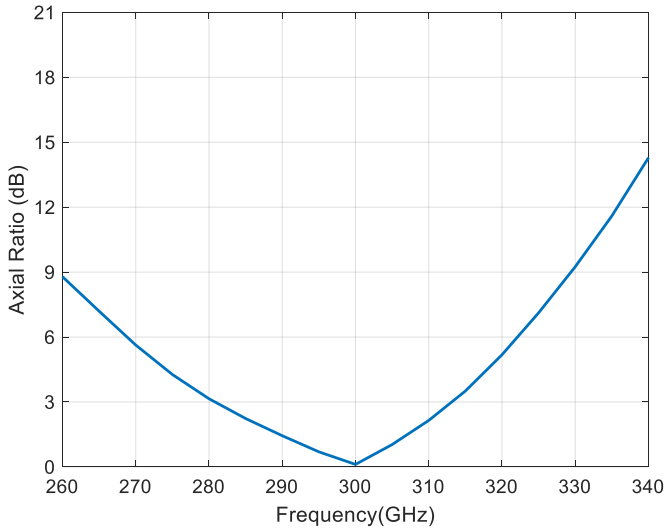

Figure 5.18: The simulated axial ratio of CP bull's eye antenna with the double-fan shaped-slot element.

The AR in the elevation plane is kept below 3dB on a range of angle theta ‘‘$\boldsymbol{\theta}$’’ up to ~ $\pm 5.23^{\circ}$ which almost covers the average half-power beamwidth (HPBW) equal to 11.73°, as defined in Figure 5.19(a). Also, it is noted that in the azimuth plane shown in Figure 5.19 (b), the AR is less than 3dB on a range of angle theta ‘‘θ’’ up to ~ $\pm 3.3^{\circ}$.

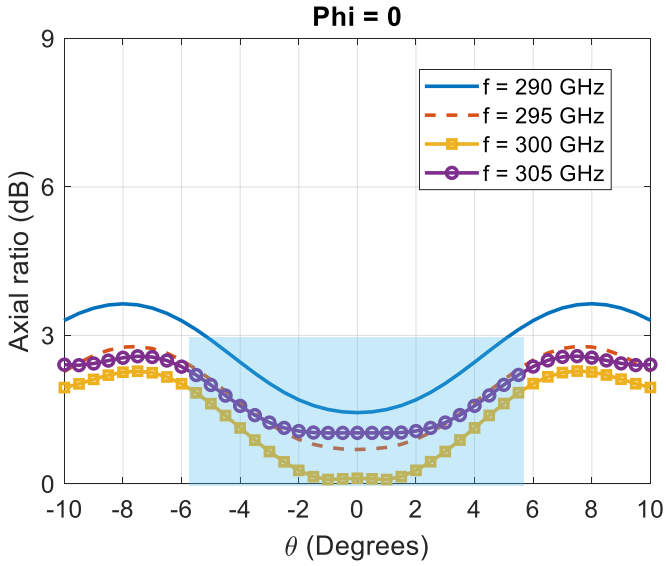

(a)

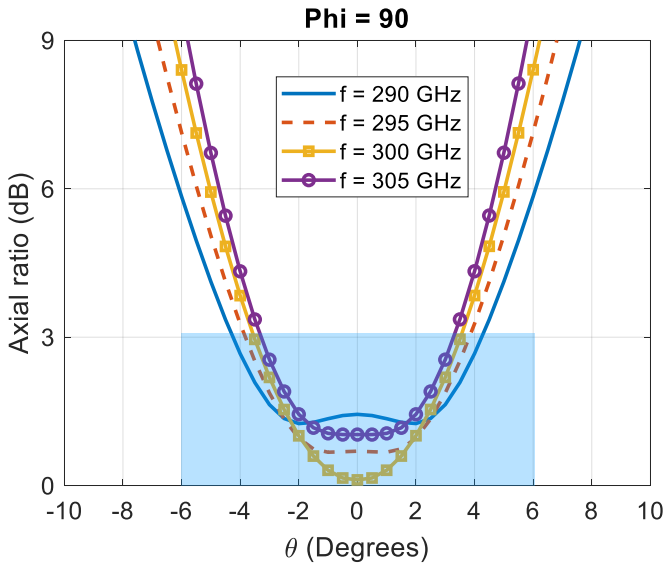

(b)

Figure 5.19: Simulated angular variation of axial ratio at (a) 290 GHz, (b) 295 GHz, (c) 300 GHz, and (d) 305 GHz.

The simulated radiation patterns of the proposed antenna in both the elevation plane and azimuth plane at 290 GHz, 300 GHz, 310 GHz, 320 GHz, 330 GHz, and 340 GHz are given in Figure 5.20. It can be seen that, because of the symmetry of the antenna, simulated radiation patterns of both planes are similar. The sidelobe levels of the radiation pattern in both planes are below -20 dB at desired frequencies.

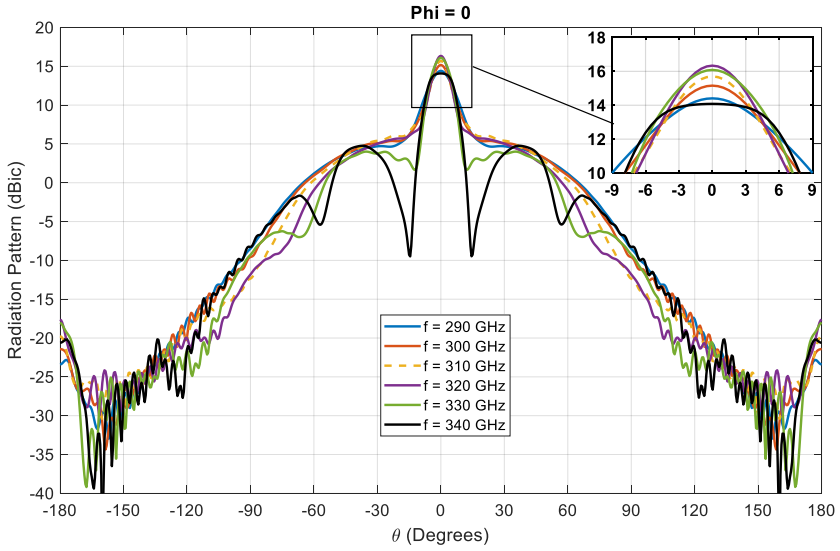

(a)

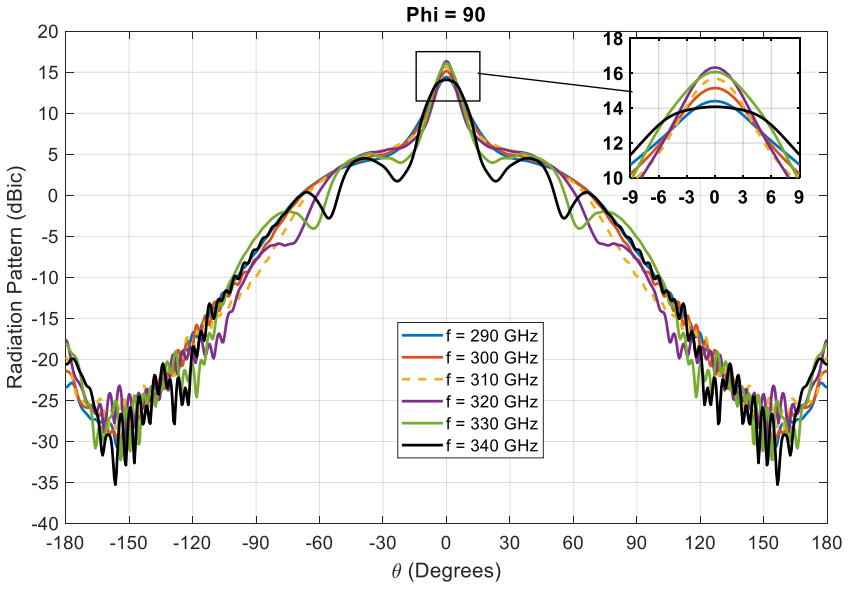

(b)

Figure 5.20: Simulated radiation patterns of the CP bull's eye antenna with the double-fan shaped-slot element of the principal planes at different frequencies.

5.4.2 Fabrication and Experimental Result

Figure 5.21 shows the main simulation and measurement results. As shown in the solid blue curve of Figure 5.21, good matching is obtained with S11 < -10 dB from 220 to 330 GHz, which represents a fractional BW of 36.67 %, in good agreement with the simulation results (solid red curve).

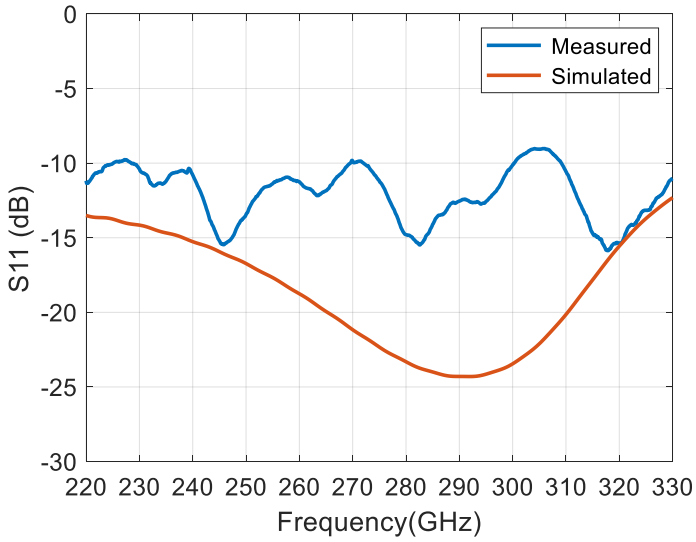

Figure 5.21: The reflection coefficient (S11) for CP bull's eye antenna with the double-fan shaped-slot element.

The bull's eye antenna was manufactured and measured. A standard computer numerical control (CNC) milling machining was selected to manufacture all the pieces. The material employed was aluminum due to its good conductivity and mechanical properties.

Figure 5.22(c) shows the WM-864 waveguide flange connected to the prototype antenna from the bottom plate, required for compatibility with our standard experimental setup. Figure 5.22 (d) shows the top plate of the antenna with six concentric periodic corrugations of period p, depth Dg, and width Wg as determined in the previous section, filling maximally the metallic plane around the central double-fan shaped slot with cavity height 0.4 mm.

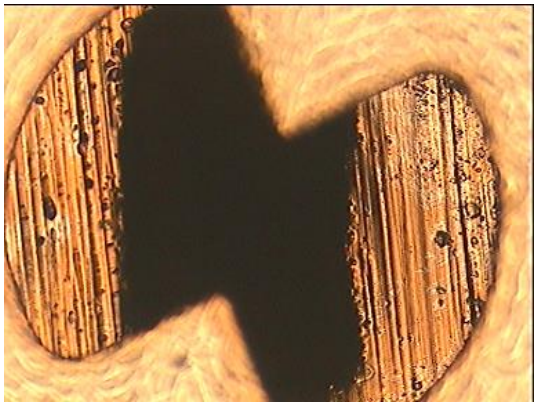

(a)

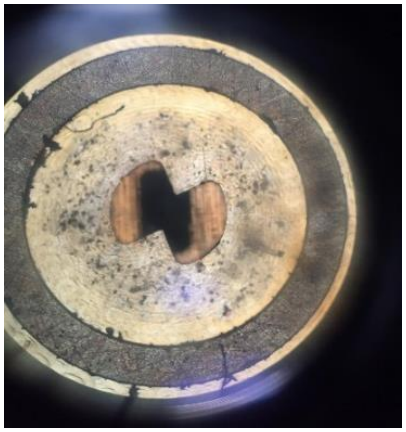

(b)

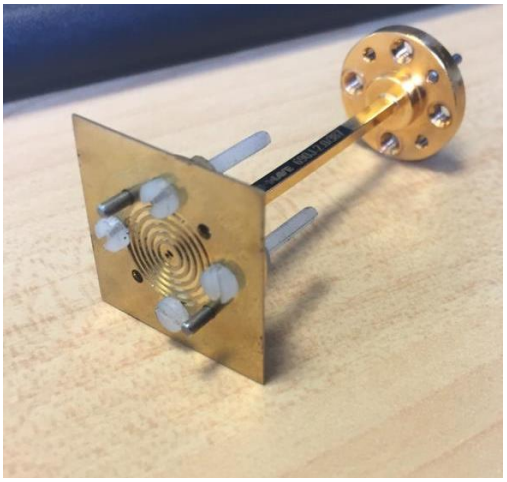

(c)

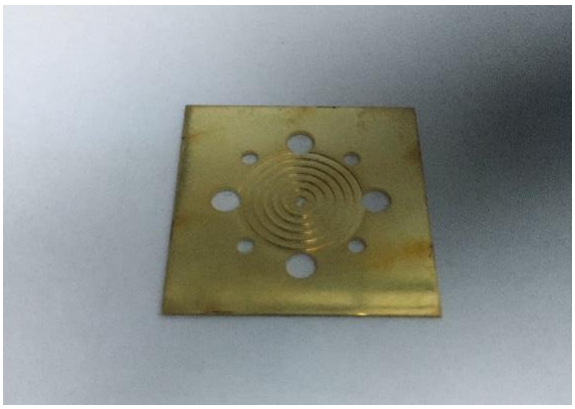

(d)

Figure 5.22: Photographs showing the fabricated bull's eye antenna. (a) enlarge microscope image of the double-fan shaped-slot element, (b) microscope image of the double-fan shaped-slot element with concentric periodic corrugations, (c) prototype of bull's eye antenna with WM-864 waveguide flange, and (d) Top view of concentric periodic corrugations around the double-fan shaped-slot.

PART II: BEAM SCANNING ANTENNA BASED ON METALLIC LUNEBURG LENS

Chapter 6 Metallic Lens based on Parallel-Plate Loaded with Variable Posts

6.1 Introduction

At high frequencies, due to high path loss and molecular absorption, the necessity of a high gain antenna becomes critical. However, the narrow beam provides only limited spatial coverage, making it not cooperative with non-LOS communications, therefore the single-directional beam needs to be steered to find a reliable substitute link. The multi-beam antennas which are capable of generating a number of independent directive beams simultaneously, with a high gain value to cover a predefined angular range, provide a solution to overcome the above limitations of antennas with a single-directive beam. At lower frequencies, huge progress has been made in fabricating passive multi-beam antennas, among which the most well-known categories are lens antennas, to create multi-beam patterns. The lens antennas such as the Rotman lens [114, 115], dielectric lens [116], Maxwell fish-eye lens [117], and Luneburg lens have attracted the interest of many researchers. The Luneburg lens with gradient refractive index (GRIN) distributions, manipulating the wavefront and transform a spherical wave into a plane wave; have rotationally symmetric [118]. Since each point on the curved Luneburg lens periphery is a focal point, 2-D wide-angle beam scanning can be obtained with less scanning loss and it has wide operational bandwidth [119, 120]. All these Luneburg lenses contain dielectric. At high frequencies, electromagnetic waves propagating along the surface of the dielectric substrate will extend many wavelengths into dielectric, causing relatively high dielectric loss. Moreover, some of them do not support TEM waves, which leads to intrinsically limited bandwidth. In contrast, metals are good conductors with large and imaginary dielectric constants at microwave frequencies. Electromagnetic waves are almost all screened out due to the high conductivity of the metal, stopping fields to propagate inward [52]. Nevertheless, as the operating frequency is increased toward millimeter waves, fully metallic designs are preferred to avoid dielectric losses. The artificial electromagnetic materials based on the periodic structure have brought more flexibility to the design and realization of Luneburg lens antennas. In [121], it is theoretically demonstrated and experimentally validated that a periodic and regular vertical metal posts array on a ground plane, can act as an isotropic artificial dielectric material, and therefore can be operated as a lens. The post's size, spacing, and height controls the refractive index. It is important to note that there is no upper ground plane on the top of the metal posts. In [54], a photonic bandgap (PBG) structure, based on periodic and regular metal posts in a parallel-plate waveguide (PPW), is proposed to guide surface waves. It has been demonstrated that periodic metal posts have arbitrary surface impedances and guide surface waves. The concept is applied to design and fabricate a PPW Luneburg lens at 76.5

GHz for radar application. Contrary to [121], there is an upper plate of top of the metal posts, and it can be noted that the PPW spacing is constant. In [55], the influence of lattices and metal posts shapes at millimeter-wave frequencies, on the performances of an asymmetric PPW Luneburg lens is studied. Square, hexagonal and circular metal post shapes were considered, and also square and hexagonal lattices. It was found that hexagonal lattice with circular-shaped metal posts is best as an actual isotropic homogeneous artificial material with angular independence. Recently, fully metallic periodic structures with holes of different depths (glide-symmetric configurations) were realized by the Luneburg lens antennas [56, 122]. It has a higher effective refractive index and ultra-wideband, resulting in a flat Luneburg lens operating from 4 to 18 GHz. In order to implement this technology at a high frequency (60 GHz), a different unit cell for the Luneburg lens was proposed [57].

In this chapter, a low loss fully metallic PPW Luneburg lens antenna realized with variable heights posts and operating in the WM-864 band (220-330 GHz), in quasi-TEM mode is designed. The refractive index is mimicked by the continuous variation of metal post thickness. Radiation flare extending the parallel plates ensures a good matching to free space. The PPW lens antenna consists of three parts: the feeding, the lens, and the radiating flare. First, the constant PPW lens antenna with a thickness of 0.2 mm is fed by a double ridged waveguide (i.e. a transition to be fed with a standard waveguide). Due to the difficulty of fabrication of this transition feed at 300 GHz, we propose the variable PPW lens antenna with a thickness of 0.432 mm, which is fed by a standard WM-864 waveguide (0.864 mm ×0.432 mm). The feeds illuminate the PPW lens from its periphery. The second main part of the system is a Luneburg lens with two different diameter configurations, 6.5 mm and 10.5 mm. The lens is synthesized with variable metallic post thickness. The unit-cell of the lens is made of a cylindrical metallic post put on a metal ground, called the bottom plate, and another plate placed above the post with an air gap called the top plate. The permittivity is controlled only by one parameter: the thickness of the metal post. The third part, which is the radiating flare of the PPW Luneburg lens antenna, simply consists of an exponential taper covering 360°. The PPW Luneburg lens antenna exhibits quite good performances in terms of broadband, gain, losses, and field-of-view. According to simulations, the design is robust.

6.2 Unit Cell Properties/Background

One of the most interesting features to describe the artificial material is the dispersion diagram, on which we can see the relation between phase and frequency. In CST Microwave Studio Suite, we use Eigenmode Solver to simulate a unit cell in an infinite periodic structure. The boundary conditions in the artificial material plane are "periodic", where we can set the phase shift in both *x*- and *y*- directions between adjacent unit cells. The boundary conditions on top and bottom (*z*-direction) are PEC ($E_t = 0$).

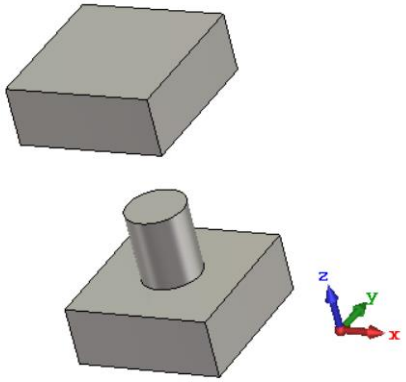

Figure 6.1: A typical unit cell in periodic artificial material.

Figure 6.1 illustrates a typical unit cell of a periodic artificial material. All boundary conditions are applied as demonstrated above. The *x*- and *y*-direction phase delays are represented by parameters "phaseX" and "phaseY" in CST. And we can cover the whole irreducible Brillouin zone by varying them.

6.3 Dispersion Diagram and Brillouin zone

In transmission lines, the propagation constant ‘’γ’’ is composed of two terms, attenuation constant ‘’α’’ and phase constant ‘β’’.

$$\gamma = \alpha + j\beta \tag{6.1}$$

Originally dispersion diagram is the function between β and frequency ω, but in the lossless case, α = 0, and phase constant ‘‘β’’ equals the wavenumber ‘‘k’’ for a plane wave. In free space, the relation is linear:

$$\beta(\omega) = k_0 = \omega\sqrt{\mu_0\varepsilon_0} \tag{6.2}$$

However, for surface waves propagating in periodic structures, it is usually hard to give an explicit expression for the wavenumber ‘’k’’. Eigenvalue equations are usually solved or full-wave simulations are performed to get the wavenumber. As is known, there might exist more than one solution for an eigenvalue equation, which means, the propagation constant might not be unique at one frequency. These different solutions are called modes. Each mode has its field

distribution, phase velocity, and group velocity. The relation between ‘‘k’’ and ‘‘ω’’ is often plotted out in curves called dispersion diagrams.

In a periodic structure, the field distribution is also periodic with a phase delay between unit cells. This phase delay is determined by phase constant ‘’k‘’ and periodicity ‘‘p’’. For a surface wave mode propagating in the *x*-direction in an infinite plane, its field can be written in a series of space harmonic waves:

$$\vec{E}\,(x.y.z) = \sum_{n=-\infty}^{\infty} \overrightarrow{E_n}(y.z)e^{-j\,\overrightarrow{k_n}\vec{x}}\,e^{j\omega t} \qquad (6.3)$$

$$k_n(\omega) = k\,(\omega) + n$$

The periodicity of ‘‘k’’ is $2\pi/p$. Therefore, the dispersion diagram only needs to be plotted in one period known as the Brillouin zone. For our 2D surface, this is a square region specified by $-\pi/p < k_x < \pi/p$ and $-\pi/p < k_y < \pi/p$. And by symmetry, it can be further reduced to the irreducible Brillouin zone, which is a triangle section whose area is 1⁄8 of the Brillouin zone area, both shown in Figure 6.2 (b), since the zone depends on the lattice. Finally, with ΓX, XM, and MΓ track in Figure 6.2 (c), we could simulate a surface wave propagating in 0◦, 90◦, and 45◦, which set the limits for waves propagating in other directions.

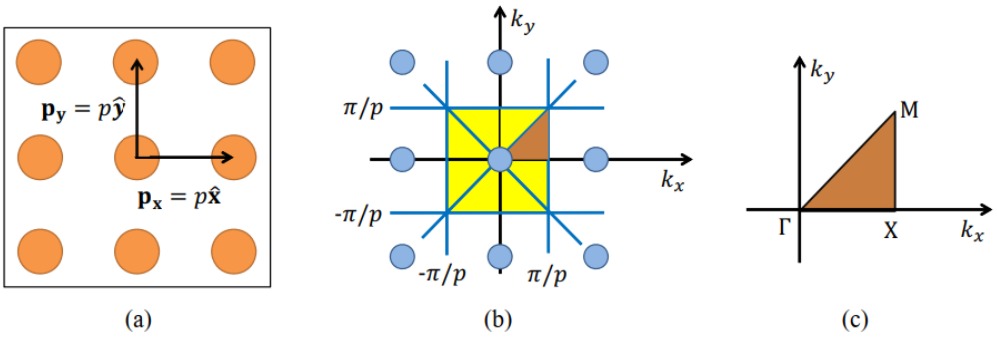

Figure 6.2: (a) Lattice vectors of a 2D periodic structure with the periodicity *p* along both *x*- and *y*-direction. (b) The Brillouin zone (yellow square) and the irreducible Brillouin zone (orange triangle). (c) Irreducible Brillouin zone and the conventional name of its special points.

In our case, the unit cell is an isotropic cylindrical in the *x*-*y* plane, hence the performance in *x*- and *y*- directions should be identical. The dispersion diagram in the *x*-direction of the sample unit cell in Figure 6.1 is presented in Figure 6.3.

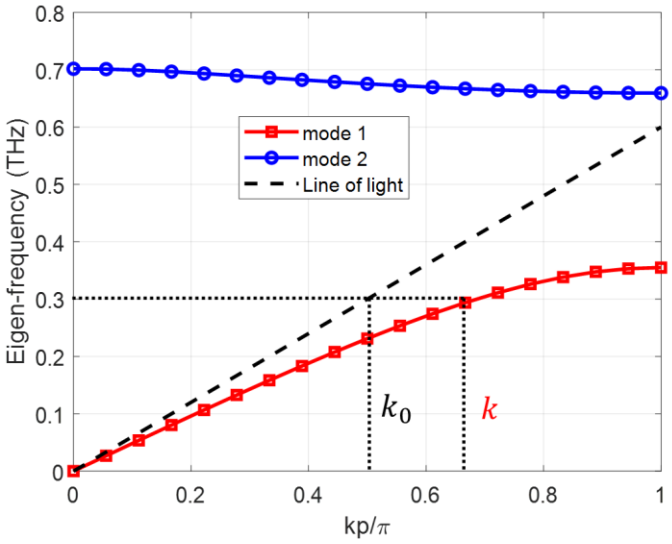

Figure 6.3: Dispersion diagram in the *x*-direction.

6.4 Effective Refractive Index

For a free space wave with frequency ω, the wavenumber k_0 is:

$$k_0 = \frac{2\pi}{\lambda_0} = \frac{\omega}{c} \tag{6.4}$$

For surface waves impinging on a periodic structure, wave propagation cannot be investigated with plane wave response, but with dispersion relation of this surface.

For a 2D-periodic structure, in a full period of $p_x = p_y = p$, the phase shift is 2π. Hence inside one period, from Γ to X, the *x*-direction phase variation is from 0 to $\boldsymbol{\pi}$, while the ***y***-direction phase stays 0.

$$\begin{cases} \boldsymbol{phase\ X = 0 \rightarrow \pi} \\ \boldsymbol{phase\ Y = 0} \end{cases}$$

Thus, wavenumber 'k' (also the propagation constant β) follows a frequency dispersion relation in equation (6.5). In CST, the phase shift is changed along the irreducible Brillouin zone boundary, and frequencies of eigenmodes are obtained accordingly.

$$k(\omega)\ p = 0 \rightarrow \pi \tag{6.5}$$

At different frequencies, the effective refractive indices n_{eff} are obtained by the ratio of k and k_0. An example of a 300 GHz frequency wave is marked by navy dashed lines in Figure 6.3.

$$n_{eff} = \frac{c}{v} = \frac{\omega/k_0}{\omega/k} = \frac{k}{k_0} \tag{6.6}$$

6.5 Dispersion Analysis of the Metallic Post Structure

The corresponding dispersion characteristics of the metallic post structures are investigated by examining their frequency contours in Figure 6.4. The 2D dispersion diagrams of the first mode, computed with the eigenmode solver of CST, for the square and cylindrical metallic post structures are presented in Figure 6.4 (a) and (b). From the frequency contours (filled circles), cylindrical metallic posts are more isotropic than the square design, especially as the frequency increases. It is observed that the cylindrical structure is isotropic for frequencies less than 350 GHz, whereas the square structure supports only up to 320 GHz.

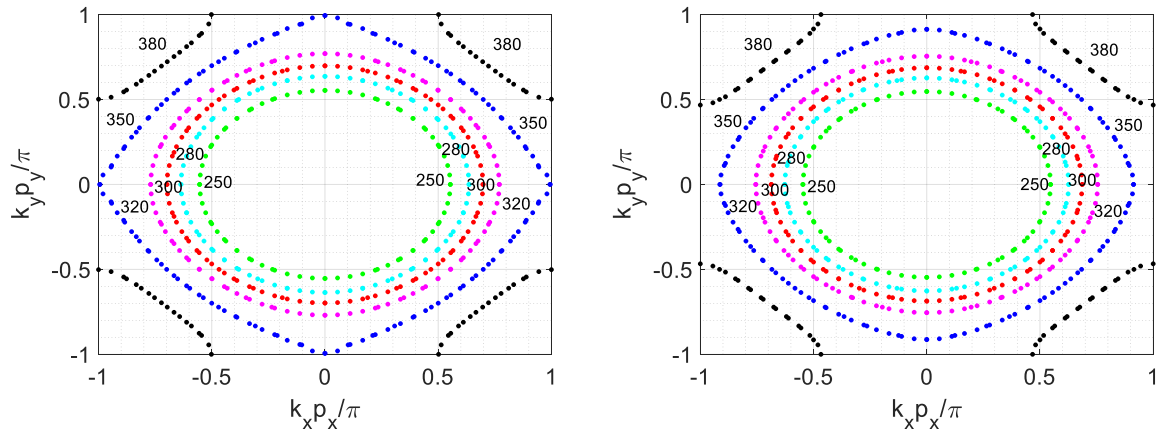

(a) (b)

Figure 6.4: 2D dispersion diagram for the first mode (a) square and (b) cylindrical metallic post structures.

6.6 Parallel Plate Waveguide (PPW)

The parallel plate waveguide (PPW) is the simplest type of guide that can support TM and TE modes; it can also support a TEM mode since it is formed from two flat conducting plates [123]. By approximating the cylindrical Luneburg lens as a PPW with plate separation ''h'' illustrated in Figure 6.5 and Figure 6.6 it is possible to identify two different E-field polarizations, namely horizontal and vertical.

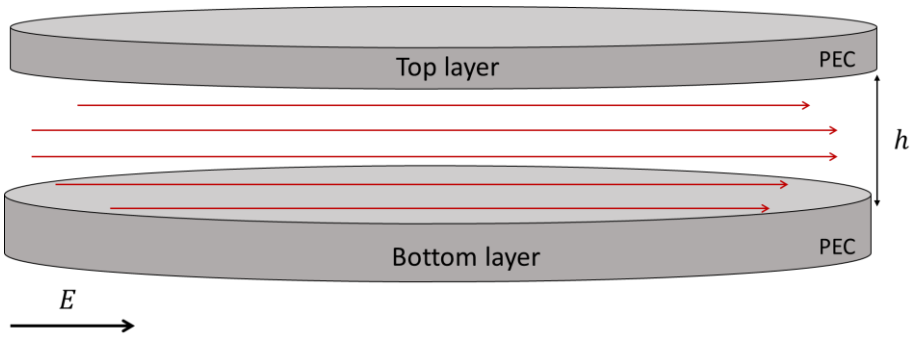

Figure 6.5: Fundamental TE-mode of a parallel plate lens waveguide.

To ensure any of the two polarizations with high signal strength, a single-mode operation is preferred and force restrictions on the plate separation ‘’h’’. The cutoff frequency of a parallel plate waveguide reveals these restrictions as limitations for the plate separation, i.e. the lens thickness ‘’h’’.

The TE-mode cutoff wavenumber of a PPW is defined as :

$$k_c = \frac{n\pi}{h}. \qquad n = 1.2.3. \ldots \ldots \tag{6.7}$$

giving the cutoff frequency

$$f_c = \frac{k_c}{2\pi\sqrt{\mu\varepsilon}} = \frac{n}{2h\sqrt{\varepsilon}}\,. \qquad n = 1.2.3. \ldots \ldots \tag{6.8}$$

To determine that the lens is operating above the cutoff frequency of the first TE_1-mode it is required that

$$h > \frac{1}{2f_c\sqrt{\varepsilon}} = \frac{\lambda}{2}. \tag{6.9}$$

and also entails suppression of the TE_2-mode through

$$h < \frac{1}{f_c\sqrt{\varepsilon}} = \lambda\,. \tag{6.10}$$

resulting in a condition on the lens thickness ‘’h’’ for TE1-mode operation

$$\frac{\lambda}{2} < h < \lambda. \tag{6.11}$$

The TM-mode cutoff wavenumber of a parallel plate waveguide is defined as :

$$k_c = \frac{n\pi}{h}. \quad n = 0.1.2.3. \ldots \ldots \tag{6.12}$$

which gives us the cutoff frequency

$$f_c = \frac{k_c}{2\pi\sqrt{\mu\varepsilon}} = \frac{n}{2h\sqrt{\varepsilon}}. \qquad n = 0.1.2.3. \ldots \ldots \tag{6.13}$$

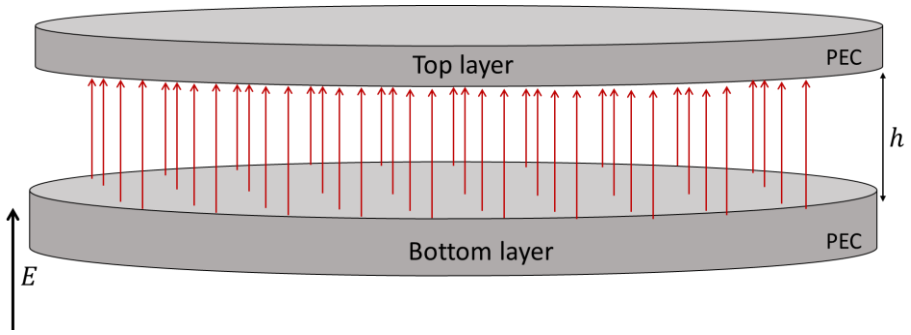

Figure 6.6: Fundamental TM-mode of a parallel plate lens waveguide.

Since μ ≈ 1. With n = 0, the cutoff frequency $f_c = 0$, the TM_0-mode is depicted in Figure 6.6. Ensuring that the first higher-order TM_1-mode is suppressed requires that

$$h < \frac{1}{2f_c\sqrt{\varepsilon}} = \frac{\lambda}{2} \tag{6.14}$$

which is a limitation on the cylindrical lens thickness for vertical E-field polarization. For a design frequency of 300 GHz the wavelength is approximately λ = 1mm, giving a lens thickness of (0.5 mm < h < 1 mm) for horizontal E-field polarization (TE_1-mode) and (h < 0.5 mm) for vertical E-field polarization (TM_0-mode).

Apart from the fact that either polarization needs a lens of different thickness their E-fields must be excited slightly different, resulting in separate antennas, one for each polarization.

6.7 Unit Cell Design

The unit cell with the required effective refractive index is designed by eigenmode simulation and dispersion diagram analysis. The realization of the Luneburg lens is based on an array of isotropic unit cells. It is known that the PPW loaded with a cylindrical metallic post can be

treated as an isotropic unit cell as shown in Figure 6.7.

For each unit, the period is determined by ‘’p’’ and the post size is determined by ‘’s’’ and ‘’t’’. The required refractive indices following Luneburg’s law are obtained by changing the height of metallic post ‘’t’’ while keeping a constant distance between the bottom plate and the upper plate of the waveguide ‘’h’’ (i.e. the PPW spacing is constant).

Parametric simulations are going to be made to study the influence of each of the geometrical parameters on the effective refractive index. The ‘’p’’ and ‘’s’’ should be as high as possible for easing the manufacturing while at the same time p/λ and s/λ should be kept as low as possible so the unit cell dispersion stays low and acceptable, and therefore the antenna is broadband. Constant values of ‘’p’’ and ‘’s’’ are better options for easing the manufacturing, but at this stage, they are kept variable in the parametric study.

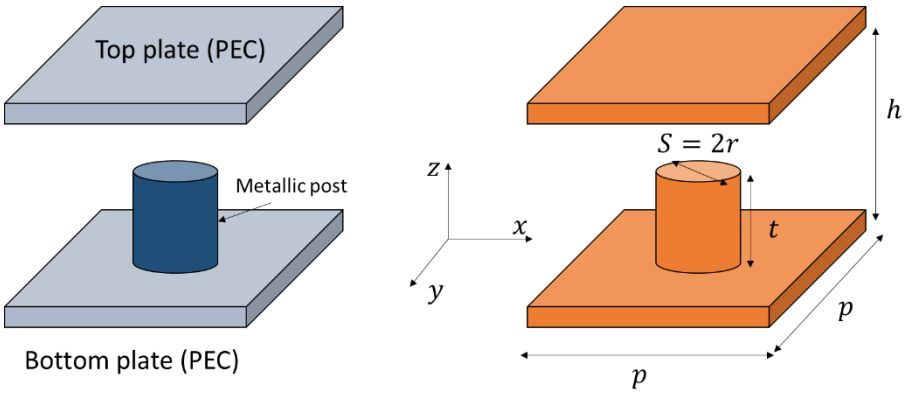

Figure 6.7: Unit cell structure and geometrical parameters.

6.7.1 Determination of Parallel Plate Spacing ‘h’

The parallel plate spacing ‘ h’ needs to be lower than ($\lambda_{min}/2$) half of the minimum wavelength in the operating bandwidth 220-320 GHz (i.e. $h < \lambda_{min}/2$), so only the quasi-TEM mode propagates in the unit-cell. The minimum wavelength in the operating bandwidth is $\lambda_{min} = c_0/f_{max} = 0.938$ mm. Therefore $h \leq 0.469$ mm, so in the parametric simulation h varies from 0.1 mm to 0.5 mm by 0.1 mm step, and t/h varies from 0 to 1 by 0.1 step. For an artificial dielectric to be considered as a homogenous media at one frequency, its unit cell dimensions need to be lower than the one-quarter wavelength (i.e. $p < \lambda/4$), and generally much less than one-quarter wavelength to achieve an effective media (i.e. $p \approx \lambda/10$). For the preliminary analysis, only ‘h’ and ‘t’ are variable, ‘p’ is set at 0.2 mm and ‘s’ at 0.1 mm. Then, p and s will be also the subject of a parametric study, and their impact on the unit-cell effective refractive index n_{eff} will be evaluated.

Let's call a unit-cell configuration, a set of three values ($p.s.h$). The different steps of the unit-cell effective refractive index calculation n_{eff} are detailed as follows:

1. After drawing the model and setting the right boundary conditions, the eigenmode solver of the full-wave simulator is used to compute the eigenfrequencies from the phase constant 'β'.
2. The eigenfrequencies data is exported from the full-wave simulator and imported into Matlab to draw the dispersion diagram, as shown in Figure 6.8.
3. In Matlab, the effective refractive index is deduced for each phase constant, by the formula $n_{eff} = \beta/\beta_0$, where $\beta_0 = 2\pi f_0/c_0$.The f_0 are the eigenfrequencies derived from the dispersion diagram and c_0 the speed of light in free space. Figure 6.9 shows the calculated unit-cell effective refractive index versus frequency.
4. Finally, Figure 6.9 can be interpolated the value of n_{eff} at any given frequency for each value of t/h, which give the mapping between the geometrical dimension t/h and the effective refractive index n_{eff} of the unit-cell.

6.7.1.1 Dispersion Diagram Analysis

Figure 6.8 shows the dispersion diagrams of the unit-cell for five configurations, i.e. for five values of h. For each value of h, t/h varies from 0 to 1 by 0.1 step. The line of light is also plotted. In Figure 6.8(a), h=0.1 mm, and when t/h=0, i.e. $t = 0$ mm, the dispersion curve and the line of light merge. This result is predictable, since there is no metal post, so the wave propagates in a media where the refractive index is 1. However, the more t/h increases, the more the dispersion curve moves away from the line of light. It means an increase of n_{eff}. For all the other values of h, the same phenomenon occurs and is shown in Figure 6.8. Additionally, it can be observed that for a non-zero and constant value of t/h, when h increases the dispersion curve moves further away from the line of light. In other words, an increase of h produces an increase of n_{eff} .

In summary, n_{eff} increases with h and t, however at this stage the values achieved by n_{eff} are unknown. In the next paragraph, n_{eff} is derived from the dispersion curves and plotted versus frequency for each configuration.

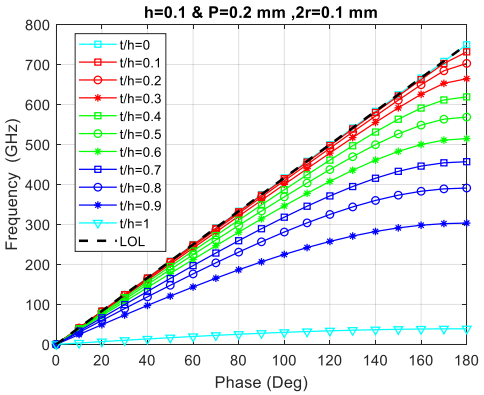

(a)

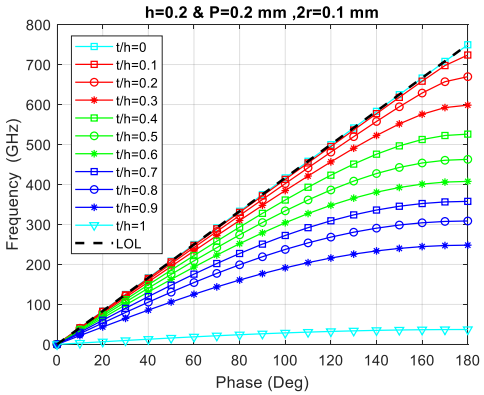

(b)

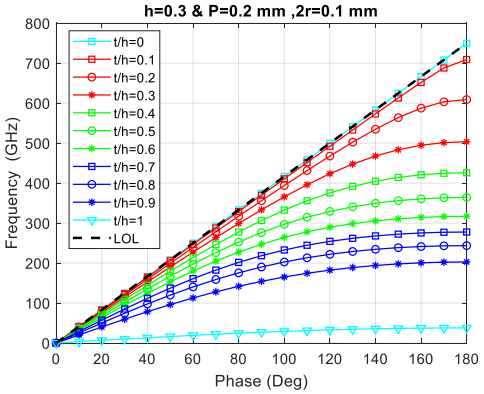

(c)

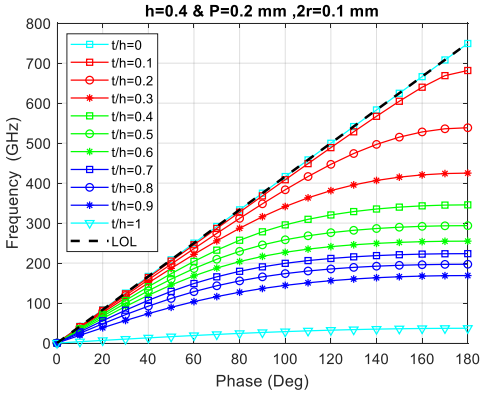

(d)

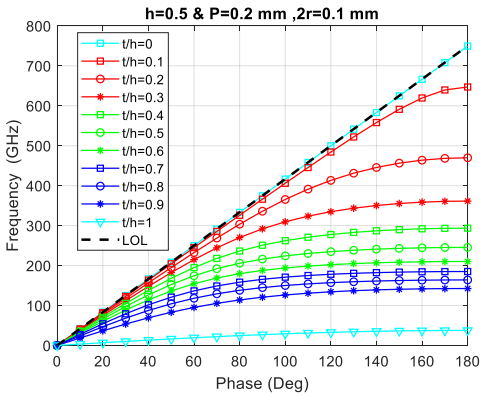

(e)

Figure 6.8: Unit cell parametric simulations dispersion diagrams. p=0.2 mm, s=0.1mm, t/h as variable and 'LoL' the line of light.

6.7.1.2 Effective Refractive Index

In Matlab, the effective refractive index is deduced for each phase constant point β, by the formula $n_{eff} = \beta/\beta_0$, where $\beta_0 = 2\pi f_0/c_0$. f_0 is the frequency derived from the dispersion diagram and c_0 the speed of light in free space. Figure 6.9 shows the calculated unit-cell effective refractive index versus frequency. It can be observed three phenomena.

1. The n_{eff} increases with frequency whatever the curve t/h and for all configurations. For example, in Figure 6.9(a) and for t/h=0.8, it can be seen that the value of n_{eff} at 300 GHz is higher than its value at 200 GHz.
2. The n_{eff} increases with t/h for a constant value of h, i.e. for each configuration. For example for h=0.1 mm, the curve t/h=0.7 is above the curve t/h=0.6.
3. The point is between two configurations and for a constant value of t/h, n_{eff} also increases with h. For example, the curve t/h = 0.9 in Figure 6.9(b) is higher than the same curve t/h= 0.9 in Figure 6.9(a).

In summary, an increase in the frequency, h or t/h produces increasing of n_{eff}. The n_{eff} range and the dispersion in the analysis bandwidth (280 -320 GHz) of each unit-cell configuration are going to be evaluated and compared to each other. This enables us to know the refractive index range achieved by each configuration and which configurations are broadband.

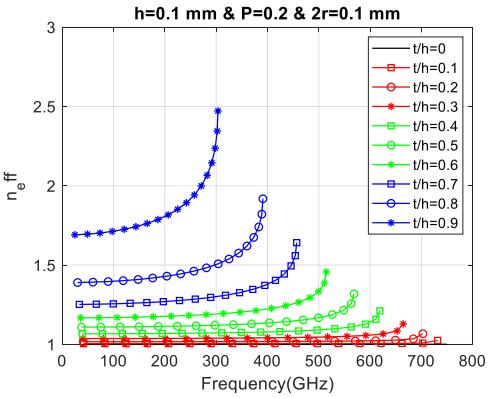

(a)

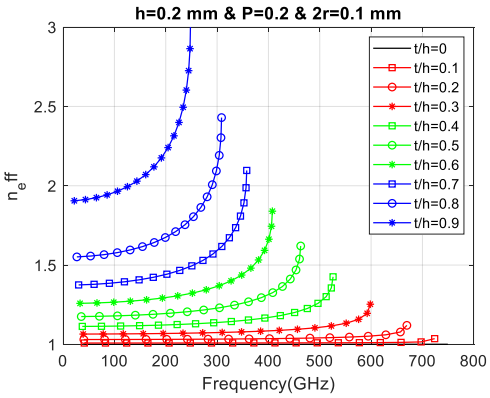

(b)

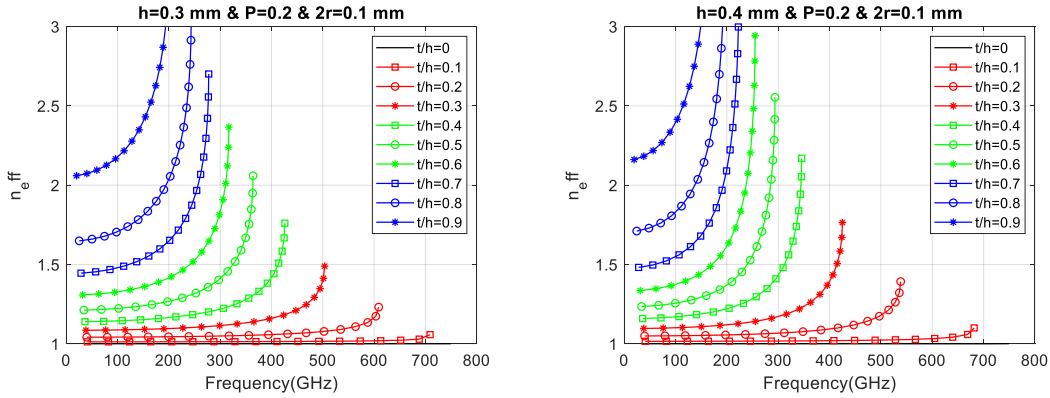

(c) (d)

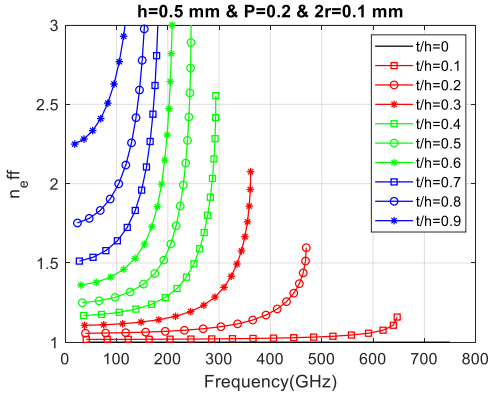

(e)

Figure 6.9: Unit cell parametric simulations: n_{eff} versus frequency, t/h as variable.

6.7.1.3 Frequency-dispersive Examination

In Figure 6.9(a), h= 0.1 mm, and let's consider the curve t/h=0.9 mm for instance n_{eff} is plotted versus frequency. As suggested by the markers, the value of n_{eff} is only calculated for few values of frequencies. However from interpolation in Matlab, the values of n_{eff} is derived for any particular value of frequency, especially for the representative frequencies of the operating bandwidth: 280, 290, 300, 310, and 320 GHz.

The interpolation is then performed for all the values of t/h and the result is shown in Figure 6.10(a), where n_{eff} versus t/h is plotted at 280, 290, 300, 310, and 320 GHz. In this mapping between unit-cell geometrical parameter t/h and the effective index parameter n_{eff}, it can be noticed that the five curves superimpose almost perfectly up to t/h =0.75. It means that in the operating bandwidth the value n_{eff} does not depend on the frequency: 280, 290,300, 310, and 320 GHz. In other words, the dispersion is extremely low, or the unit-cell configuration is broadband. This figure also enables us to see directly the unit-cell configuration refractive

index ranges from 1 to 1.41. This unit-cell configuration can therefore be used to realize a Luneburg lens.

In the same way as for h=0.1 mm and t/h=0.9mm, n_{eff} is interpolated at 280, 290, 300, 310, and 320 GHz for each configuration and each curve t/h. The results are illustrated in Figure 6.10. In all the configurations, Figure 6.10 (a) to Figure 6.10(e), n_{eff} versus t/h ranges from 1 to at least 1.41.Therefore, they all can be used to realize a Luneburg lens. However the unit-cell dispersion is different, it depends on the configuration.

The dispersion, extremely low for h= 0.1 mm and h = 0.2 mm for all values of t/h, see Figure 6.10(a) and Figure 6.10(b), starts to increase when h= 0.3mm, especially after the value of t/h = 0.25, as shown in Figure 6.10(c). Indeed, in this figure the five curves superimpose from t/h=0 to t/h=0.25, but from t/h=0.3, the gap between frequencies increases and is more and more visible. It means the dispersion increases with t/h. The superimposition of the five curves stops at lower values of t/h, as h increases. In Figure 6.10(d) where h=0.4mm, it stops around t/h=0.2, in Figure 6.10(e) where h=0.5 mm, it stops at t/h=0.1.

In summary, the dispersion of the unit-cell configurations is acceptable for n_{eff} =1.41 up to h=0.2 mm. For higher values of h, the gap between 280, 290, 300, 310, and 320 GHz becomes important and could limit the bandwidth. Furthermore, when h increases mean that the manufacturing tolerance also increases, making ease of manufacture.

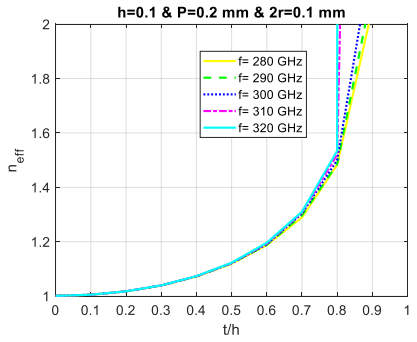

(a)

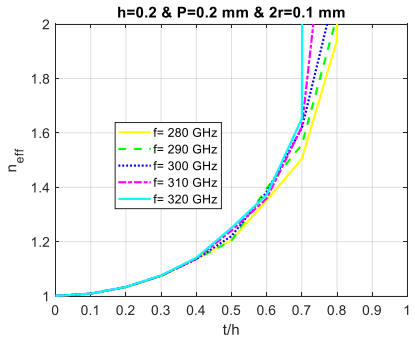

(b)

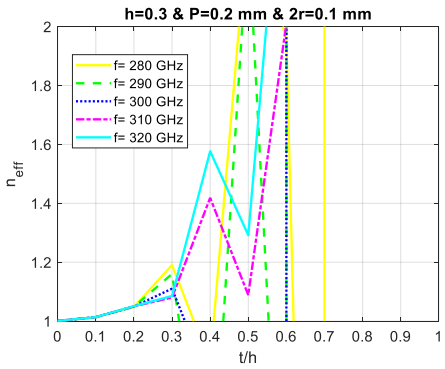

(c)

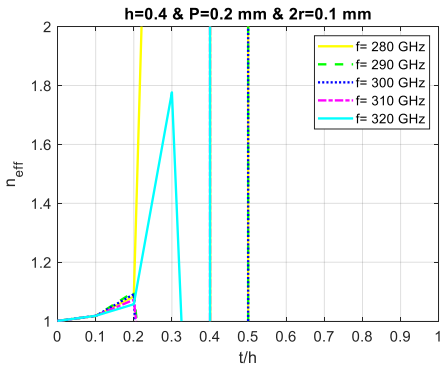

(d)

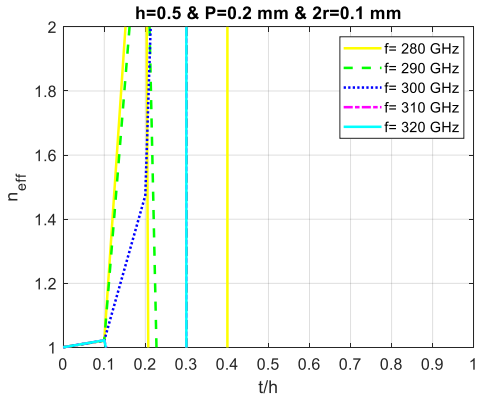

(e)

Figure 6.10: Unit cell parametric simulations: n_{eff} versus t/h, frequency as variable.

6.7.2 Determination of Periodicity 'p'

In the previous section, a dispersion analysis of unit-cell enabled to study of the impact of h, t/h , and frequency on the unit-cell n_{eff}. In that study the periodicity p= 0.2 mm, $s = 2r$ = 0.1 mm, h varied from 0.1mm to 0.5 mm, t/h from 0 to 0.9, and the tradeoff between the dispersion and manufacturing tolerances has enabled to select of one value of h = 0.2 mm.

In this section, the impact of periodicity p on n_{eff} is analyzed and eventually, a tradeoff on the values of p is made as well. In the following parametric study p takes four values: 0.2 mm, 0.25 mm ,0.3 mm and 0.4 mm. h=0.2 mm and t/h varies from 0 to 0.9 by 0.1 step. The mapping between n_{eff} and t/h at 280 GHz, 290 GHz, 300 GHz, 310 GHz, and 320 GHz are illustrated in Figure 6.11.

Between Figure 6.11(a) and Figure 6.11(d), it can be observed that increasing p decreases n_{eff}. For instance, when p=0.2 mm, the n_{eff} ≈1.3 around t/h=0.5, whereas when p=0.25 mm, the n_{eff}=1.2 around t/h=0.5. In other words, higher values of 'p' induces higher ranges of t/h to achieve the necessary refractive indexes to realize a Luneburg lens, therefore a better manufacturing tolerance to 't'. As the result the p= 0.25mm is selected.

Figure 6.11: Unit cell parametric simulations: n_{eff} versus t/h, with the influence of p on the effective refractive index.

In the comparison between Figure 6.11(c) and Figure 6.11(d), the dispersion of unit-cell significantly increases with the increase of p. Therefore, p= 0.25mm is selected to increase freedom of the metal posts mechanical, and thus avoid breaking them.

In

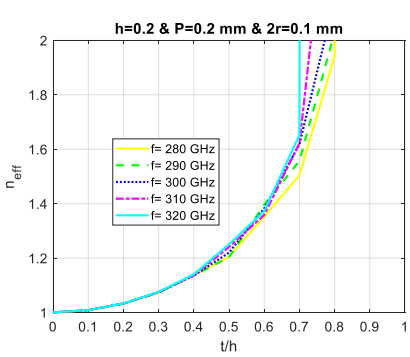

(a)

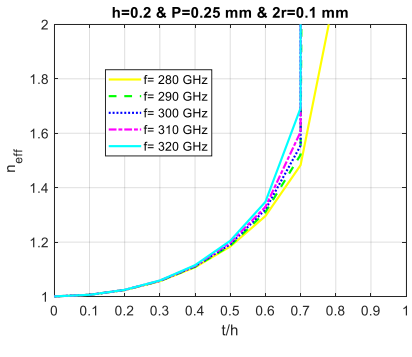

(b)

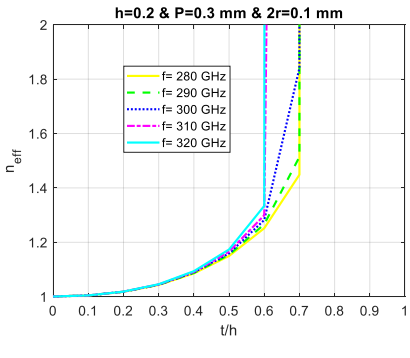

(c)

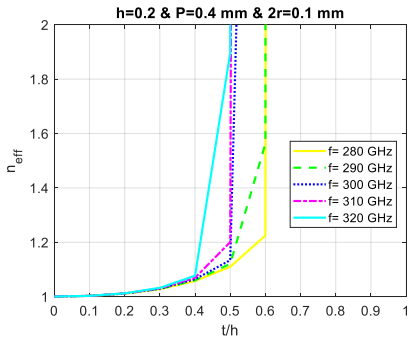

(d)

the summary, in this section, the unit-cell analysis has been presented. It is based on a metal post laying on a metal ground plane. There is another metal ground plane on top of the metal post with an air gap between them. The dispersion analysis of the unit-cell enabled to study of the influence of each unit-cell geometrical parameters on the effective refractive index n_{eff}. The'n_{eff}' increases significantly with frequency, h, and t/h, and slightly with p.

Dispersion and manufacturing criteria have been considered to select the values of 'h' (0.2 mm), 'p' (0.25 mm), and 's' (0.1mm) to meet the specifications, i.e. to design an all-metal Luneburg lens with constant 'h' at 300 GHz band. Finally, the value of n_{eff} is controlled only by the value of t/h.

6.8 Metallic Lens Antenna Design

6.8.1 Introduction

An inhomogeneous artificial dielectric Luneburg lens based on a parallel-plate waveguide (PPW) is shown in Figure 6.12, where the effective refractive index varies radially, simply by varying the height of metallic post on the bottom plate of the PPW. In Figure 6.12, the top view and cross-sectional view of the lenses are displayed. As shown in Figure 6.12 (a), primary feeds excite the lens at the circumference. Figure 6.12 (b) shows the cross-sectional view of the air-filled lenses. It is shown that the post height is varied, to satisfy the required refractive index

of $n(r')$ for a Luneburg lens at a normalized radius r' as follows :

$$n(r') = \sqrt{2 - (r')^2}\ , 0 \leq r' \leq 1$$
$$n(r') = 1\ , \qquad r' \geq 1. \tag{6.15}$$

The lens is realized by concentric circles of cylindrical metallic posts of varying height on the bottom plate of the PPW, providing the refractive index profile, as shown in Figure 6.12. This creates a circular lattice. Radii and refractive index of these concentric circles/areas that create the Luneburg lens can be obtained by utilizing the following formulas

$$n_i = \sqrt{\varepsilon_i} = \sqrt{2 - (2i-1)\mathrm{M}}$$
$$r_i = \sqrt{2i\mathrm{M}} \times R_{\mathrm{Lens}} \tag{6.16}$$

where $\mathrm{M} = 1/(2\mathrm{N}+1)$, N is the number of concentric circles/areas, and R_{Lens} is the radius of the Luneburg lens.

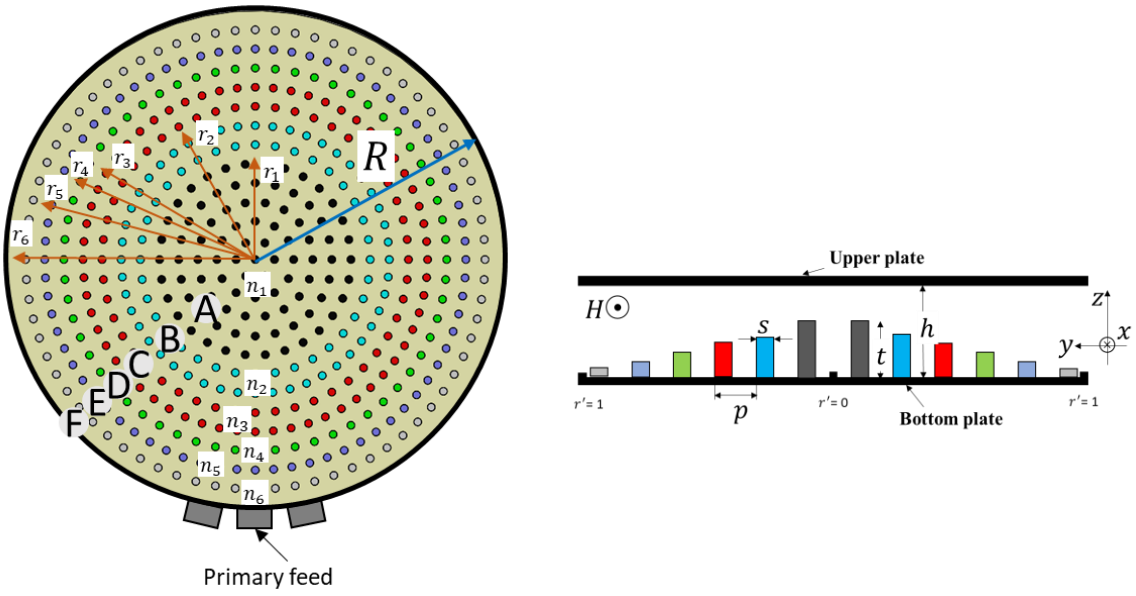

(a) (b)

Figure 6.12: Artificial dielectric Luneburg lens based on the PPW: (a) Top view, and (b) cross-sectional view. p = 0.25, s = 0.1, h = 0.2, t has variable heights, all dimensions in mm.

The center-to-center distance between the metallic posts in one circle is also approximately equal to 'p', ($p \ll \lambda_0$) locally satisfying the periodicity condition of the eigenmode analysis. These concentric circles cause an effective refractive index gradient that approximately realizes

a Luneburg lens. The radii of the concentric circles with different heights of metallic posts along with the 'n_{eff}' values to realize a 6.5 λ_0 and 10.5 λ_0 diameters lens is given in Table 3.1.

Table 6.1: Design parameters of metallic Luneburg lens with variable metallic posts.

diameter	**6.5 λ_0**	**10.5 λ_0**	t/h (mm)	t (mm)	Δt (μm)
n_{eff}	radius	radius			
1.39	r_1 = 1.27 λ_0	r_1 = 2 λ_0	0.6297	0.126	126
1.33	r_2 = 1.82 λ_0	r_2 = 2.94 λ_0	0.6045	0.121	5
1.273	r_3 = 2.21 λ_0	r_3 = 3.57 λ_0	0.5632	0.113	8
1.2	r_4 = 2.54 λ_0	r_4 = 4.1 λ_0	0.5064	0.1013	11.7
1.145	r_5 = 2.86 λ_0	r_5 = 4.62 λ_0	0.4424	0.0885	12.8
1.072	r_6 = 3.12 λ_0	r_6 = 5 λ_0	0.3262	0.0653	23.2

The diameter of the artificial Luneburg lens is determined by the desired azimuth beamwidth [124] :

$$\Delta\theta_{3dB} = 51^{\circ} \times \frac{\lambda_0}{aperture\ width} \qquad (6.17)$$

Since our requirement of 3-dB beamwidth are 8° and 5°, the Luneburg lens diameters, equivalent to aperture width in equation (6.17), will be $2R$ = 6.5 λ_0 and $2R$ = 10.5 λ_0 Thus, the Luneburg lens diameter determines the HPBW of the proposed multi-beam antenna.

To tune the effective refractive index from 1 at the edge to 1.4 at the center of the lens, the ratio 't/h' is changed from 0 to 1 at a constant spacing of PPW with h = 0.2 mm, obtaining the dispersion response, as shown Figure 6.13. A Luneburg lens can be mimicked by using a different height of metallic posts at different positions, as represented in Figure 6.12.

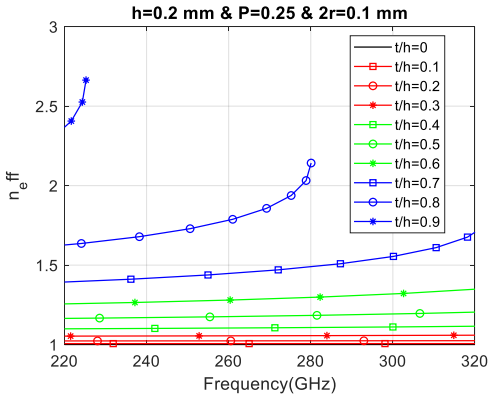

(a)

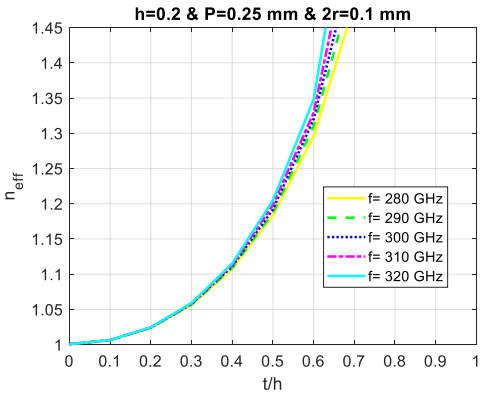

(b)

Figure 6.13: Dispersion diagram of the unit-cell (a) effective refractive index vs frequency (b) frequency-dispersive vs unit cell geometry.

Based on the rotational symmetry of the Luneburg lens, we choose a section across the center of the lens and divide the section into six areas, A, B, C, D, E, and F corresponding to different equivalent refractive indices, as shown in Figure 6.12 (b). The expected effective refractive indices in the points A, B, C, D, E, and F are computed according to Luneburg's law. The structure is shown in Figure 6.12 (b), where each color represents a different height of the cylinders. For h = 0.2 mm and p = 0.25 mm and $2r$ = 0.1 mm, we deduced the value of the thickness of metallic post ''t'' according to Luneburg lens law from Figure 6.13(b) as shown in Table 6.1. Based on the unit cells with required effective refractive indices, we can form the Luneburg lens. The radii of the Luneburg lens are determined to be 3.25 and 5.25 mm. The periodic posts of the unit cells with their size: p = 0.25 mm, s= 0.1 mm, and h = 0.2 mm.

6.8.2 Radiating Flare Design

The lens is ended with a flare to minimize reflections between the lens and free space (i.e. match the impedance inside the PPW to the free space one $\eta \approx 120\pi$, so the energy can be efficiently radiated). The radiating part (i.e. flare) of the lens consists of an exponential tapering in the E-plane of the bottom and top plates starting from the periphery of the lens. Figure 6.16(a) shows the top view of the lens and the radiating aperture and Figure 6.16(b) the cross-section view, where the optimum aperture size d=1.288 mm, and taper length l= 3mm for the 10.5 λ_0 lens.

6.8.3 Feed Design

As we want to design a beam scanning antenna over a wide range of scan angles in the azimuth plane and with a narrow beam (8˚) for a lens diameter of 6.5 λ_0 or with a narrow beam (5˚) for a lens diameter of 10.5 λ_0, a lot of sources around the lens are needed. It means that each source must be small enough (< 0.6 mm) to ensure a 3-dB overlap between the beams. Then, an open-ended waveguide at 300 GHz (WR-03/WM-864) cannot be used for this future beam scanning antenna. The classical open-ended waveguide (WR-03/ WM-864) cannot be used if we want to feed the lens with several sources, because this source is too wide (0.864 mm). Furthermore, the parallel plate space h between the top and bottom plates is equal to 0.2 mm. Therefore, the following section shows the design of a ridged waveguide to feed the lens.

The use of a ridged waveguide allows the reduction of the width of the classical waveguide without increasing the cut-off frequency. By adding a central ridge to either the top, the bottom, or both of a rectangular waveguide, the cutoff frequency can be lowered due to the capacitive effect it introduces. The distance between the ridges (for the double-ridged case) or the ridge and opposite waveguide wall (for the single-ridged case) affects the effective impedance of the

waveguide. As this distance has decreased the impedance is also decreased. The design is described, respectively, in Figure 6.14 for (a) front, (b) backside views, and (c) the cross-section view with the different optimized dimensions. The transition between the open-ended waveguide and the height of the lens is achieved by stepping the height of the waveguide to match the impedance.

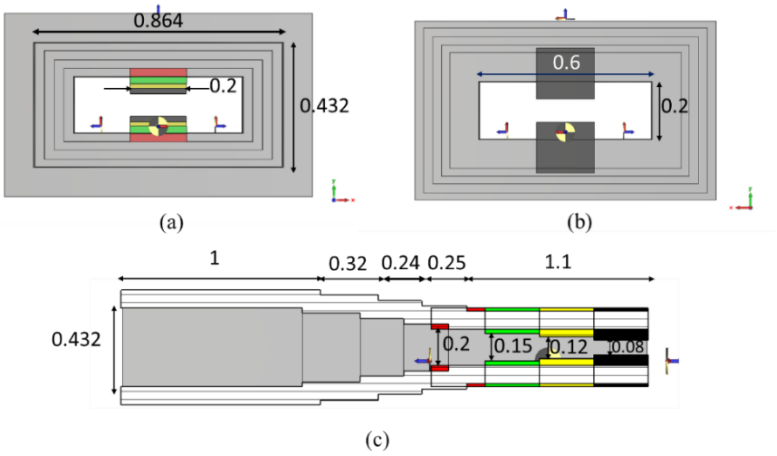

Figure 6.14: Double-ridged waveguide (DR-WG) (a) front side view, (b) backside view, and (c) cross-section view. All dimensions in milliliters.

This double-ridged waveguide (DR-WG) fed by waveguide ports has been simulated and optimized using CST Microwave Studio Software. The simulated matching level is better than 10 dB on the bandwidth of interest (220–320 GHz) as shown in Figure 6.15. The DR-WG fed by the WM-864 waveguide is studied to illuminate the lens and to realize the design of a beam-scanning antenna with a narrow beam (8˚/5˚) over a wide scan angle.

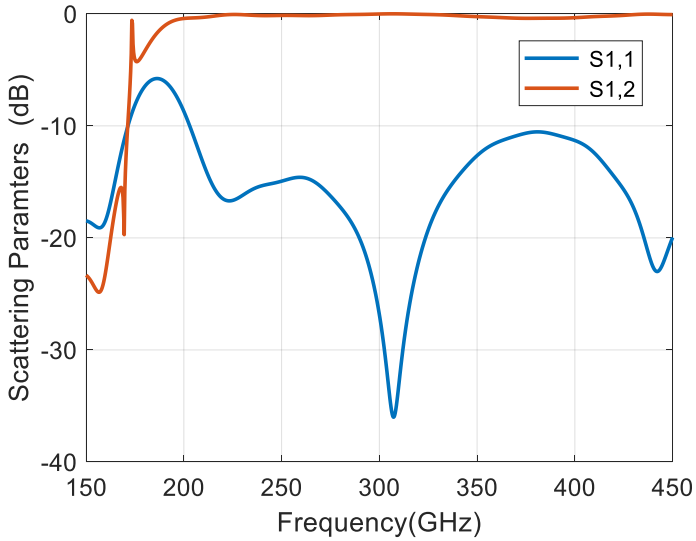

Figure 6.15: The scattering parameters of double-ridged waveguide (DR-WG).

6.9 Mutlibeam Antenna Integration

Figure 6.16 (a) and (b) show the whole antenna system integrating multiple feeds of the lens and the radiation aperture (i.e. flare).

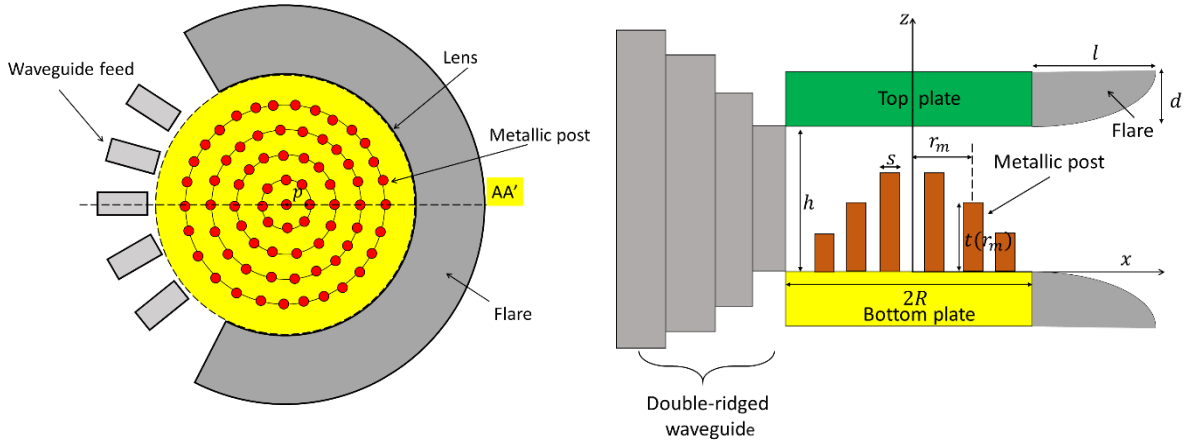

(a) Feeds, lens, and flare: top view

(b) Feed, lens, and flare: section view

Figure 6.16: Beam scanning antenna architecture. (a) Top view, and (b) cross-sectional view.

6.10 Metallic Lens Antenna Simulations

6.10.1 Double Ridged Waveguide Feed-based Metallic Lens

6.10.1.1 Configurations of Lens with 6.5 λ Diameter

The performance of the metallic Luneburg lens with a double-ridged waveguide (DR-WG) feed is tested and evaluated. The proposed 6.5 λ diameter lens, is shown in Figure 6.17.

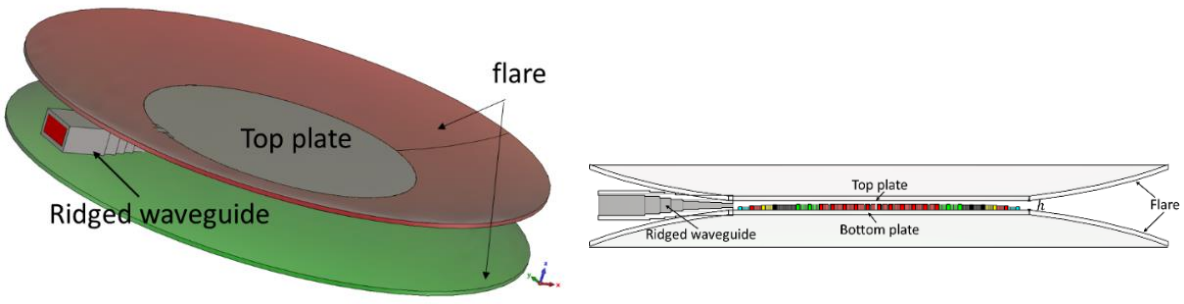

(a)

(b)

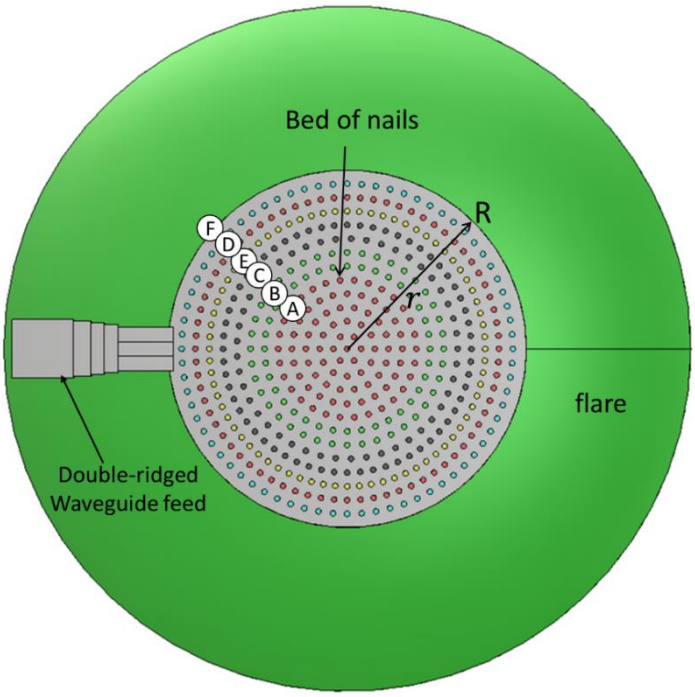

(c)

Figure 6.17: Metallic Luneburg lens fed by a double-ridged waveguide. (a) perspective view (b) cross-sectional view, and (c) top view.

A. S-parameters

To verify the impedance matching performance, the S-parameters have been computed as shown in Figure 6.18. In the range of 250-350 GHz frequency band, the return loss is lower than -7 dB. The bad matching performance is due to the reflection of the DR-WG feed with metallic beds post of the lens at the rim.

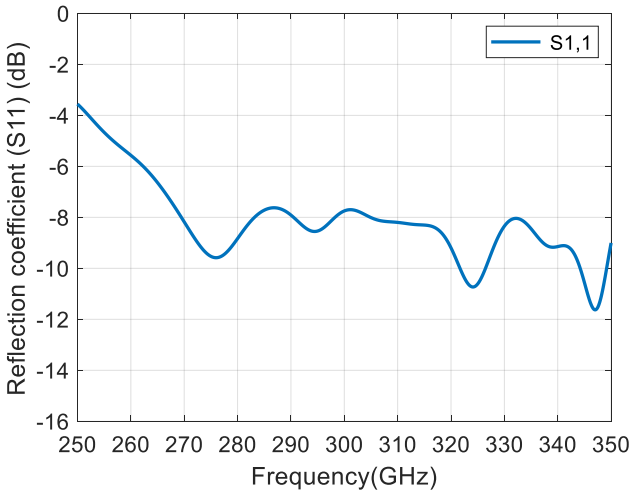

Figure 6.18: Return loss (S11) of $6.5\lambda_0$ Luneburg lens feed by DR-WG.

B. Radiation pattern

The Luneburg lens antenna beams are all fan beams. The H-plane pattern of the antenna is a narrow beam pattern, as shown in Figure 6.19(a). The 3 dB beamwidth is 9.6° for an H-plane beam at 300 GHz. The E-plane pattern of the metallic Luneburg lens antenna is a wide beam pattern, as shown in Figure 6.19 (b). The 3 dB beamwidth is 36.4° for an E-plane beam at 300 GHz. The far-field comparison of seven frequencies (270-330 GHz) is presented in Figure 6.19. Detailed performances are listed in Table 6.2. The maximum realized gain is 20.5 dBi at 330 GHz.

Table 6.2. The H-plane far-field Performance of DR-WG integrated with $6.5\lambda_0$ metallic Luneburg lens.

Frequency (GHz)	270	280	290	300	310	320	330
Realized gain (dBi)	17.3	17.7	18.2	18.8	19.7	20.4	20.5
3dB beamwidth	10.9°	11°	10°	9.6°	8.7°	8.4°	8.1°
Side lobe level (dB)	-15.2	-14.1	-17.1	-20.6	-21.7	-16.4	-18.7

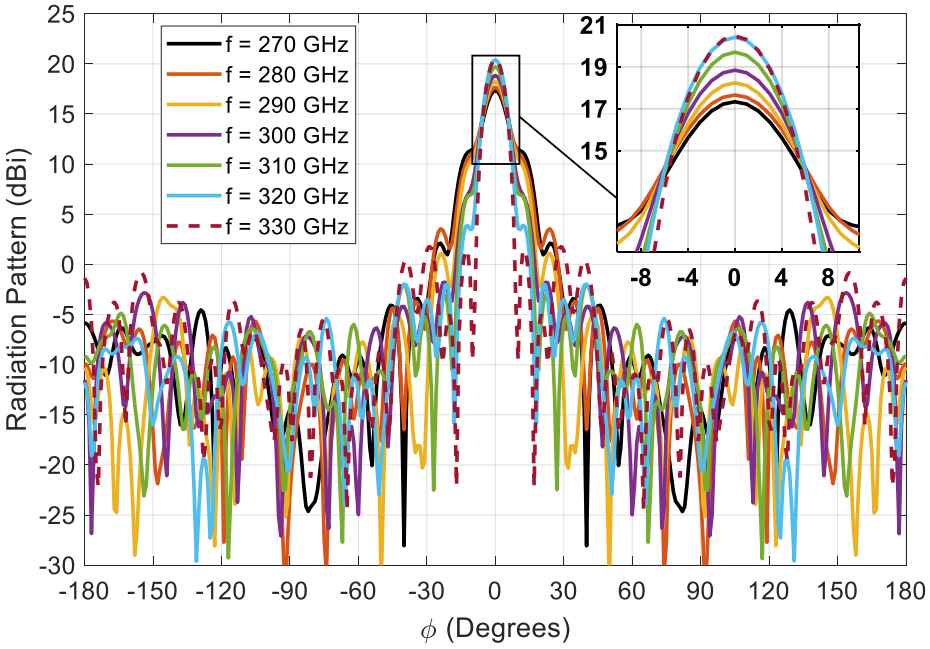

(a)

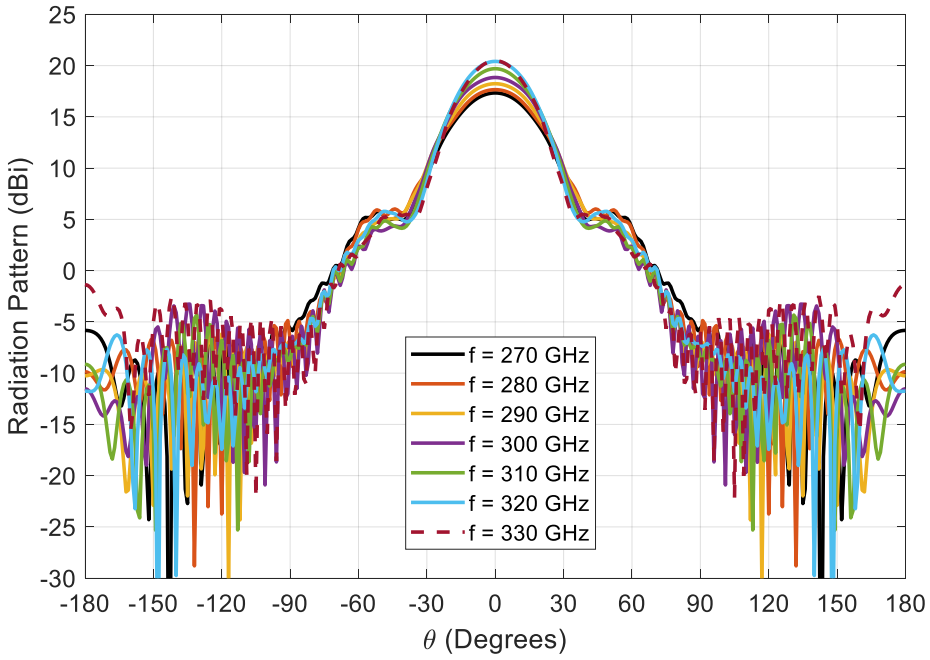

(b)

Figure 6.19: Simulated 2D radiation pattern of DR-WG integrated with $6.5\lambda_0$ metallic Luneburg lens antenna in (a) H-plane ($\theta = 90^{\circ}$). (b) E-plane ($\phi = 0^{\circ}$).

Figure 6.20 shows the 3-D radiation pattern of the antenna proposed at 300 GHz. The metallic Luneburg lens antenna achieves a high performance that can be a suitable choice to use in the new generation of wireless communication devices.

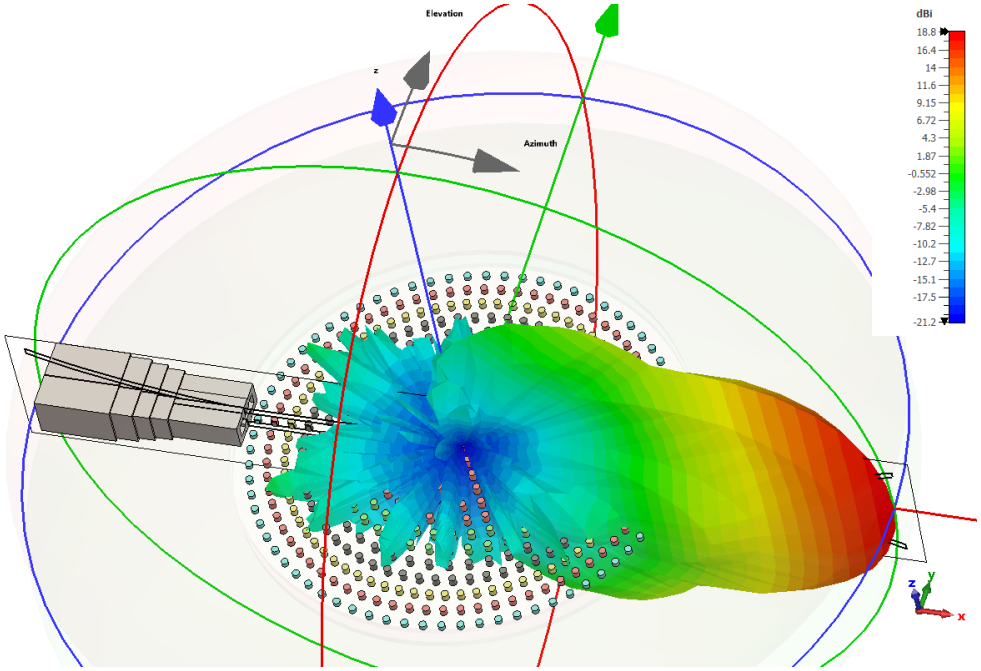

Figure 6.20: 3D radiation pattern of 6.5λ_0 metallic lens antenna at 300 GHz.

6.10.1.2 Configurations of Lens with 10.5 λ Diameter

A. S-parameters

To verify the impedance matching performance, the S-parameters have been computed as shown in Figure 6.21. In the range of 260-345 GHz frequency band, the return loss is lower than -8 dB. The bad matching performance is due to the reflection of double ridged waveguide feed with metallic posts of the lens at the rim.

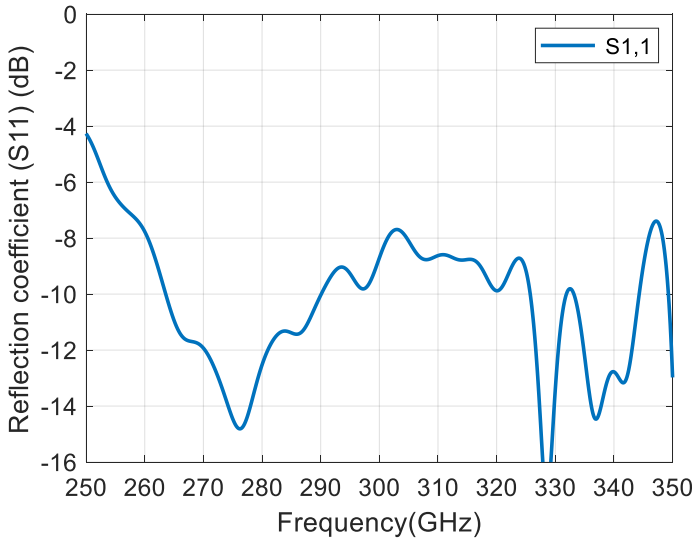

Figure 6.21: Return loss (S11) of $10.5\lambda_0$ Luneburg lens feed by DR-WG.

B. Radiation pattern

Figure 6.22 shows the radiation patterns of different frequencies. The H-plane pattern of the antenna is a narrow beam pattern, as shown in Figure 6.22 (a). The 3 dB beamwidth is 5.6° for the H-plane beam at 300 GHz. The E-plane pattern of the metallic Luneburg lens antenna is a wide beam pattern, as shown in Figure 6.22 (b). The 3 dB beamwidth is 27.4° for the E-plane beam at 300 GHz. The far-field comparison of seven frequencies (270-330 GHz) is presented in Figure 6.22. Detailed performances are listed in Table 6.3. The maximum realized gain is 22.8 dBi at 320 GHz.

Table 6.3. The H-plane far-field Performance of DR-WG integrated with $10.5\lambda_0$ metallic Luneburg lens.

Frequency (GHz)	270	280	290	300	310	320	330
Realized gain (dBi)	20	20.6	21.3	21.8	22.3	22.8	22
3dB beamwidth	7.9°	7.3	6.4°	5.6°	5.2°	4.9°	4.9°
Side lobe level (dB)	-19.8	-21	-21.5	-14.2	-16.5	-17.4	-14.6

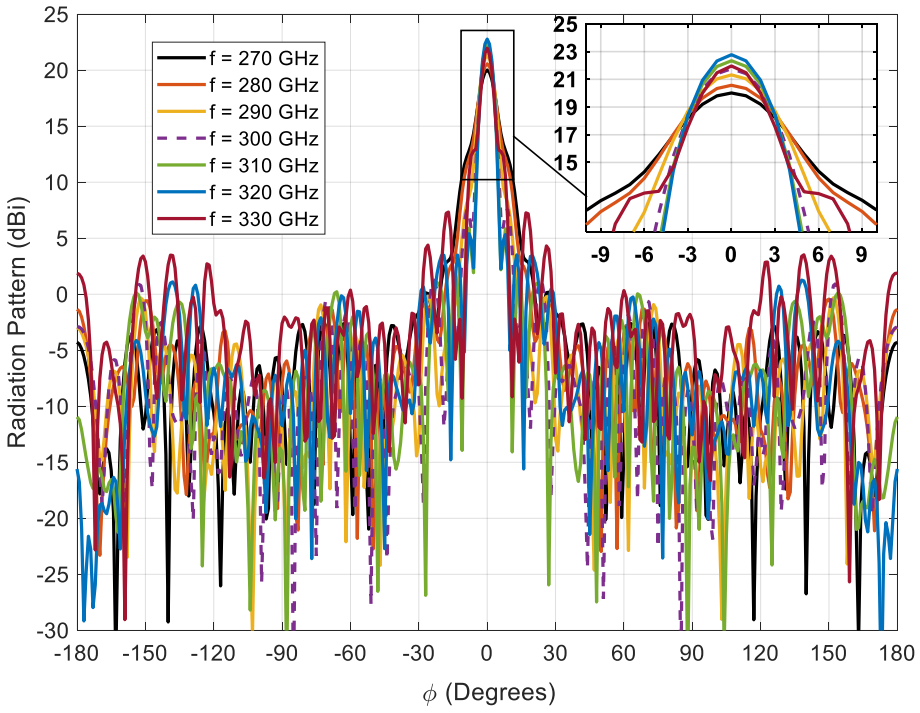

(a)

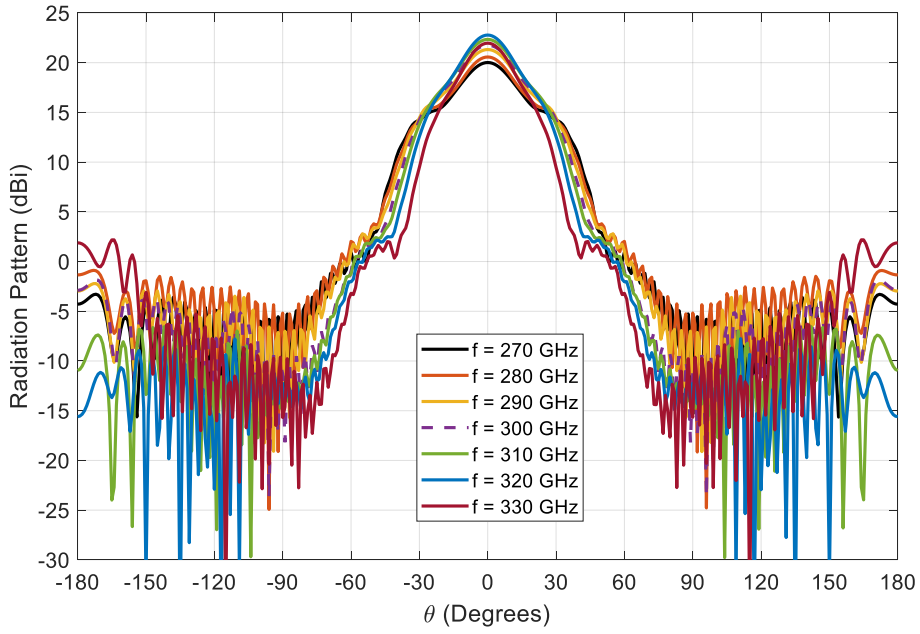

(b)

Figure 6.22: Simulated 2D radiation pattern of DR-WG integrated with $10.5\lambda_0$ metallic Luneburg lens antenna in (a) H-plane ($\theta = 90^{\circ}$). (b) E-plane ($\phi = 0^{\circ}$).

6.10.2 Standard WM-864 Waveguide Feed-based Metallic Lens

This section represents the extension and the next step of the previous section. As artificial martial aims to design a fully metallic 2-D Luneburg lens operating in the 300 GHz band and made of a bed of nails technology. In the previous section, the PPW spacing was constant and set at h = 0.2 mm, whereas in this section the top plate is gradually decreased and set at h_g = 0.432 mm only at the periphery of the lens so that the antenna can be fed by WM-864 standard rectangular waveguides (0.864 x 0.432 mm^2), without the need for transitions as shown in Figure 6.23.

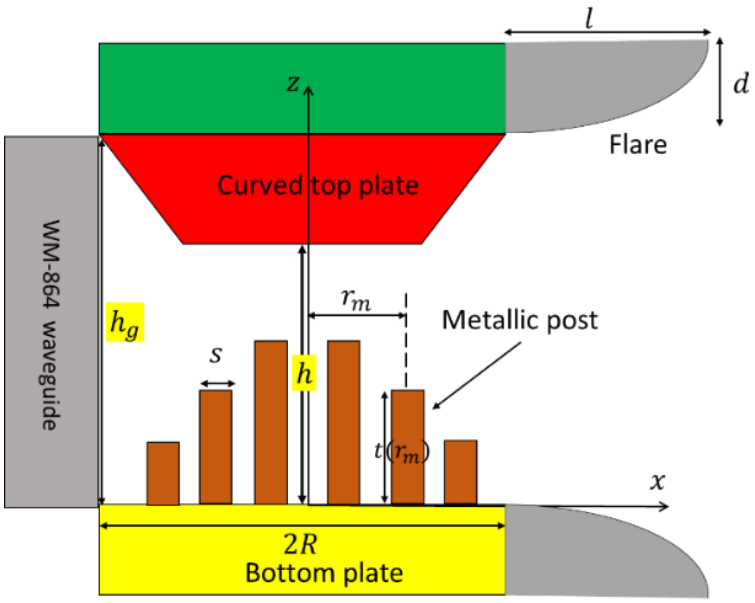

Figure 6.23: Cross-sectional views of the bed of nail 2-D Luneburg lens structure with variable PPW.

6.10.2.1 Configurations of Lens with 6.5 λ Diameter

The performance of the metallic Luneburg lens with standard WM-864 (i.e. single feed configuration) feed is tested and evaluated. The proposed 6.5 λ0 diameter lens, is shown in Figure 6.24.

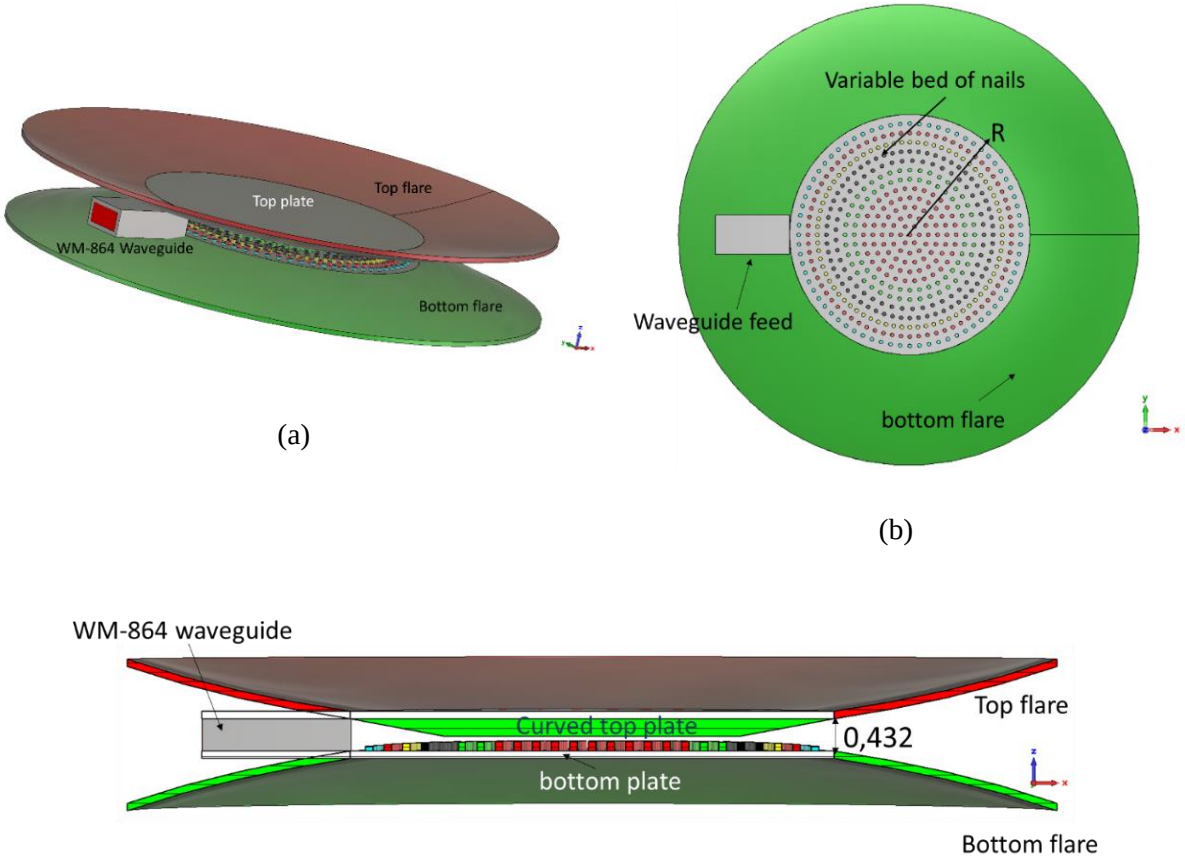

Figure 6.24: Metallic Luneburg lens fed by standard WM-864 waveguide. (a) perspective view (b) top view, and (c) cross-sectional view.

A. S-parameters

To verify the impedance matching performance, the S-parameters have been computed as shown in Figure 6.25. In the range of 250-350 GHz frequency band, the return loss is lower than -10 dB.

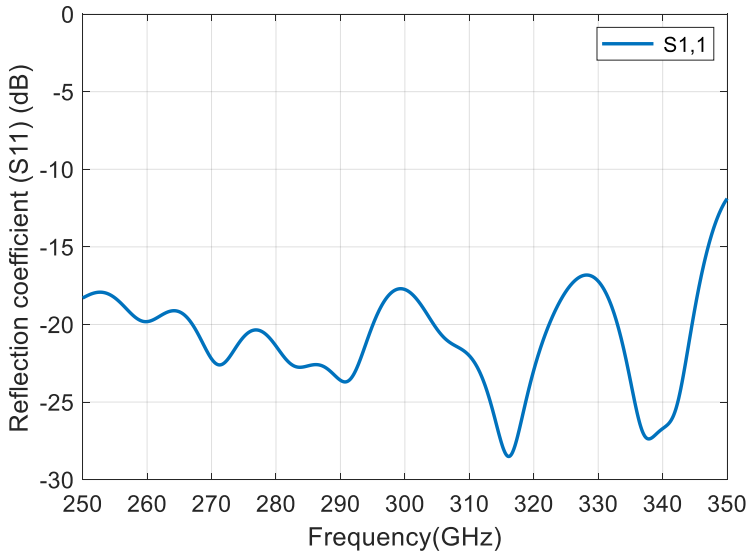

Figure 6.25: Return loss (S11) of 6.5 λ_0 Luneburg lens feed by standard waveguide.

B. Radiation pattern

The Luneburg lens antenna beams are all fan beams. The H-plane pattern of the antenna is a narrow beam pattern, as shown in Figure 6.26 (a). The 3 dB beamwidth is 9.4° for the H-plane beam at 300 GHz. The E-plane pattern of the metallic Luneburg lens antenna is a wide beam pattern, as shown in Figure 6.26 (b). The 3 dB beamwidth is 28.7° for the E-plane beam at 300 GHz. The far-field comparison of five frequencies (280-320 GHz) is presented in Figure 6.26. Detailed performances are listed in Table 6.4. The maximum realized gain is 21 dBi at 310 GHz.

Table 6.4. Far-field performance of standard WM-864 integrated with 6.5λ_0 metallic Luneburg lens.

Frequency (GHz)	280	290	300	310	320
Realized gain (dBi)	20.3	20.6	20.8	21	20.8
3dB beamwidth	10.1°	9.8°	9.4°	9.3°	9.7°
Side lobe level (dB)	-17	-18.8	-19.9	-19.5	-18

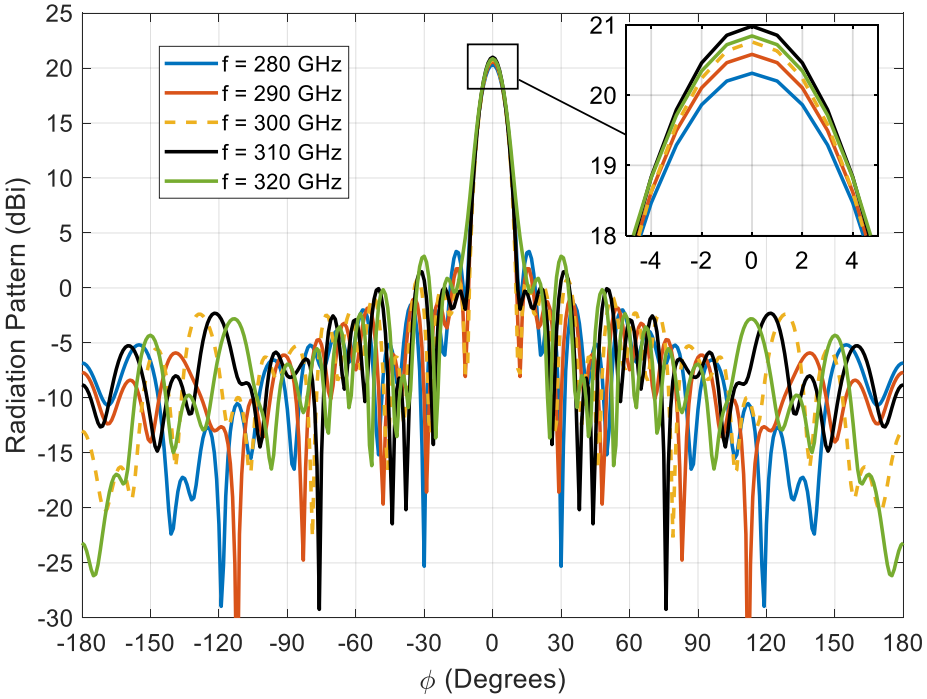

(a)

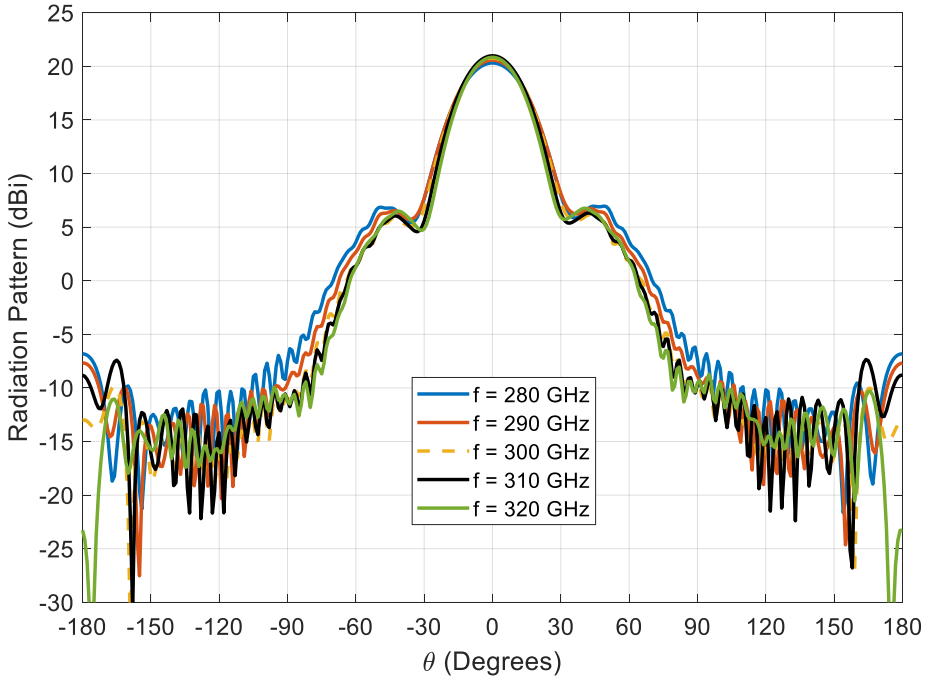

(b)

Figure 6.26: Simulated 2D radiation pattern of standard WM-864 integrated with 6.5 λ_0 metallic Luneburg lens antenna in (a) H-plane ($\theta = 90^{\circ}$). (b) E-plane ($\phi = 0^{\circ}$).

6.10.2.2 Configurations of Lens with 10.5 λ Diameter

A. S-parameters

To verify the impedance matching performance, the S-parameters have been computed as shown in Figure 6.27. In the range of 250-350 GHz frequency band, the return loss is lower than -10 dB.

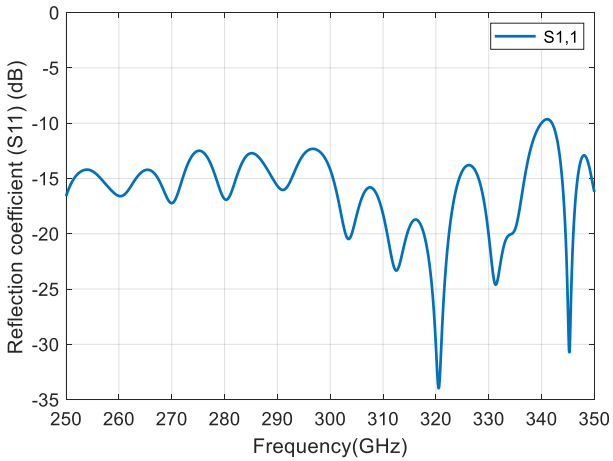

Figure 6.27: Return loss (S11) of 10.5 λ_0 Luneburg lens feed by standard waveguide.

B. Radiation pattern

The Luneburg lens antenna beams are all fan beams. The H-plane pattern of the antenna is a narrow beam pattern, as shown in Figure 6.28(a). The 3 dB beamwidth is 5.5° for the H-plane beam at 300 GHz. The E-plane pattern of the metallic Luneburg lens antenna is a wide beam pattern, as shown in Figure 6.28((b). The 3 dB beamwidth is 21.4° for the E-plane beam at 300 GHz. The far-field comparison of seven frequencies (270-330 GHz) is presented in Figure 6.26. Detailed performances are listed in Table 6.4. The maximum realized gain is 22.9 dBi at 290 GHz.

Table 6.5. Far-field performance of standard WM-864 integrated with 10 λ_0 metallic Luneburg lens.

Frequency (GHz)	270	280	290	300	310	320	330
Realized gain (dBi)	22.4	22.8	22.9	22.7	22.1	20.6	17.7
3dB beamwidth	6.3°	6.1°	5.8°	5.5°	6°	7.9°	16.6°
Side lobe level (dB)	-16.9	-19.1	-18.8	-14.9	-17.6	-14.3	-9.2

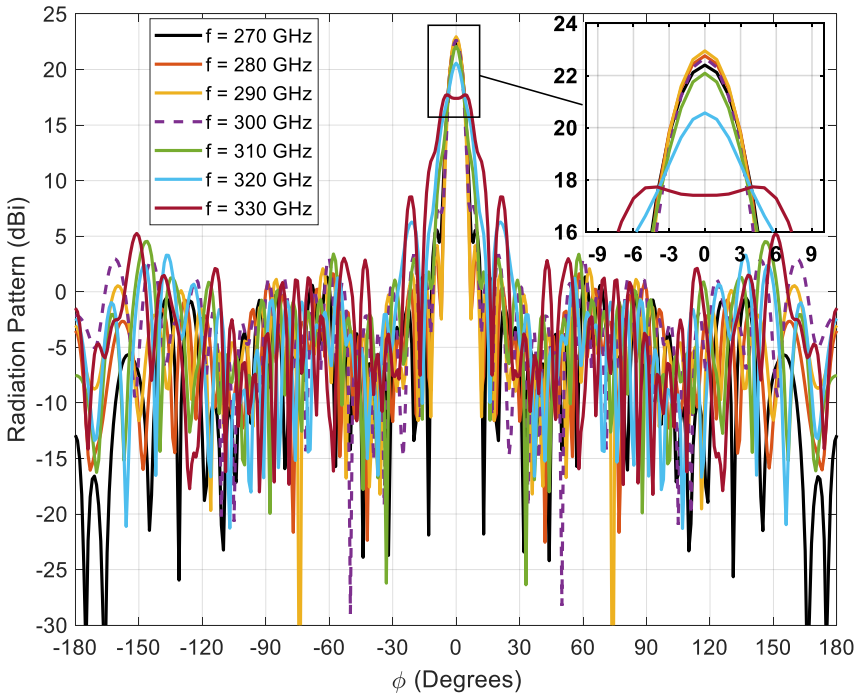

(a)

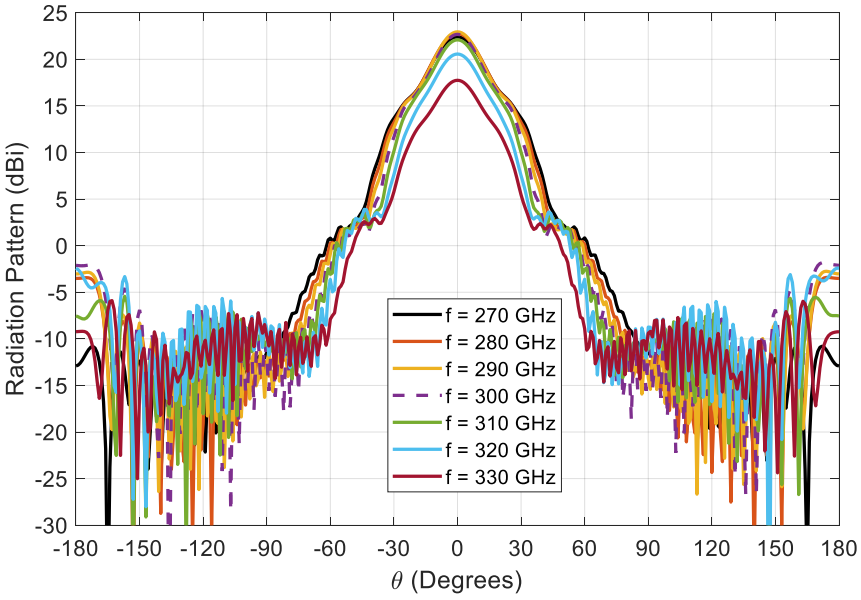

(b)

Figure 6.28: Simulated 2D radiation pattern of standard WM-864 integrated with $10.5\lambda_0$ metallic Luneburg lens antenna in (a) H-plane ($\theta = 90^{\circ}$) , and (b) E-plane ($\phi = 0^{\circ}$).

6.11 Sub-THz Beam-scanning Antenna

6.11.1 Feeding Approach

Concerning the waveguide feeds of metallic Luneburg lens antenna, to ensure 3-dB beam scanning in H-plane, a limitation of this design is the space occupied by the feeds, which cannot be placed too close to each other. The feeding should be small enough to provide the 3-dB beam overlap as shown in Figure 6.29(a). 'θ_H' which represents the 3-dB beamwidth in H-plane is set as 5°. In consideration of measurements, the input port of the feeding should be a standard waveguide WM-864 (0.864 mm x 0.432 mm). Therefore, the feeding with a gradually narrowed waveguide (i.e. stepped waveguide transition) will be difficult to fabricate at 300 GHz.

To solve this problem, we introduce a novel configuration in which the metallic Luneburg lens antenna can be duplicated with a second identical one in the vertical plane, as shown in Figure 6.29(b). The lens is excited by the feeding ports (WM-864 waveguide feedings), which will be changing alternatively between the bottom and top Luneburg lens antennas according to the desired beam directions as shown in Figure 6.29(b).

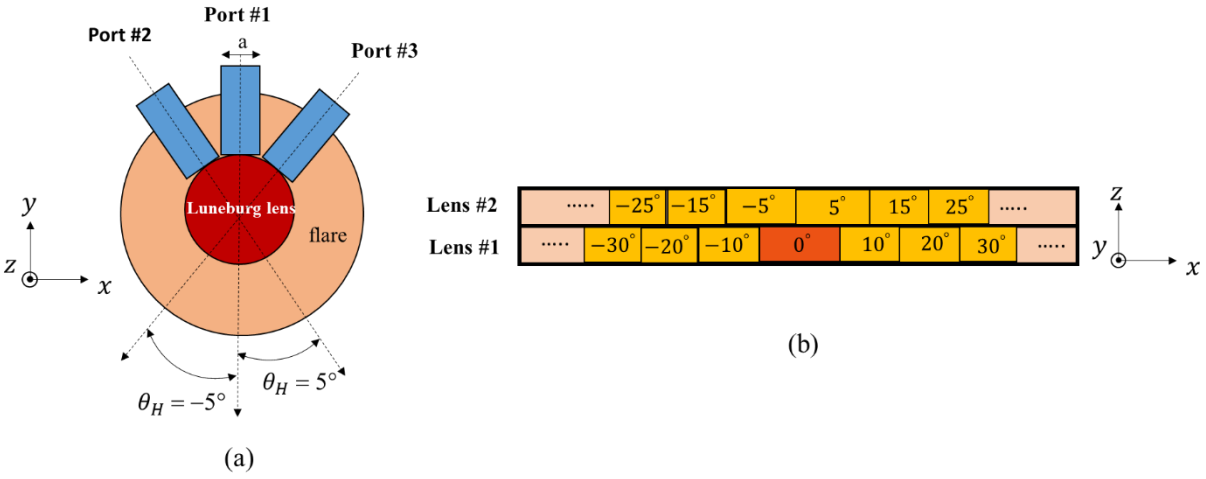

Figure 6.29: Arrange of WM-864 waveguide feeds for artificial Luneburg lens antenna of 10.5 λ_0. (a) Top view; (b) side view.

6.11.2 Integration of 3-WM-864 Feeds with 6.5 λ Diameter Metallic Luneburg Lens

The proposed multi-beam metallic Luneburg lens antenna fed by waveguide WR-03 was simulated to verify the design. The metallic Luneburg lens prototype is exhibited in Figure 6.30, where a second lens structure has been added as a novel idea to realize the 3dB overlap

between the beams. During S-parameter simulation, three of the input ports were connected with WR-03. Only one port was excited at one time for testing the radiating performance.

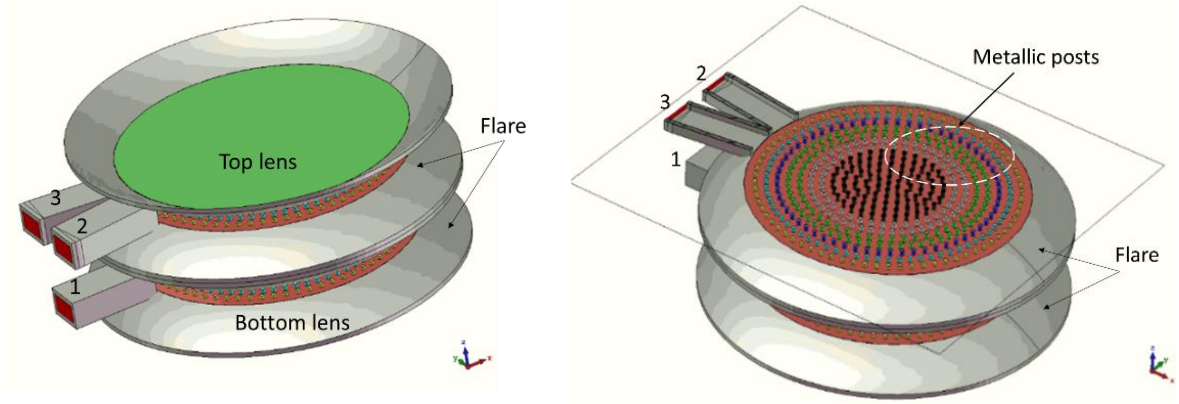

(a) (b)

Figure 6.30: Geometry of the proposed multi-beam metallic 6.5 λ Luneburg lens antenna with multiple feeds. (a) Perspective view. (b) Top cutting view.

A. S-Parameter

Simulated reflection coefficients of ports 1–3 as given in Figure 6.31. The simulated overlapped impedance bandwidth for the reflection coefficient of less than -12 dB is wider than 100 GHz, which can cover the 300 GHz band. On the other hand, it is seen from Figure 6.32 that the simulated mutual couplings between Port 1 and the other two ports. The simulated mutual coupling between the two adjacent ports, i.e., Ports 2 and 3, is the highest, which is lower than -20 dB throughout the operating band. In addition, simulated |S12 |and |S13| are less than -35 dB.

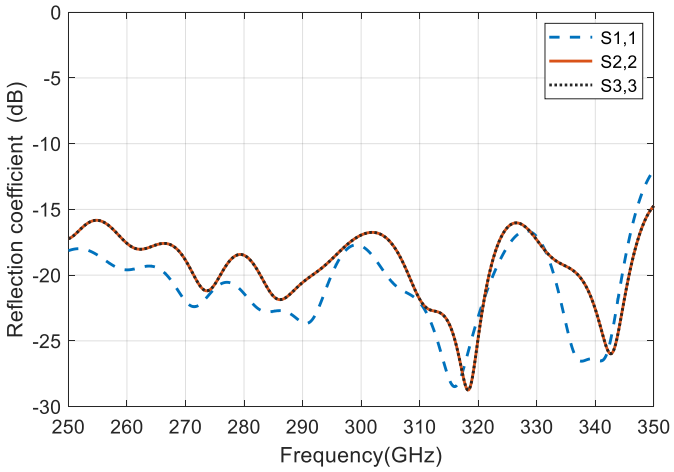

Figure 6.31: Simulated reflection coefficient of the multibeam 6.5 λ Luneburg lens antenna.

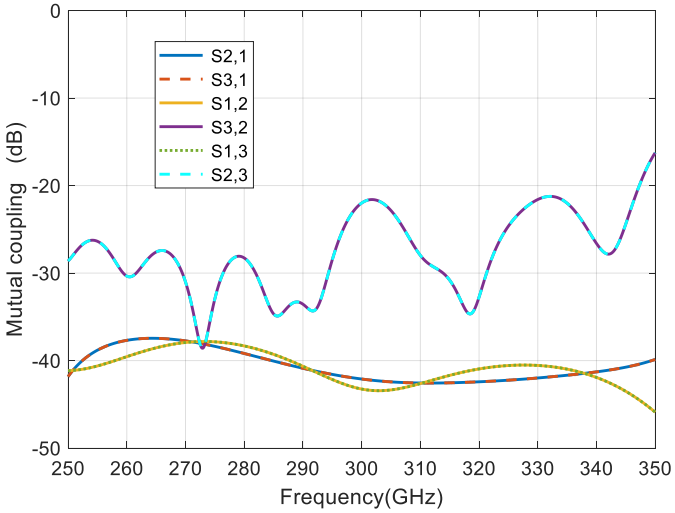

Figure 6.32: Simulated mutual coupling of the multibeam 6.5 λ Luneburg lens antenna.

B. Radiation Pattern

Figure 6.33 shows the simulated H-plane radiation patterns of the multibeam antenna scanning in the horizontal plane at 270, 280, 290, 300, 310, 320, and 330 GHz, respectively. The radiation performance is almost identical when the input ports are excited separately. The three radiating beams can cover an angular range between ±8°. The simulated cross-polarization of less than -20 dB is omitted for simplification. The maximum realized gain of 20.9 dBi is obtained at 0° and ±8° at 310 GHz as shown in Figure 6.33 (e).

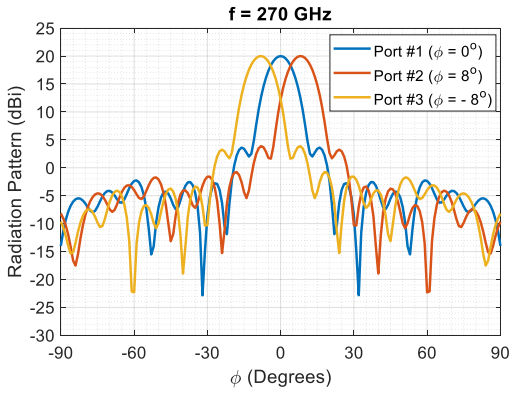

(a)

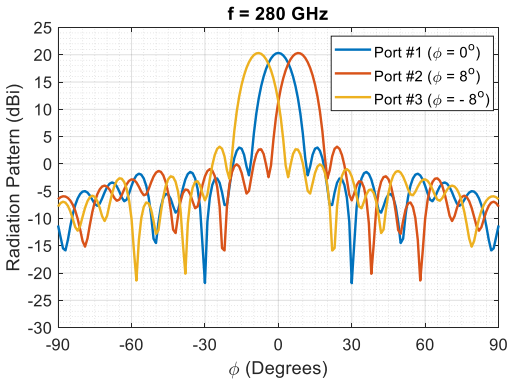

(b)

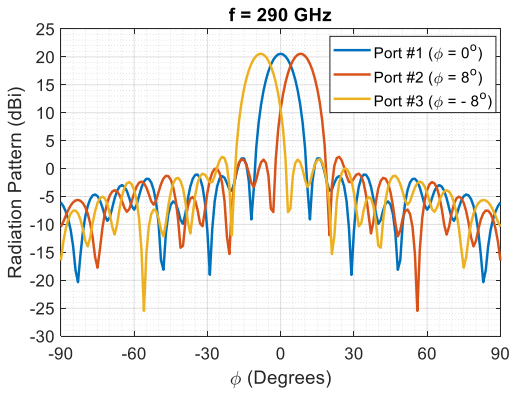

(c)

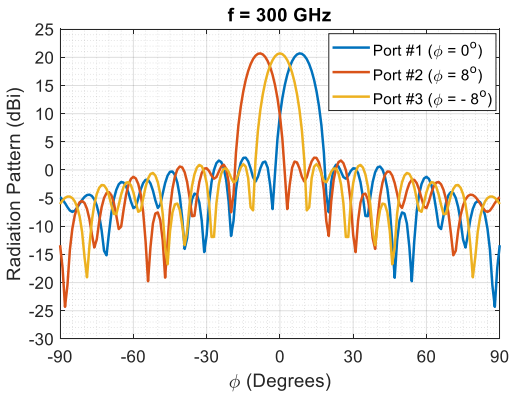

(d)

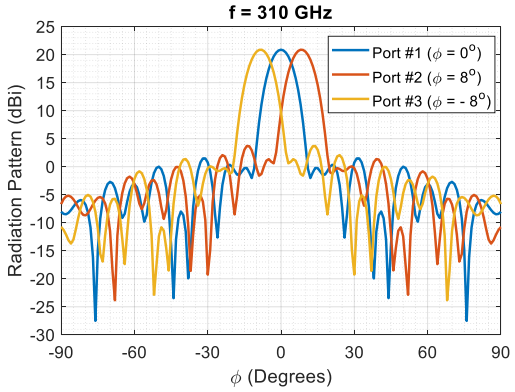

(e)

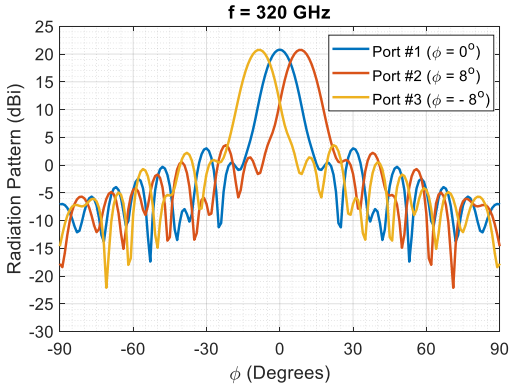

(f)

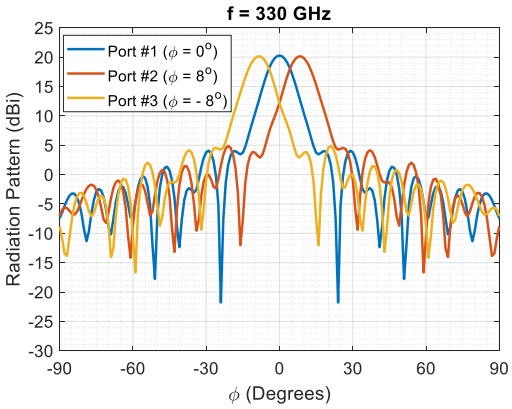

(g)

Figure 6.33 : Simulated radiation patterns of the multibeam 6.5 λ Luneburg lens antenna. (a) f = 270 GHz, (b) f = 280 GHz, (c) f = 290 GHz, (d) f = 300 GHz, (e) f = 310 GHz, (f) f = 320 GHz and (g) f = 330 GHz.

Figure 6.34 illustrates the computed gain with different scanning angles for the proposed beam steering 6.5 λ lens antenna. It can be observed that the maximum gain reaches 20.9 dBi at 310 GHz.

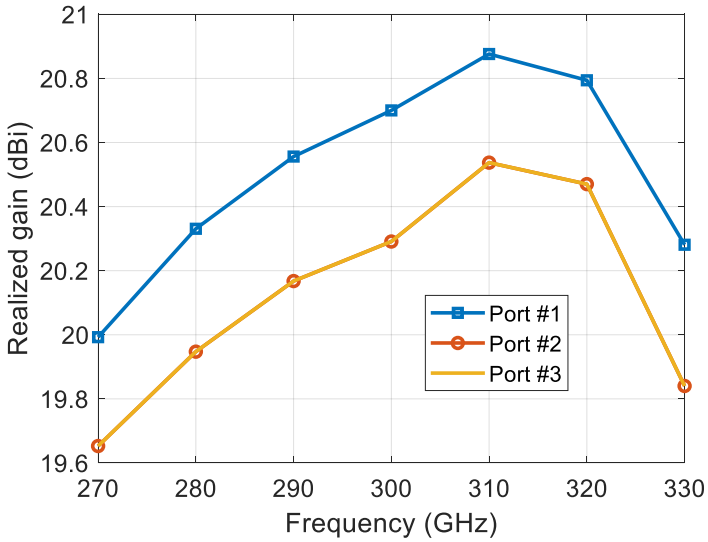

Figure 6.34: The maximum realized gain for 3 different feeding ports.

6.11.3 Integration of 37-Waveguide Feeds with 10.5 λ Diameter Metallic Luneburg Lens

37 waveguide feeds are placed along the focal arc of the lens, the odd number of waveguides between (1-37) feed the bottom/original lens and the even number of waveguides between (2-36) feeds the top/duplicate lens (see inset of Figure 6.35).

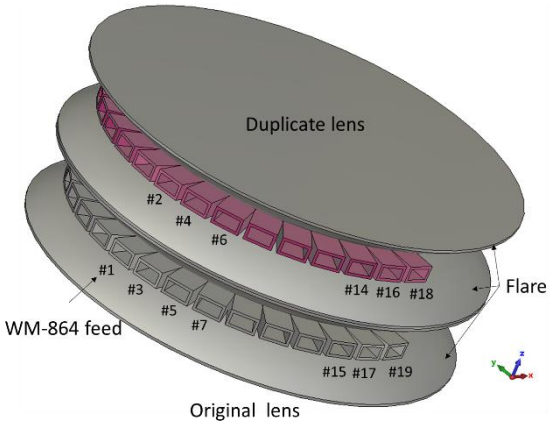

(a)

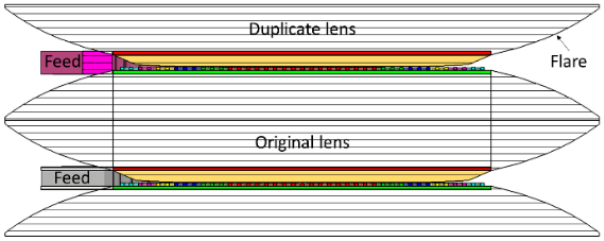

(b)

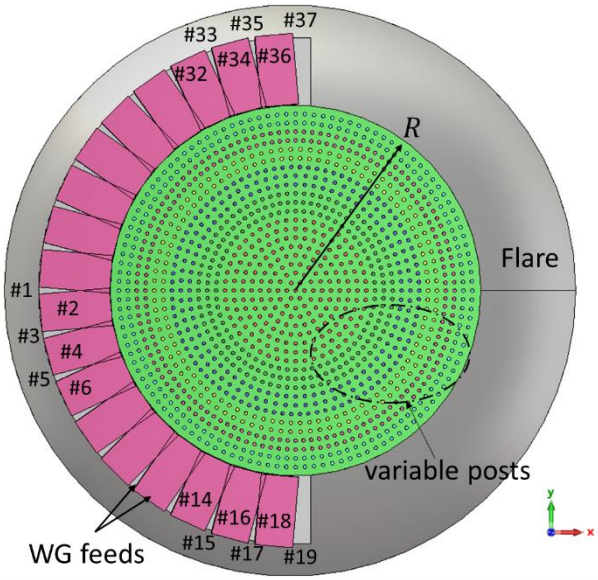

(c)

Figure 6.35: (a) 2D schematic view of Luneburg lens representing the focal arc and all the waveguide feeds (b) side view (c) top view.

6.11.3.1 S-Parameters

Figure 6.36 and Figure 6.37 demonstrate the reflection coefficients and the isolation performances among 1-37 waveguide feeding ports of the proposed Luneburg lens antenna. In the range of 250-350 GHz frequency band, the return loss and the mutual coupling are lower than -10 dB, except for the edge feeding ports of the lens.

A. Matching

The reflection coefficient for the proposed beam steering Luneburg lens antenna is presented in Figure 6.36. It is shown that reflection coefficients are all below -10 dB from 250 GHz to 330 GHz for feeding ports 1 to 8, except for the reflection coefficients for the edge feeding ports **of the bottom lens** (15,17,19,33,35, and 37) and the reflection coefficients for the edge feeding ports **of the top lens** (14, 16,18, 32, 34, and 36). The proposed beam steering Luneburg lens antenna has a wide bandwidth of 80 GHz (250-330 GHz).

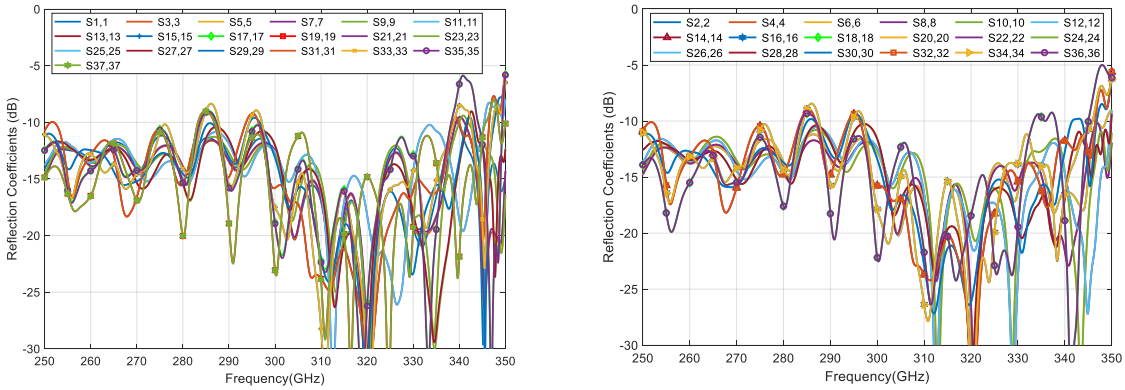

(a) (b)

Figure 6.36: Computed reflection coefficients (Sii) of the feeding port from (a) odd-numbered (1-37) a bottom lens and (b) even-numbered (2-36) top lens for the proposed beam-steering antenna.

B. Isolation

Figure 6.37 illustrates the mutual coupling coefficients between feeding port 1 and other feeding ports. It is shown that the mutual coupling coefficients between the testing ports are all below -20 dB from 250 GHz to 340 GHz for the proposed beam-steering lens antenna, except the mutual coupling coefficients for the edge feeding ports **of the bottom lens** (15,17,19,33,35, and 37) and the reflection coefficients for the edge feeding ports **of the top lens** (14, 16,18, 32, 34, and 36). The excellent isolation performance is presented between the waveguide feeding ports.

Bottom Lens:

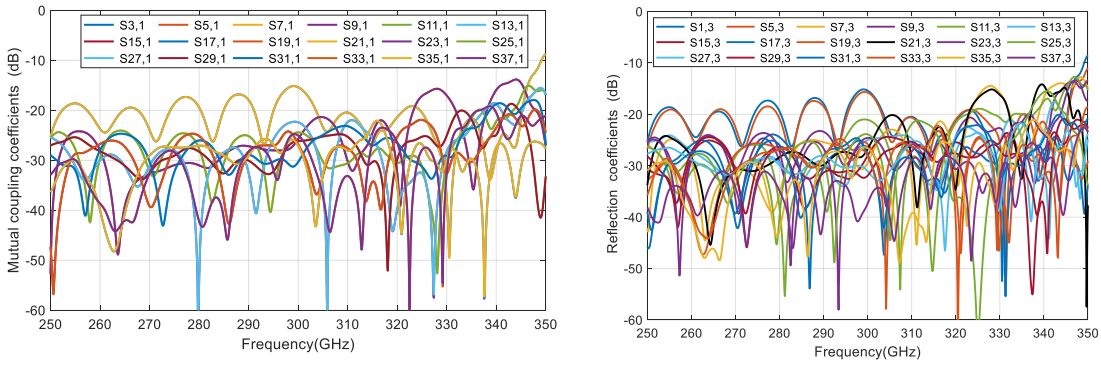

(a) (b)

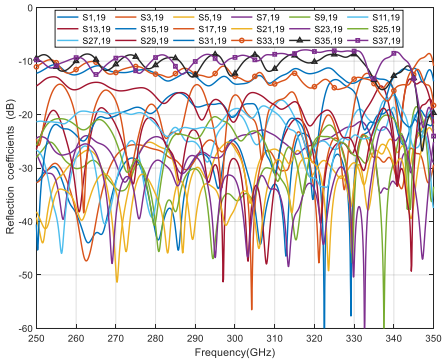

(c)

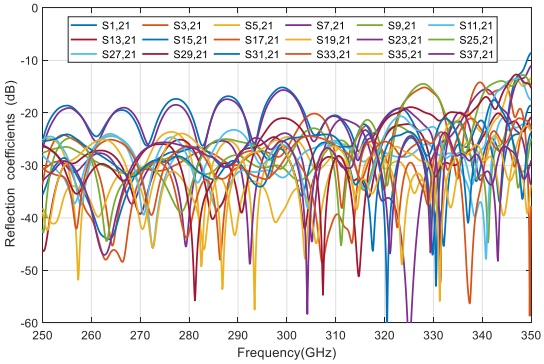

(d)

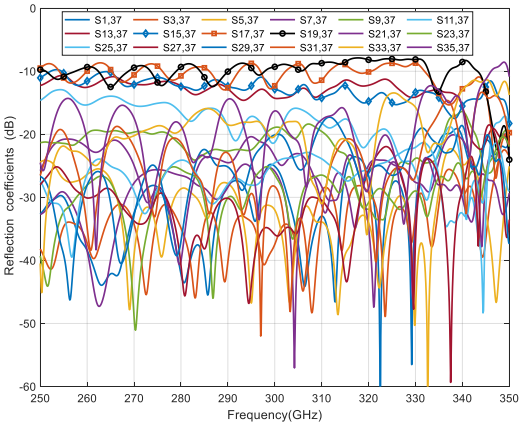

(e)

Top Lens:

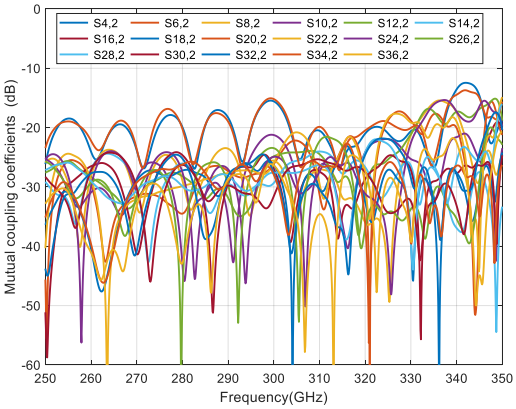

(a)

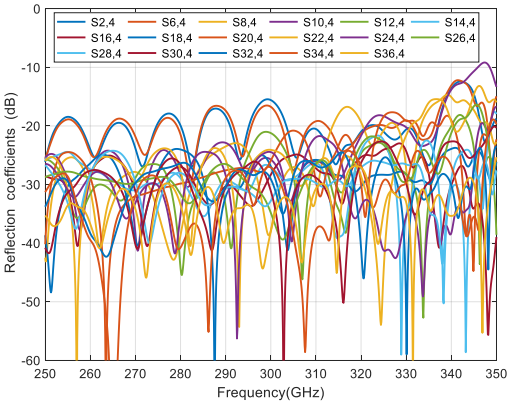

(b)

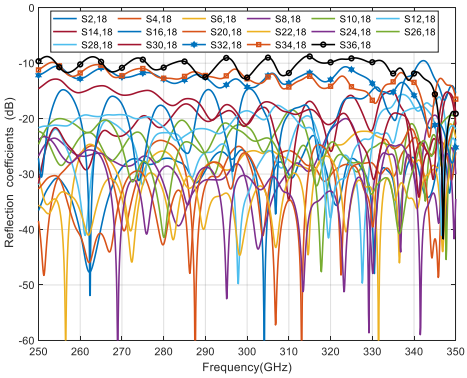

(c)

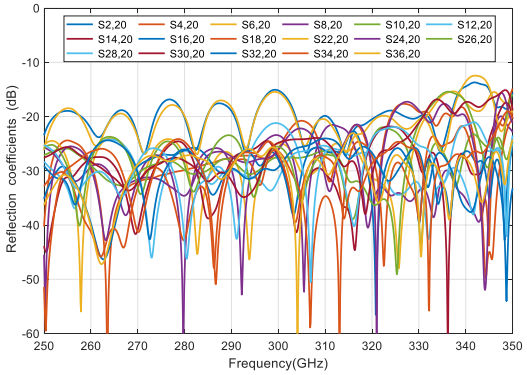

(d)

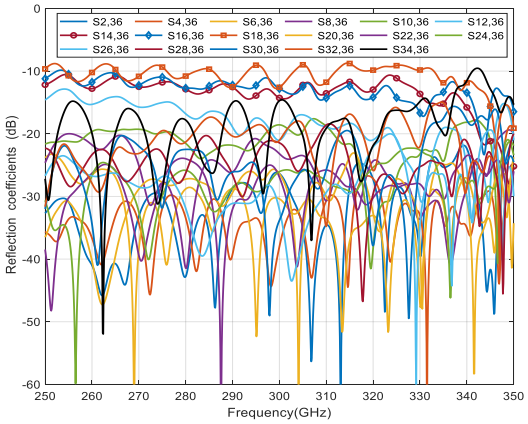

(e)

Figure 6.37: Mutual coupling coefficients among multiple feeding ports for the proposed beam steering metallic lens.

6.11.3.2 H-plane Radiation Pattern

The adjacent spacing of the feeders is designed to be 5°, to achieve a 3-dB overlap between contiguous beams. Therefore, the beam angles include 0°, ±5°, ±10°, ±15°, ±20°, ±25°, ±30°, ±35°, ±40°, ±45°, ±50°, ±55°, ±60°, ±65°, ±70°, ±75°, ±80°, ±85°, ±90° and the radiation patterns at different typical frequencies are illustrated in Figure 6.38. The maximum gain ranges approximately from 22.6 dB at 290 GHz to 18 dB at 330 GHz. High directive beams are achieved with 3 dB overlap and a wide field of view up to ±65◦. Considering the relative effective refractive index dispersion and the mismatch in the higher band, the scan loss is higher than 4.6 dB, at different typical frequencies as shown in Figure 6.39.

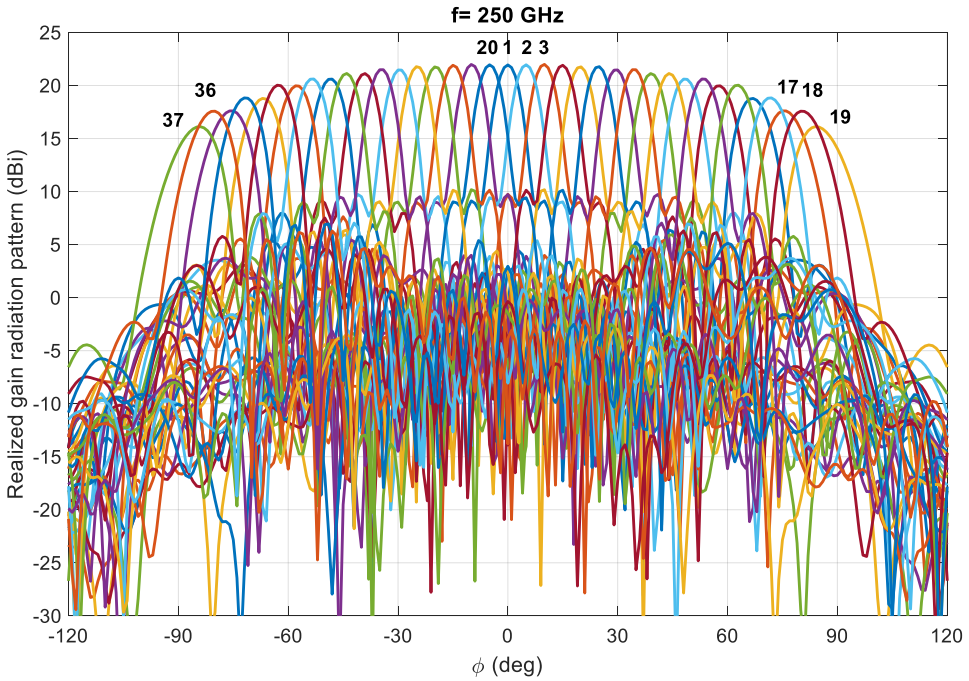
f= 250 GHz
20 1 2 3
36
37
17 18
19
Realized gain radiation pattern (dBi)
ϕ (deg)

(a)

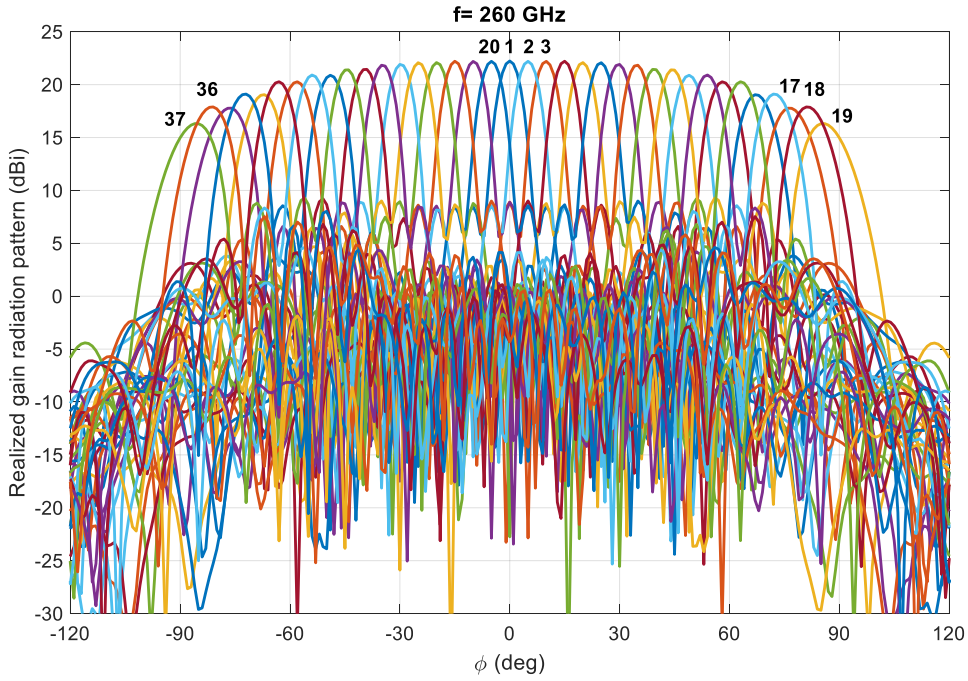
f= 260 GHz
20 1 2 3
36
37
17 18
19
Realized gain radiation pattern (dBi)
ϕ (deg)

(b)

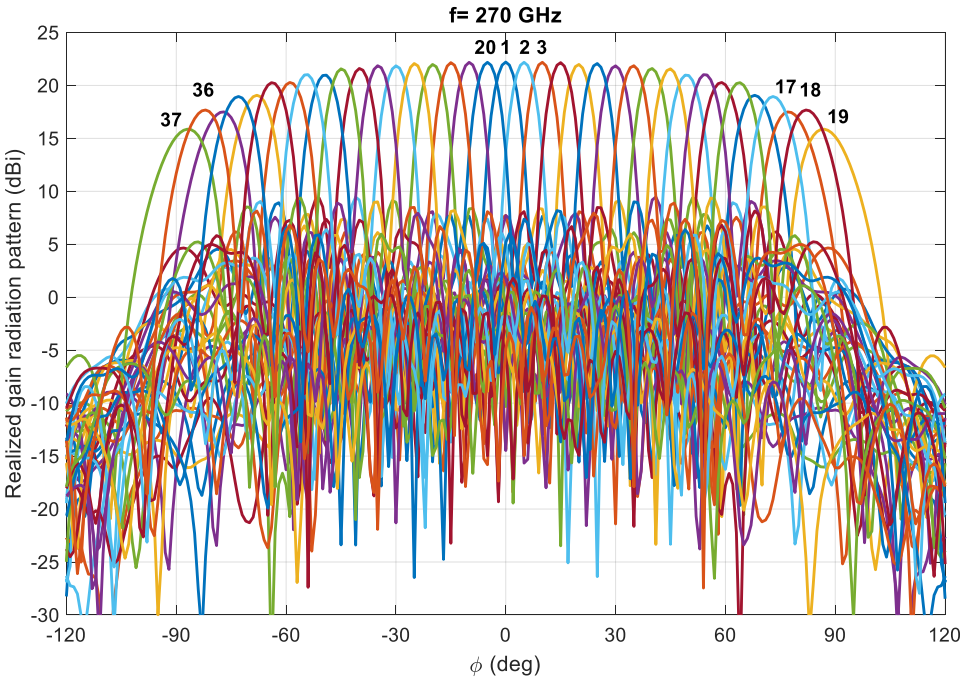
f= 270 GHz
20 1 2 3
36
37
17 18
19
Realized gain radiation pattern (dBi)
25
20
15
10
5
0
-5
-10
-15
-20
-25
-30
-120
-90
-60
-30
0
30
60
90
120
ϕ (deg)

(c)

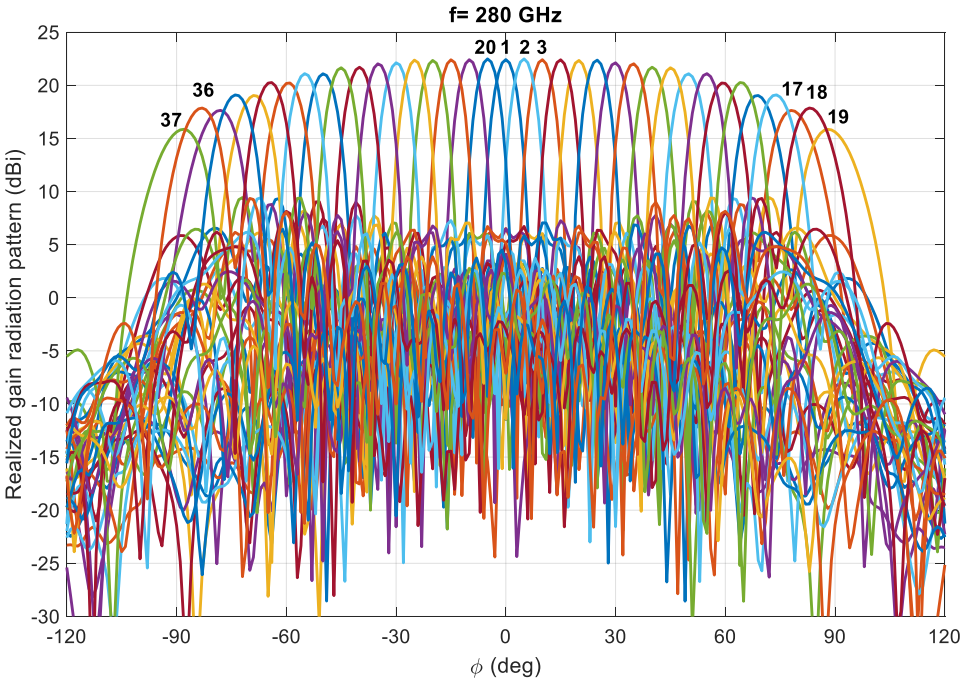
f= 280 GHz
20 1 2 3
36
37
17 18
19
Realized gain radiation pattern (dBi)
25
20
15
10
5
0
-5
-10
-15
-20
-25
-30
-120
-90
-60
-30
0
30
60
90
120
ϕ (deg)

(d)

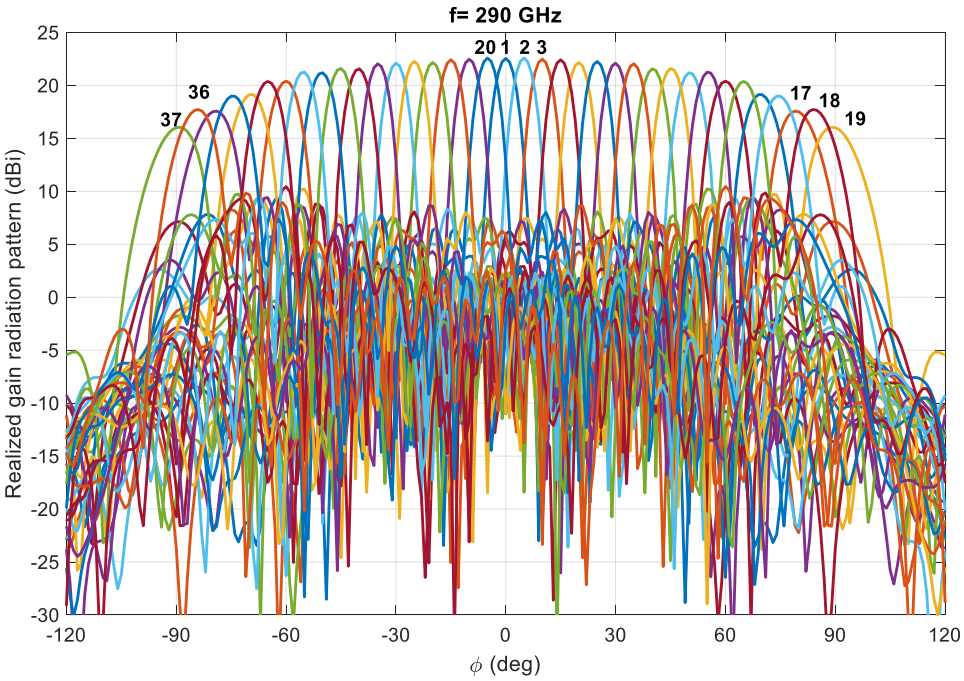
f= 290 GHz
20 1 2 3
36
37
17 18
19
Realized gain radiation pattern (dBi)
25
20
15
10
5
0
-5
-10
-15
-20
-25
-30
-120
-90
-60
-30
0
30
60
90
120
ϕ (deg)

(e)

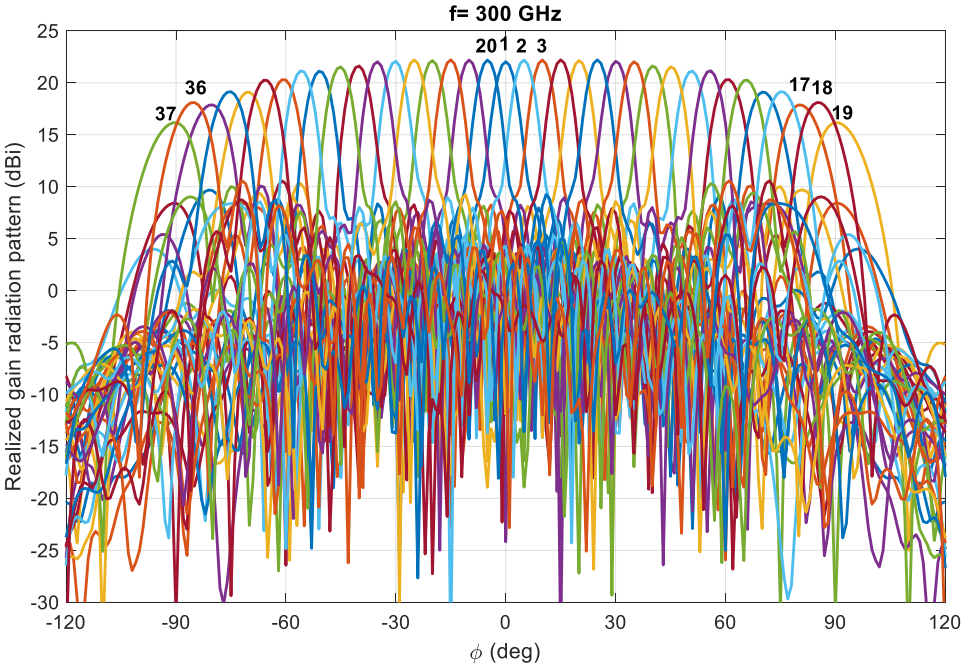
f= 300 GHz
20 1 2 3
36
37
17 18
19
Realized gain radiation pattern (dBi)
25
20
15
10
5
0
-5
-10
-15
-20
-25
-30
-120
-90
-60
-30
0
30
60
90
120
ϕ (deg)

(f)

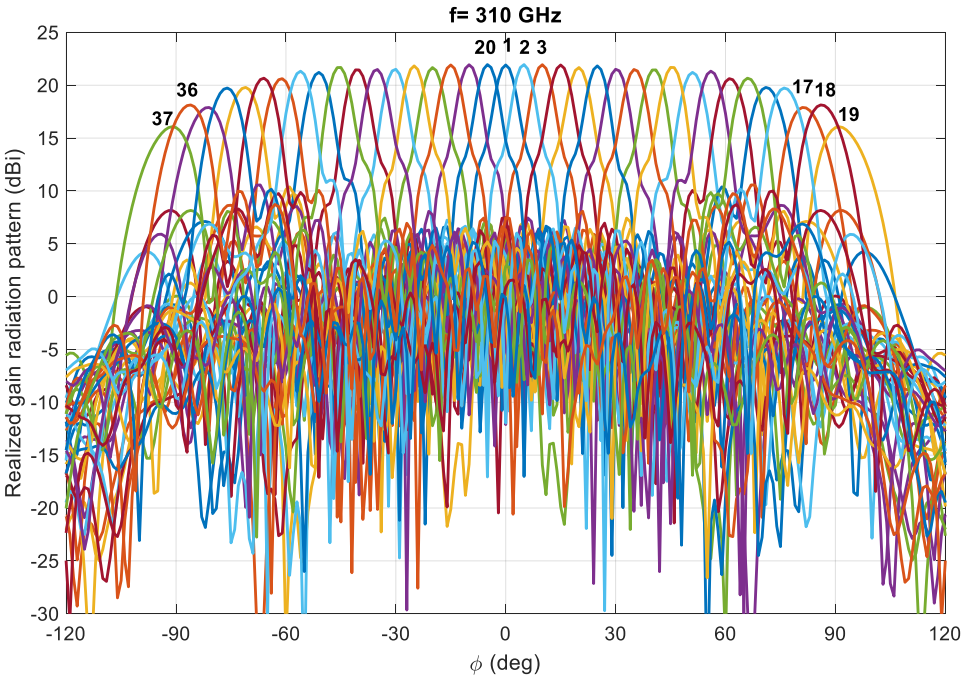

(g)

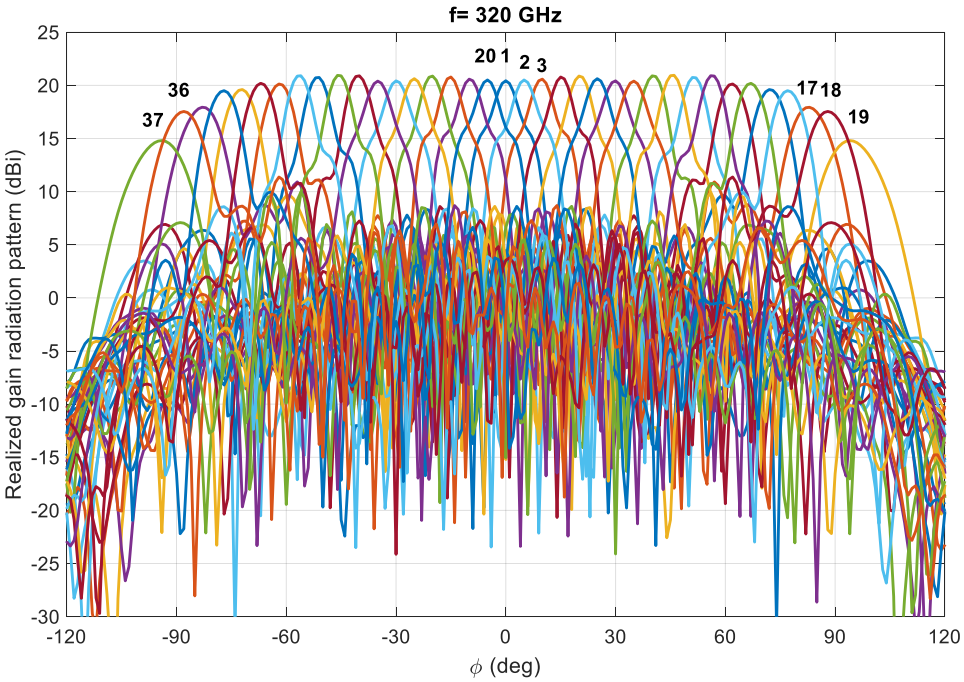

(h)

Figure 6.38: H-plane Radiation Patterns at different frequencies.

6.11.3.3 Maximum Realized Gain and Beam Direction

Figure 6.39 shows the maximum realized gain over frequency for the bottom and top lenses. It better shows the decrease of maximum gain with the scanning angle of the feed in the targeted bandwidth. Figure 6.39 illustrates the computed gain with different scanning angles for the proposed beam-steering lens antenna. It can be observed that the maximum gain reaches 22.6 dBi at 290 GHz.

Meanwhile, the computed overlapping 3-dB gain radiation patterns of all scanning angles are from 250 GHz to 310 GHz for the beam steering lens antenna loaded with variable metallic posts as shown in Figure 6.38.

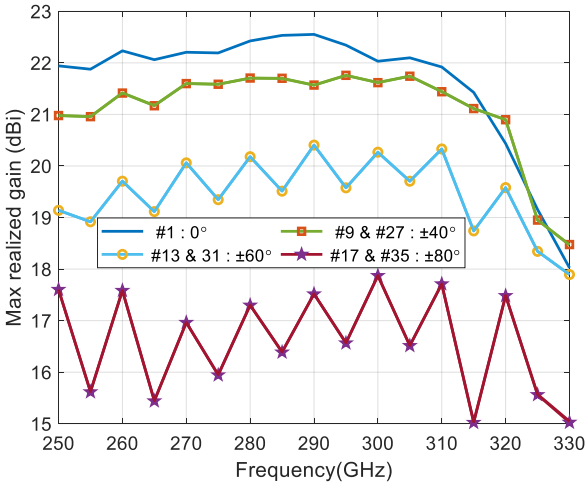

(a)

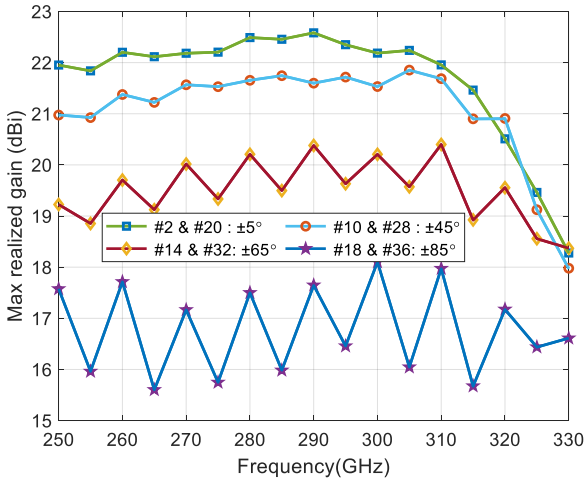

(b)

Figure 6.39: Computed maximum realized gain (a) bottom lens and (b) top lens.

Figure 6.40 reports the simulated total efficiency of the broadside beam over the frequency range of 250–330 GHz. The simulated total efficiency ranges from 50% to 95% over the whole operating frequency range.

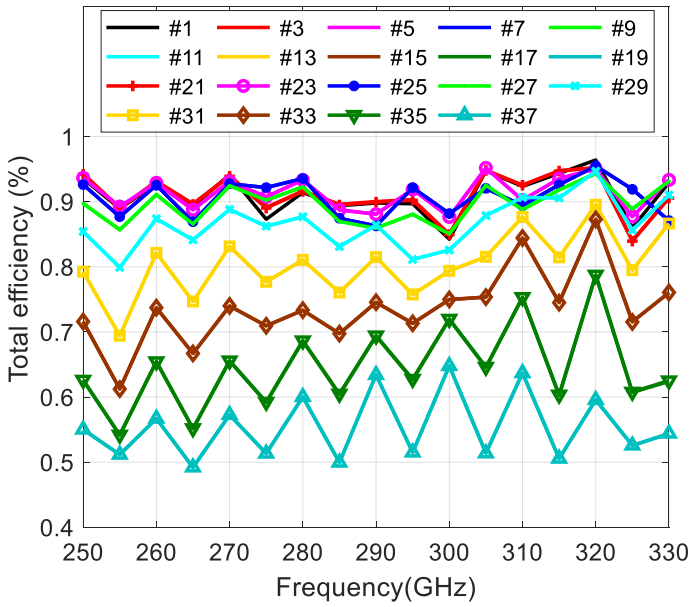

(a)

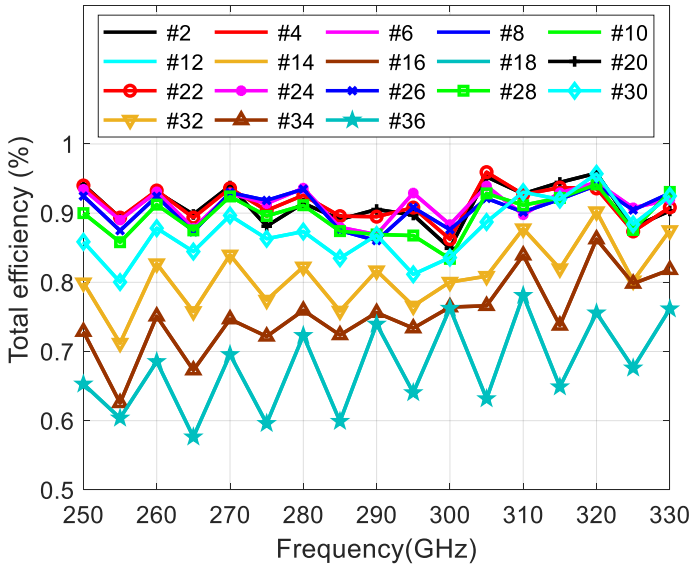

(b)

Figure 6.40: The total efficiency of (a) 19-beams for the bottom lens antenna and (b)18-beams for the top lens antenna.

The most important result of this study is to verify the direction of the main lobe. As illustrated in Figure 6.41(a) for the bottom lens, the computed direction of the main lobe for each feed is correct with an error lower than 5° for the edges feeds 13, 15, 17, 19, 31, 33, 35, and 37.

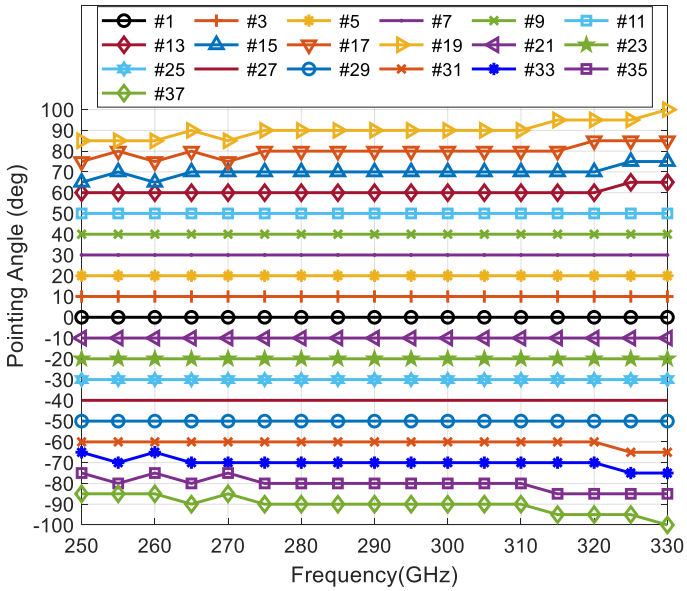

(a)

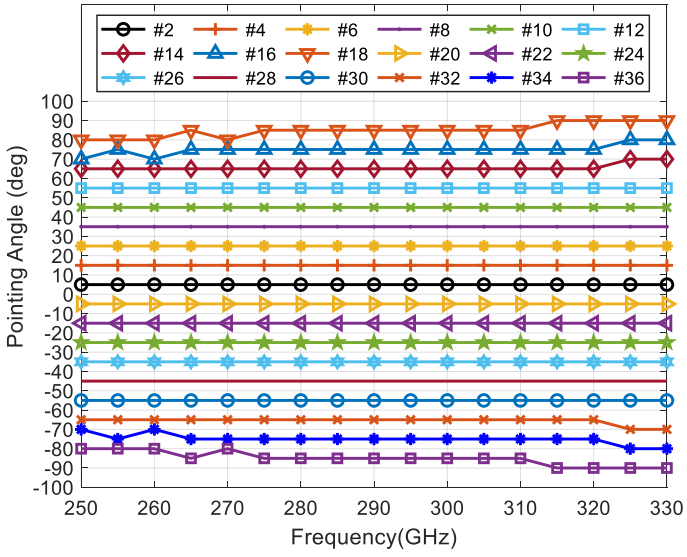

(b)

Figure 6.41: Computed H-plane main lobes direction of (a) 19-beams for bottom lens antenna and (b)18-beams for top lens antenna.

The peak gains for each port of the bottom lens at 290 GHz are given in Table 6.6(a). The outermost ports, numbers 37 and 19 both show a gain of 16 dBi, while the highest gain is for port one with a gain of 22.6 dBi. The beam widths of each port are shown in Table 6.6, where the widest beamwidth is 12.2° and the narrowest 5.9°. Similar behavior for the top lens is noted as shown in Table 6.6(b).

Table 6.6: Beam widths and peak gain for the 37 individual ports of the beam scanning Luneburg lens antenna loaded with variable posts (a) bottom, (b) top lenses.

Port #	1	21/3	23/5	25/7	27/9	29/11	31/13	33/15	35/17	37/19
main direction	0°	±10°	±20°	±30°	±40°	±50°	±60°	±70°	±80°	±90°
HPBW	5.9°	5.9°	6.1°	6°	6.5°	6.9°	7.8°	9°	10.6°	12.2°
Gain (dBi)	**22.6**	**22.5**	**22.2**	**22.1**	**21.6**	**21.2**	**20.4**	**19.1**	**17.6**	**16**
SLL (dB)	-16	-15.3	-14.6	-13.8	-12.8	-12	-13.3	-11.3	-8.2	-5.8

(a)

Port #	2/20	4/22	6/24	8/26	10/28	12/30	14/32	16/34	18/36
main direction	±5°	±15°	±25°	±35°	±45°	±55°	±65°	±75°	±85°
HPBW	5.9	5.9°	5.9	6.1°	6.6°	6.9°	7.8°	9.1°	10°
Gain (dBi)	**22.6**	**22.4**	**22.3**	**22**	**21.6**	**21.3**	**20.4**	**19**	**17.7**
SLL (dB)	-15.4	-16.1	-14.3	-13.4	-12.8	-12	-12.6	-11.6	-7.3

(b)

6.11.3.4 E-Field Distribution

Figure 6.42 shows the E-field distribution inside the proposed metallic Luneburg lens (LL) at 300 GHz when different feed angular positions are exciting. From Figure 6.42 (a), it is seen that the proposed LL can transform a spherical wavefront into a planar one. Figure 6.42 (a) and (b) show the E-field distribution of the proposed metallic Luneburg lens in (a) H-plane and (b) E-plane when port 1 is excited. It can be observed that the field going out of the feed and entering the lens has cylindrical wavefronts. After going through the lens, the phase fronts

become planar in the diametrically opposite direction of the lens, as expected for a Luneburg lens.

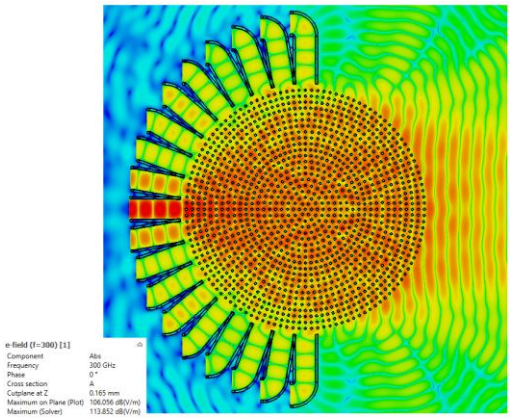

$\theta_{Scan} = 0^{\circ}$

(a)

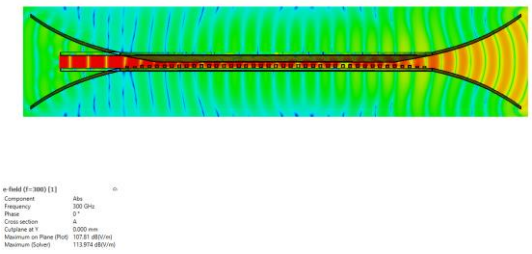

$\theta_{Scan} = 0^{\circ}$

(b)

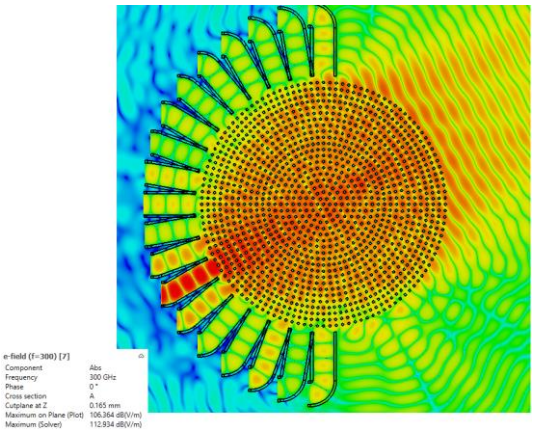

$\theta_{Scan} = 30^{\circ}$

(c)

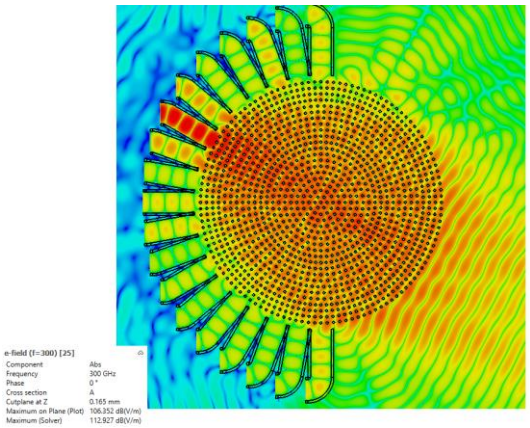

$\theta_{Scan} = -30^{\circ}$

(d)

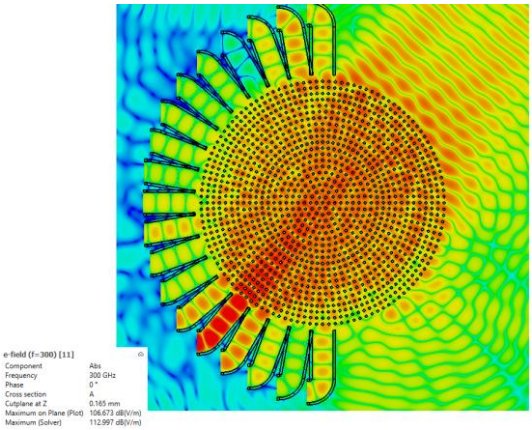

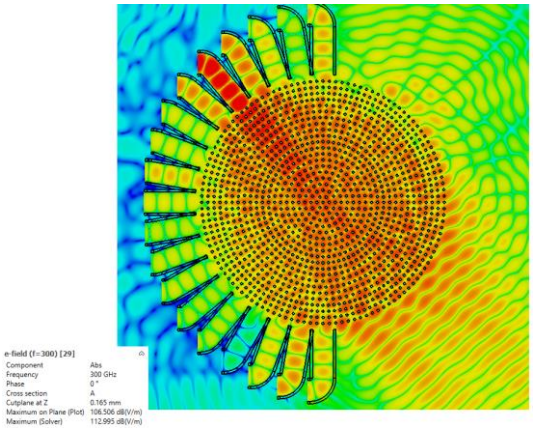

$\theta_{Scan} = 50^{\circ}$

(e)

$\theta_{Scan} = -50^{\circ}$

(f)

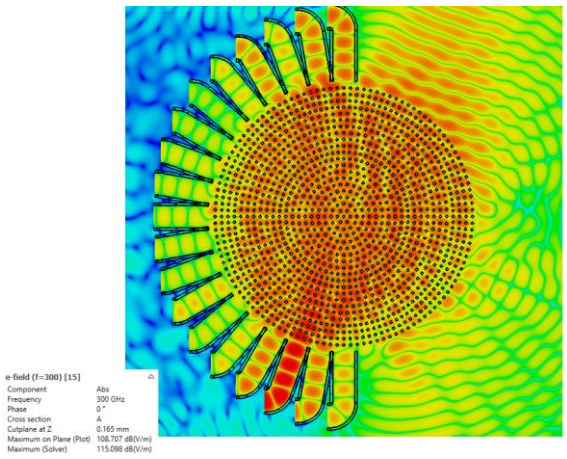

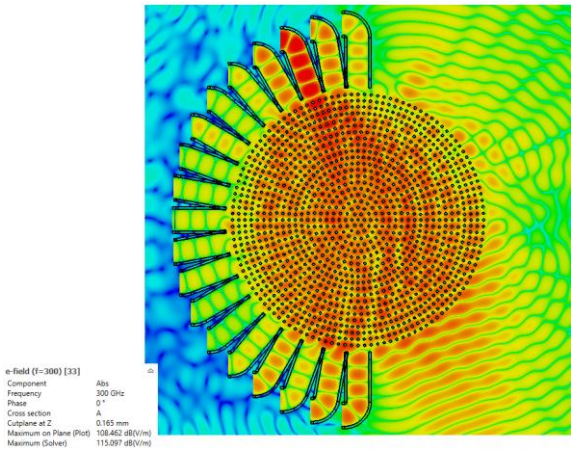

$\theta_{Scan} = 70^{\circ}$

(g)

$\theta_{Scan} = -70^{\circ}$

(h)

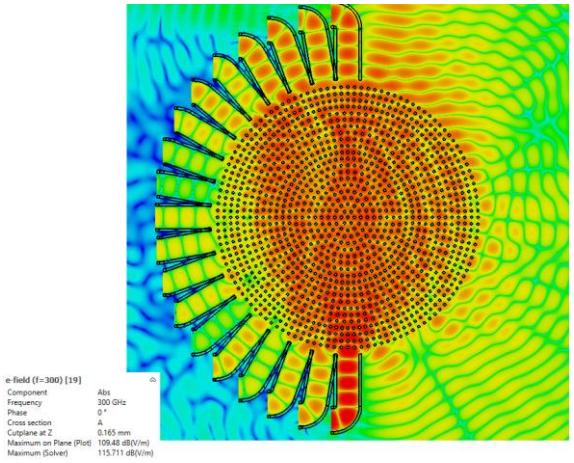

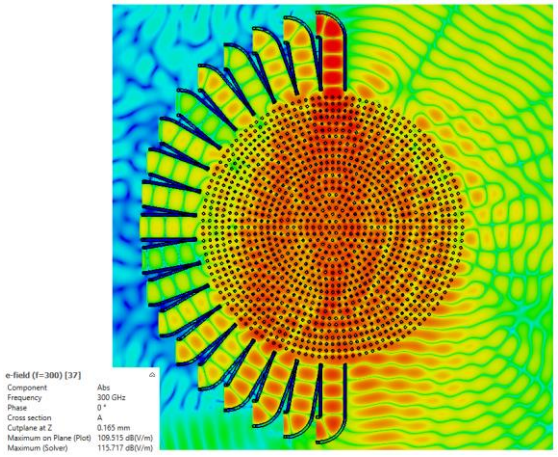

$\theta_{Scan} = 90^{\circ}$

(l)

$\theta_{Scan} = -90^{\circ}$

(m)

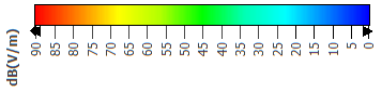

Figure 6.42: 2D E-field distribution of the metallic lens antenna in different feed angular positions.

6.12 Conclusion

In this chapter, a fully metallic sub-THz beam-scanning antenna based on the PPW Luneburg lens is presented. A low loss PPW Luneburg lens antenna realized with different height posts is designed, which operates in the WM-864 band (220-330 GHz), in quasi-TEM mode. The refractive index is mimicked by the continuous variation of metal post thickness. The proposed beam scanning antenna shows narrow beams with a crossover point between two adjacent beams typically 3 dB below the beam peak, due to the novel method of duplicating. However, the variation between different heights of metallic posts is very small and critical in terms of fabrication at 300 GHz, which is less than 5 m . This is increased the costs and the complexity of fabrication at 300 GHz due to the increasing number of masks for variable metallic posts using silicon micromachining technology.

In the next chapter, we will use a uniform size of the metallic post to reduce the costs and the complexity of fabrication at 300 GHz.

In this chapter, a fully metallic PPW Luneburg lens antenna with 37 waveguide feeds of 10.5 λ_0 diameter has been designed at 300 GHz and simulated between 250 GHz and 350 GHz in CST. An angle of view of ±65° has been covered. The simulation results show very good antenna characteristics. The matching level is lower than -10 dB from 250 GHz to 330 GHz excluding the reflection coefficients for the edge feeding ports. Similarly, the isolation level is -20 dB from 250 GHz to 340 GHz, excluding the mutual coupling coefficients for the edge feeding ports. The symmetry of both matching and isolation parameters has been verified. The H-plane radiation patterns confirm that the multiple feeds fully metallic PPW Luneburg lens works perfectly fine as a sub-THz beam-scanning antenna throughout the (250-320 GHz) operating bandwidth. The maximum gain ranges approximately from 18 dB at 330 GHz to 22.6 dB at 290 GHz. The beams point out correct angular directions with a small degree of error at the edged feeding ports. The sidelobe levels are -16 dB below the main beam at 290 GHz. The beam overlap level is 3dB between 250 - 310 GHz**.** The multiple feed configuration of the Luneburg lens antenna shows excellent results.

However, the PPW Luneburg lens antenna with variable metallic post thicknesses needs a high accuracy technology for the fabrication in order to mimic the permittivity values required by the Luneburg law. In the next chapter, an improvement of the PPW Luneburg lens antenna with variable metallic post thicknesses, resolving these issues, is developed.

Chapter 7 Metallic Lens Based on Parallel-Plate Loaded with Uniform Posts

7.1 Introduction

In this chapter, a metallic Luneburg lens antenna based on a parallel-plate waveguide loaded with uniform equal size posts is designed and analyzed. The proposed lens has a uniform thickness of metallic posts as compared to variable heights that have been proposed in the previous chapter, which means that the manufacturing tolerance is increased, making ease of manufacture at 300 GHz.

7.2 Unit-cell Design

As the theory in [54], the period $p \ll \lambda$ and the width of post $2r \leq p/2$. To support the guiding waves, the height of the post should meet the condition $h_p < \lambda/4$. For 300 GHz band, considering the manufacturing difficulty, we determine that $2r$ = 0.1 mm and p = 0.25 mm.

7.2.1 Unit cell Geometry and Parameters

The realization of the artificial Luneburg lens is based on an array of isotropic unit cells. It is known that a PPW loaded with a cylindrical post can be treated as an isotropic unit-cell which is shown in Figure 7.1. For each unit, the period is determined by p and the post size is determined by $2r$ and h_p. The required refractive indices following Luneburg's law are obtained by changing the height of the gap ''g'' between the top of the post and the top plate.

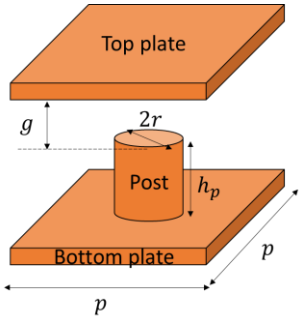

Figure 7.1: Schematic of a unit cell.

7.2.2 Determination of air gap height ‘‘g’’ and metallic post thickness ‘‘h_p’’

The unit cell with the required effective refractive index is designed by eigenmode simulation and dispersion diagram analysis. The first mode, quasi-TEM mode, is excited in the proposed lens. To illustrate the characteristics of the selected unit cells, the dispersion diagrams and effective refractive indices of the periodic structures with different ‘‘g’’and h_p, are given in Figure 7.2 and Figure 7.3, where 2r = 0.1 mm and p = 0.25 mm.

Figure 7.2 shows the dispersion diagrams of the unit-cell for three configurations, i.e. for three values of h_p . For each value of hp, g/hp varies from 0.2 to 1.5 by 0.1 step. The line of light is also plotted. The determination of hp is related to the realization ability of an effective refractive index.

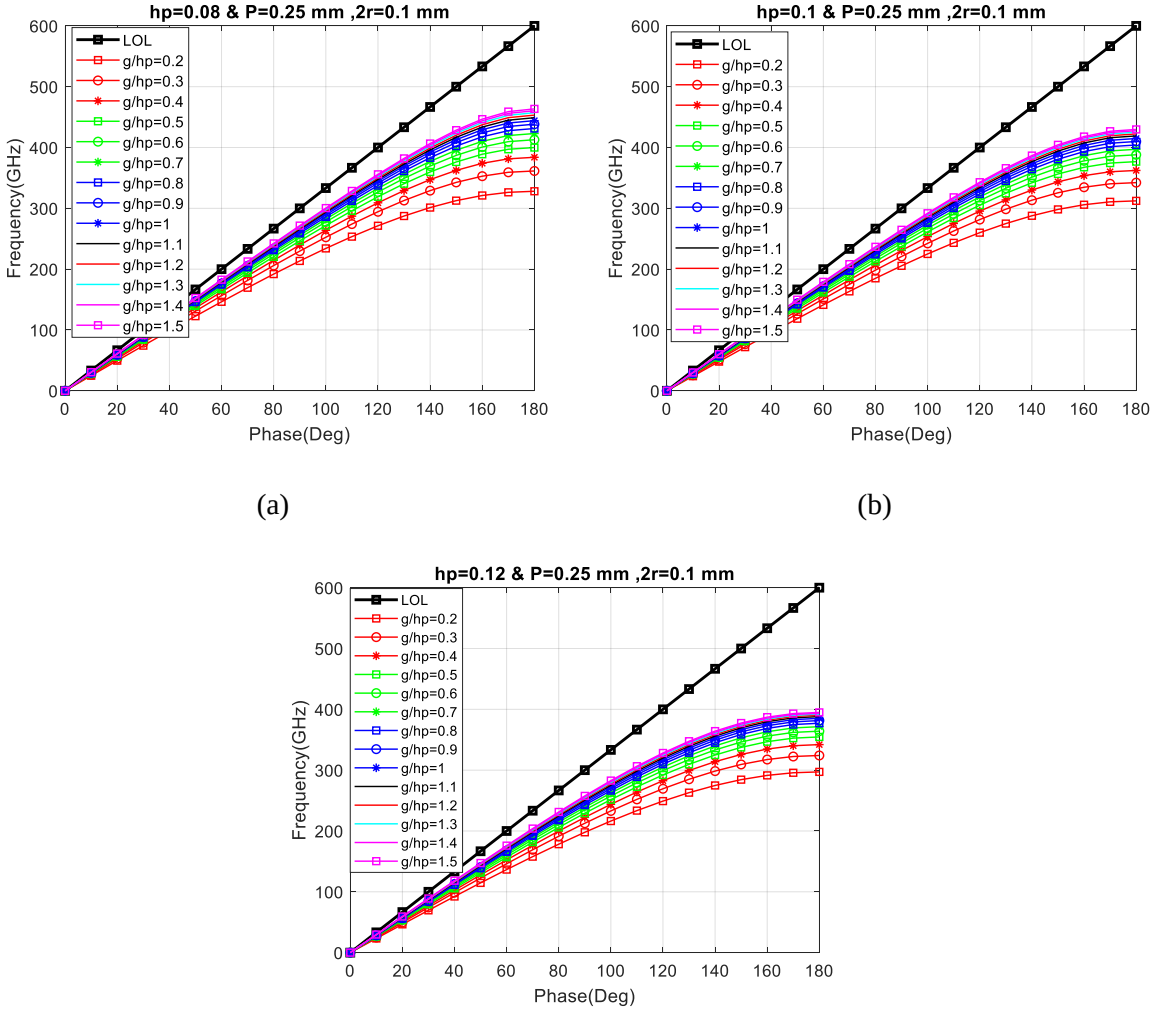

Figure 7.2: Unit cell parametric simulations dispersion diagrams. p = 0.25 mm, 2r= 0.1 mm, g/hp as variable and ’LoL’ the line of light.

To illustrate the effect of h_p on the refractive index, the index curves corresponding to h_p = 0.08, 0.1, and 0.12 mm are simulated and plotted in Figure 7.3, where g/h_p varies from 0.2 to 1.5 by 0.1 step.

As seen, with the changing of 'g', the characteristics of the designed unit-cells can approximately cover the refractive index requirements of the Luneburg lens. With the decrease in ''g'' and the increase in the equivalent refractive index, the dispersion becomes more obvious. However, it is worth noting that, compared with that at frequencies higher than 350 GHz, the variations in the effective refractive index within the (220 -320 GHz) band are relatively gentle. For instance, when g/hp = 0.3 mm, the effective refractive index varies from 1.302 to 1.401 in the 300 GHz band (220 -320 GHz) and can meet the requirement of the Luneburg lens, despite the deviation from the ideal Luneburg's law.

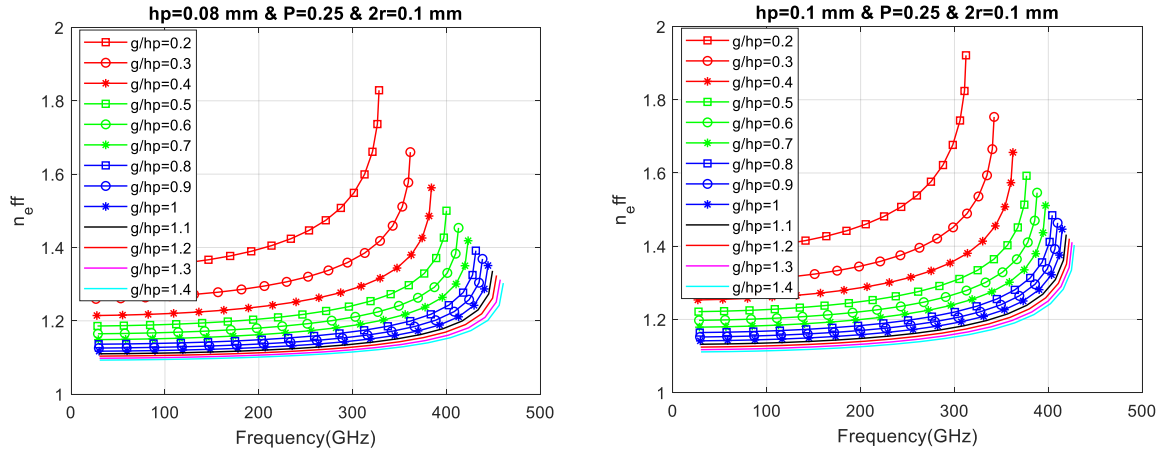

(a) (b)

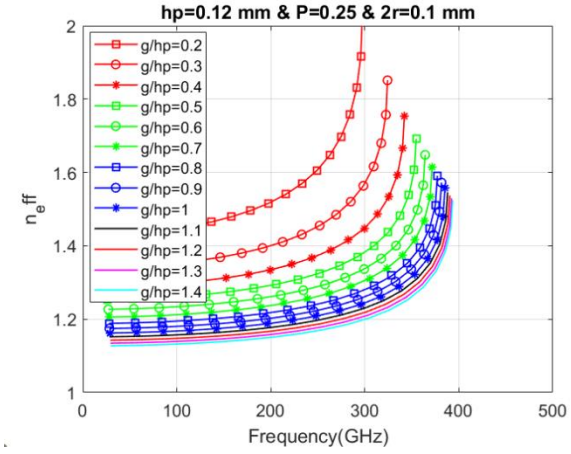

(c)

Figure 7.3: Unit cell parametric simulations: n_{eff} versus frequency, g/hp as variable for different h_p.

As seen in Figure 7.2 and Figure 7.3, the effective refractive index can be adjusted only by changing h_p or g. Compared with g, h_p is a more sensitive parameter which is not suitable to be used to control the refractive index precisely. Thus, the gradient refractive indices are realized by only changing g in this work. Besides, the increase of h_p makes the refractive index show more obvious dispersion and change with frequency more sharply as shown in Figure 7.3(c). But the decrease of h_p requires a narrower g to maintain the same equivalent refractive index as before.

So in order to ensure the g is not too narrow and the dispersion is acceptable in 300 GHz band when the refractive index gets close to 1.41 (the highest refractive index in the Luneburg lens), the h_p is determined to be 0.1 mm as shown in Figure 7.3(b). According to the above analysis, it can be seen that, different equivalent refractive indices for the design of the Luneburg lens could be realized by the almost-PPW loaded with uniform metallic posts which are easy to fabricate.

To observe the broadband properties, we also give the index profiles at 280, 290, 300, 310, and 320 GHz as shown in Figure 7.4. The results indicate that non-the dispersive behavior is obvious in the configuration in Figure 7.4. For the tradeoff between the manufacturing process and dispersive properties, we select the configuration as shown in Figure 7.4(b).

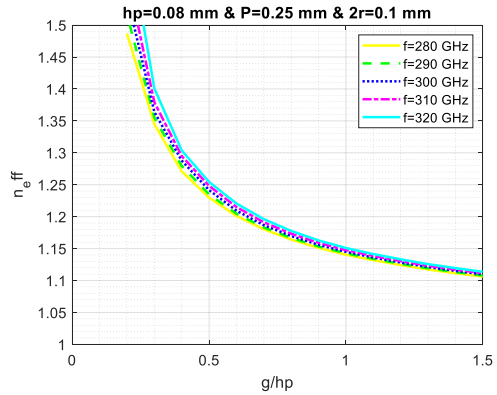

(a)

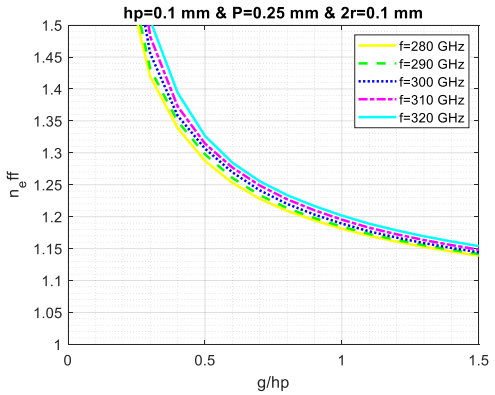

(b)

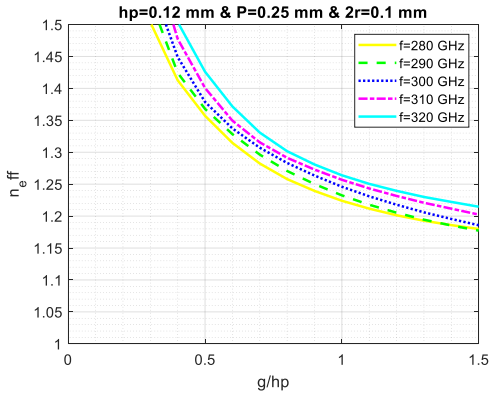

(c)

Figure 7.4: Unit cell parametric simulations: n_{eff} versus g/hp, frequency as variable.

There is no need for much proof to say now that the uniform metallic post suits best the lens center and around, but certainly not the lens periphery, where the refractive index is approximately equal to or lower than 1.1 as shown in Figure 7.4.

For hp = 0.1 mm and p = 0.25 mm and $2r$ = 0.1 mm, we deduced the value of gap g according to Luneburg lens law from Figure 7.4(b) as shown in Table 7.1.

Table 7.1: Design parameters of metallic Luneburg lens with uniform posts.

radius	n_{eff}	g/h_p(mm)	g (mm)	Δg (μm)
r_1	1.39	0.3671	0.03671	36.71
r_2	1.3	0.517	0.0517	14.99
r_3	1.2733	0.59	0.06	8.3
r_4	1.2	0.92	0.092	32
r_5	1.145	1.5	0.15	58
r_6	1.072	>1.5	0.332	182

7.3 Metallic Antenna Design: Lens, Flare, and Feed

7.3.1 Introduction

In this section, the desired profile of the effective refractive index is realized by the almost-PPW with a curved top plate and a planar bottom plate loaded with uniform metallic posts. The uniform metallic posts between the parallel plates can be treated as a kind of periodic structure, whose unit cell is shown in Figure 7.1. The different effective refractive indices are achieved

only by changing g, the air gap between the top of the post and the top plate, with the $2r$, h_p , and p remaining unchanged.

7.3.2 Uniform Metallic Posts

The quasi-Luneburg lens consists of an almost-PPW with a curved top plate and an array of uniform metallic posts loaded on the bottom plate. Based on the unit cells with required effective refractive indices, we can form the Luneburg lens. The radius of the Luneburg lens R, is determined to be 5.25 mm. The periodic posts of the unit cells are all the same size: 2r = 0.1 mm, hp = 0.1 mm, and p = 0.25 mm. Particularly, the heights of the gaps in different areas of the proposed Luneburg lens are arranged by the following method:

First, based on the rotational symmetry of the Luneburg lens, we choose a section across the center of the lens and divide the section into six areas by five points, A, B, C, D, and E, corresponding to different radii of r_A = 2 mm, r_B = 2.94 mm, r_c = 3.57 mm, r_D = 4.1 mm and r_E = 4.62 mm, as shown in Figure 7.5.

Second, the expected effective refractive indices in the points A, B, C, D, and E are computed according to Luneburg's law.

Third, the heights of the gaps in A, B, C, D, and E (g_A, g_B, g_C, g_D and g_E) are determined based on the relationship between the effective refractive index and ''g'' as shown in Table 7.1. Especially, the ''g'' in the point O, g_O, is equal to g_A, and the g in the point F, g_F, is selected to match the dimension of the WR-03 waveguide. Thus, the g_O, g_A, g_B, g_C, g_D, g_E and g_F are set as 36.71 μm, 51.7 μm, 60 μm, 92 μm, 150 μ, and 432 μm (the height of WM-864 waveguide), respectively.

Fourth, the heights of the gaps in the other areas are obtained by connecting the points O, A, B, C, D, E and F with straight lines, as shown in Figure 7.5 (b).

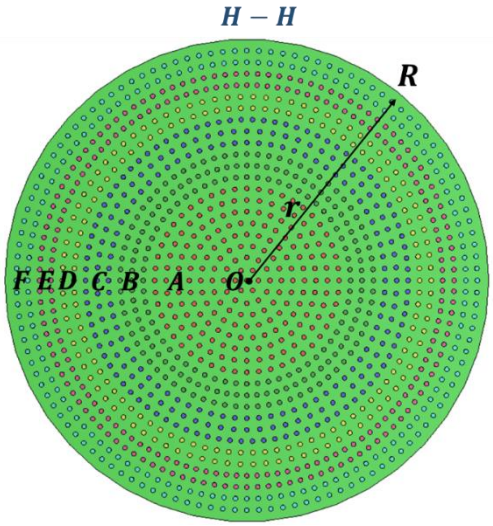

(a)

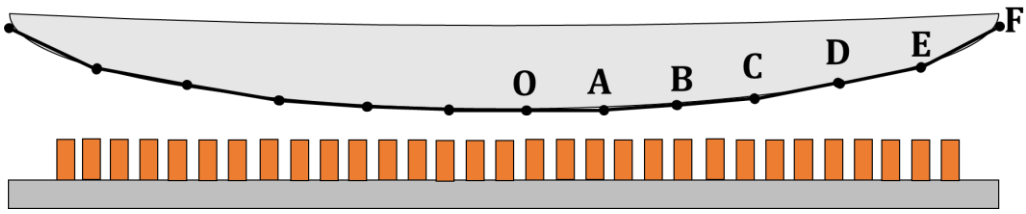

Figure 7.5: (a) Schematic of proposed air-filled Luneburg lens and (b) points determining the profile of the upper plate.

7.3.3 Metallic Luneburg Lens Antenna

The lens consists of a PPW with gradient spacing loaded with periodic uniform cylindrical posts, which can be treated as an array of isotropic sub-wavelength unit-cells with gradient effective refractive indices. The WM-864 waveguides are employed as the input ports. A flare is added to improve the radiation and impedance matching of antenna feeds. Especially, the uniform metallic posts are only placed on the bottom plate, while the top plate is smooth with a curve contour to realize the expected refractive index profiles of the isotropic lens.
The complete proposed air-filled Luneburg lens antenna and its section views are shown in Figure 7.6. The feed point can be changed by moving the waveguide to get different beam directions.

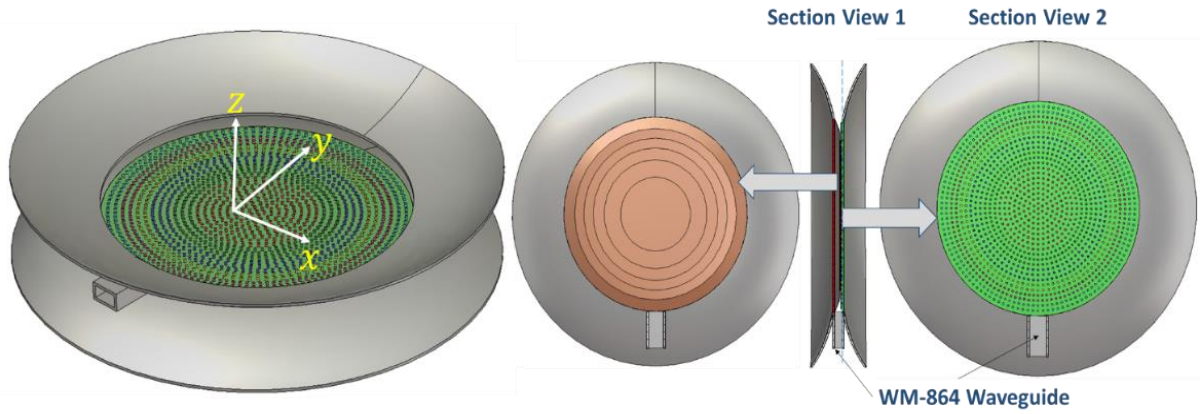

Figure 7.6: Schematic of the Luneburg lens antenna loaded with uniform metallic posts.

7.3.4 Radiation Aperture and Feeder

An expanded PPW with a circular ring profile is added around the Luneburg lens, as the initial radiation aperture. As shown in Figure 7.7, a flare is introduced to adjust the height of the PPW from g_F to 'd' and improve the matching between the radiation aperture and the open space, where d = 3 mm and l = 3 mm.

The rectangular waveguide of WR-03 (WM-864), indicated in Figure 7.7, is applied as the feeder of the proposed Luneburg lens antenna. It is simplified and easy to be integrated. By employing the WR-03 rectangular waveguides as the feeders, the Luneburg lens antennas with a single beam and multiple beams are designed in the whole 300 bands.

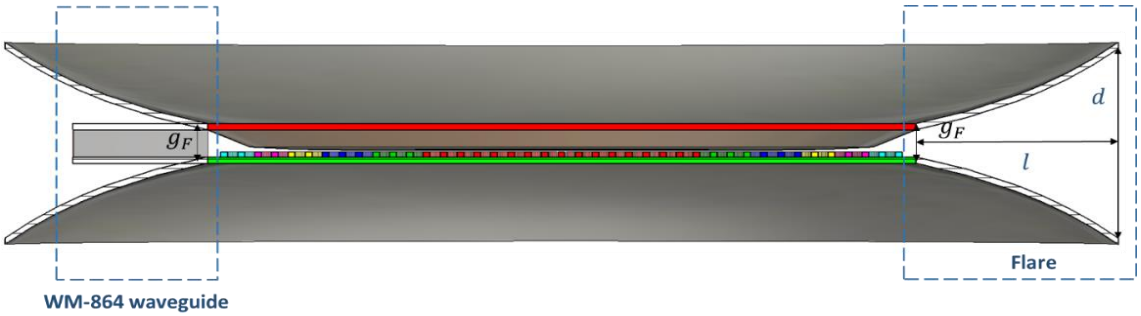

Figure 7.7: Schematic of the feed waveguide and the flare.

7.3.5 Mutlibeam Antenna Integration

Figure 7.8 (a) and (b) show the whole antenna system integrating multiple feeds the lens loaded with uniform metallic posts and the radiation aperture (i.e. flare).

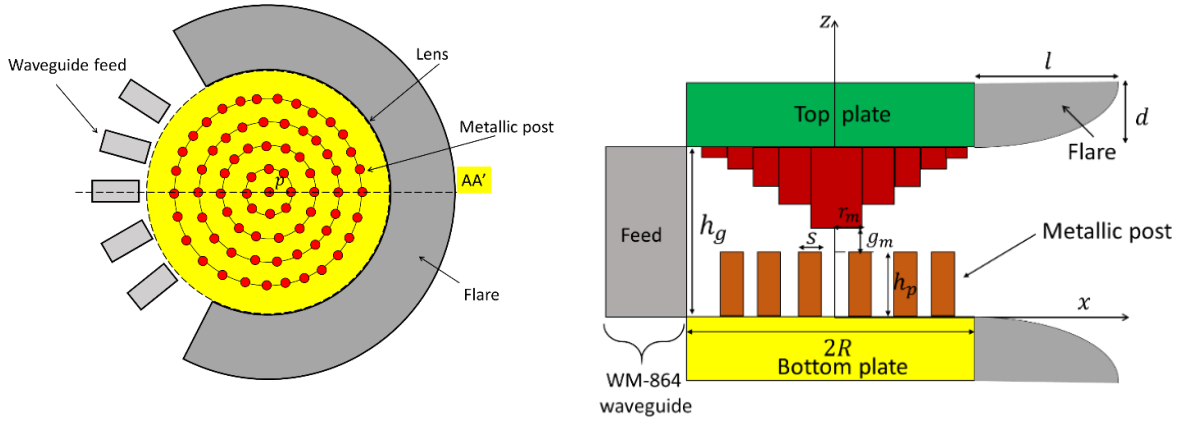

Figure 7.8: (a)Top view (b) section view of the antenna lens structure loaded with uniform metallic posts.

7.4 Metallic Lens Antenna Simulations

7.4.1 Single Feed Configuration

7.4.1.1 S-parameters

To verify the impedance matching performance, the S-parameters have been computed as shown in Figure 7.9. In the range of 250-350 GHz frequency band, the return loss is lower than -10 dB, except for a few frequency points higher than 315 GHz.

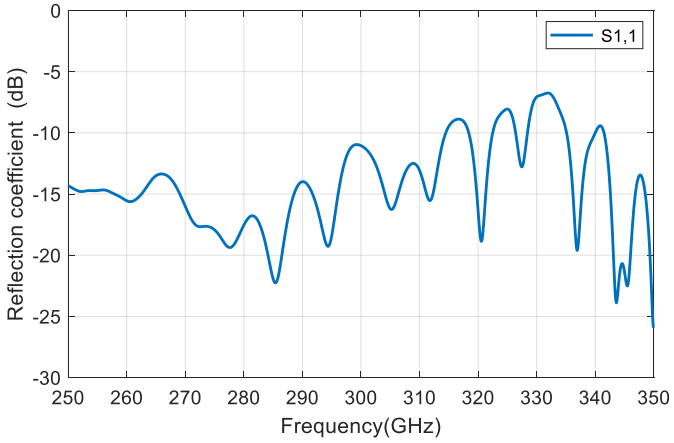

Figure 7.9: Return loss (S11) of 10.5 λ_0 Luneburg lens loaded with uniform metallic posts feed by a standard waveguide.

7.4.1.2 Radiation Pattern

The Luneburg lens antenna beams are all fan beams. The H-plane pattern of the antenna is a narrow beam pattern, as shown in Figure 7.10(a). The 3 dB beamwidth is 5.2° for the H-plane beam at 300 GHz. The E-plane pattern of the metallic Luneburg lens antenna is a wide beam pattern, as shown in Figure 7.10(b). The 3 dB beamwidth is 20.8° for the E-plane beam at 300 GHz. The far-field comparison of five frequencies (270-320 GHz) is presented in Figure 7.10. Detailed performances are listed in Table 7.2. The maximum realized gain is 23.2 dBi at 280 and 290 GHz.

Table 7.2. The H-plane far-field Performance of standard WM-864 integrated with 10.5 λ_0 metallic Luneburg lens loaded with uniform metallic posts .

Frequency (GHz)	270	280	290	300	310	320
Realized gain (dBi)	22.8	23.2	23.2	22.7	22.2	20.7
3dB beamwidth	5.8°	5.7°	5.5°	5.2°	5.4°	6.8°
Side lobe level (dB)	-15.8	-21.1	-18.4	-16.8	-16	-12.7

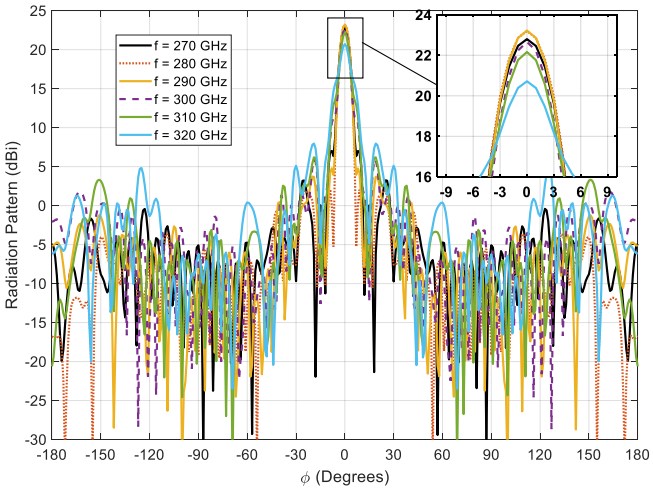

(a)

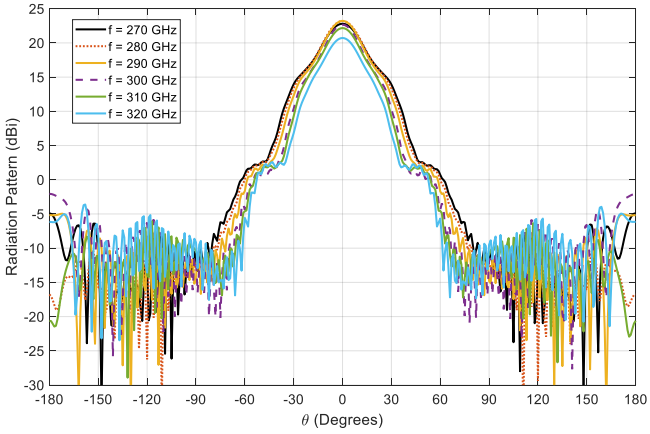

(b)

Figure 7.10: Simulated 2D radiation pattern of standard WM-864 integrated with 10.5λ_0 metallic Luneburg lens antenna loaded with uniform posts in (a) H-plane ($\theta = 90^{\circ}$). (b) E-plane ($\phi = 0^{\circ}$).

7.4.2 Multiple Feeds Configuration

The proposed multi-beam metallic Luneburg lens antenna fed by a standard waveguide (WM-864) was simulated to verify the design. The metallic Luneburg lens antenna loaded with uniform posts with 6 feeds is displayed in Figure 7.11, where a second lens structure has been added as a novel idea to realize the 3dB overlap between the beams. During S-parameter simulation, 6 of the input ports were connected with the WM-864 waveguide. Only one port was excited at one time for testing the radiating performance.

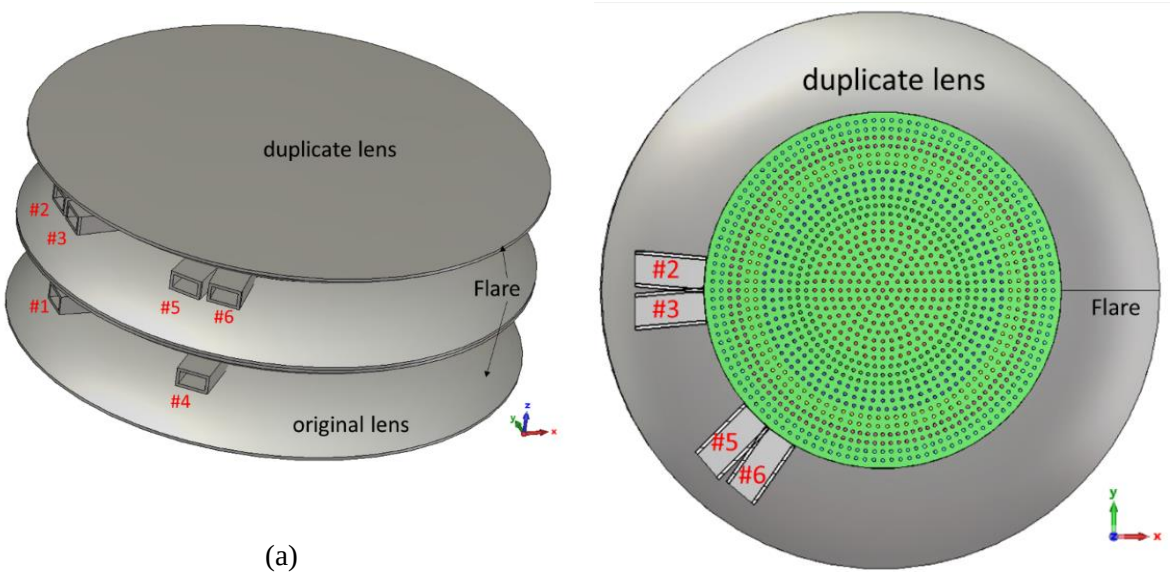

(a)

(b)

Figure 7.11: Geometry of the proposed multi-beam metallic Luneburg lens antenna loaded with uniform posts with multiple feeds. (a) Perspective view. (b) Top cutting view.

7.4.2.1 S-parameters

Simulated reflection coefficients of ports 1, 2, 3, 4, 5, and 6 are given in Figure 7.12. The simulated overlapped impedance bandwidth for the reflection coefficient of less than -10 dB from 250 to 315 GHz. On the other hand, it is seen from Figure 7.13 that the simulated mutual couplings between Port 1 and the other five ports. The simulated mutual coupling between the two adjacent ports, i.e., Ports 2 and 3 is lower than 10 dB throughout the operating band. In addition, simulated |S12 |**,** |S13 |**,** |S14|**,** |S15 | and |S16| are less than -35 dB.

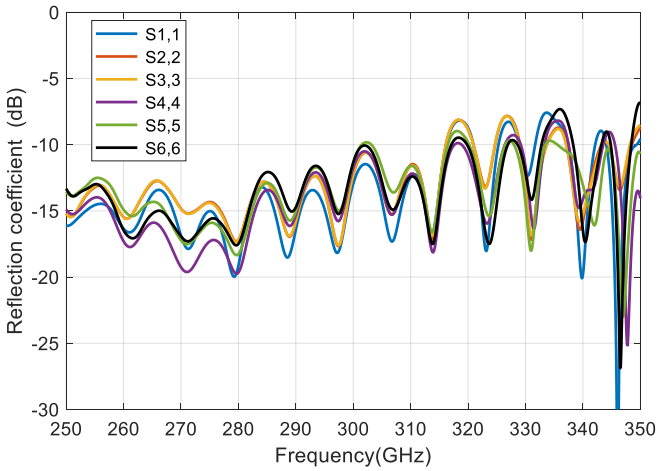

Figure 7.12: Simulated reflection coefficient of the multibeam 10.5 λ Luneburg lens antenna loaded with uniform metallic posts.

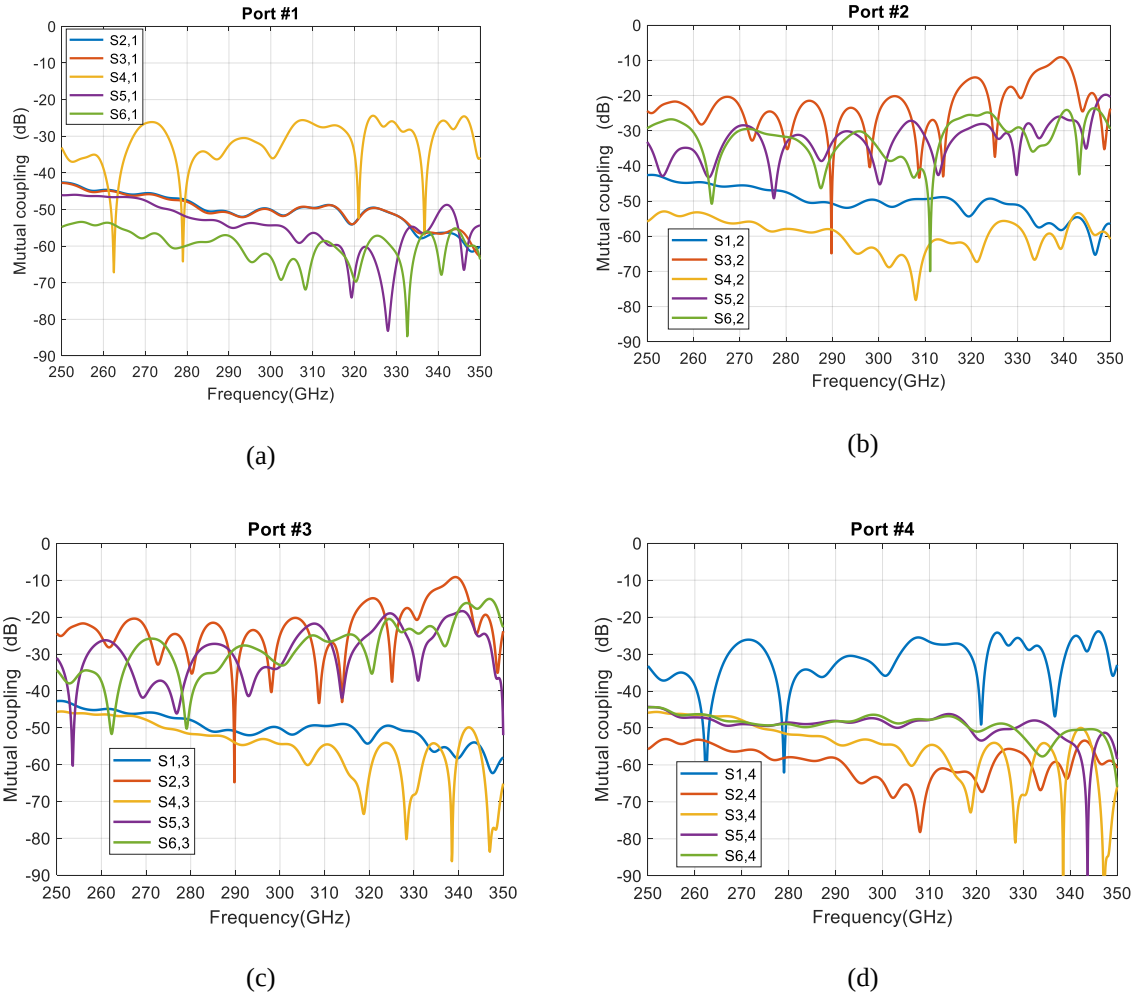

Figure 7.13: Simulated mutual coupling of the multibeam 10.5 λ Luneburg lens antenna loaded with uniform metallic posts.

7.4.2.2 H-plane Radiation Pattern

Beam steering in the H-plane of the Luneburg lens can be observed by feeding different excitations ports from Port#1 (bottom lens) to Port#6 (top lens). The simulated H-plane radiation patterns are shown in Figure 7.14. The beam steering angles for the radiation patterns are -5° , 0°, 5° , 45° , 50° , and 55° for port#1 to port#6, respectively. The HPBW of the radiation patterns is around 5.7° between 270-310 GHz and 6.2° at 320 GHz.

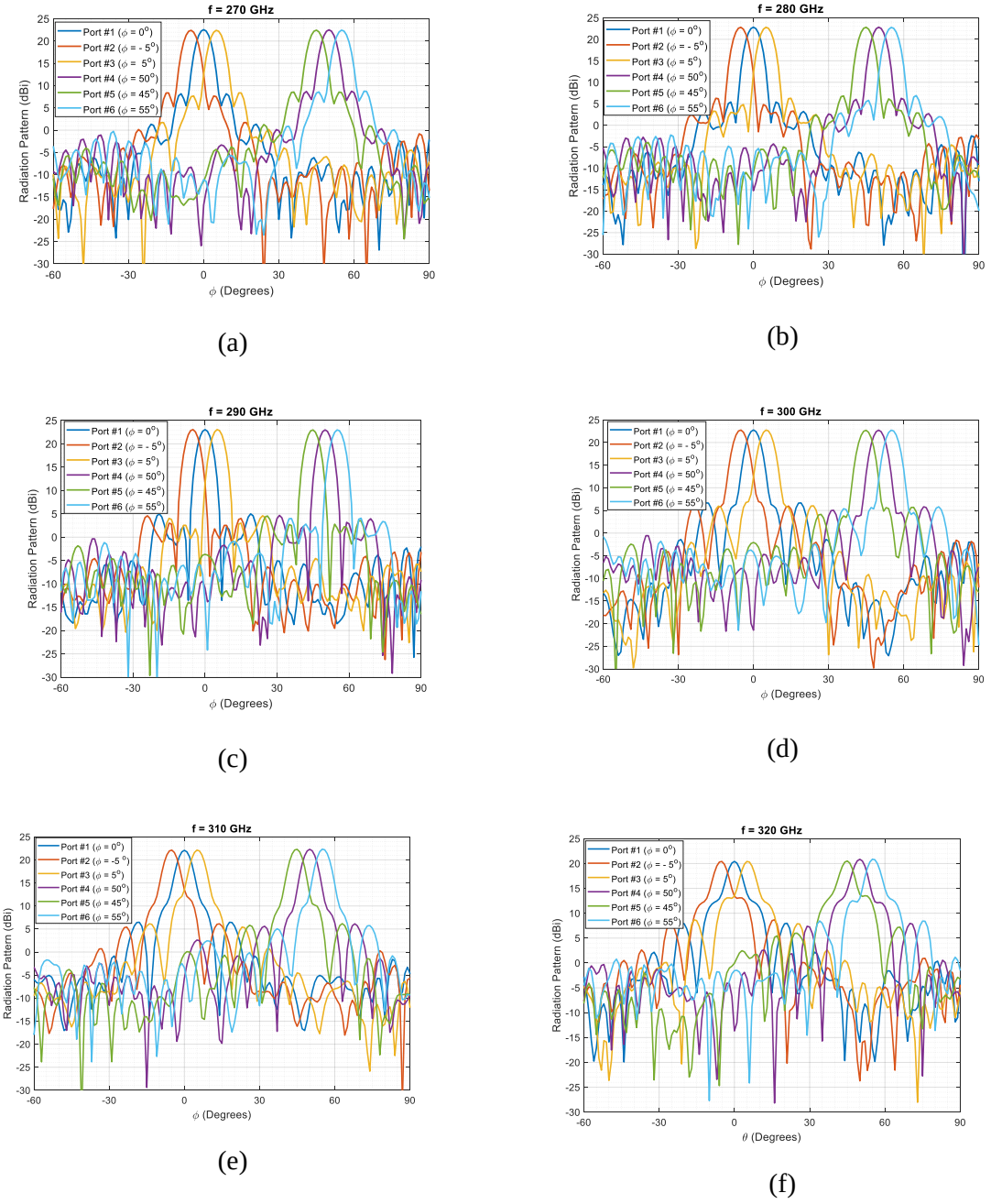

Figure 7.14: Beam steering of the 10.5 λ Luneburg lens antenna loaded with uniform metallic post structure.

7.4.2.3 Maximum Gain

Figure 7.15 shows the good performances of the simulated maximum realized gain over frequency of the lens antenna for each of the 6 feeds. The curves superimpose. The gain is not degraded if the beam is scanned, which means the scanning losses are low. The maximum gain decreases with frequency, ranging from 23 dB at 290 GHz to 18.3 dB at 330 GHz.

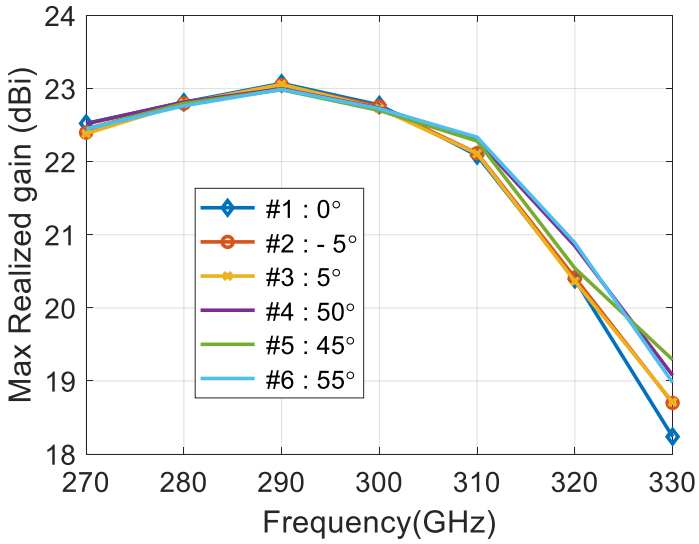

Figure 7.15: The maximum gain over frequency of 10.5 λ_0 lens antenna loaded with uniform metallic posts for 6 waveguide feeds.

7.4.3 Multibeam using Artificial Luneburg Lens

37 ports of beam width 5° makes the total ports equal to 19, which room one-half of the original lens on the bottom with the odd number of ports and a center port (#1 to #37). While 18 ports room one the half of the duplicate lens on the top with the even number of ports (#2 to #36). While making the total number of the ports 37 ports, the outermost ports will lose some performance owing to increased reflections and reduced gain. The finished model with 37 ports is depicted in Figure 7.16 including a flare with a uniform metallic post. The odd number of the ports are labeled to the bottom lens from the center port being number one (#1).

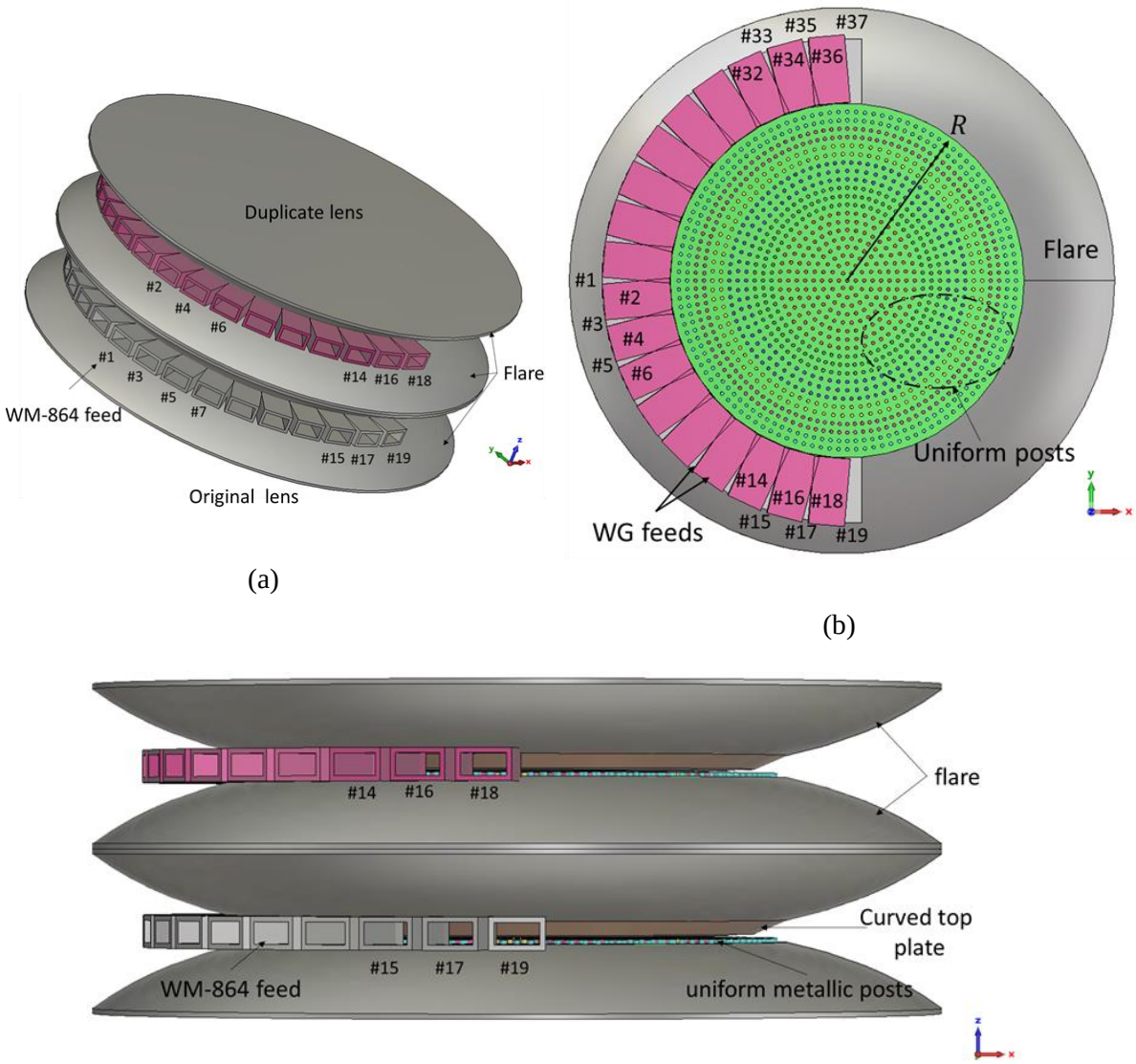

Figure 7.16: (a) 2D schematic view of Luneburg lens loaded with uniform metallic posts representing the focal arc and all the waveguide feeds (b) top view (c) side view.

7.4.3.1 S-parameters

A. Matching

Examining the reflection coefficient of each port, opposing ports are grouped with the same color/marker in Figure 7.17 due to symmetry around the center port. Between 250 GHz to 315 GHz, the return loss is below 10 dB for all ports except for the edge feeding ports **of the bottom lens** (13, 15,17,19,33,35, and 37), and the reflection coefficients for the edge feeding ports **of the top lens** (14, 16,18, 32, 34, and 36).

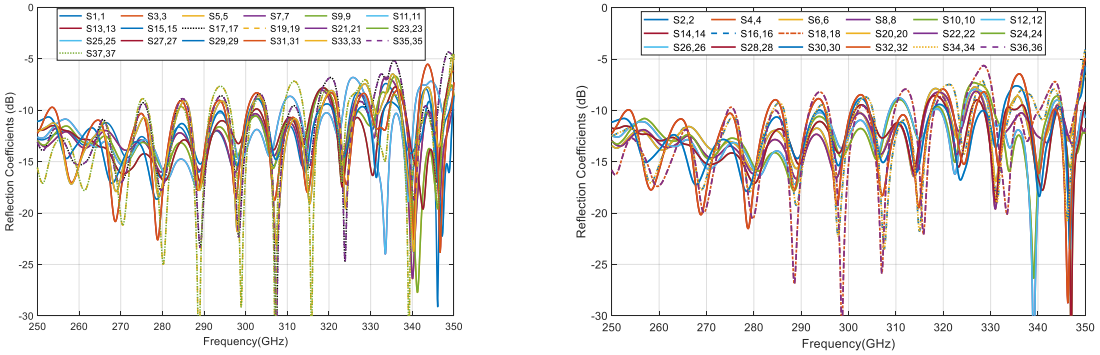

(a) (b)

Figure 7.17: Computed reflection coefficients of the feeding port from (a) odd-numbered (1-37) of the bottom lens and (b) even-numbered (2-36) of top lens for metallic lens loaded with uniform metallic posts.

B. Isolation

The mutual coupling between all ports is shown in Figure 7.18 noting that it is generally higher for higher frequencies between 315-350 GHz but from there stays well below 20 dB. Positioning ports close to the middle of the lens (i.e. 90 degrees apart from port 1) is problematic since the line of sight pathway is partly covered by the port section on the other side of the lens and will cause reflections. As result, the mutual coupling coefficients for the edge feeding ports **of the bottom lens** (15,17,19,33,35, and 37) and the reflection coefficients for the edge feeding ports **of the top lens** (14, 16,18, 32, 34, and 36) are very high.

Bottom Lens:

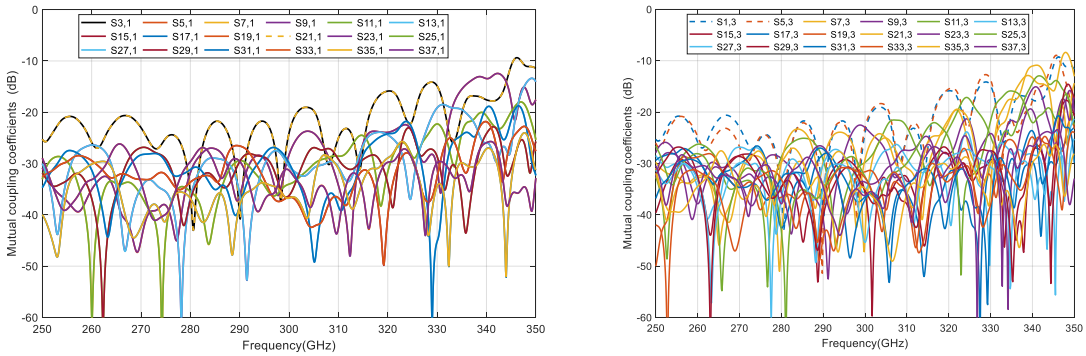

(a) (b)

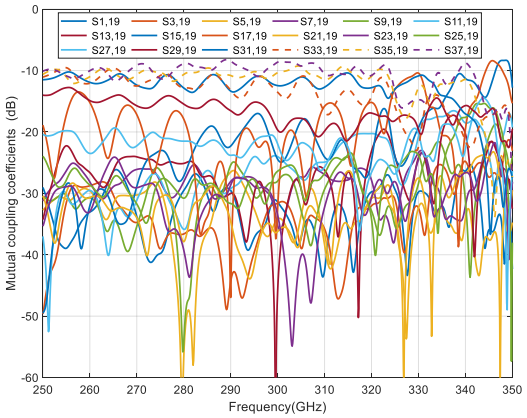
S1,19 S3,19 S5,19 S7,19 S9,19 S11,19
S13,19 S15,19 S17,19 S21,19 S23,19 S25,19
S27,19 S29,19 S31,19 S33,19 S35,19 S37,19
Mutual coupling coefficients (dB)
Frequency(GHz)

(c)

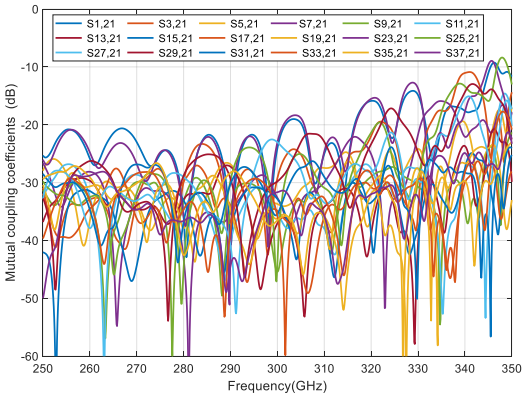
S1,21 S3,21 S5,21 S7,21 S9,21 S11,21
S13,21 S15,21 S17,21 S19,21 S23,21 S25,21
S27,21 S29,21 S31,21 S33,21 S35,21 S37,21
Mutual coupling coefficients (dB)
Frequency(GHz)

(d)

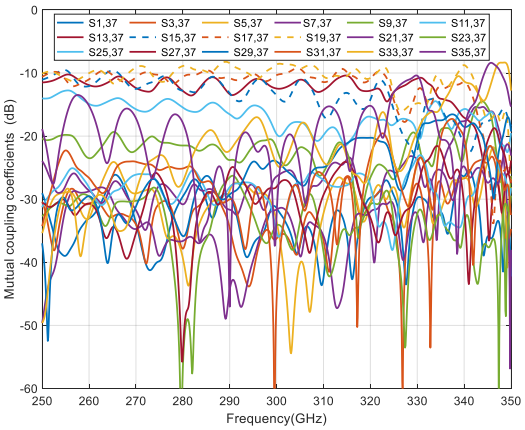
S1,37 S3,37 S5,37 S7,37 S9,37 S11,37
S13,37 S15,37 S17,37 S19,37 S21,37 S23,37
S25,37 S27,37 S29,37 S31,37 S33,37 S35,37
Mutual coupling coefficients (dB)
Frequency(GHz)

(e)

Top Lens:

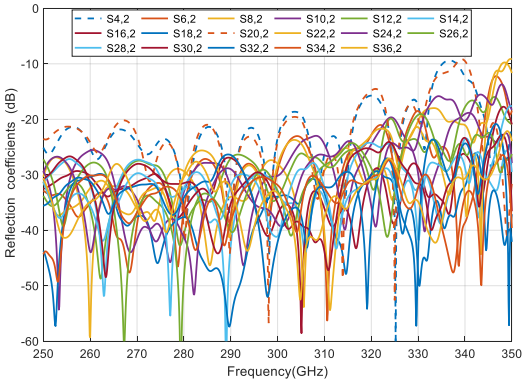
S4,2 S6,2 S8,2 S10,2 S12,2 S14,2
S16,2 S18,2 S20,2 S22,2 S24,2 S26,2
S28,2 S30,2 S32,2 S34,2 S36,2
Reflection coefficients (dB)
Frequency(GHz)

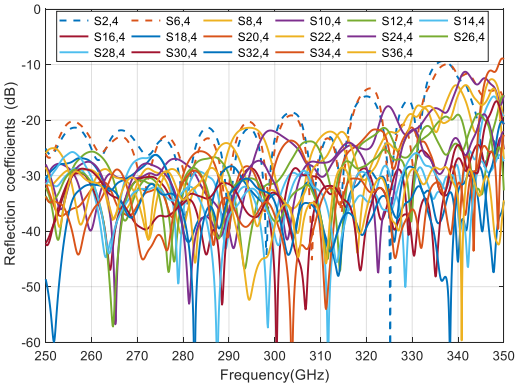
S2,4 S6,4 S8,4 S10,4 S12,4 S14,4
S16,4 S18,4 S20,4 S22,4 S24,4 S26,4
S28,4 S30,4 S32,4 S34,4 S36,4
Reflection coefficients (dB)
Frequency(GHz)

(a) (b)

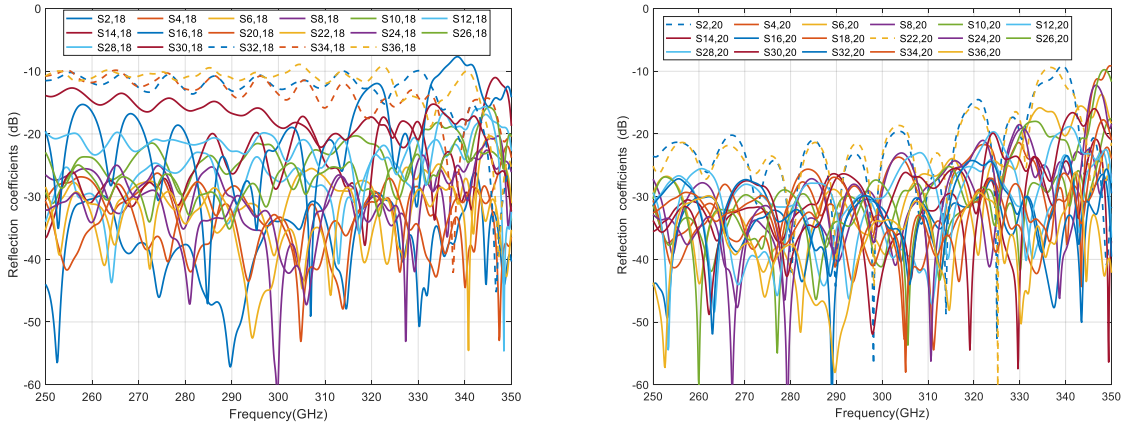

(c) (d)

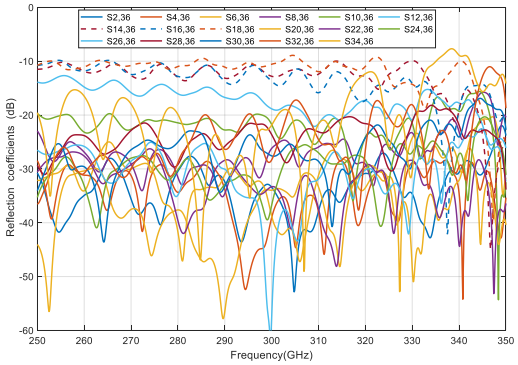

(e)

Figure 7.18: Mutual coupling coefficients among multiple feeding ports for the beam steering metallic lens loaded with uniform posts.

7.4.3.2 H-plane Radiation Pattern

37 feeds are placed along the focal arc of the lens (see inset of Figure 7.16) and the radiation patterns at different frequencies are illustrated in Figure 7.19. High directive beams are achieved with a wide field of view up to ± 75 between 250-310 GHz and 4.5 dB scan losses. The cross over level is 3° between contiguous beams and for the extreme beam at 75° the SLL equals -12.5 dB at 290 GHz. The realized gain of the radiation patterns reduces from 22.8 dBi (broadside) to 20 dBi (for $\approx \pm 75^{\circ}$ steer angles).

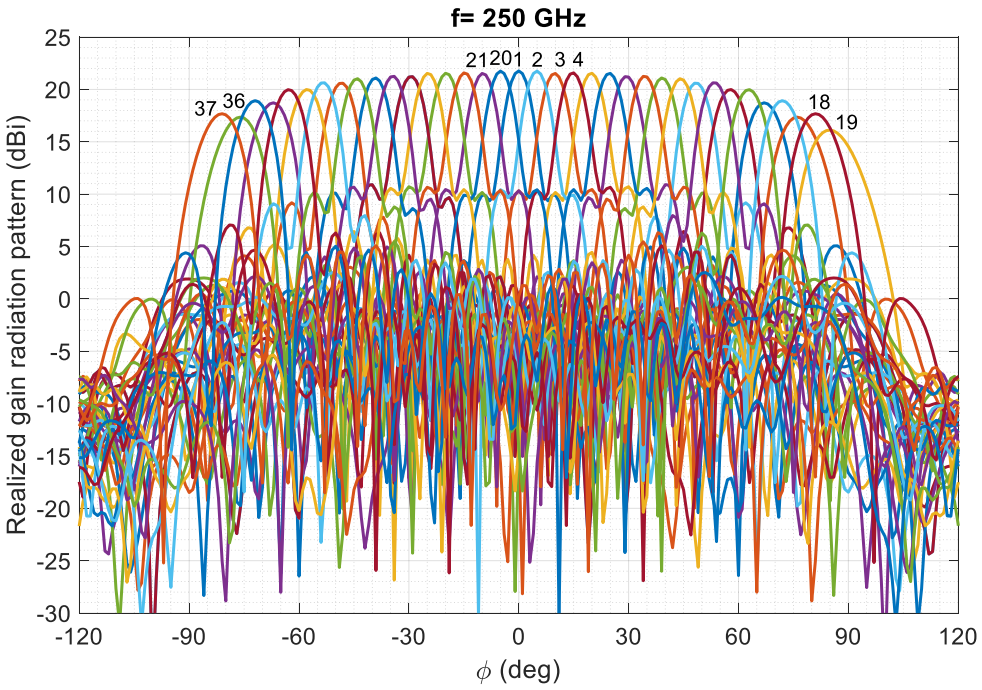
f= 250 GHz
Realized gain radiation pattern (dBi)
ϕ (deg)
21 20 1 2 3 4
37 36
18
19

(a)

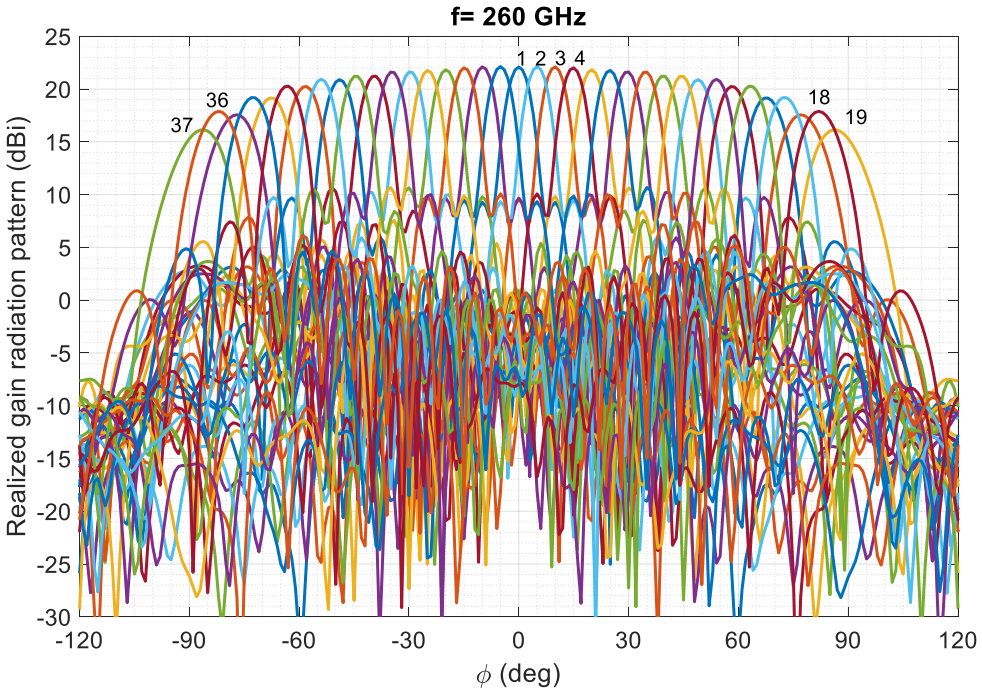
f= 260 GHz
Realized gain radiation pattern (dBi)
ϕ (deg)
1 2 3 4
36
37
18
19

(b)

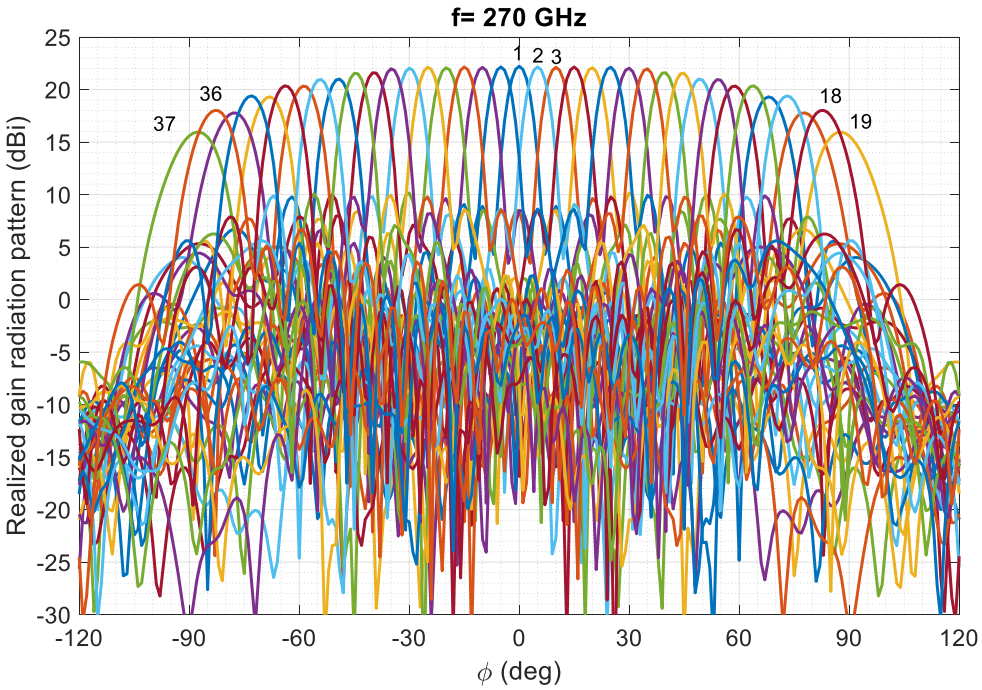
f= 270 GHz
1 2 3
36
37
18
19
Realized gain radiation pattern (dBi)
25
20
15
10
5
0
-5
-10
-15
-20
-25
-30
-120
-90
-60
-30
0
30
60
90
120
ϕ (deg)

(c)

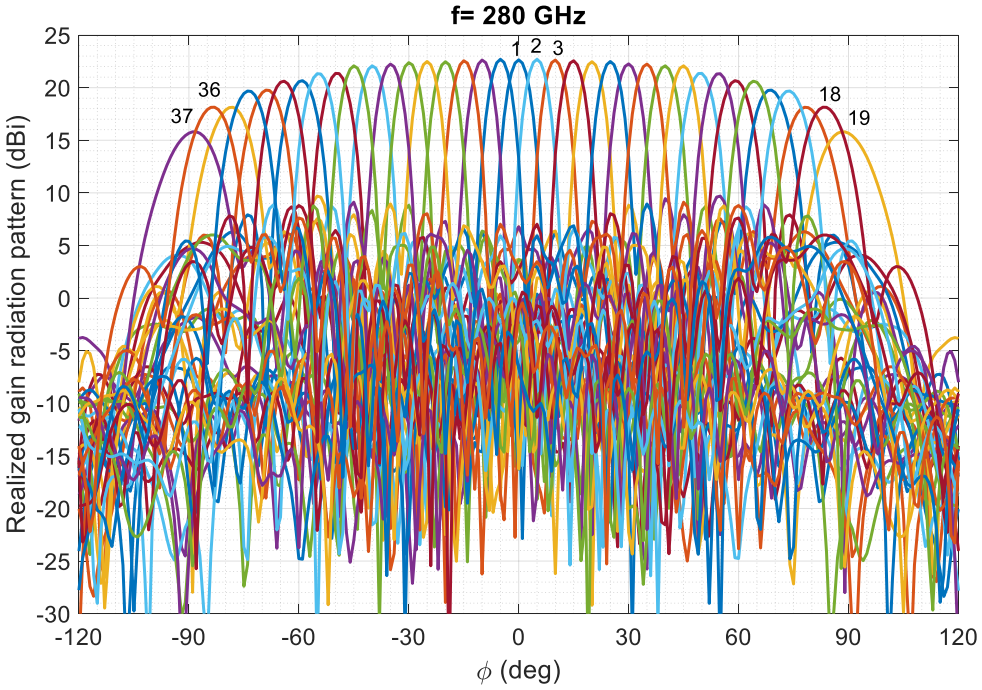
f= 280 GHz
1 2 3
36
37
18
19
Realized gain radiation pattern (dBi)
25
20
15
10
5
0
-5
-10
-15
-20
-25
-30
-120
-90
-60
-30
0
30
60
90
120
ϕ (deg)

(d)

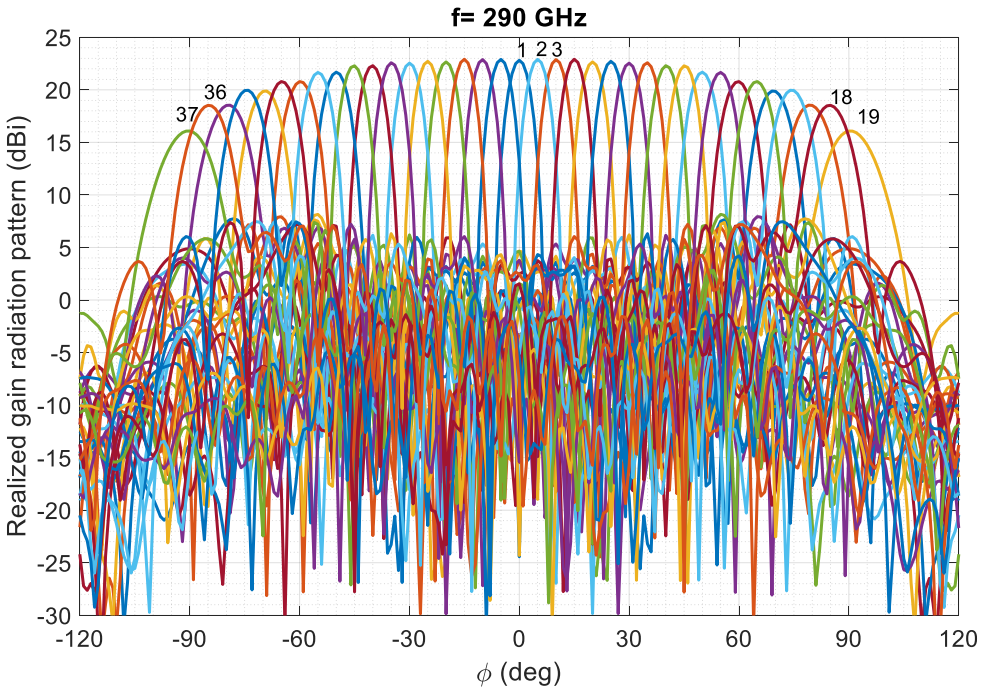
f= 290 GHz
1 2 3
36
37
18
19
Realized gain radiation pattern (dBi)
25
20
15
10
5
0
-5
-10
-15
-20
-25
-30
-120
-90
-60
-30
0
30
60
90
120
ϕ (deg)

(e)

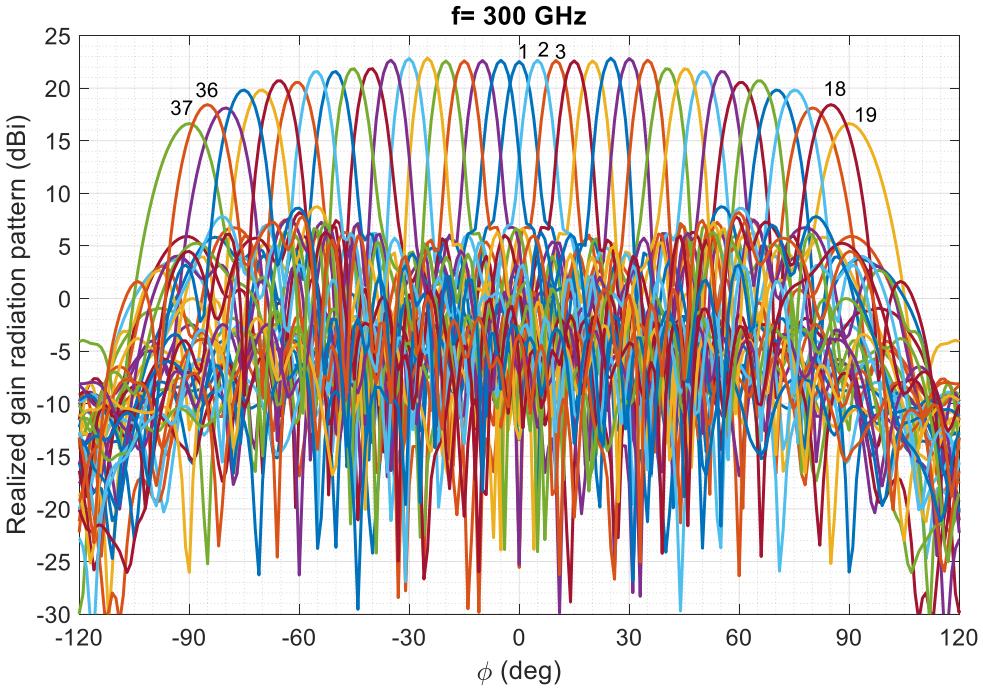
f= 300 GHz
1 2 3
36
37
18
19
Realized gain radiation pattern (dBi)
25
20
15
10
5
0
-5
-10
-15
-20
-25
-30
-120
-90
-60
-30
0
30
60
90
120
ϕ (deg)

(f)

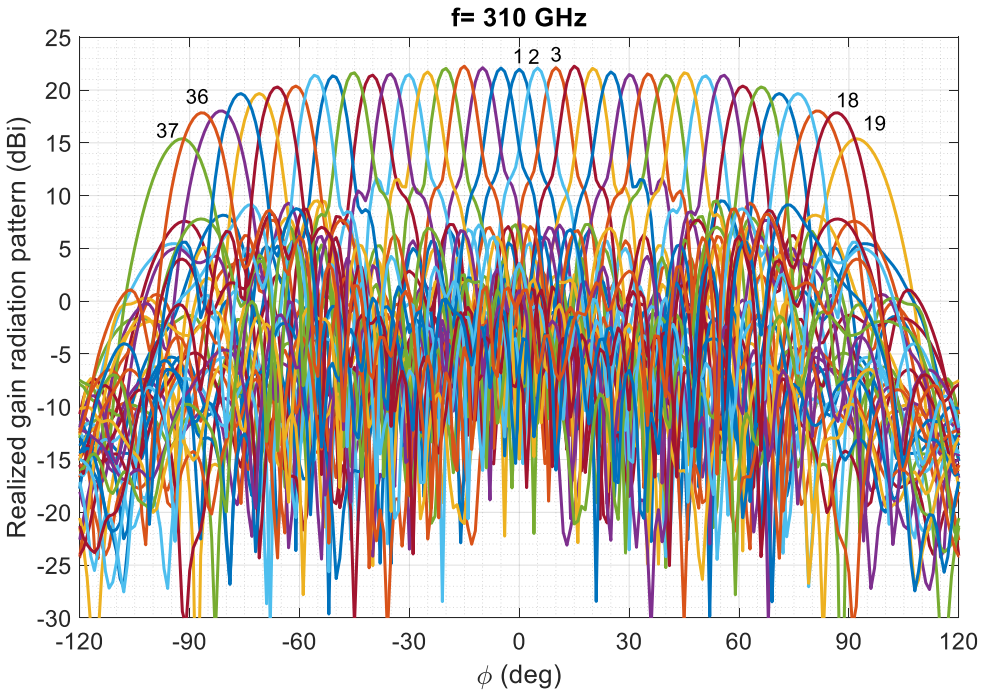

(g)

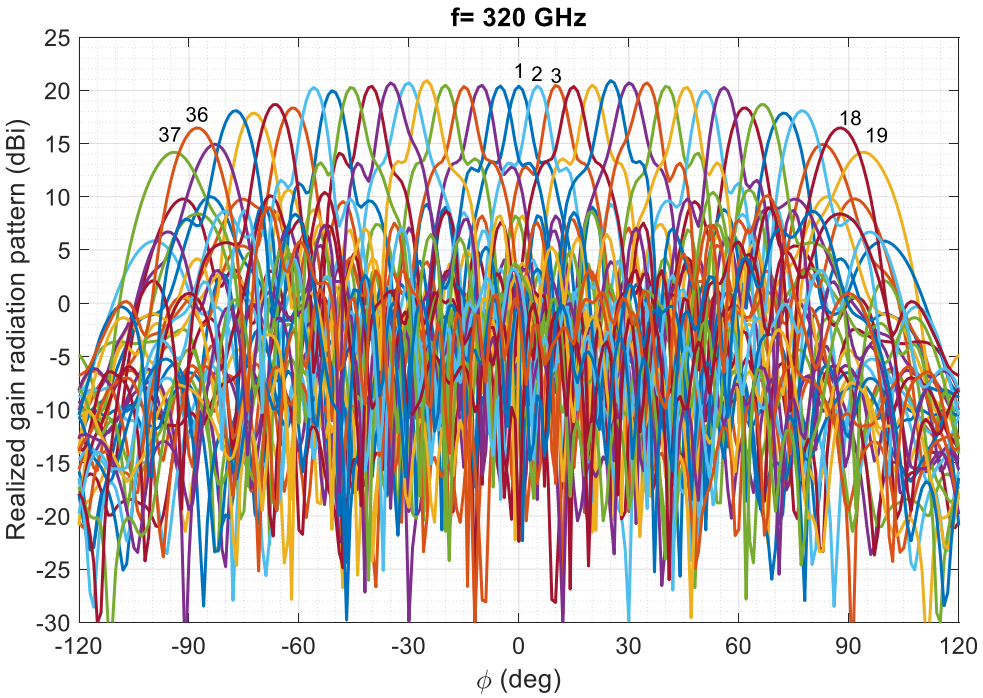

(h)

Figure 7.19: Computed H-plane radiation patterns for Luneburg lens loaded with uniform posts at different frequencies.

7.4.3.3 Maximum Realized gain and Beam Direction

The maximum realized gain for some of the 37 feeds metallic Luneburg lens antenna loaded with uniform posts at the targeted bandwidth (250-330 GHz) is depicted in Figure 7.20. The two outermost peaks that reach 15 dBi are caused by reflections from the edged ports 19 and 37. The maximum gain starts decreasing around 310 GHz. The scanning losses are high at the edge feeding ports of the Luneburg lens (i.e. after scan angle $\pm 75^{\circ}$).

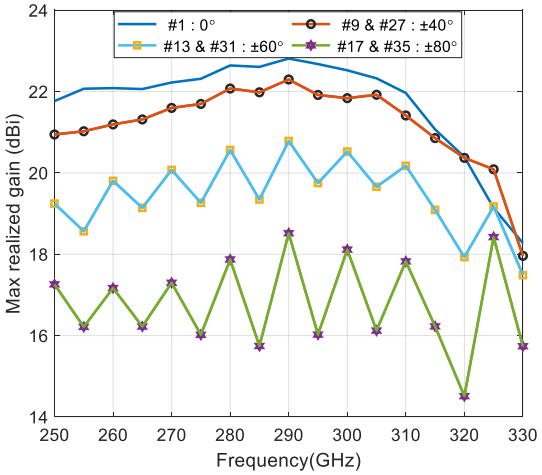

(a)

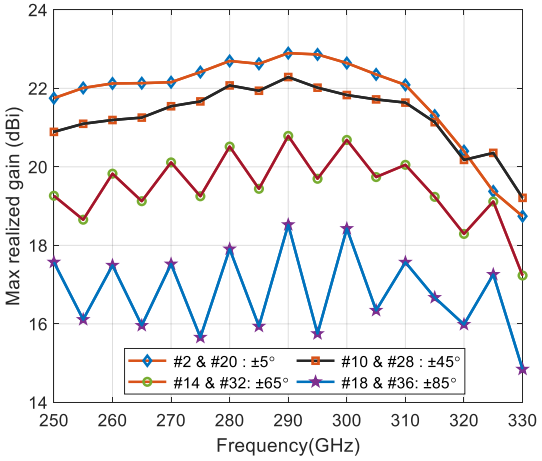

(b)

Figure 7.20: Computed maximum realized gain vs. frequency of the selected 37-feeds antenna.

The most important result of this study is to verify the direction of the main lobe. As illustrated in Figure 7.21(a) for the bottom lens, the computed direction of the main lobe for each feed is correct with an error lower than 5° for the edges of feeds 15, 17, 19, 33, 35, and 37. For the top lens, the computed direction of the main lobe is shown in Figure 7.21(b) for each feed is correct with an error lower than 5° for the edges feeds 16, 18, 34, and 36.

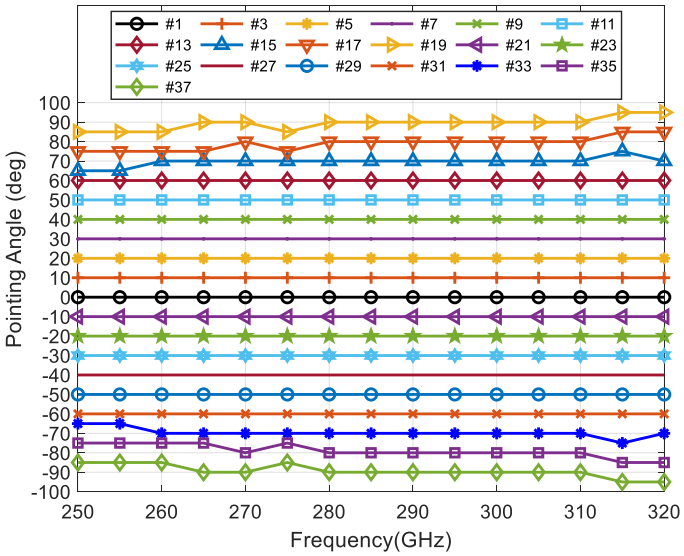

(a)

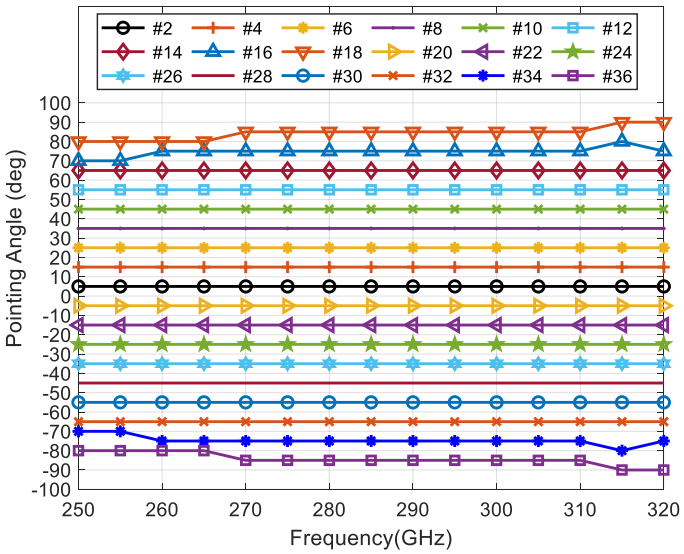

(b)

Figure 7.21: Computed H-plane main lobes direction of (a) 19-beams for bottom lens and (b)18-beams for top lens antenna loaded with uniform posts.

The peak gain for each port of the bottom lens at 290 GHz is given in Table 7.3 . The outermost ports, numbers 37 and 19 both show a gain of 16.1 dBi, while the highest gain is for ports 3 and 21 with a gain of 22.9 dBi. The beam widths of each port are shown in Table 7.3(a) , where the widest beamwidth is 13.2◦ and the narrowest 5.9◦. Similar behavior for the top lens is noted as shown in Table 7.3(b).

.

Table 7.3: Beam widths and peak gain for the 37 individual ports of the beam scanning Luneburg lens antenna loaded with variable posts (a) bottom, (b) top lenses.

Port #	1	21/3	23/5	25/7	27/9	29/11	31/13	33/15	35/17	37/19
main direction	0°	±10°	±20°	±30°	±40°	±50°	±60°	±70°	±80°	±90°
HPBW	6°	5.9°	6.1°	6.2°	6.4°	6.9°	8°	8.8°	10.3°	13.2°
Gain (dBi)	**22.8**	**22.9**	**22.7**	**22.5**	**22.3**	**21.7**	**20.8**	**19.9**	**18.5**	**16.1**
SLL (dB)	-19.5	-18.5	-16.5	-16.4	-15.2	-14.2	-13.6	-12.2	-10.6	-7.9

(a)

Port #	2/20	4/22	6/24	8/26	10/28	12/30	14/32	16/34	18/36
main direction	±5°	±15°	±25°	±35°	±45°	±55°	±65°	±75°	±85°
HPBW	5.9	5.8°	6.1°	6.2°	6.4°	7°	7.9°	8.8°	10.2°
Gain (dBi)	**22.9**	**22.9**	**22.7**	**22.6**	**22.3**	**21.7**	**20.8**	**20**	**18.5**
SLL (dB)	-18.9	-19	-16.4	-16.5	-14.9	-14.2	-13.4	-12.5	-11.3

(b)

7.4.4 Conclusion

Due to the difficulties of fabrication of posts for the metallic lens with a uniform 0.1 mm thickness and curved top plate (i.e. the top plate is smooth with a curve contour to realize the expected refractive index profiles of the isotropic lens), which is more sensitive for our design which is mimicked the equivalent refractive index of Luneburg law. We will move to the dielectric lens at 300 GHz in the next chapter and find a suitable thickness that can be fabricated at high frequencies with a wavelength thickness.

7.5 Dielectric 2D Luneburg Lens

7.5.1 Design of Cylindrical Luneburg Lens

The inhomogeneous Luneburg lens as shown in Figure 7.22 is the dielectric gradient index (GRIN) lens whose relative permittivity 'ε_r' varies radially according to the specific law given by [125]

$$\varepsilon_r = 2 - r^2 \tag{7.1}$$

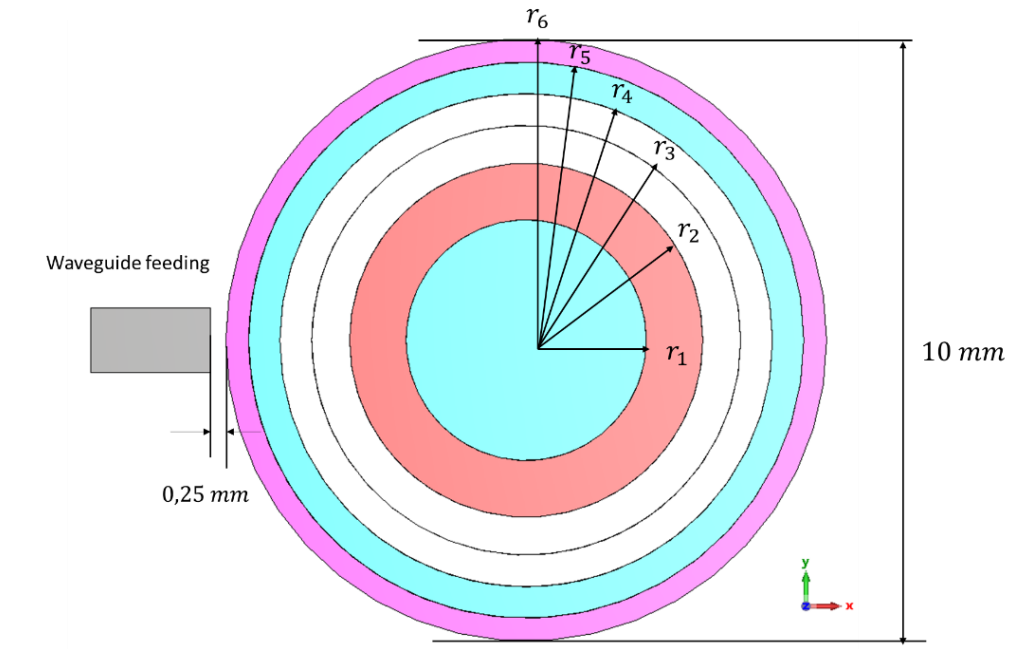

(a)

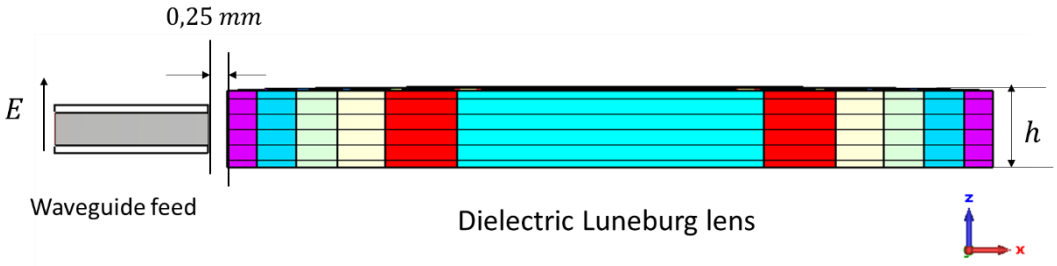

(b)

Figure 7.22: Six layer Luneburg lens (a) top view, and (b)cutting-side view.

where ‘r’ is the normalized radius of the Luneburg lens. This inhomogeneous dielectric lens has infinite focus points, which makes it a promising candidate for wide scan antennas. The radius and permittivity of different areas/layers inside the Luneburg lens can be obtained by utilizing the following formulas [126]:

$$\varepsilon_i = 2 - (2i - 1)\mathrm{M}$$
$$r_i = \sqrt{2i\mathrm{M}} \times R_{\mathrm{Lens}} \quad (7.2)$$

Where M = (1/(2×N+1)) and N is the number of areas/layers. Utilizing above mentioned equations a six-layer Luneburg lens is designed having an outer diameter of $5\lambda_0$(where, λ_0 is free space wavelength at a frequency of 300 GHz). The radius and permittivity of each layer inside the Luneburg lens are shown in Table 7.4.

Table 7.4: Permittivity and radius of each layer in the Luneburg lens having an outer diameter of $5\lambda_0$.

Area/layers	1	2	3	4	5	6
Radius (mm)	r_1 = 2 λ_0	r_2 = 2.94 λ_0	r_3 = 3.57 λ_0	r_4 = 4.1 λ_0	r_5 = 4.62 λ_0	r_6 = 5 λ_0
Permittivity	1.92	1.77	1.62	1.46	1.31	1.15
Loss Tangent	0.015	0.014	0.013	0.01	0.008	0.007

7.5.2 Antenna Fabrication and Measurements

The diameter of the outer shell of the Luneburg lens is chosen to be $10\lambda_0$ (10 mm), where λ_0 is the free space wavelength at 300 GHz The thickness of the Luneburg lens is chosen to be 3.5 mm, 2 mm, and 1 mm to encounter the possibility of fabrication even though the best thickness of the Luneburg lens is similar to the metallic Luneburg lens (i.e. 0.2 mm and 0.432 mm) as explained in chapter 6.

The AirexR82 (ε_r = 1.12) is utilized as basic foam material which is initially cut in 30 mm, 20 mm, and 10 mm thicknesses as shown in Figure 7.23. The six-layer Luneburg lens is developed by following the approach given in [127] i.e. pressing a basic foam material in a controlled manner to obtain different permittivity values in the required area to have 3.5 mm, 2 mm, and 1 mmm final thicknesses. This kind of foam is filled with air bubbles which are removed by pressing at 90° C. So it becomes possible to control the dielectric constant of pressed foam by approximately choosing the right area density ratio $\xi = H_i/H_f$. Where H_i is the initial foam thickness pressed to the final thickness H_f. An initial foam cylinder-shaped slab is drilled with

a 2D mechanical process to obtain the different areas with different thicknesses (Figure 7.23) reported in Table 7.5. Dielectric constant and loss tangent of pressed foam have been measured using a characterization free space measurement setup composed of an AB Millimeter VNA and lens-horns antennas [128].

Table 7.5: Dielectric Properties obtained from Airex R82 depending on the density ratio.

ζ=Hi/Hf	Hi (mm)	Hf (mm)	Permittivity	Loss tangent
8	28	**3.5**	1.92	0.015
6.5	22.75	**3.5**	1.77	0.014
5.35	18.725	**3.5**	1.62	0.013
4.2	14.7	**3.5**	1.46	0.01
2.75	9.625	**3.5**	1.31	0.008
1.5	5.25	**3.5**	1.15	0.007

(a)

ζ=**Hi/Hf**	Hi (mm)	Hf (mm)	Permittivity	Loss tangent
8	16	**2**	1.92	0.015
6.5	13	**2**	1.77	0.014
5.35	10.7	**2**	1.62	0.013
4.2	8.4	**2**	1.46	0.01
2.75	5.5	**2**	1.31	0.008
1.5	3	**2**	1.15	0.007

(b)

ζ=**Hi/Hf**	Hi (mm)	Hf (mm)	Permittivity	Loss tangent
8	8	**1**	1.92	0.015
6.5	6.5	**1**	1.77	0.014
5.35	5.35	**1**	1.62	0.013
4.2	4.2	**1**	1.46	0.01
2.75	2.75	**1**	1.31	0.008
1.5	1.5	**1**	1.15	0.007

(c)

The final manufactured Luneburg lens with required thickness and permittivity values are given in Table I is shown in Figure 7.23.

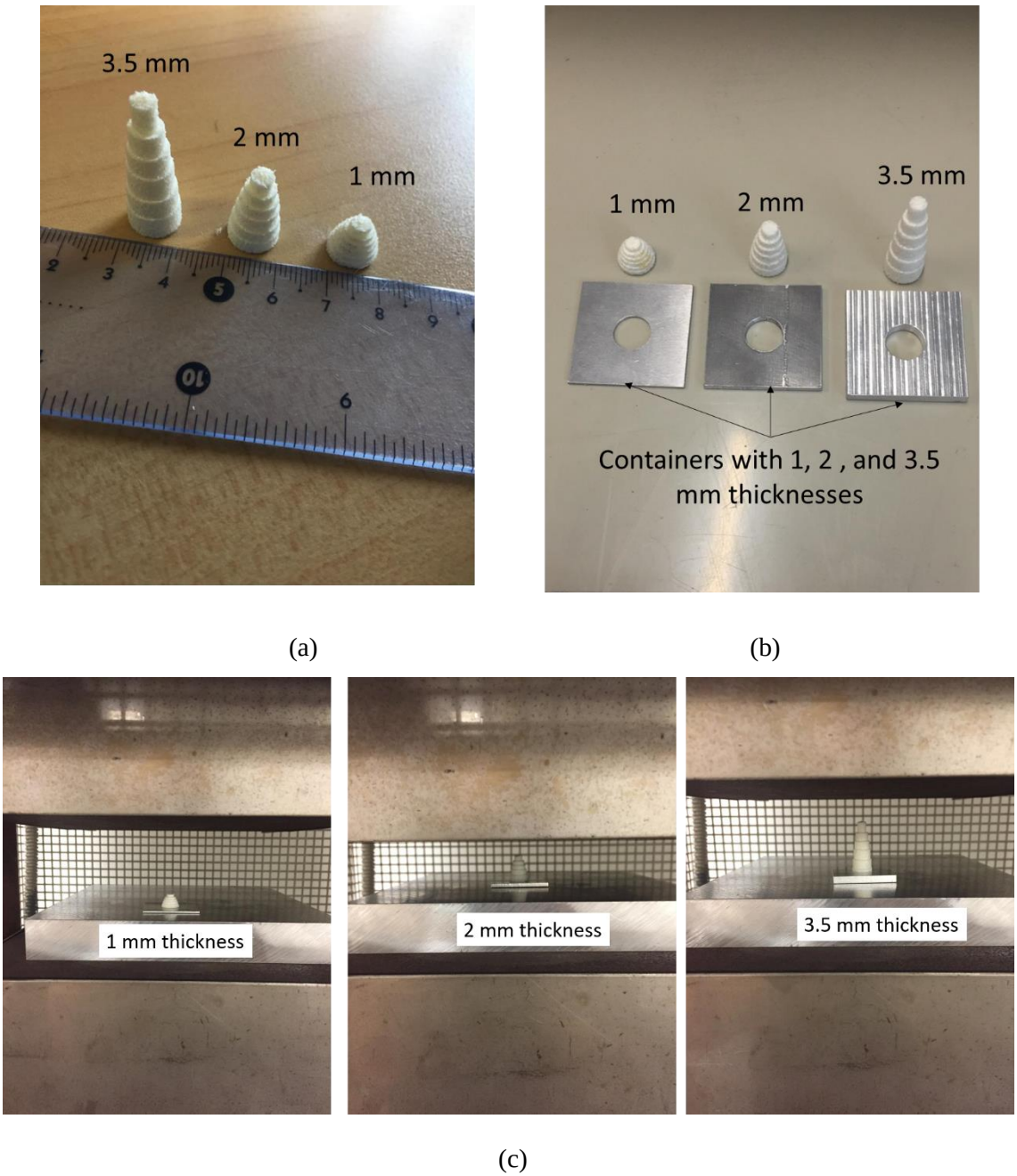

Figure 7.23: Manufacturing of Luneburg lens. (a) & (b) side view of the initial 6 layered foam for Luneburg lens (c) Foam lens before being pressed with a width of 1 cm.

7.6 Linearly Polarized 2D Luneburg Lens Antenna

7.6.1 Vertical Polarization Feed

This section shows when the dielectric Luneburg lens is fed by a standard waveguide with vertical polarization as shown in Figure 7.24.

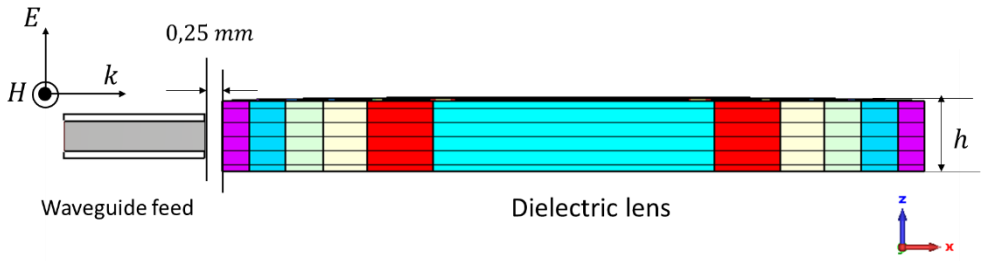

Figure 7.24: The dielectric Luneburg lens when E-filed parallel to lens.

7.6.1.1 Lens with Foam Support

Figure 7.25 presents the proposed structure of the dielectric Luneburg lens without flare. The development design consists of a Luneburg lens, standard waveguide flange (WM-864), and foam part. We used this foam part as support to the lens. The lens has a thickness of 'h' with a focal point of $0.25\lambda_0$ from feeding part.

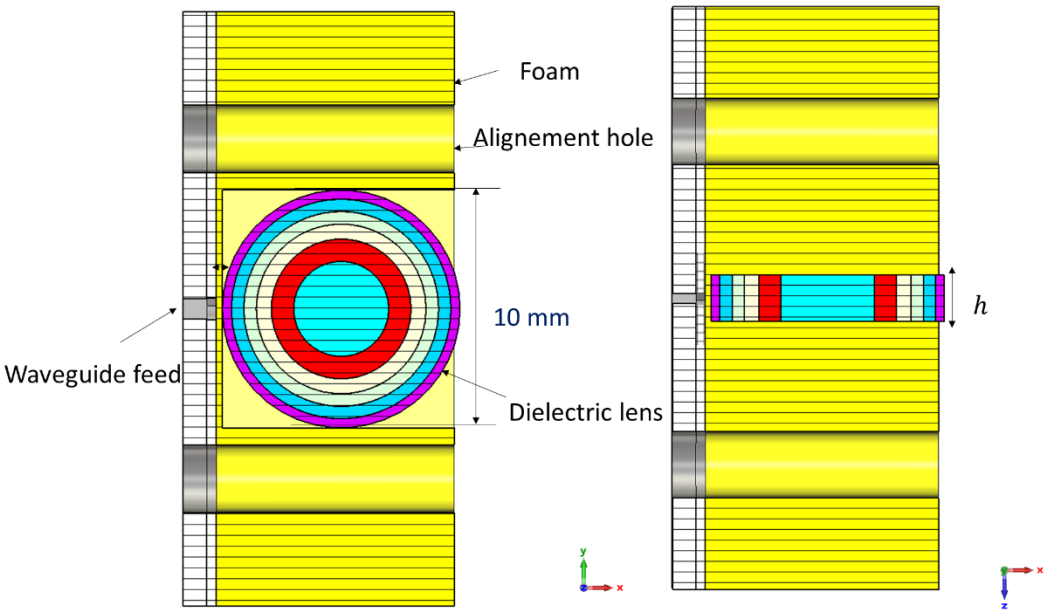

Figure 7.25: The dielectric Luneburg lens without flare.

The reflection coefficient (S11), realized gain, and total efficiency is presented in Figure 7.26. The thickness of the Luneburg lens is chosen to be 3.5 mm, 2 mm, and 1 mm. The results showed that the lens with a thickness of 2 mm is better than the thickness of 3.5 mm in terms of efficiency. The realized gain for thicknesses of 2 mm and 3.5 mm is in fair agreement with desired bandwidth.

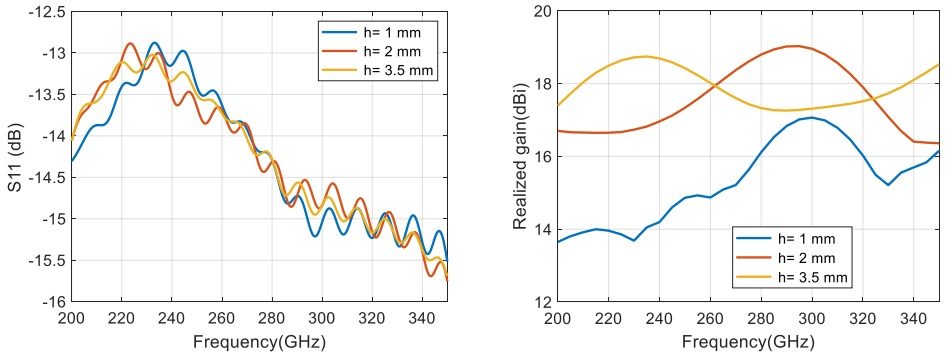

(b)

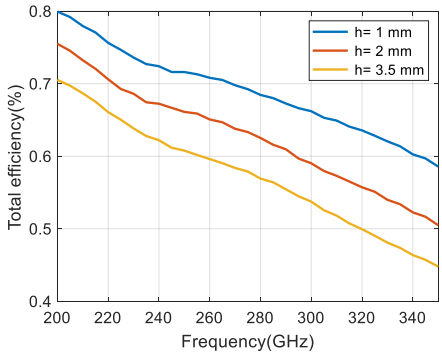

(c)

Figure 7.26: Luneburg lens without flare-based-vertical polarization feed (a) reflection coefficient (S11),(b) realized gain, and (c) total efficiency.

7.6.1.2 Lens with Metallic Flare

Figure 7.27 presents the proposed structure of the dielectric Luneburg lens with a metallic flare. The development design consists of a Luneburg lens with flare, standard waveguide flange (WM-864), and fixing part. We used this fixing part as support to the lens. The lens has a thickness of 'h' with a focal point of $0.25\lambda_0$ from feeding part.

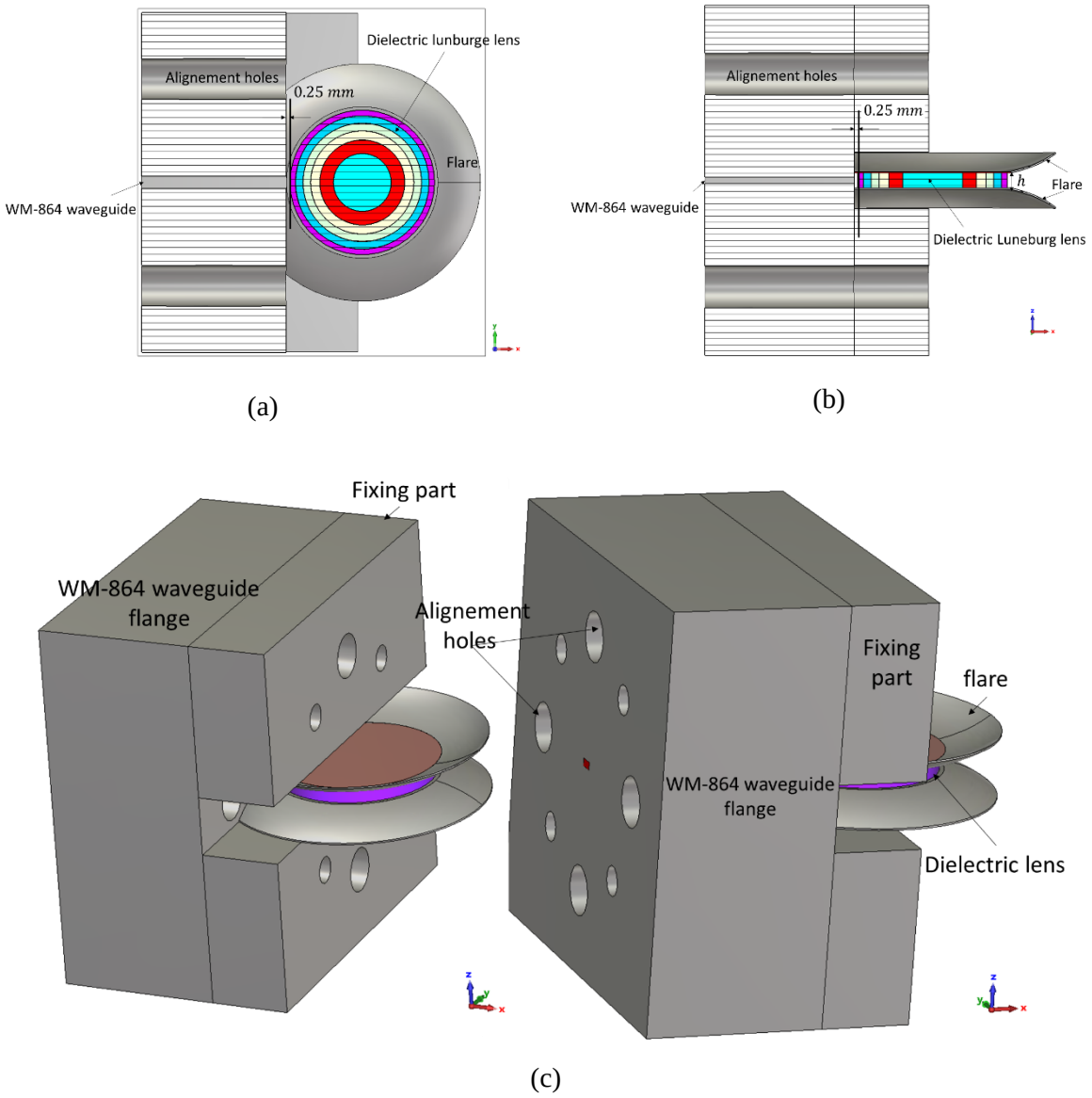

Figure 7.27: The dielectric Luneburg lens with metallic flare (a) cutting-top view,(b) cutting-side view, and (c) perspective view.

The reflection coefficient (S11), realized gain, and total efficiency is presented in Figure 7.28. The thickness of the Luneburg lens is chosen to be 3.5 mm, 2 mm, and 1 mm. The results showed that the best thickness is 2 mm in terms of realized gain and efficiency. The total efficiency for all thicknesses is lower than 50 % over desired bandwidth due to dielectric loss at high frequency which is avoided when using the metallic lens as explained in chapter 6. We can have concluded that the lens without flare is better than the lens with the metallic lens.

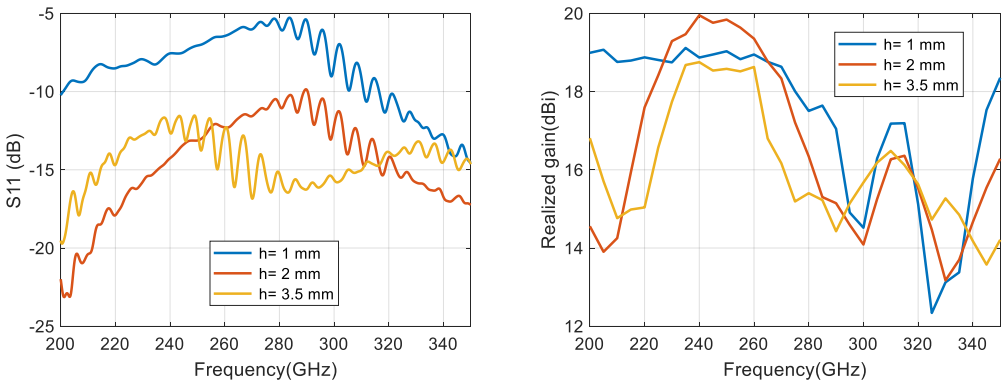

(a) (b)

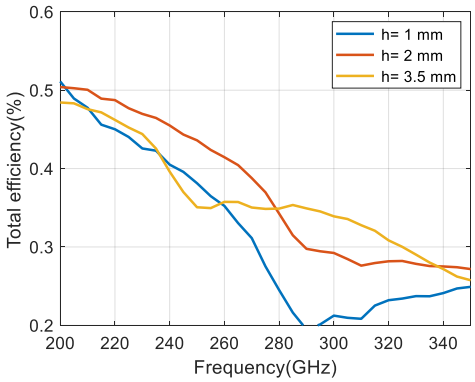

(c)

Figure 7.28: Luneburg lens with flare-based-vertical polarization feed (a) reflection coefficient (S11),(b) realized gain, and (c) total efficiency.

7.6.2 Horizontal Polarization Feed

This section shows when the dielectric Luneburg lens is fed by a standard waveguide with horizontal polarization as shown in Figure 7.29.

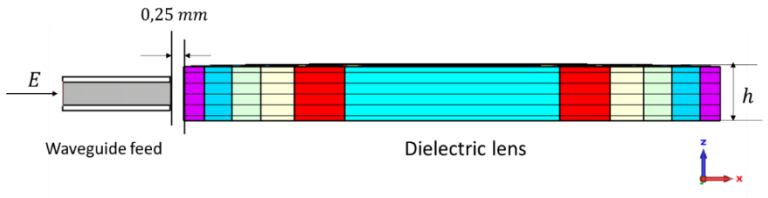

Figure 7.29: The dielectric Luneburg lens when E-filed normal to lens.

7.6.2.1 Lens with Foam Support

The reflection coefficient (S11), realized gain, and total efficiency for a lens without flare with horizontal polarization feed is presented in Figure 7.30. The results showed that the lens thickness of 2 mm is the best in terms of efficiency as compared to 3.5 thickness. The total efficiency for all thicknesses is higher than 50 % over desired bandwidth (220-330 GHz). We can note that as the thickness of the lens without flare increased the total efficiency decreased.

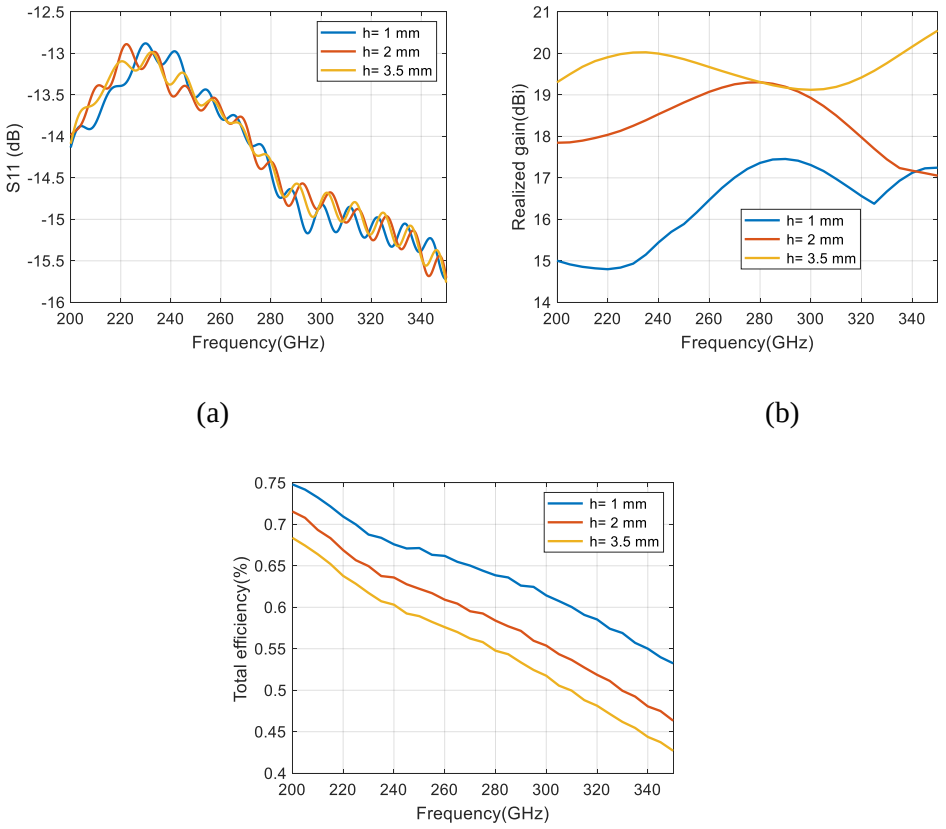

(a) (b)

(c)

Figure 7.30: Luneburg lens without flare-based-horizontal polarization feed (a) reflection coefficient (S11),(b) realized gain, and (c) total efficiency.

7.6.2.2 Lens with Metallic Flare

The reflection coefficient (S11), realized gain, and total efficiency for a lens with horizontal polarization feed is presented in Figure 7.31. The thickness of the Luneburg lens is chosen to be 3.5 mm, 2 mm, and 1 mm as we did with vertical polarization feed. The results showed that the lens thickness of 2 mm is the best in terms of reflection coefficient, realized gain, and efficiency as compared to other thicknesses. The total efficiency for all thicknesses is higher than 50 % over desired. We can conclude that the horizontal polarization feed has a better result as compared with the vertical polarization feed for the lens with metallic flare.

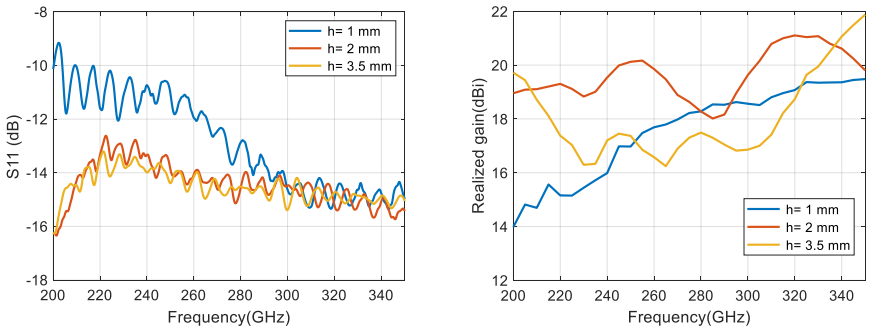

(a)

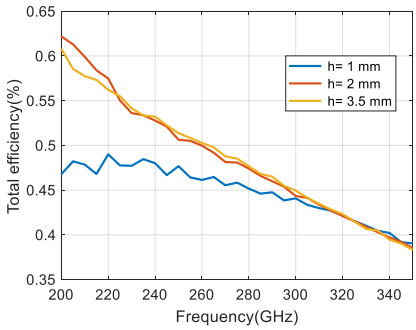

(c)

Figure 7.31: Luneburg lens with flare-based-horizontal polarization feed (a) reflection coefficient (S11),(b) realized gain, and (c) total efficiency.

7.6.3 Conclusion

We can conclude that the response of the dielectric lens is different for vertical and horizontal polarization as a result the lens will degrade the gain. For example, the thick lens with 2 mm = 2 λ_0 , if we are excited by vertical and horizontal polarization the results we noted is different in term of the gain, which means the E_θ and E_ϕ will be different.

7.6.4 Simulation Results

7.6.4.1 Lens with Foam Support

The simulated radiation patterns of azimuth (Theta = 90) and elevation (Phi=0) planes at different frequencies for the dielectric lens with foam support for different thicknesses (1mm, 2 mm, and 3.5 mm) are shown in Figure 7.32 for vertical (V-pol) and horizontal (H-pol) polarization feeds. It is observed that for all different thicknesses of the lens the best thickness is 2 mm and the worst case is 3.5 mm (thick thickness = 3.5 λ_0).

a. Lens of thickness 1 mm

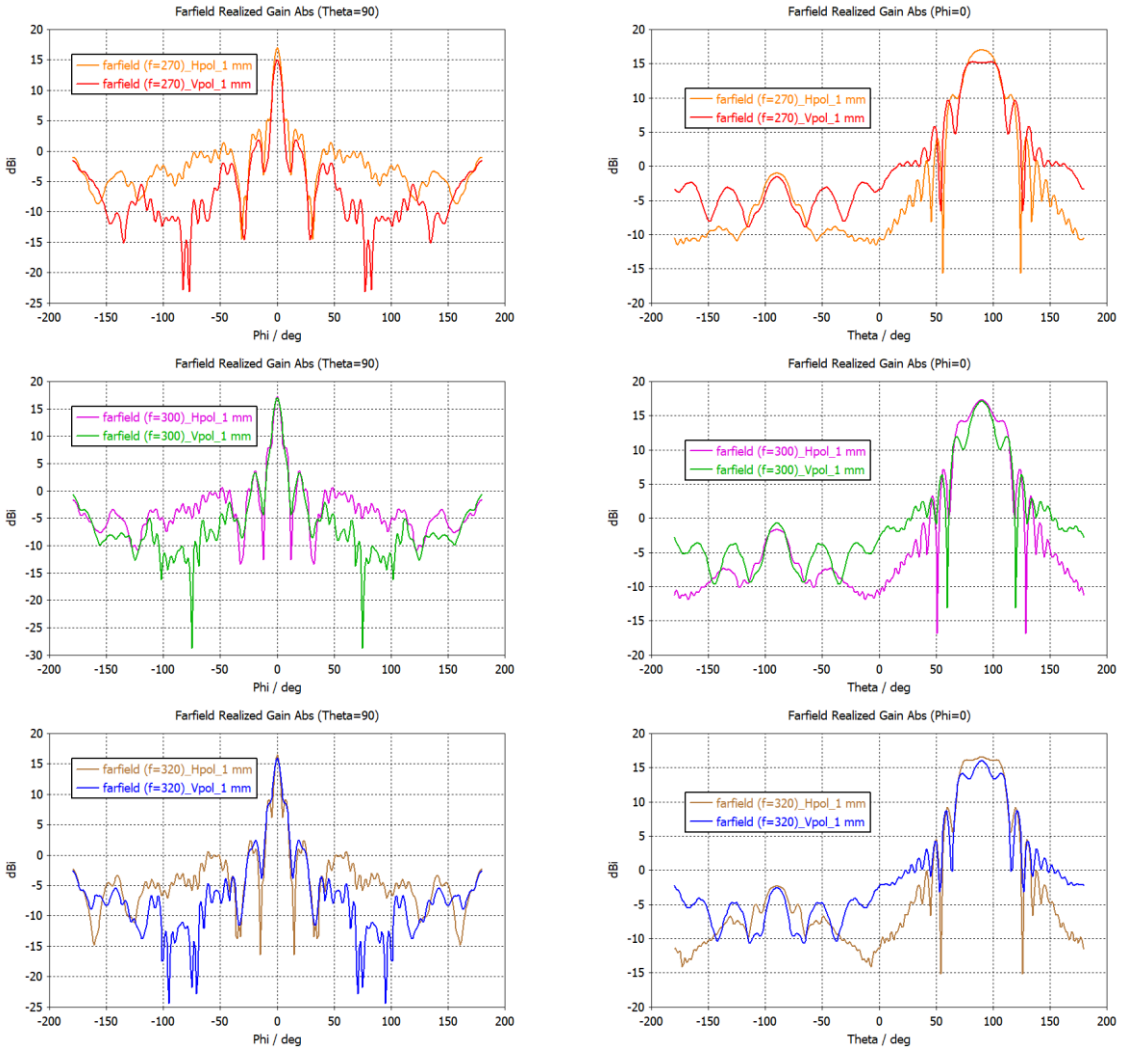

(a)

b. Lens of thickness 2 mm

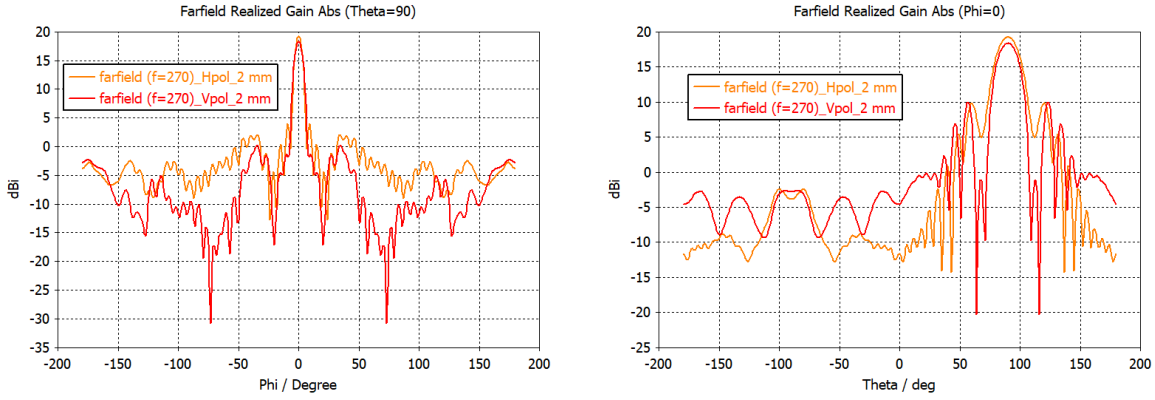

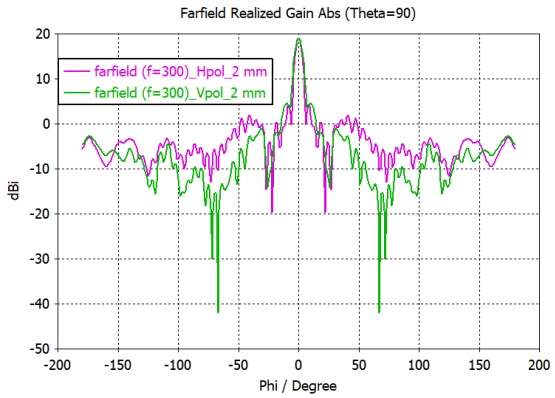

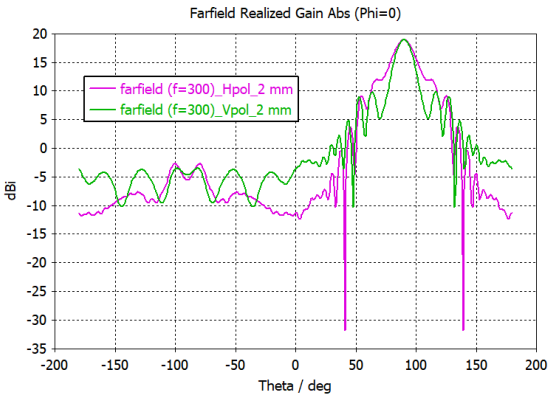

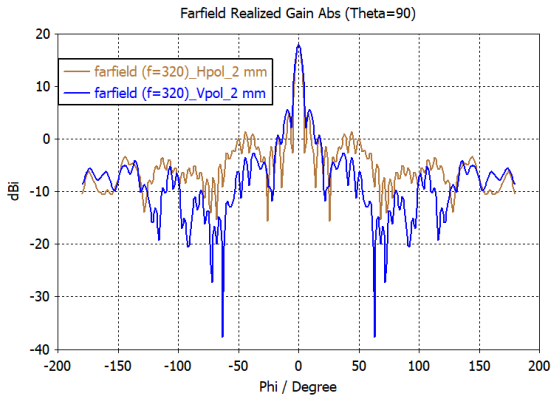

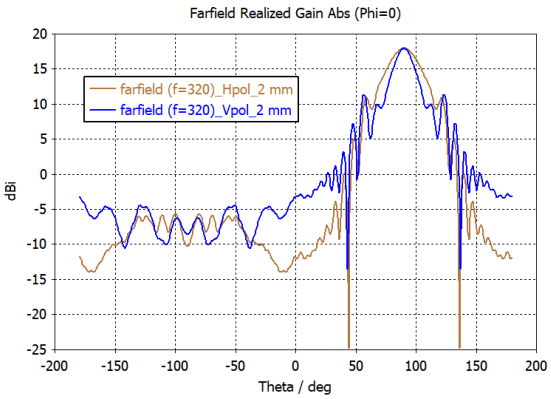

(b)

c. Lens of thickness 3.5 mm

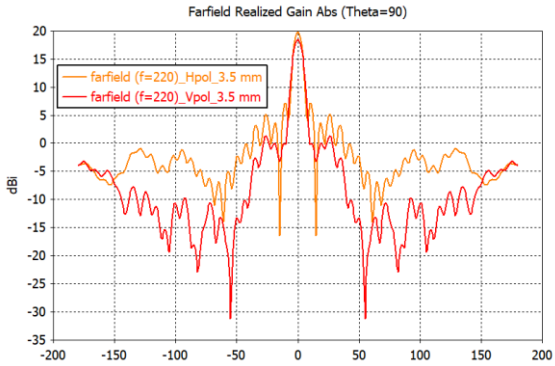

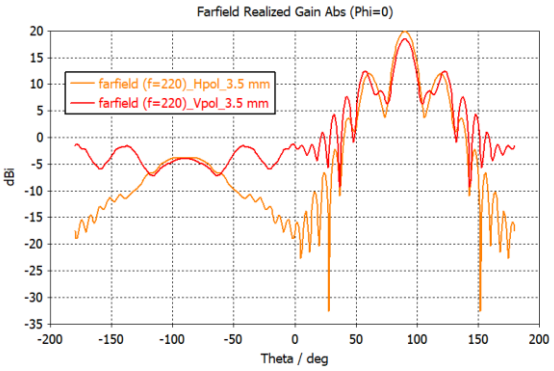

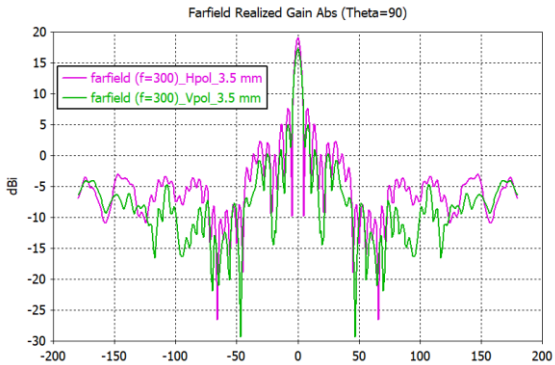

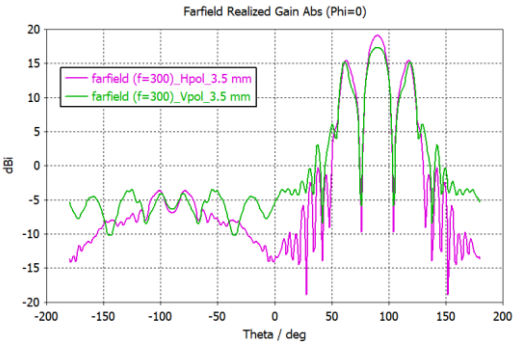

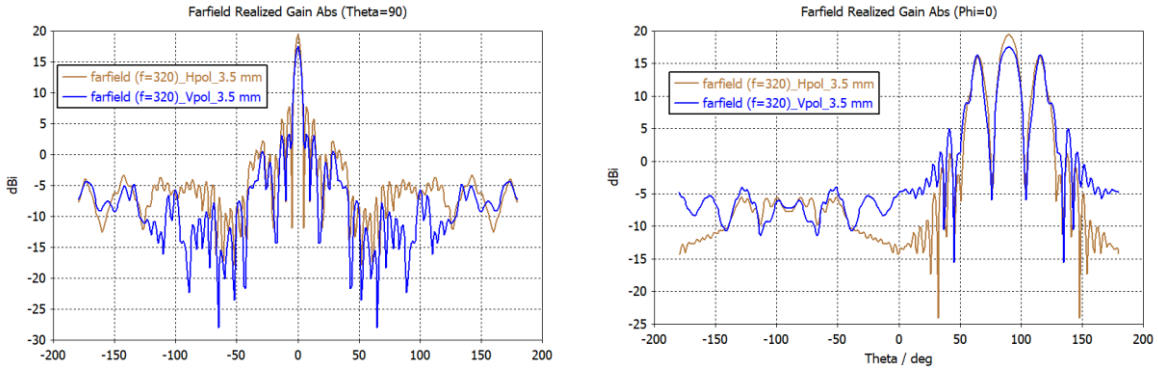

(c)

Figure 7.32: The simulated radiation patterns of horizontal (Theta = 90) and elevation (Phi=0) planes of the dielectric lens with foam support (a) 1mm (b) 2 mm and (c) 3.5 mm thicknesses.

7.6.4.2 Lens with Metallic Flare

The simulated radiation patterns of azimuth (Theta = 90) and elevation (Phi=0) planes at different frequencies for the dielectric lens with a metallic flare for different thicknesses (1mm, 2 mm, and 3.5 mm) are shown in Figure 7.32 for vertical (V-pol) and horizontal (H-pol) polarization feeds.

It is observed that for the lens thickness of 1 mm it works very well, especially for horizontal polarization feed at 320 GHz for elevation plane. The same behavior is noted for the 2 mm thickness of the lens at lower frequencies (i.e. 270 GHz) both azimuth and elevation plane works very well but when the frequency increases (i.e. 300 GHz and 320 GHz) the elevation plane is very bad when the feed is vertical-pol. Because at high frequencies 2 mm is too thick (the thickness of the lens is $2\lambda_0$) but this is not the case for 1 mm (the thickness of the lens is $1\lambda_0$). For a very thick of 3.5 mm lens, we can note that even at lower frequencies the elevation plane is very bad.

The objective of this section is to have the same azimuth and elevation plane in order to purpose circularly polarized dielectric Luneburg lens.

a) Lens of thickness 1 mm

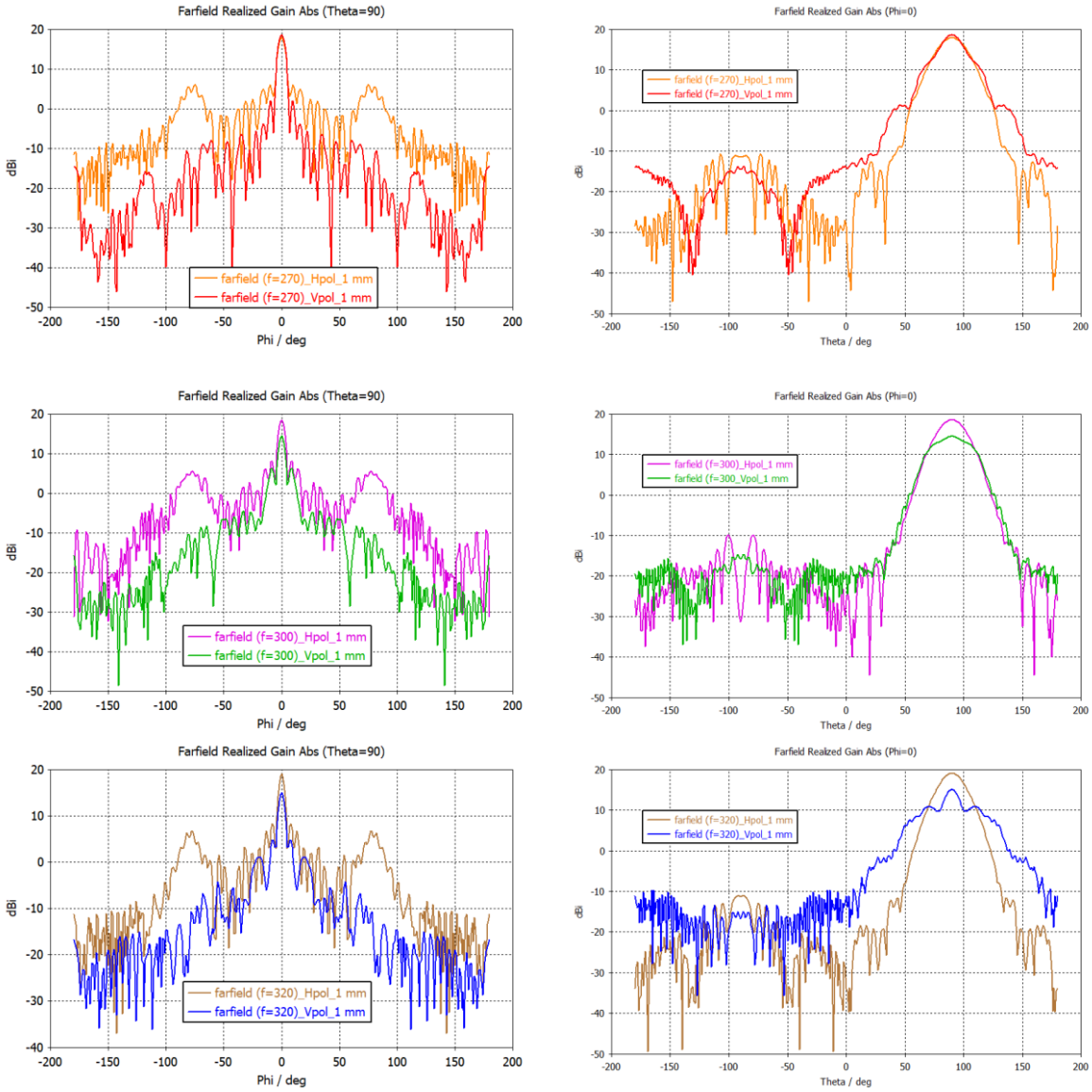

(a)

b) Lens of thickness 2 mm

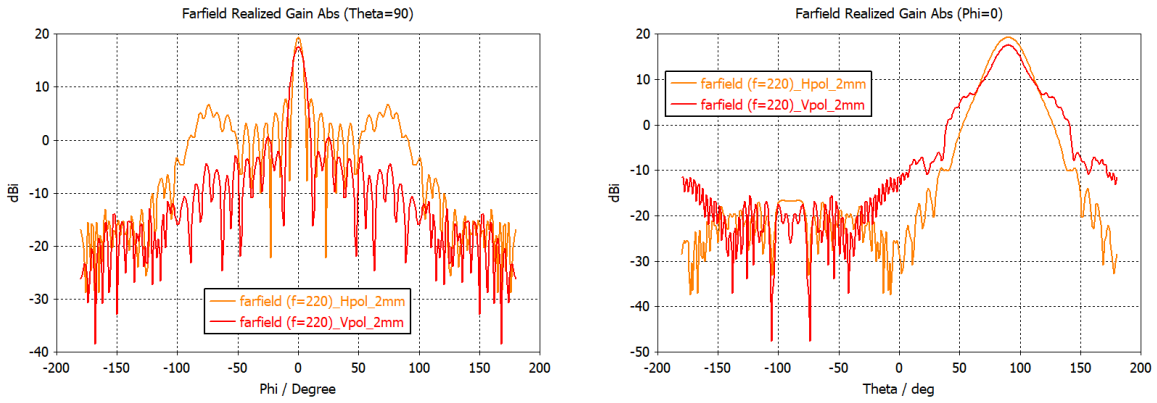

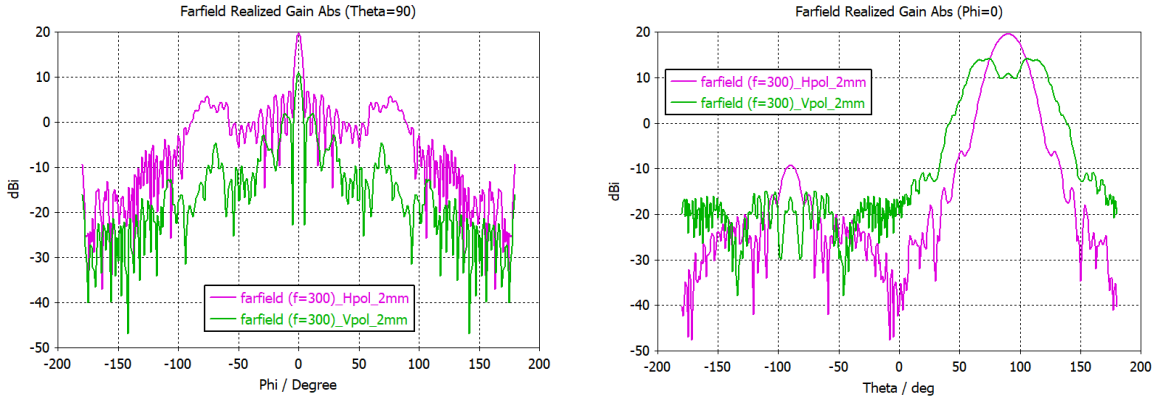

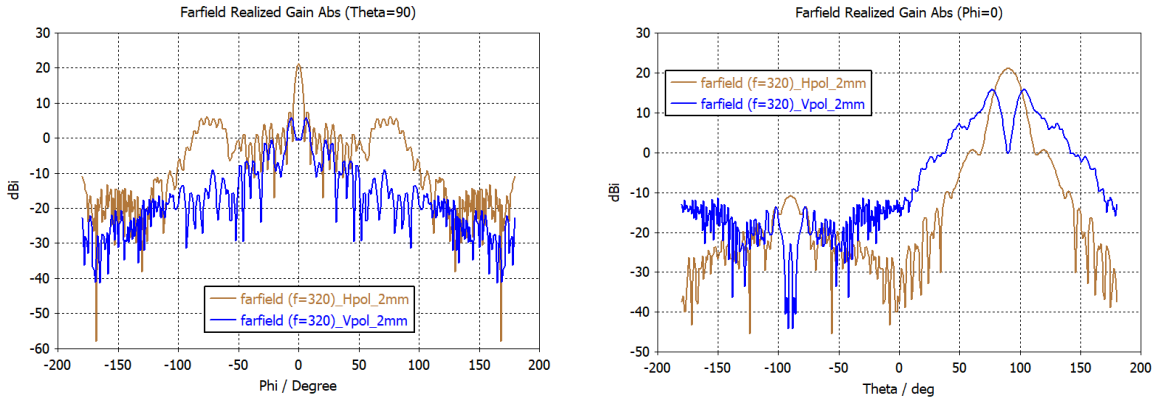

(b)

c) <u>Lens of thickness 3.5 mm</u>

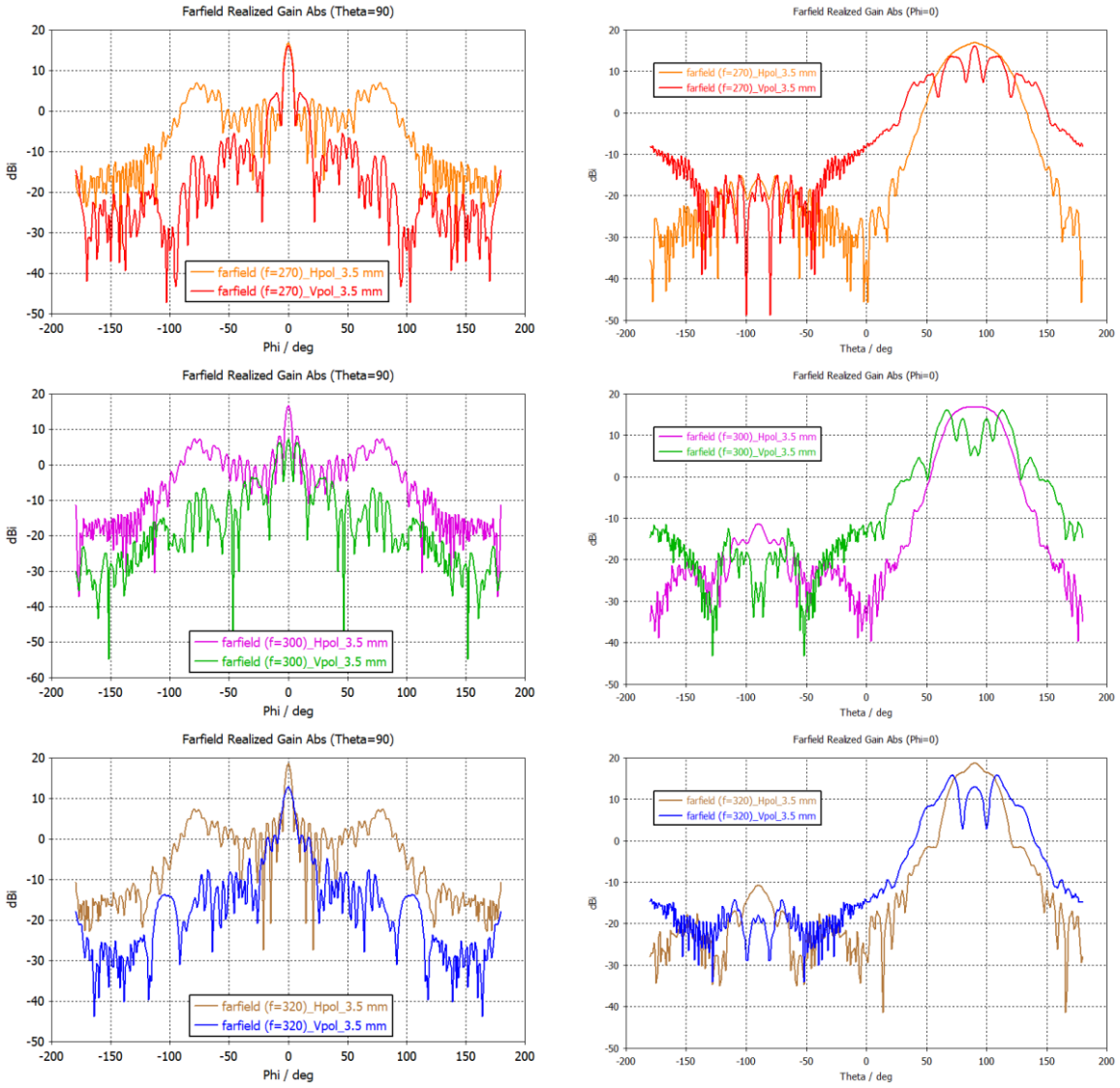

(c)

Figure 7.33: The simulated radiation patterns of horizontal (Theta = 90) and elevation (Phi=0) planes of the dielectric lens with metallic foam (a) 1mm (b) 2 mm and (c) 3.5 mm thicknesses.

7.6.4.3 Conclusion

We can conclude that for 1 mm without flaring the radiation patterns are very bad for vertical and horizontal polarization excited but when we put the metallic flare we remove the problem for both polarization, especially for horizontal polarization.

For the 2 mm without the flare for both V&H -Pol, the radiation patterns are tolerant. For the 2 mm with metallic flare with V-pol the radiation pattern is catastrophic, but for H-pol is very good.

For a very thick lens of 3.5 mm, we have multibeam (3 beams) which works as an array with multi-source with a distance of 'λ', which means we do not succeed to excited to in phase all the aperture 3.5 thickness we have some phase rotation i.e big aperture not excited in phase but with metallic flare, the multibeam in V-pol excited became as a ripple and for H-pol we remove the multibeam and the radiation pattern became very good.

For all thicknesses with metallic flare, we noted there are two beams generated beside the main beam in the azimuth plane when the lens is excited by H-pol. The reason for that is because the end of the lens is like an aperture and this aperture is excited by another aperture (flare aperture), in this case, if we excite the flare in phase, the results will be good.

It is discovered from Figure 7.34 that The electric field of the lens with foam for vertical and horizontal excitation is not equal for all different thickness lenses as we noted in the gain radiation patterns for azimuth and elevation planes.

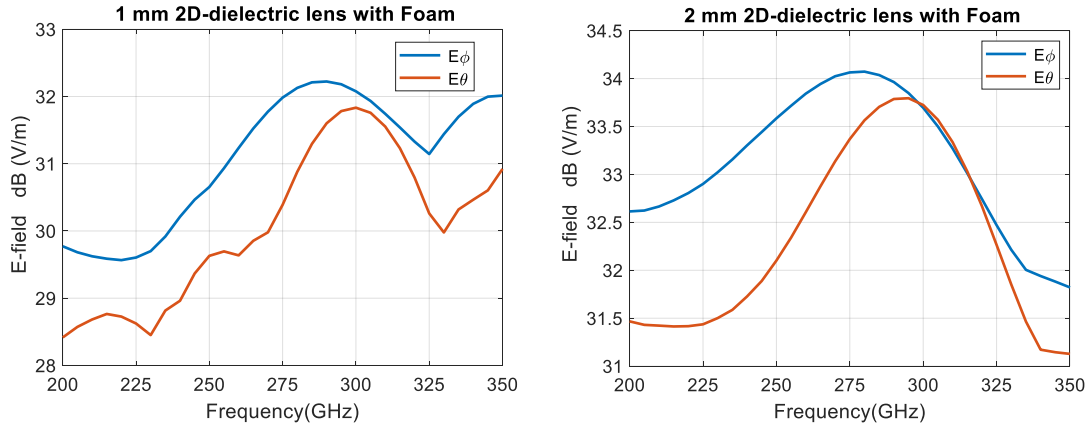

(a) (b)

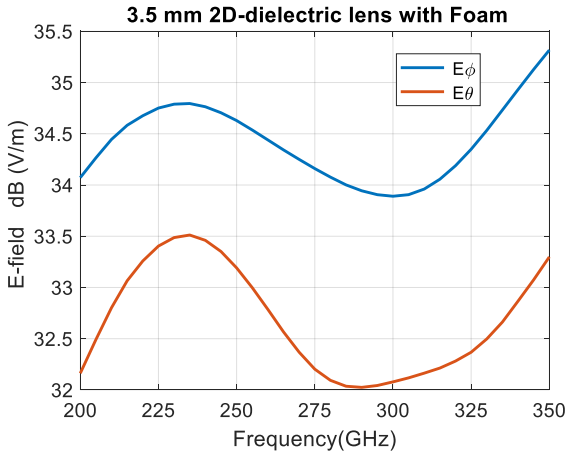

(c)

Figure 7.34: The electric field of the lens with foam for vertical and horizontal excitation.

It is discovered from Figure 7.35 that the electric field of the lens with a flare for vertical and horizontal excitation is not equal for all different thickness lenses as we noted that without flare (i.e with foam).

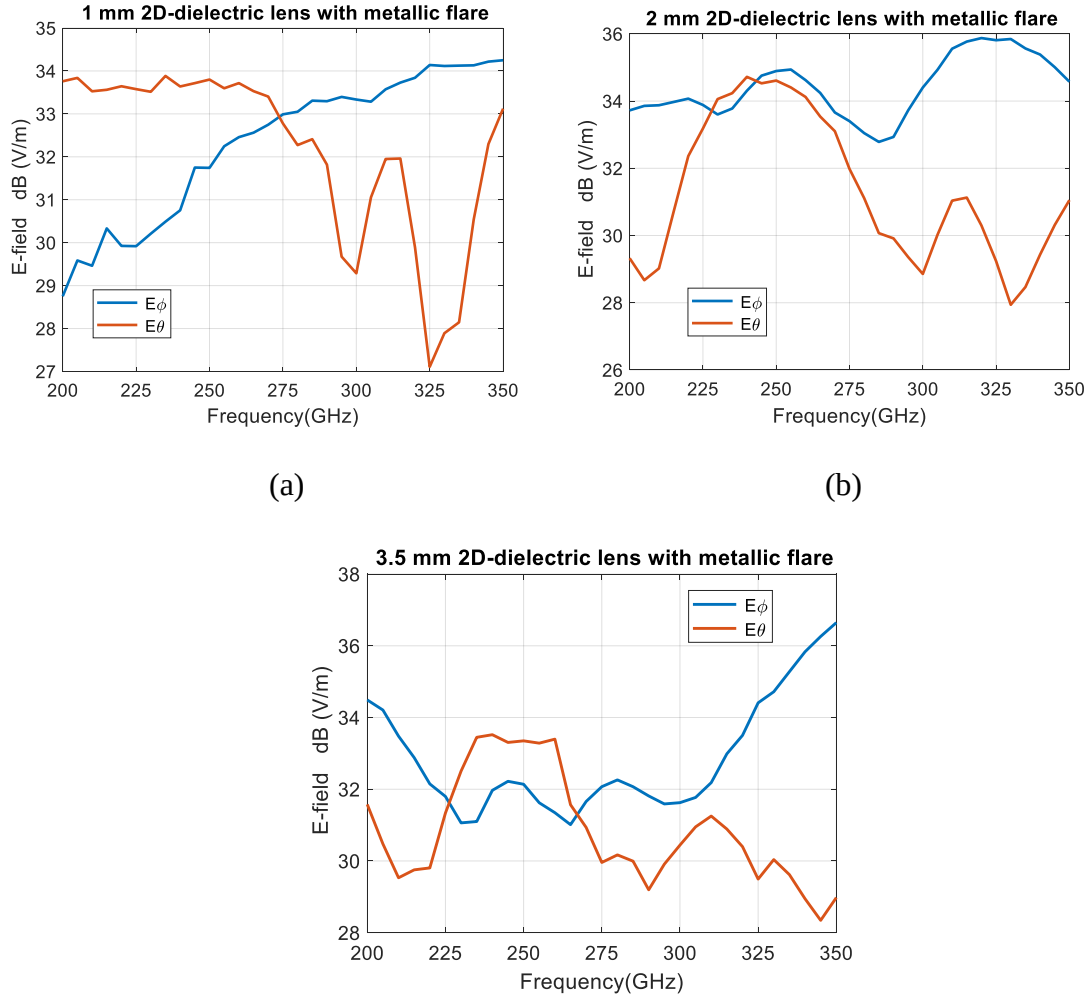

(a) (b)

(c)

Figure 7.35: The electric field of the lens with a metallic flare for vertical and horizontal excitation.

7.6.5 Antenna Fabrication and Measurement

The prototypes of the metallic flare with different thicknesses of 1 mm, 2 mm, and 3.5 mm are fabricated using CNC machining as shown in Figure 7.36.

Figure 7.36: The prototypes of the metallic flare with different thicknesses.

The prototypes of the metallic flare connected to the WM-864 waveguide flange (220- 330 GHz) with different thicknesses are shown in Figure 7.37.

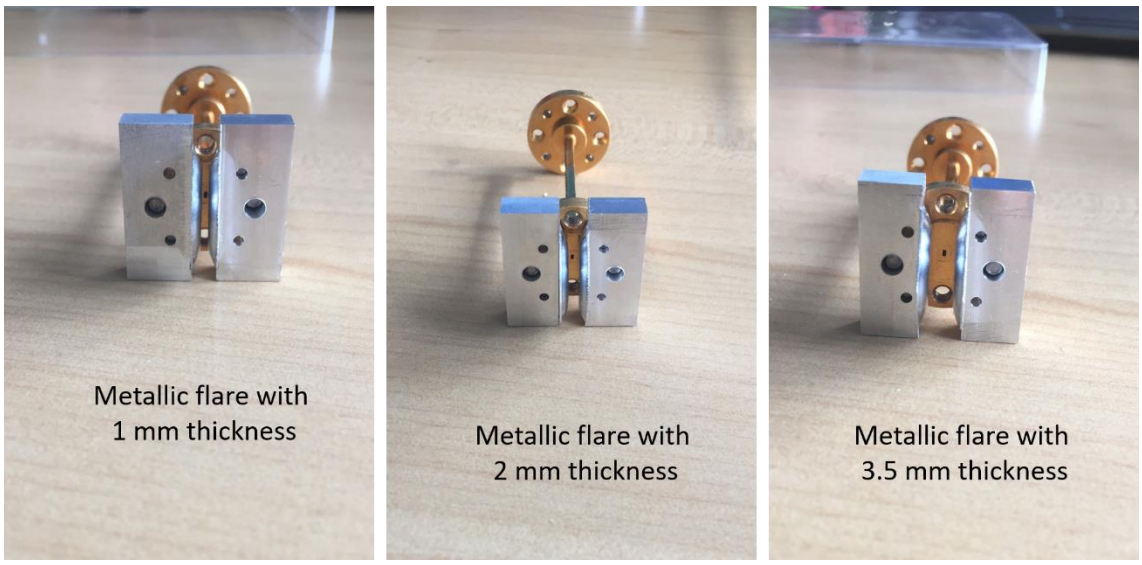

Figure 7.37: The prototypes of the metallic flare connected to the WM-864 waveguide flange with different thicknesses.

The prototypes of the dielectric lens with metallic flare connected to WM-864 waveguide flange with different thicknesses are shown in Figure 7.38.

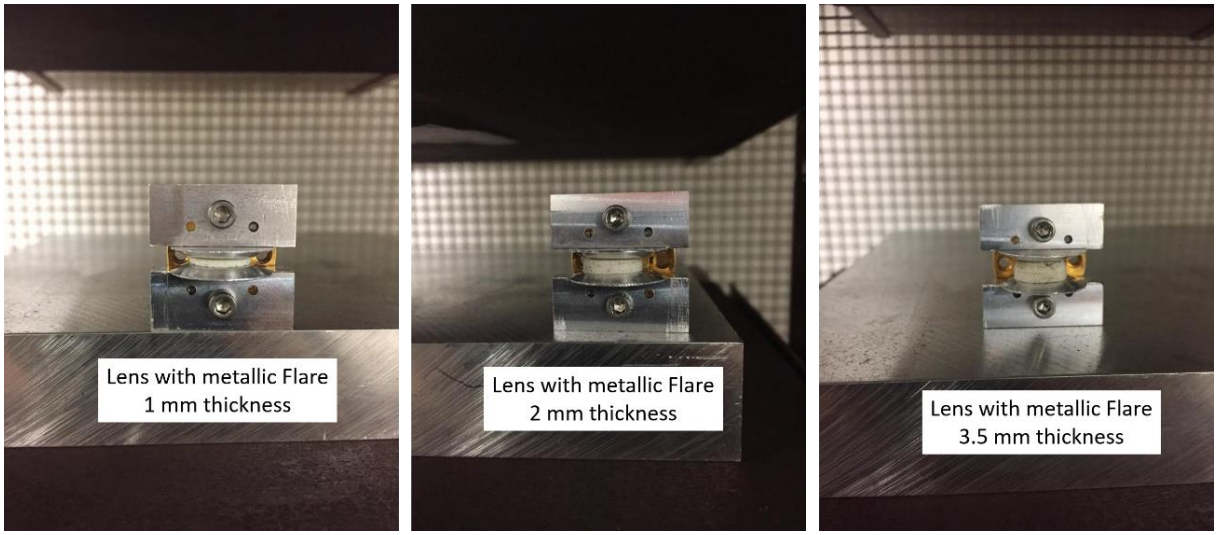

Figure 7.38: The prototypes of the dielectric lens with metallic flare connected to WM-864 waveguide flange with different thicknesses.

The prototype of a 2 mm dielectric lens with a metallic flare connected to the WM-864 waveguide flange and frequency extender using vertical horizontal polarization feed is shown in Figure 7.39.

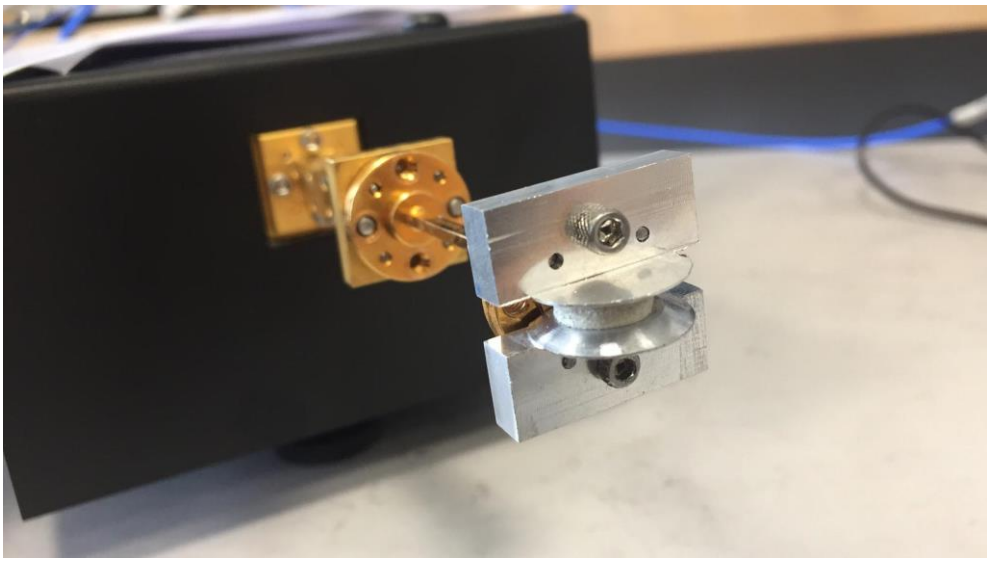

(a)

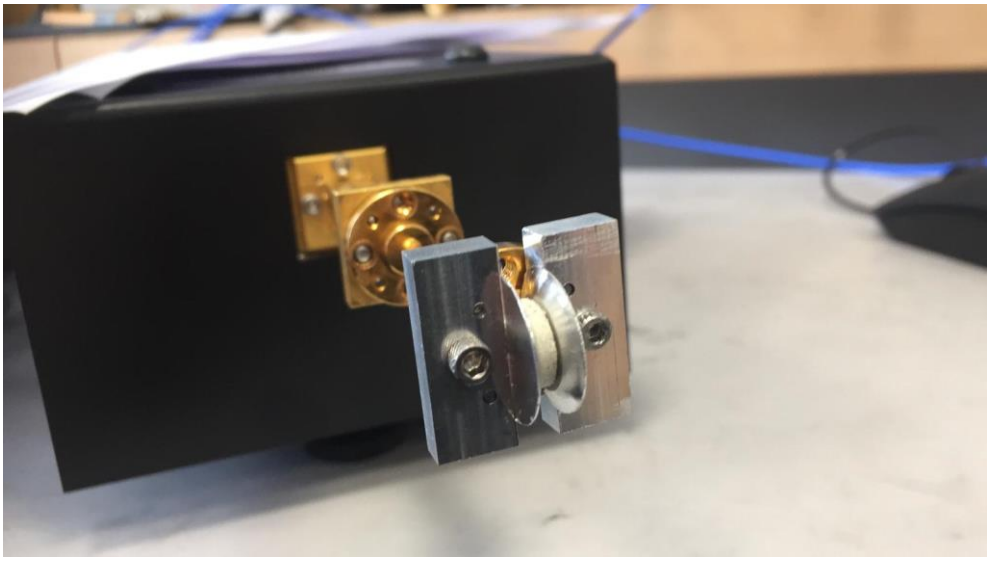

(b)

Figure 7.39: The prototype of a 2 mm dielectric lens with metallic flare connected to WM-864 waveguide flange (a) vertical (b) horizontal polarization feed.

The measured reflection coefficient (S11) of the vertical polarization feed for a dielectric lens with metallic flare is presented in Figure 7.40 (a). We can note the matching is improved with the lens as compared without the lens as shown in Figure 7.40 (b).

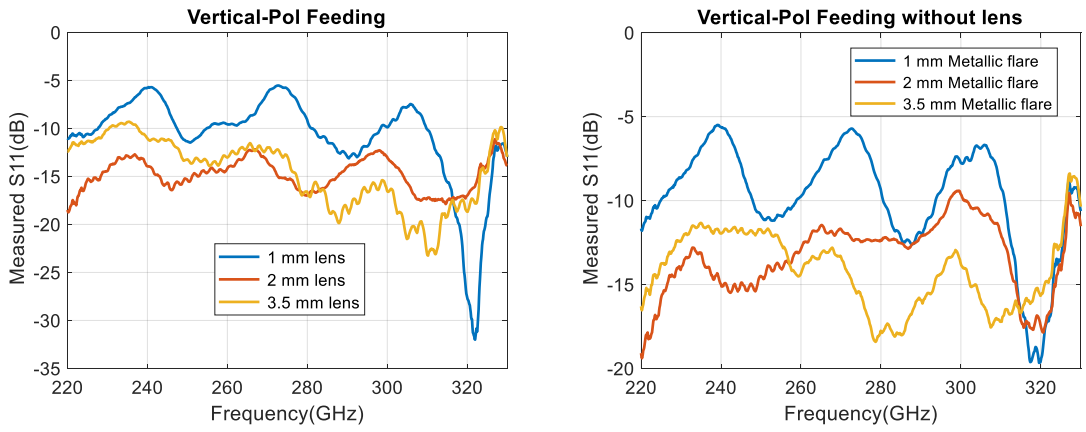

(a) (b)

Figure 7.40: The measured reflection coefficient (S11) of vertical polarization feed (a) with lens (b) without the lens.

The measured reflection coefficient (S11) of the horizontal polarization feed for a dielectric lens with metallic flare is presented in Figure 7.41(a). We can note the matching is improved with the lens as compared without the lens as shown in Figure 7.41 (b).

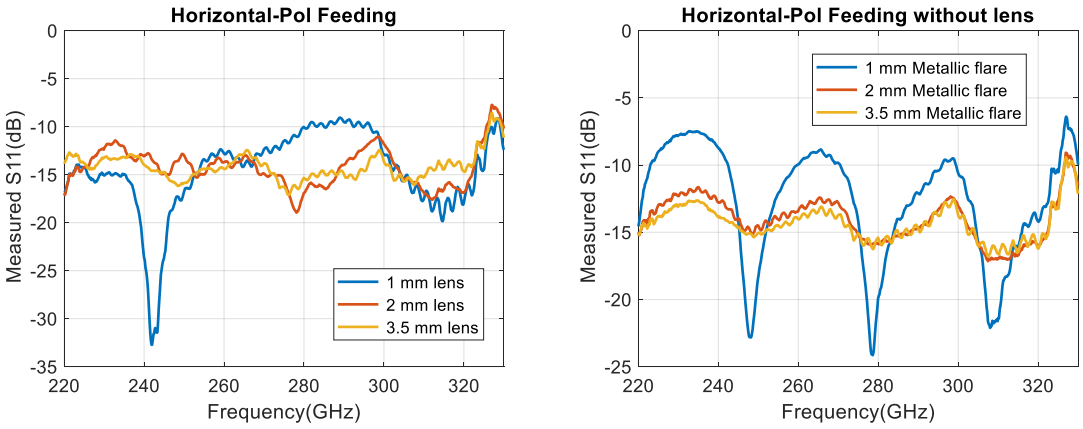

(a) (b)

Figure 7.41: The measured reflection coefficient (S11) of horizontal polarization feed (a) with lens (b) without the lens.

The measured reflection coefficient (S11) of a 2 mm dielectric lens with foam support with vertical and horizontal polarization feeding is presented in Figure 7.42. The foam support without a lens works over the 220-330 GHz which is corrected similarly to the WM-864 waveguide.

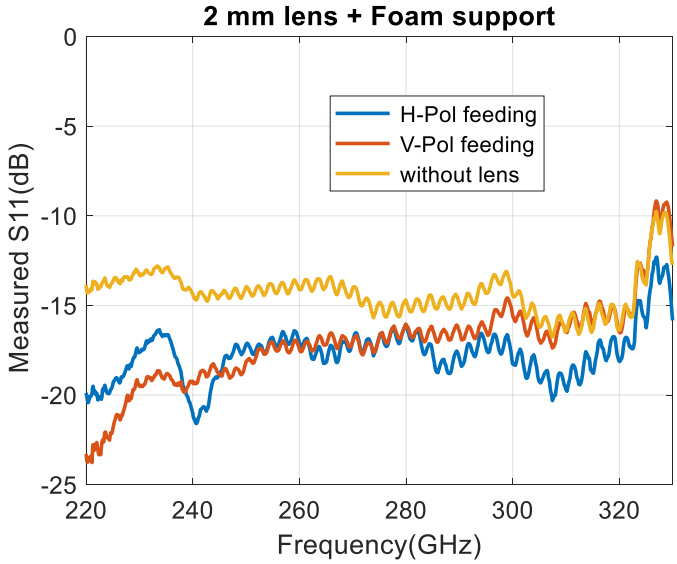

Figure 7.42: The measured reflection coefficient (S11) of a 2 mm dielectric lens with foam support with different polarization feeding.

The measured radiation patterns are not provided at this stage due to relocating the chamber room at IETR to another building, maybe will be ready in next day and we can present the results on the day of defense.

7.7 Circularly Polarized 2D Luneburg Lens Antenna

7.7.1 CP-Lens with Foam Support

The design structure of the circularly polarized Luneburg lens antenna at 300 GHz is shown in Figure 7.43. The structure consists of three parts, waveguide feeding, circularly polarized (CP) part, and dielectric Luneburg lens. The CP element is a double-fan shaped-slot shown in Figure 7.43(c). The dielectric lens has a thickness of 2 mm. The foam with permittivity close to one (i.e. Rohacell foam), is used as support for the Luneburg lens antenna.

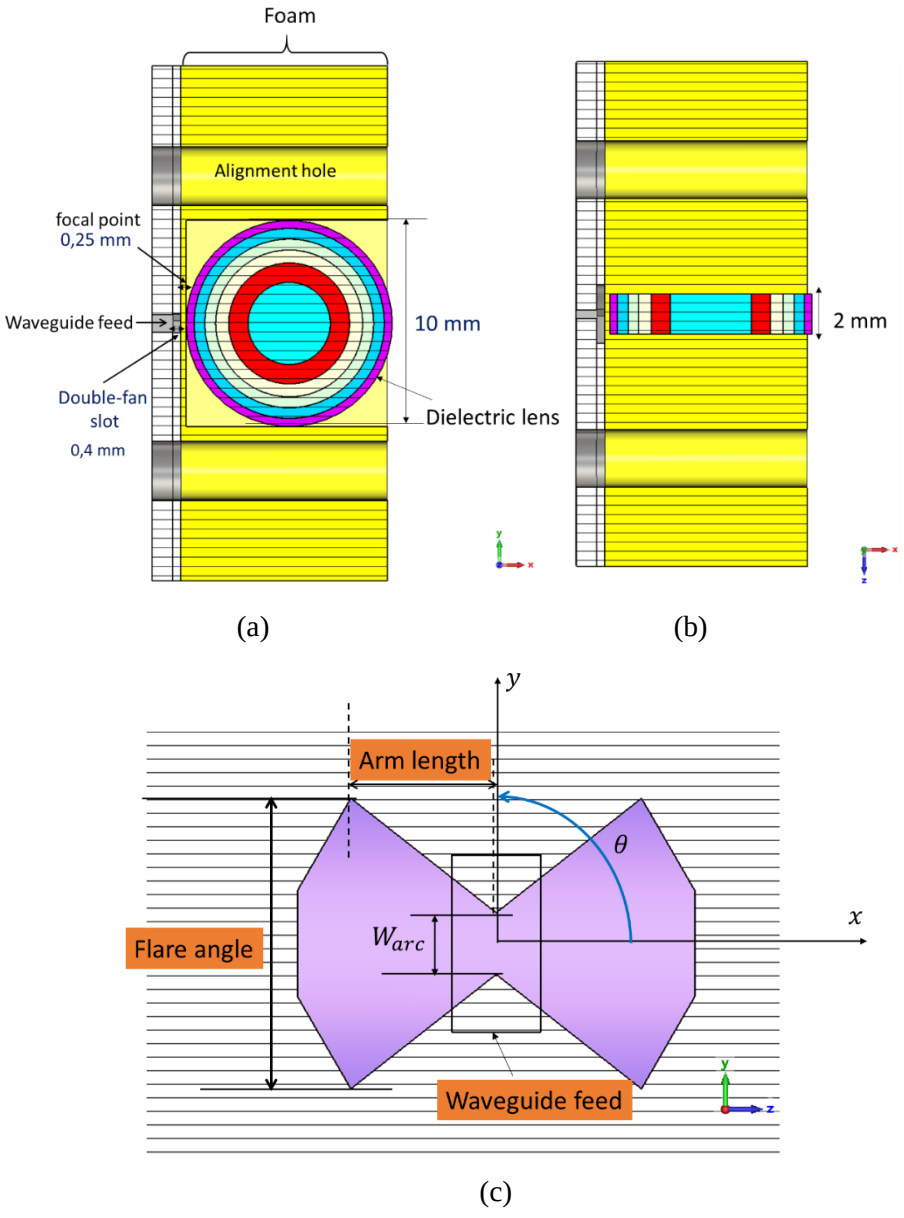

Figure 7.43: Circularly Polarized Luneburg Lens Antenna (a) top view (b) side view and (c) double-fan shaped-slot element.

The simulated results of reflection coefficient (S11), realized gain total efficiency, and axial ratio (AR) for five different double-fan-shaped slot designs in Table 3.1 are shown in Figure 7.44. Design numbers #3, and #5 are given the best results in terms of stability of gain and total efficiency compared with other designs.

Table 7.6: The optimum design parameters.

	Flare angle (degree)	Arm length (mm)	W_{are} (mm)	θ (degree)
Design #1	90	0.6	0.4	30
Design #2	90	1	0.3	30
Design #3 (Prototype #1)	90	1.5	0.3	30
Design #4	90	1	0.3	35
Design #5 (Prototype #1)	90	1.5	0.3	35

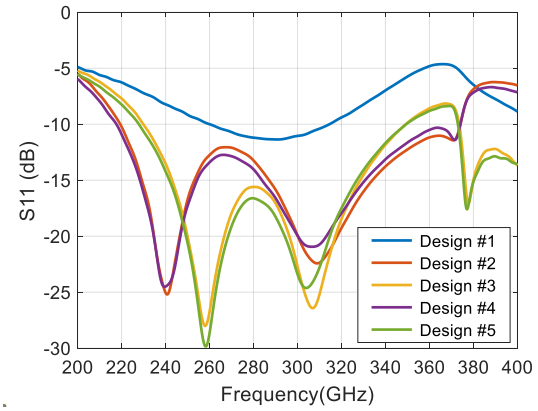

(a)

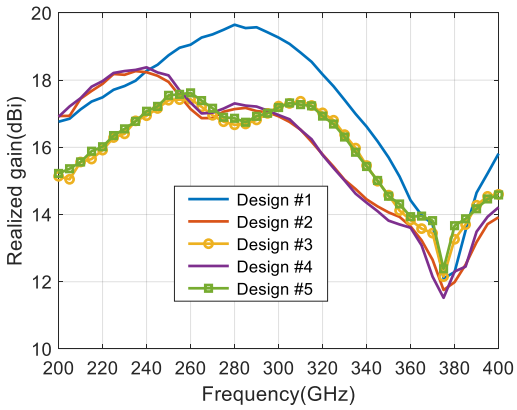

(b)

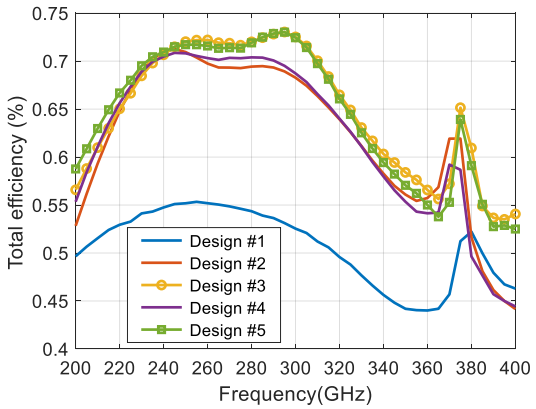

(c)

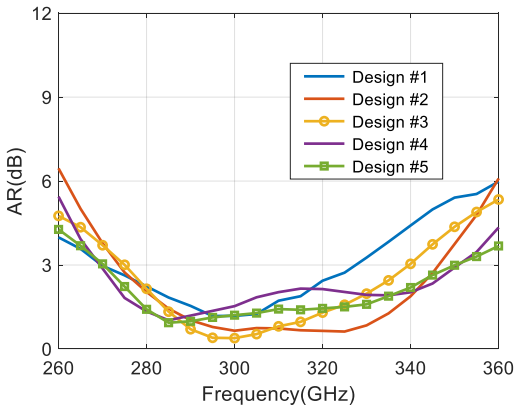

(d)

Figure 7.44: Simulated (a) reflection coefficient, (b) realized gain ,(c) total efficiency and (d) axial ratio (AR) for design#3.

Figure 7.45 presents the simulated realized gain radiation pattern and 3dB-AR vs theta, respectively for Design #3. As shown in the figure, the antenna exhibits good directional radiation characteristics over the operating frequency range and achieves an HPBW of lower than 5.8 ˚with a maximum gain of 17.4 dBic at 310 GHz. An axial-ratio beamwidth of 6.54 ˚is presented below 3 dB.

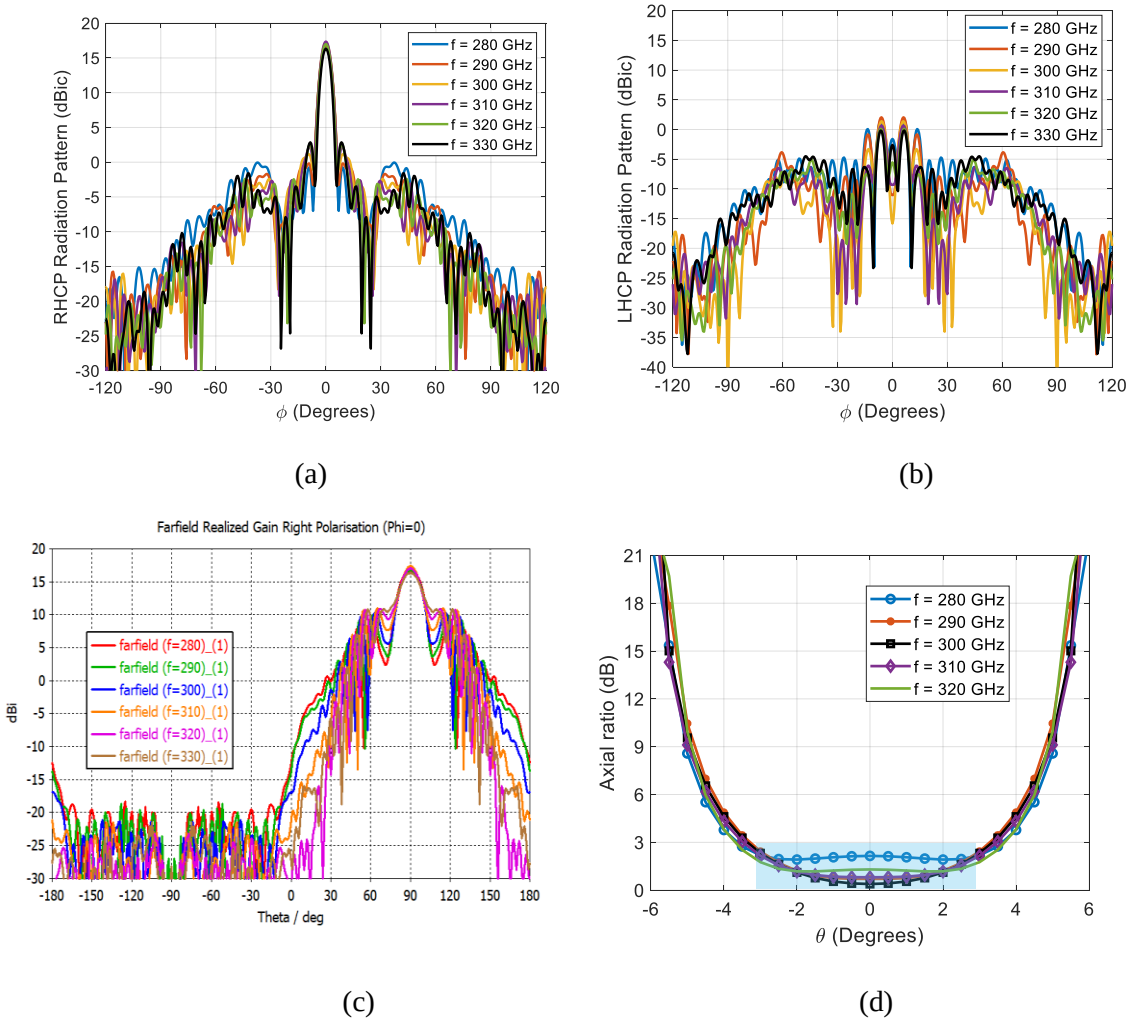

Figure 7.45: Simulated (a) RHCP, (b) LHCP azimuth -plane ,(c) elevation radiation patterns and (d) AR vs.theta.

In Figure 7.46 the double-fan slot alone (red curve), the AR is good between 215-250 GHz, and in the range (275-340 GHz) is linear polarization. The lens with a double-fan slot (dashed line) is corrected the polarization of the fan slot alone in the range (275-340 GHz) but there is degradation in the range (215-250 GHz) as the fan slot alone works well.

We conclude that the lens has improved the AR compared to the double-fan-shaped slot alone (i.e. increased the AR bandwidth) as shown in Figure 7.46.

The AR of a double fan slot with metallic flare is catastrophic which is near to the linear polarization however the combination of the double fan slot with lens and metallic flare gives a better AR bandwidth due to the metallic flare is improved the elevation plane at 300 GHz which noted in the linear dielectric lens in vertical polarization.

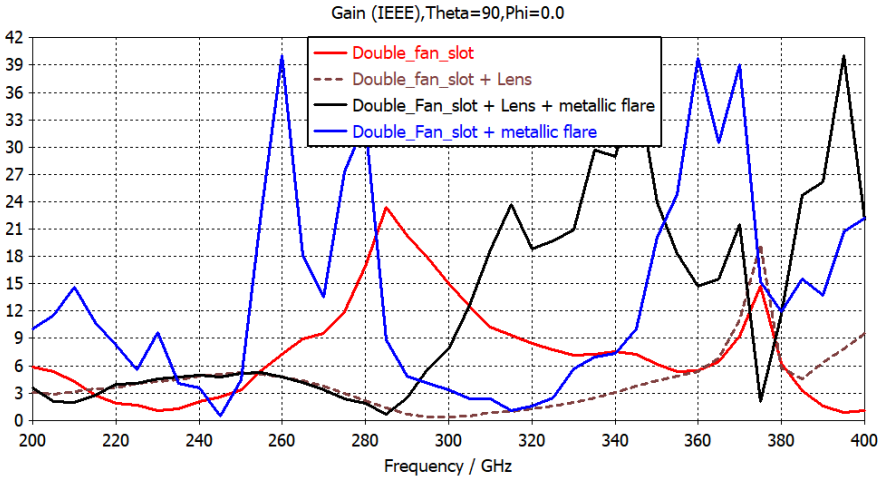

Figure 7.46: The AR double-fan shaped-slot CP element with different structures.

7.7.2 CP-Lens with Metallic Flare

The CP dielectric lens with metallic flare is similar to the CP lens with foam only the structure has been changed in the parameters of the double-fan shaped slot element with metallic flare. Two different design structures have been proposed as shown in Table 7.7.

Table 7.7: The optimum design parameters.

Design	W_{are} (mm)	θ (degree)	Arm length (mm)	Flare angle (degree)
#1	0.4	30	0.6	120
#2	0.45	45	0.5	120

The simulated results of reflection coefficient (S11), realized gain, and axial ratio (AR) for two different in Table 3.1 are shown in Figure 7.47.

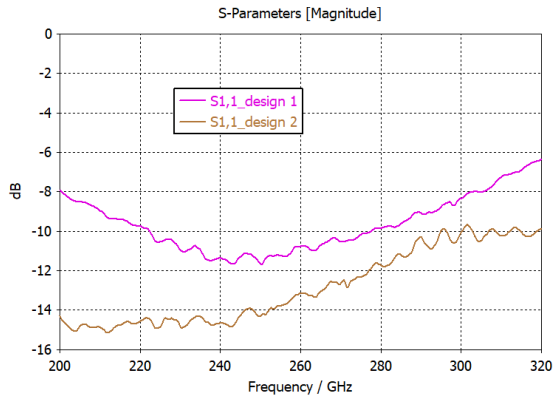

(a)

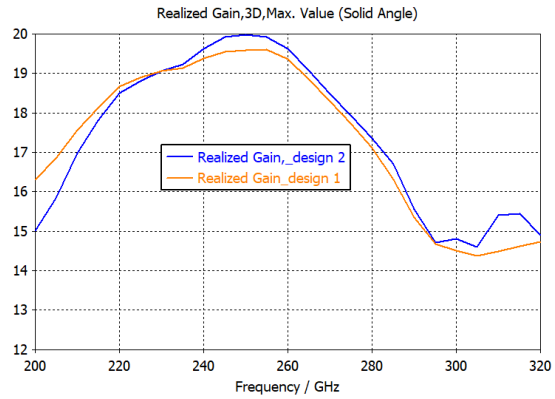

(b)

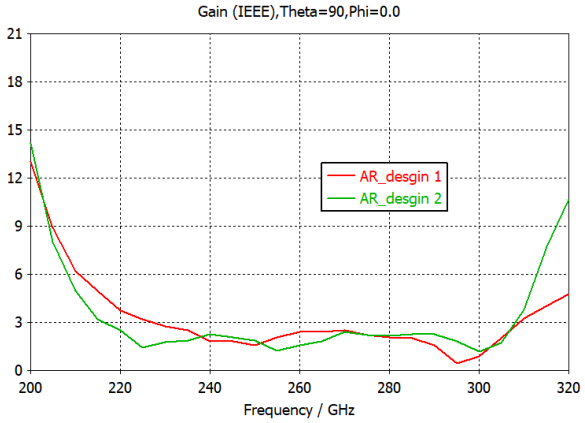

(c)

Figure 7.47: Simulated (a) reflection coefficient, (b) realized gain, and (c) axial ratio (AR) for designs #1 and#2.

Figure 7.45 presents the simulated realized gain radiation pattern for Designs #1 and #2 at different frequencies. As shown in the figure, the antenna exhibits good directional radiation characteristics over the operating frequency range and achieves an HPBW of lower than 6.4 with a maximum gain of 19.9 dBic at 250 GHz.

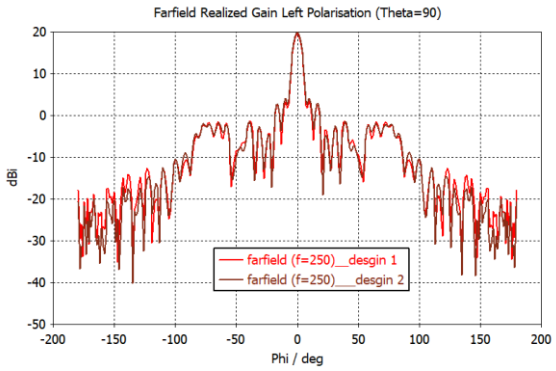

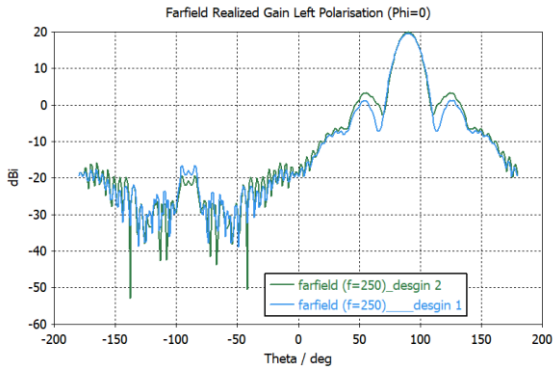

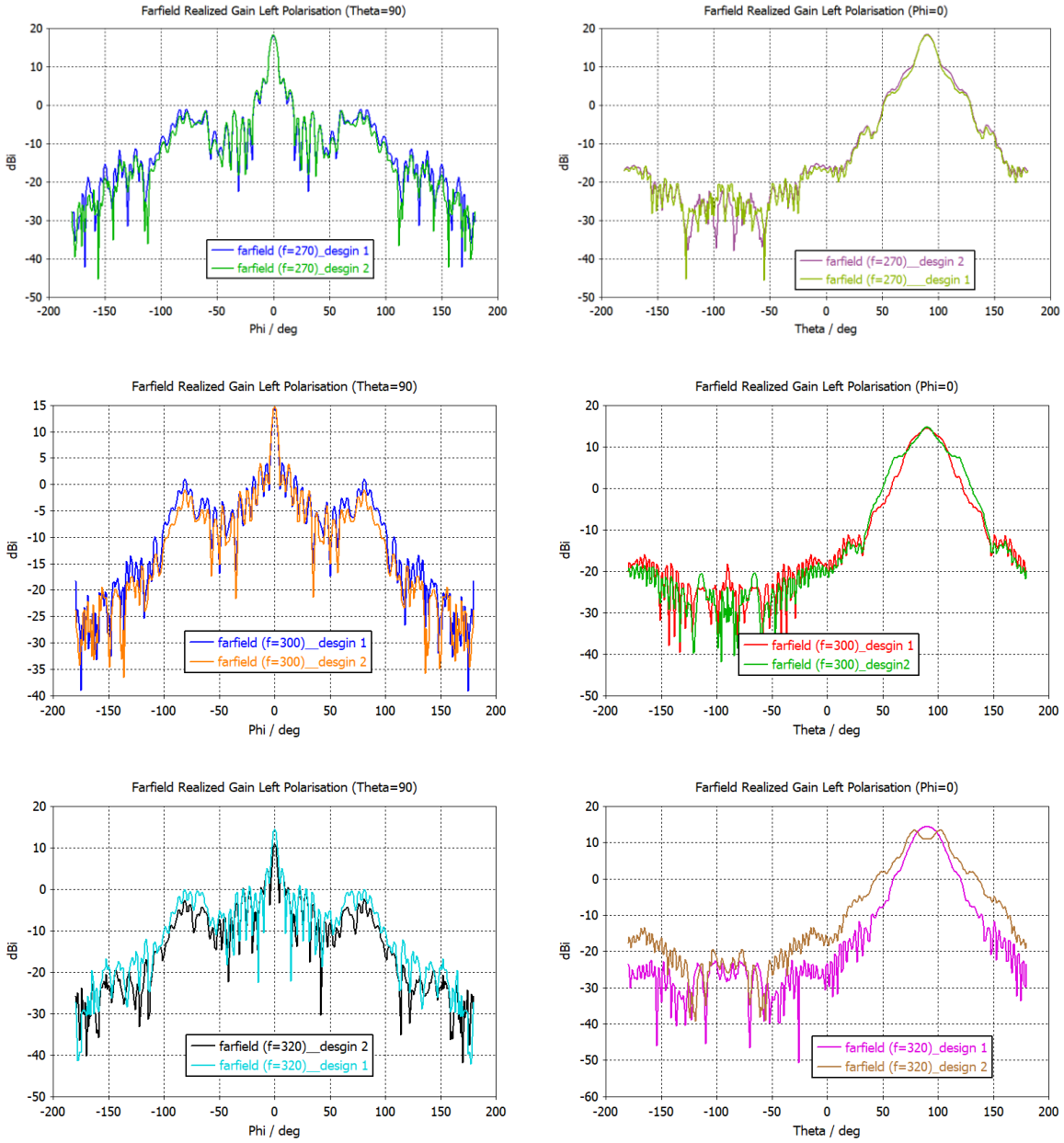

Figure 7.48: Simulated LHCP horizontal and elevation radiation patterns

7.7.3 Antenna Fabrication and Measurement

Figure 7.49 shows the WM-864 waveguide flange connected to the prototype CP dielectric lens antenna with support foam, required for compatibility with our standard experimental setup. A laser cutting machining was selected to manufacture the double-fan-shaped slot CP element. The material employed was brass due to its good conductivity and mechanical properties.

Figure 7.50 shows the simulation and measurement results for the CP Luneburg Lens antenna with foam support. As shown in the solid blue curve of Figure 7.50, good matching is obtained

with S11 < -10 dB from 220 to 330 GHz, which represents a fractional BW of 36.67 %, in good agreement with the simulation results (dashed red curve).

The measured radiation patterns are not provided at this stage due to relocating the chamber room at IETR to another building, maybe will be ready in next day and we can present the results on the day of defense.

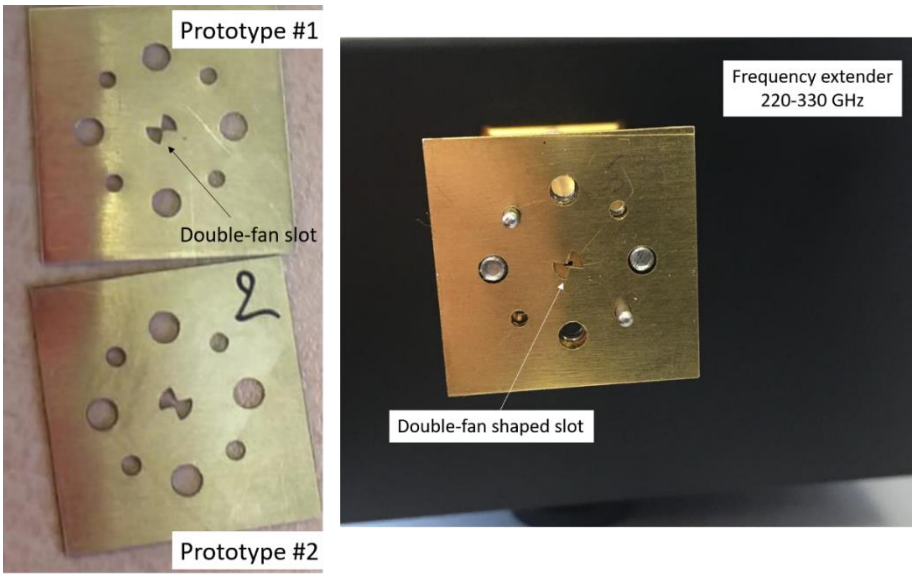

(a)

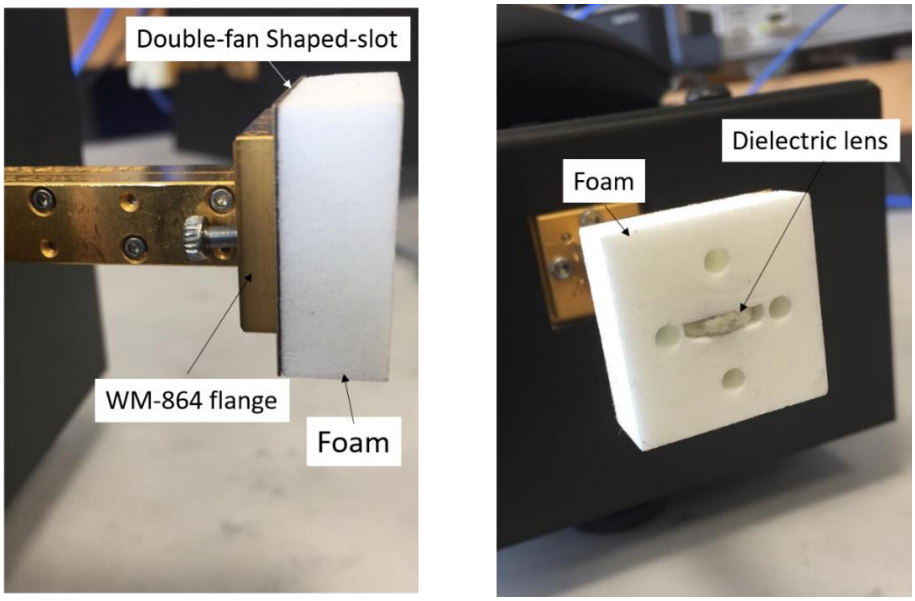

(b)

Figure 7.49: Manufacturing of CP Luneburg lens. (a) side view of the two prototypes of double-fan shaped slot and (b) CP dielectric Luneburg lens.

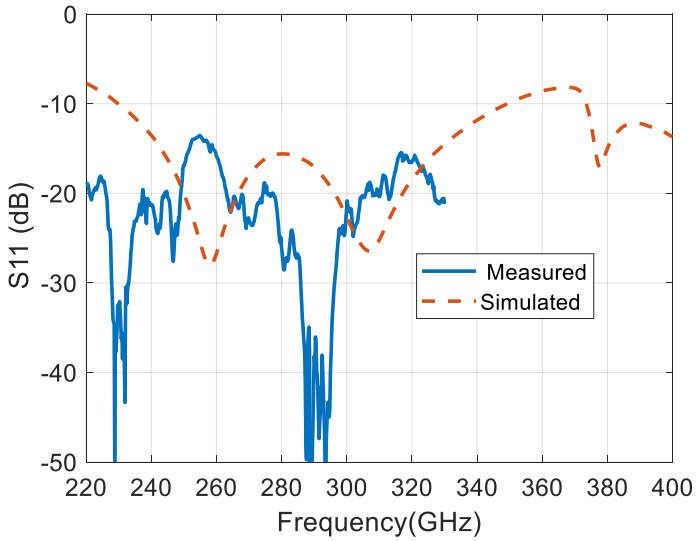

Figure 7.50: The reflection coefficient (S11) for CP Luneburg Lens antenna with foam support.

Chapter 8 General conclusion and perspectives

The main objective of this thesis is to develop and fabricate all-metal high gain sub-THz antennas utilizing different fabrication technologies at 300 GHz frequency bands. The thesis covers a wide range of topics related to the designs and fabrication processes of the mentioned designs. Six antennas are constructed utilizing four distinct fabrication technologies: wire-electrical discharge machining (EDM) (one prototype), laser-cutting machining (three prototypes), Silicon micromachining (one prototype), and CNC milling (one prototype) (one prototype).

At the end of this Ph.D. thesis, 2D completely metallic PPW Luneburg lens antennas perform as beamforming for 6G wireless communications in the WM-864 bands (220 -330 GHz). Two different designs were created, both of which work in the TEM mode, are broadband, and have a low loss. The first one, the PPW Luneburg lens loaded with variable cylindrical metallic posts, has wider bandwidth, and high gain has the advantage of enabling all-metal material. The second one, is the PPW Luneburg lens loaded with uniform-size cylindrical metallic posts.

With these two designs, several lenses were designed and simulated, among them, two configurations of 10.5 diameters fed by a standard waveguide (WM-864), were chosen and integrated into multi-beam antennas. Two multi-beam antennas were designed and simulated with excellent performances.

Summary

In Chapter 1:

The general background of the terahertz spectrum is described, as well as its uses and emerging B5G possibilities. In terms of propagation and generation sources, the major THz band restrictions and hardware constraints are presented.

- In Chapter 2:

A state-of-the-art on different fabrication technology is presented as reviewing for exiting fabricated antennas in the sub-terahertz band. Most of the structures discussed in this thesis are based on metallic structures which can be replaced with substrate structures to avoid dielectric loss which big problem in the terahertz band. The passive multibeam antennas based on Lenses are thoroughly discussed to achieve the desired beamforming in the RF domain without using any active components. The Luneburg lenses have a more stable performance with a wider bandwidth and are so used in the development of many of the presented designs in this thesis. As our main focus is high gain antennas, a comparison between the existing antennas in literature in terms of the fabrication technology, radiation losses, operating frequency, highest

achieved realized gain, and the system structure to assess its complexity for fabrication and its usability for mass production are all discussed.

- In Chapter 3:

Wire-cutting electrical discharge machining is used to fabricate circularly polarized conical horn antenna in one block of metal at 300 GHz. Circular polarization (CP) was achieved by exiting two orthogonal modes through the crossed slot of the circular polarizer disk of the horn antenna. We used mechanical drilling technology for a novel footprint disk of CP part with a thickness of 100 μm and 4 holes alignments parts of the whole structure. We have added a small disk to the CP part to keep the crossed slot in the exact position (tail of big disk) to avoid movement of a big desk of CP. A laser etching technique has been used to create crossed slot of CP part in the horn antenna as narrower as 100 µm. The waveguide part is manufactured by wire-cutting EDM technique in a brass block due to the waveguide flange (WM-864) not being available at the first stage of our work in IETR. The antenna yields a measured impedance bandwidth of 60 GHz from 270 GHz to 330 GHz. The measured directivity of 18.3 dBic at broadside direction at 312 GHz. The measured 3-dB AR bandwidth of 7 GHz from 309 GHz to 316 GHz. Radiation patterns of the fabricated Sub-THz CP conical horn antenna have been measured and the results agree well with the simulations. Its high performance provides a low-cost enabling solution for several applications in the sub-THz region, including radar or 6G communications. The full thickness of the prototype is 5 mm. (conical horn part and CP polarizer), which is a bulky structure in terms of wavelength and is difficult to ingrate with other active components. Future work for this prototype is to replace it with a low-profile and planar structure.

- In Chapter 4:

The challenges faced in Chapter 3 (bulky structure and the need to fabricate the waveguide part) are faced and solved. A low-cost laser-cutting technology is applied for the first time on brass metallic to design three Fabry-Perot cavity (FPC) planar antennas at 300 GHz. The three antennas are built on seven brass layers with a low profile of only 1.24 mm (i.e. total thickness.)

The **first prototype** is the linearly polarized FPC antenna consists of seven metallic layers; a ground layer, an integrated stepped horn element (three-layers), a coupling layer, a cavity layer, and an aperture-frequency selective surface (FSS) layer. The aperture-FSS layer acts as a partially reflective surface, contributing to a directive beam radiation. The linearly polarized FPC antenna has a measured reflection coefficient below - 10 dB from 282 to 304 GHz with a bandwidth of 22 GHz. The maximum measured gain observed is 17.7 dBi at 289 GHz, and the

gain is higher than 14.4 dBi from 285 to 310 GHz. The measured radiation pattern shows a highly directive pattern with a cross-polarization level below - 25 dB over the whole band in all cut planes, which confirms the simulation results. A deviation of 5° between the measured and simulated main beam in azimuth-plane cuts from the broadside direction was observed. This is because we discovered that one of the waveguide flanges that have been used as a small tilt we avoid this problem with a circularly polarized FPC antenna.

The second prototype is the circularly polarized (CP) FPC antenna. The CP-FPC antenna consists of seven metallic layers. The first six layers arranged from the bottom to the top, are similar to linearly polarized FPC. The seventh layer was working as a polarizer to convert LP waves into CP waves. The high gain and self-generation of circular polarization are made by using this FSS layer by introducing a periodic hexagonal–shaped aperture in a thin metallic layer. The aperture–FSS layer is used to excite two orthogonal modes of equal in magnitude and in phase quadrature, thus obtaining the RHCP radiation. The CP-FPC antenna prototype achieves a measured peak RHCP gain of 16.5 dBic at 292 GHz. The 300 GHz CP-FPC antenna has been characterized using a millimeter-wave compact range anechoic chamber, obtaining radiation patterns characteristics between the frequency from 285 to 315 GHz. The antenna achieves a measured impedance bandwidth of 281– 305 GHz for the reflection coefficient less than -10 dB. The axial ratio (AR) bandwidth AR ≤ 3 dB is 5.12 GHz from 292.8 to 297.92 GHz.

The third prototype is a circularly polarized resonant cavity antenna (CP-RCA), with a novel single-layer metasurface as a superstrate operating at 300 GHz. The unit cell of the metallic metasurface layer consists of perforated grids of hexagonal and octagonal-shaped radiating apertures. The metasurface superstrate layer acts as a polarization converter from linear to circular, which provides left-handed circularly polarized (LHCP) radiation. The CP-RCA yields a measured LHCP gain of 16.2 dBic with directivity of 16.7 dBic at 302 GHz. A 3 dB measured AR bandwidth of approximately 1.41% (4.24 GHz) with a central frequency of 296 GHz is achieved. All prototypes have been designed with the standard WM-864 waveguide flange, which contains holes for the alignment pins and screws, enabling a direct connection to the standard UG-387 waveguide flange without any additional test fixtures or interfaces. This direct-mount procedure is easier than alternative setups of silicon-micromachining which needs the bonding alignment method. This technology is attractive in terms of low cost and less complexity compared with silicon micromachining technology. Finally, all prototypes have a low profile, low fabrication cost, high gain, and wide operating bandwidth. of 2.6 λ_0×2.6 λ_0×1.24 λ_0, which can be applied to future terahertz 6G wireless communication systems in the sub-THz band. The 3dB AR bandwidth for both circularly polarized prototypes is less than 5 GHz. Future work for these prototypes is to replace them with low-profile Planar Corrugated structures.

- In Chapter 5:

The challenges faced in Chapter 4 (i.e. narrow 3dB-AR bandwidth) are faced and solved. Two different technologies are used to fabricate a circularly polarized (CP) bull's eye antenna at 300 GHz.

The first technology is silicon micromachining which is applied to design a circularly polarized bull's eye antenna with a crossed-slot element at 300 GHz. The prototype consists of three silicon layers with a thickness of 200-µm, and two of 400-µm. The feeding WM-864 waveguide is etched in the bottom wafer. The crossed-slot and the six-ring slots are etched in a wafer of the thickness of 200-µm. After sputtering gold, the three silicon wafers are bonded together by gold–gold thermocompression. We scribed the wafers to get the CP bully's eye antenna with a dimension of $20 \times 20 \times 1$ mm^3. The measured reflection coefficient of the antenna is lower than -10 dB from 279.2 GHz to 314 GHz with a bandwidth of 34.8 GHz. There is a shift between measurement and simulation results due to fabrication tolerance. A maximum simulated LHCP realized gain of 16.13 dBic is achieved. The total efficiency is more than 80%, between 295- 325 GHz. The minimum simulated AR at 290 GHz is 0.675 dB with the 3-dB AR bandwidth of 21 GHz between 287 GHz to 308 GHz being 7 %.

The second technology is a computer numerical control (CNC) milling which is applied to design a circularly polarized bull's eye antenna with a double-fan shaped-slot element at 300 GHz. The prototype is fabricated on one layer with a thickness of 400-µm. The material employed was aluminum due to its good conductivity and mechanical properties. We used this CNC milling with the double-fan shaped-slot element due to the difficulty to reach a high thickness of 1000 –µm using silicon micromachining and expansive. The six concentric periodic corrugations with period p, depth Dg, and width Wg are similar to the porotype fabricated using silicon micromachining. Only Two differences between the two porotypes. The first one is the total thickness (1000-µm and 400-µm) and the second one is the element to generate circular polarization characteristics (crossed-slot and double-fan shaped-slot).
The measured reflection coefficient of the antenna is lower than -10 dB from 220 GHz to 330 GHz with a bandwidth of 110 GHz, which is in good agreement with the simulation results. A maximum simulated RHCP realized gain of 16.37 dBic is achieved The total efficiency is more than 88%, between 260 - 360 GHz. The minimum simulated AR at 300 GHz is 0.12 dB with the 3-dB AR bandwidth of 32.39 GHz

Due to the new building construction of the IETR lab and the time to move the facilities maybe on May/June 2022 we don't have a chance to measure gain, axial ratio, and far-field radiation patterns for both prototypes

- In Chapter 6:

In this chapter, the complete design and simulation of the sub-THz beam-scanning antenna were presented. The antenna is a fully metallic PPW Luneburg lens antenna excited by a standard waveguide. The antenna is designed at 300 GHz and operates in the WM-864 band between 220 GHz and 330 GHz. The lens has 10.5 mm in diameter and is made of metallic posts. The permittivity is controlled by one degree of freedom: the metal post thickness. This parameter changes according to the radial distance to the lens' center and achieves the permittivity values required by the Luneburg law. The design has been performed with Matlab, CST. Mainly, the unit cell has been analyzed in the Eigenmode solver in CST and the overall antenna in the Time domain solver in CST. Matlab has been used for computing the mapping between unit cell geometrical and effective refractive index parameters.

The full-wave simulation of the sub-THz beam-scanning antenna has been done in CST in a single feed and multiple feed configurations. First, the single two types of feeds (double-ridge waveguide and standard WM-864 waveguide) have been studied at different diameters (6.5 λ_0 and 10.5λ_0), then beam-scanning antenna with 37 feeds.

In the single double-ridge waveguide feed with 6.5 λ_0 configuration, the antenna is matched in the operating bandwidth below at -8 dB between 270-350 GHz. The sidelobe levels are low, -15 dB below the main beam maximum level. The maximum gain ranges approximately from 17.3 dBi at 270 GHz to 20.5 dBi at 330 GHz. Furthermore, with 10.5 λ_0 configuration, the antenna is matched in the operating bandwidth below at -8 dB between 260-345 GHz. The sidelobe levels are low, -14 dB below the main beam maximum level. The maximum gain ranges approximately from 20 dBi at 270 GHz to 22.8 dBi at 320 GHz.

In the single standard WM-864 waveguide feed with 6.5 λ_0 configuration, the antenna is matched in the operating bandwidth below at -15 dB between 250-350 GHz. The sidelobe levels are low, -17 dB below the main beam maximum level. The maximum gain ranges approximately from 20.3 dBi at 280 GHz to 21 dBi at 310 GHz. Furthermore, with 10.5 λ_0 configuration, the antenna is matched in the operating bandwidth below at -10 dB between 250-350 GHz. The sidelobe levels are low, -14 dB below the main beam maximum level excluded at 330 GHz is below -9 dB. The maximum gain ranges approximately from 22.9 dBi at 290 GHz to 20.6 dB at 320 GHz excluding at 330 GHz 17.7 dBi. Since the antenna is fed by standard waveguides, there is no need for a transition, which avoids introducing more losses and adding more difficulty in fabrication of small size at 300 GHz.

The sub-THz beam-scanning antenna with 37 waveguide feeds of 10.5 λ_0 diameter has been designed at 300 GHz and simulated between 250 GHz and 350 GHz in CST. An angle of view of ±65° has been covered. The simulation results show very good antenna characteristics. The matching level is lower than -10 dB excluding the reflection coefficients for the edge feeding ports. Similarly, the isolation level is -20 dB. The symmetry of both matching and isolation parameters has been verified.

The H-plane radiation patterns confirm that the multiple feeds fully metallic PPW Luneburg lens works perfectly fine as a beam-scanning antenna throughout the (250-320 GHz) operating bandwidth. The maximum gain ranges approximately from 18 dB at 330 GHz to 22.6 dB at 290 GHz. The beams point out at correct angular directions with a small degree of error at the edged feeding ports. The sidelobe levels are -16 dB below the main beam at 290 GHz. The beam overlap level is 3 dB between 250 - 310 GHz. The multiple feed configuration of the Luneburg lens antenna shows excellent results.

However, the PPW Luneburg lens antenna with variable metallic post thicknesses needs a high accuracy technology for the fabrication to mimic the permittivity values required by the Luneburg law. In the next chapter, an improvement of the PPW Luneburg lens antenna with variable metallic post thicknesses, resolving these issues, is developed.

- In Chapter 7:

In this chapter, the complete design and simulations of the sub-THz beam-scanning antenna loaded with uniform metallic posts were presented. The beam-scanning antenna is a fully metallic Luneburg lens antenna excited by 37 standard waveguides (WM-864) and loaded by a 360° angle exponential flare as a radiating element. The antenna is designed at 300 GHz and operates in the WM864-band between 220 GHz and 330 GHz. The lens has 10.5 mm diameter and is made of uniform metallic posts. The permittivity is controlled by one degree of freedom: the PPW spacing of the top plate (i.e. air gap). This parameter, depending on the radial distance to the lens' center, achieve the permittivity values required by the Luneburg law.

The design has been performed with Matlab, and CST. Mainly, the unit cell has been analyzed in the Eigenmode solver of CST and the overall antenna in the time domain solver of CST. Matlab has been used for computing the mapping between unit cell geometrical and effective reflective index parameters. The upper metallic plate shape with different air gaps are mimicked the permittivity values required by the Luneburg law and thicknesses of 100 um uniform metallic posts lying on the bottom metallic plate.

The full-wave simulation of the sub-THz beam scanning antenna has been done in CST. First, the single standard waveguide feed has been studied, then the multiple feeds: 6, then 37. In the single standard WM-864 waveguide feed with **10.5 λ_0 configuration**, the antenna is matched in the operating bandwidth below -10 dB between 250-320 GHz. The sidelobe levels are low, -13 dB below the main beam maximum level. The maximum gain ranges approximately from 20.7 dBi at 320 GHz to 23.2 dBi at 280, and 290GHz.

The beam-scanning antenna loaded with a uniform metallic post using 37 waveguide feeds has been designed at 300 GHz and simulated between 250 GHz and 350 GHz in CST. An angle of

view of ±65° has been covered with exact beam direction and low scanning loss. The simulation results show very good antenna characteristics. The matching level is lower than -10 dB excluding the reflection coefficients for the edge feeding ports. Similarly, the isolation level is -20 dB. The symmetry of both matching and isolation parameters has been verified.

The H-plane radiation patterns confirm that the multiple feeds fully metallic PPW Luneburg lens with uniform-size posts works perfectly fine as a beam-scanning antenna throughout the (250-320 GHz) operating bandwidth. The maximum gain ranges approximately from 18.2 dB at 320 GHz to 22.8 dB at 290 GHz. The beams point out at correct angular directions with a small degree of error at the edged feeding ports. The sidelobe levels are -13 dB below the main beam. The beam overlap level is 3 dB between 250 - 320 GHz. The multiple feed configuration of the Luneburg lens antenna shows excellent results.

In conclusion, the PPW lens antenna loaded with uniform metallic post performances is remarkable. It is broadband, has more than 20 % bandwidth, low loss, and has a wide scan angle, ±65°. Moreover, the sub-THz beam scanning antenna is completely made of metal, so that low loss and high efficiency are achieved. However, still, the fabrication of the top plate of the lens has different air gaps more difficult with high accuracy at 300 GHz.

The fully metallic PPW lens antenna is a good candidate as a quasi-optical beamformer for future multiple beams 6G wireless communications in the sub-THz band. The next section deals with the possibility of manufacturing the dielectric Luneburg lens antenna despite high dielectric loss at 300 GHz.

Perspective and future work

In chapter 3

The circularly polarized (CP) horn antenna has a non-planar structure that makes integration and packing problematic, yet it can be utilized as a source in a short-range wireless communication system for 6G.

In chapter 4

Because of their low-profile and low-cost high-gain and planar structure, LP/CP FPC antennas can be integrated with active components in wireless communication systems. Examine the feasibility of improving the CP-FPC antenna's 3 dB bandwidth.

In chapter 5

The CP bull's eye prototypes are fabricated with simulated wide 3dB AR bandwidth; we hope to measure the far-field radiation patterns soon.

In chapter 6 and 7

The sub-THz beamforming antenna is designed and simulated to operate well; however, there is no good technology for fabricating the metallic post with high accuracy and the top plate with small air gaps. We'll see whether we can do it with silicon micromachining. Perhaps we can make these prototypes using nanotechnology at the nR (NanoRennes) lab, or we can collaborate with IEMN at Lille University.

The prototypes can be utilized as a source or reconfigurable antennas at 300 GHz by using a phase shifter. At present time, there is no high-frequency phase shifter on the market. Perhaps it will be useful soon.

We will investigate the feasibility of efficiently coupling low-profile high-gain antennas to continuous-wave THz sources. We will also test a high-gain photomixing antenna array with a wide bandwidth. We will look into combining UTC-photodiodes with planar wideband antennas.

List of Publications

Journal publications

1. **B. Aqlan**, M. Himdi, L. Le Coq and H. Vettikalladi, "Sub-THz Circularly Polarized Horn Antenna Using Wire Electrical Discharge Machining for 6G Wireless Communications," in *IEEE Access*, vol. 8, pp. 117245-117252, 2020, doi: 10.1109/ACCESS.2020.3003853.
2. **Aqlan, B**.; Himdi, M.; Vettikalladi, H.; Le-Coq, L. Experimental Realization of Sub-THz Circularly Polarized Antenna Based on Metasurface Superstrate at 300 GHz. *Materials* **2021**, *14*, 4796. https://doi.org/10.3390/ma14174796.
3. **Aqlan, B**., Himdi, M., Vettikalladi, H. *et al.* A 300-GHz low-cost high-gain fully metallic Fabry–Perot cavity antenna for 6G terahertz wireless communications. *Sci Rep* **11,** 7703 (2021). https://doi.org/10.1038/s41598-021-87076-3.
4. **B. Aqlan**, M. Himdi, H. Vettikalladi and L. Le-Coq, "A Circularly Polarized Sub-Terahertz Antenna with Low-Profile and High-Gain for 6G Wireless Communication Systems," in *IEEE Access*, vol. 9, pp. 122607-122617, 2021, doi: 10.1109/ACCESS.2021.3109161.

International conference papers

1. **B. Aqlan**, H. Vettikalladi, and M. Himdi, "A Low-cost Sub-Terahertz Circularly Polarized Antenna for 6G Wireless Communications," 2021 IEEE International Symposium on Antennas and Propagation and USNC-URSI Radio Science Meeting (APS/URSI), 2021, pp. 833-834, doi: 10.1109/APS/URSI47566.2021.9704272.

National conference papers

1. **Aqlan, B**., Himdi, M., Vettikalladi, H. et al, "All-Metal Planar Antenna Using Laser-Cutting Technology for 6G Sub-THz Wireless Communications" in JOURNÉE GDR-ISIS SUR/ON: ''Enabling Technologies For (Sub)-Terahertz Communications*''*- on the 20th Mai/May 2021

Uncategorized References

[1] M. Giordani, M. Polese, M. Mezzavilla, S. Rangan, and M. J. I. C. M. Zorzi, "Toward 6g networks: Use cases and technologies," vol. 58, no. 3, pp. 55-61, 2020.

[2] T. S. Rappaport *et al.*, "Wireless Communications and Applications Above 100 GHz: Opportunities and Challenges for 6G and Beyond," *IEEE Access,* vol. 7, pp. 78729-78757, 2019.

[3] F. B. M. Saad, J. Palicot, Y. Corre, G. Gougeon, and J.-B. Doré, "Beyond-5G wireless Tbps scenarios and requirements," in "French funded project-ANR-17-CE25-0013 (BRAVE), Tech. Report D1.0, 2018," Available: https://hal.archives-ouvertes.fr/hal-01947363/document.

[4] H. Elayan, R. M. Shubair, J. M. Jornet, and P. Johari, "Terahertz Channel Model and Link Budget Analysis for Intrabody Nanoscale Communication," *IEEE Transactions on NanoBioscience,* vol. 16, no. 6, pp. 491-503, 2017.

[5] P. Baron *et al.*, "7-4 AMATERASU: model for atmospheric terahertz radiation analysis and simulation," vol. 55, no. 1, 2008.

[6] T. S. Rappaport, J. N. Murdock, and F. Gutierrez, "State of the Art in 60-GHz Integrated Circuits and Systems for Wireless Communications," *Proceedings of the IEEE,* vol. 99, no. 8, pp. 1390-1436, 2011.

[7] J. Wells, "Faster than fiber: The future of multi-G/s wireless," *IEEE Microwave Magazine,* vol. 10, no. 3, pp. 104-112, 2009.

[8] Y. Xing and T. S. Rappaport, "Propagation Measurement System and Approach at 140 GHz-Moving to 6G and Above 100 GHz," in *2018 IEEE Global Communications Conference (GLOBECOM)*, 2018, pp. 1-6.

[9] K. Sengupta, T. Nagatsuma, and D. M. J. N. E. Mittleman, "Terahertz integrated electronic and hybrid electronic–photonic systems," vol. 1, no. 12, pp. 622-635, 2018.

[10] D. M. Pozar, *Microwave engineering*. John Wiley & Sons, 2009.

[11] Z. Pi and F. Khan, "An introduction to millimeter-wave mobile broadband systems," *IEEE Communications Magazine,* vol. 49, no. 6, pp. 101-107, 2011.

[12] M. Ando, J. Hirokawa, T. Yamamoto, A. Akiyama, Y. Kimura, and N. Goto, "Novel single-layer waveguides for high-efficiency millimeter-wave arrays," *IEEE Transactions on Microwave Theory and Techniques,* vol. 46, no. 6, pp. 792-799, 1998.

[13] T. L. Marzetta, "Noncooperative Cellular Wireless with Unlimited Numbers of Base Station Antennas," *IEEE Transactions on Wireless Communications,* vol. 9, no. 11, pp. 3590-3600, 2010.

[14] A. Gonzalez, K. Kaneko, T. Kojima, S. Asayama, and Y. Uzawa, "Terahertz Corrugated Horns (1.25-1.57 THz): Design, Gaussian Modeling, and Measurements," *IEEE Transactions on Terahertz Science and Technology,* vol. 7, no. 1, pp. 42-52, 2017.

[15] J. Leech, B. K. Tan, G. Yassin, P. Kittara, and S. Wangsuya, "Experimental Investigation of a Low-Cost, High Performance Focal-Plane Horn Array," *IEEE Transactions on Terahertz Science and Technology,* vol. 2, no. 1, pp. 61-70, 2012.

[16] N. Chahat, T. J. Reck, C. Jung-Kubiak, T. Nguyen, R. Sauleau, and G. Chattopadhyay, "1.9-THz Multiflare Angle Horn Optimization for Space Instruments," *IEEE Transactions on Terahertz Science and Technology,* vol. 5, no. 6, pp. 914-921, 2015.

[17] K. Fan, Z. Hao, Q. Yuan, and W. Hong, "Development of a High Gain 325–500 GHz Antenna Using Quasi-Planar Reflectors," *IEEE Transactions on Antennas and Propagation,* vol. 65, no. 7, pp. 3384-3391, 2017.

[18] D. Kim, J. Hirokawa, M. Ando, J. Takeuchi, and A. Hirata, "4 x4 -Element Corporate-Feed Waveguide Slot Array Antenna With Cavities for the 120 GHz-Band," *IEEE Transactions on Antennas and Propagation,* vol. 61, no. 12, pp. 5968-5975, 2013.

[19] D. Kim, J. Hirokawa, M. Ando, J. Takeuchi, and A. Hirata, "64 x 64-Element and 32x 32-Element Slot Array Antennas Using Double-Layer Hollow-Waveguide Corporate-Feed in the 120 GHz Band," *IEEE Transactions on Antennas and Propagation,* vol. 62, no. 3, pp. 1507-1512, 2014.

[20] Y. Beniguel, A. Berthon, C. V. Klooster, and L. Costes, "Design realization and measurements of a high performance wide-band corrugated horn," *IEEE Transactions on Antennas and Propagation,* vol. 53, no. 11, pp. 3540-3546, 2005.

[21] D. Hotte, R. Siragusa, Y. Duroc, and S. Tedjini, "Directive and high-efficiency slotted waveguide antenna array for V-band made by wire electrical discharge machining," *Electronics Letters,* vol. 51, no. 5, pp. 380-382, 2015.

[22] A. Vosoogh, P. Kildal, and V. Vassilev, "A multi-layer gap waveguide array antenna suitable for manufactured by die-sink EDM," in *2016 10th European Conference on Antennas and Propagation (EuCAP)*, 2016, pp. 1-4.

[23] J. Xu, Z. N. Chen, and X. Qing, "270-GHz LTCC-Integrated Strip-Loaded Linearly Polarized Radial Line Slot Array Antenna," *IEEE Transactions on Antennas and Propagation,* vol. 61, no. 4, pp. 1794-1801, 2013.

[24] J. Xu, Z. N. Chen, X. Qing, and W. Hong, "140-GHz TE_{20}-Mode Dielectric-Loaded SIW Slot Antenna Array in LTCC," *IEEE Transactions on Antennas and Propagation,* vol. 61, no. 4, pp. 1784-1793, 2013.

[25] T. Tajima, H. Song, K. Ajito, M. Yaita, and N. Kukutsu, "300-GHz Step-Profiled Corrugated Horn Antennas Integrated in LTCC," *IEEE Transactions on Antennas and Propagation,* vol. 62, no. 11, pp. 5437-5444, 2014.

[26] Z. Wu, M. Liang, W. Ng, M. Gehm, and H. Xin, "Terahertz Horn Antenna Based on Hollow-Core Electromagnetic Crystal (EMXT) Structure," *IEEE Transactions on Antennas and Propagation,* vol. 60, no. 12, pp. 5557-5563, 2012.

[27] P. Nayeri *et al.*, "3D Printed Dielectric Reflectarrays: Low-Cost High-Gain Antennas at Sub-Millimeter Waves," *IEEE Transactions on Antennas and Propagation,* vol. 62, no. 4, pp. 2000-2008, 2014.

[28] H. Yi, S. Qu, K. Ng, C. H. Chan, and X. Bai, "3-D Printed Millimeter-Wave and Terahertz Lenses with Fixed and Frequency Scanned Beam," *IEEE Transactions on Antennas and Propagation,* vol. 64, no. 2, pp. 442-449, 2016.

[29] A. Boryssenko and K. Vanhille, "300 GHz microfabricated waveguide slotted arrays," in *2014 39th International Conference on Infrared, Millimeter, and Terahertz waves (IRMMW-THz)*, 2014, pp. 1-2.

[30] E. D. Cullens, L. Ranzani, K. J. Vanhille, E. N. Grossman, N. Ehsan, and Z. Popovic, "Micro-Fabricated 130–180 GHz Frequency Scanning Waveguide Arrays," *IEEE Transactions on Antennas and Propagation,* vol. 60, no. 8, pp. 3647-3653, 2012.

[31] B. Beuerle, J. Campion, U. Shah, and J. Oberhammer, "A Very Low Loss 220–325 GHz Silicon Micromachined Waveguide Technology," *IEEE Transactions on Terahertz Science and Technology,* vol. 8, no. 2, pp. 248-250, 2018.

[32] H. Zhu, Q. Xue, J. Hui, and S. W. Pang, "A 750–1000 GHz H -Plane Dielectric Horn Based on Silicon Technology," *IEEE Transactions on Antennas and Propagation,* vol. 64, no. 12, pp. 5074-5083, 2016.

[33] K. Tekkouk *et al.*, "Corporate-Feed Slotted Waveguide Array Antenna in the 350-GHz Band by Silicon Process," *IEEE Transactions on Antennas and Propagation,* vol. 65, no. 1, pp. 217-225, 2017.

[34] C. Lee *et al.*, "Corrugated (2 × 2) silicon platelets horn antenna array at 560 GHz," in *2017 42nd International Conference on Infrared, Millimeter, and Terahertz Waves (IRMMW-THz)*, 2017, pp. 1-1.

[35] A. Gomez-Torrent *et al.*, "A 38 dB Gain, Low-Loss, Flat Array Antenna for 320–400 GHz Enabled by Silicon-on-Insulator Micromachining," *IEEE Transactions on Antennas and Propagation,* vol. 68, no. 6, pp. 4450-4458, 2020.
[36] A. Mahmoud, "Flat antenna arrays for high data rate communications," 2021.
[37] Y. M. Cheng, P. Chen, W. Hong, T. Djerafi, and K. Wu, "Substrate-Integrated-Waveguide Beamforming Networks and Multibeam Antenna Arrays for Low-Cost Satellite and Mobile Systems," *IEEE Antennas and Propagation Magazine,* vol. 53, no. 6, pp. 18-30, 2011.
[38] R. C. Johnson and H. J. N. Y. Jasik, McGraw-Hill Book Company, , p. No individual items are abstracted in this volume., "Antenna engineering handbook," 1984.
[39] R. K. Luneburg, *Mathematical theory of optics*. Univ of California Press, 1964.
[40] C. Pfeiffer and A. Grbic, "A Printed, Broadband Luneburg Lens Antenna," *IEEE Transactions on Antennas and Propagation,* vol. 58, no. 9, pp. 3055-3059, 2010.
[41] G. Peeler and H. Coleman, "Microwave stepped-index luneberg lenses," *IRE Transactions on Antennas and Propagation,* vol. 6, no. 2, pp. 202-207, 1958.
[42] S. R. Baev, S. M. Gechev, B. N. Hadjistamov, and P. I. Dankov, "Modeling and simulations of lüneburg lens antennas for communication purposes," in *16th Telecommunications forum FOR, Serbia, Belgrad*, 2008, pp. 488-491.
[43] G. Peeler and D. Archer, "A two-dimensional microwave luneberg lens," *Transactions of the IRE Professional Group on Antennas and Propagation,* vol. 1, no. 1, pp. 12-23, 1953.
[44] K. Sato, H. J. E. Ujiie, and C. i. Japan, "A plate Luneberg lens with the permittivity distribution controlled by hole density," vol. 85, no. 9, pp. 1-12, 2002.
[45] L. Xue and V. F. Fusco, "24 GHz automotive radar planar Luneburg lens," *IET Microwaves, Antennas & Propagation,* vol. 1, no. 3, pp. 624-628, 2007.
[46] J. Reinholdt, "Cylindrical Luneburg lens antenna for multi-beam small cell wireless backhaul applications," ed, 2014.
[47] Q. Cheng, H. F. Ma, and T. J. J. A. P. L. Cui, "Broadband planar Luneburg lens based on complementary metamaterials," vol. 95, no. 18, p. 181901, 2009.
[48] M. G. Silveirinha, C. A. Fernandes, and J. R. Costa, "Electromagnetic Characterization of Textured Surfaces Formed by Metallic Pins," *IEEE Transactions on Antennas and Propagation,* vol. 56, no. 2, pp. 405-415, 2008.
[49] M. Casaletti, F. Caminita, and S. Maci, "A luneburg lens designed by using a variable artificial surface," in *2010 IEEE Antennas and Propagation Society International Symposium*, 2010, pp. 1-4.
[50] M. Bosiljevac, M. Casaletti, F. Caminita, Z. Sipus, and S. Maci, "Non-Uniform Metasurface Luneburg Lens Antenna Design," *IEEE Transactions on Antennas and Propagation,* vol. 60, no. 9, pp. 4065-4073, 2012.
[51] X. Xiong, Y. Liu, Z. Yao, L. Zhang, W. Li, and Q. H. Liu, "Design of a metasurface Luneburg lens antenna with flared structure," in *Proceedings of 2014 3rd Asia-Pacific Conference on Antennas and Propagation*, 2014, pp. 375-378.
[52] J. Dockrey, M. J. Lockyear, S. Berry, S. Horsley, J. R. Sambles, and A. P. J. P. R. B. Hibbins, "Thin metamaterial Luneburg lens for surface waves," vol. 87, no. 12, p. 125137, 2013.
[53] C. Walter, "Surface-wave Luneburg lens antennas," *IRE Transactions on Antennas and Propagation,* vol. 8, no. 5, pp. 508-515, 1960.
[54] P. Young-Jin, A. Herschlein, and W. Wiesbeck, "A photonic bandgap (PBG) structure for guiding and suppressing surface waves in millimeter-wave antennas," *IEEE Transactions on Microwave Theory and Techniques,* vol. 49, no. 10, pp. 1854-1859, 2001.
[55] P. Young-Jin and W. Wiesbeck, "Angular independency of a parallel-plate Luneburg lens with hexagonal lattice and circular metal posts," *IEEE Antennas and Wireless Propagation Letters,* vol. 1, pp. 128-130, 2002.

[56] O. Quevedo-Teruel, M. Ebrahimpouri, and M. N. M. Kehn, "Ultrawideband Metasurface Lenses Based on Off-Shifted Opposite Layers," *IEEE Antennas and Wireless Propagation Letters,* vol. 15, pp. 484-487, 2016.
[57] A. Torki, M. Ebrahimpouri, and O. Quevedo-Teruel, "A planar steerable 60 GHz leaky wave antenna with Luneburg lens feed," in *2016 IEEE International Symposium on Antennas and Propagation (APSURSI)*, 2016, pp. 1405-1406.
[58] M. Ebrahimpouri, O. Quevedo-Teruel, and E. Rajo-Iglesias, "Design Guidelines for Gap Waveguide Technology Based on Glide-Symmetric Holey Structures," *IEEE Microwave and Wireless Components Letters,* vol. 27, no. 6, pp. 542-544, 2017.
[59] M. Ebrahimpouri, E. Rajo-Iglesias, Z. Sipus, and O. Quevedo-Teruel, "Cost-Effective Gap Waveguide Technology Based on Glide-Symmetric Holey EBG Structures," *IEEE Transactions on Microwave Theory and Techniques,* vol. 66, no. 2, pp. 927-934, 2018.
[60] K. Liu, F. Ghasemifard, and O. Quevedo-Teruel, "Broadband metasurface Luneburg lens antenna based on glide-symmetric bed of nails," in *2017 11th European Conference on Antennas and Propagation (EUCAP)*, 2017, pp. 358-360.
[61] M. Saad, C. F. Bader, J. Palicot, Y. Corre, G. Gougeon, and J.-B. Doré, "Beyond-5G wireless Tbps Scenarios and Requirements," 2018.
[62] J. W. Britton *et al.*, "Corrugated silicon platelet feed horn array for CMB polarimetry at 150 GHz," in *Millimeter, Submillimeter, and Far-Infrared Detectors and Instrumentation for Astronomy V*, 2010, vol. 7741, p. 77410T: International Society for Optics and Photonics.
[63] J. P. Nibarger *et al.*, "An 84 pixel all-silicon corrugated feedhorn for CMB measurements," vol. 167, no. 3-4, pp. 522-527, 2012.
[64] X. Cheng *et al.*, "Analysis and Design of a Wideband Endfire Circularly Polarized Septum Antenna," *IEEE Transactions on Antennas and Propagation,* vol. 66, no. 11, pp. 5783-5793, 2018.
[65] C. Lee *et al.*, "Terahertz antenna arrays with silicon micromachined-based microlens antenna and corrugated horns," in *2015 International Workshop on Antenna Technology (iWAT)*, 2015, pp. 70-73.
[66] S. Bhardwaj and J. L. Volakis, "Hexagonal Waveguide Based Circularly Polarized Horn Antennas for Sub-mm-Wave/Terahertz Band," *IEEE Transactions on Antennas and Propagation,* vol. 66, no. 7, pp. 3366-3374, 2018.
[67] C. A. Balanis, *Modern antenna handbook*. John Wiley & Sons, 2011.
[68] C. Sommer and S. Sommer, *Complete EDM handbook*. Advance Publishing Incorporated, 2017.
[69] J. Singh, R. Singh, R. J. I. j. o. I. R. i. S. Kumar, Engineering, and Technology, "Review on effects of process parameters in wire cut EDM and wire electrode development," vol. 2, pp. 701-706, 2016.
[70] Y. Liu *et al.*, "Millimeterwave and Terahertz Waveguide-Fed Circularly Polarized Antipodal Curvedly Tapered Slot Antennas," *IEEE Transactions on Antennas and Propagation,* vol. 64, no. 5, pp. 1607-1614, 2016.
[71] P. Zhao, Y. Liu, H. Lu, Y. Wu, and X. Lv, "Experimental Realization of Terahertz Waveguide-Fed Circularly Polarized Double-Fan-Shaped Slot Antenna," *IEEE Antennas and Wireless Propagation Letters,* vol. 16, pp. 2066-2069, 2017.
[72] G. B. Wu, Y. Zeng, K. F. Chan, S. Qu, and C. H. Chan, "High-Gain Circularly Polarized Lens Antenna for Terahertz Applications," *IEEE Antennas and Wireless Propagation Letters,* vol. 18, no. 5, pp. 921-925, 2019.
[73] "Terahertz Communication for Vehicular Networks," *IEEE Transactions on Vehicular Technology,* vol. 66, no. 7, pp. 5617-5625, 2017.

[74] "IEEE Standard for High Data Rate Wireless Multi-Media Networks--Amendment 2: 100 Gb/s Wireless Switched Point-to-Point Physical Layer," *IEEE Std 802.15.3d-2017 (Amendment to IEEE Std 802.15.3-2016 as amended by IEEE Std 802.15.3e-2017),* pp. 1-55, 2017.
[75] H. Song and T. Nagatsuma, "Present and Future of Terahertz Communications," *IEEE Transactions on Terahertz Science and Technology,* vol. 1, no. 1, pp. 256-263, 2011.
[76] A. Gonzalez, K. Kaneko, T. Kojima, S. i. Asayama, and Y. Uzawa, "Terahertz Corrugated Horns (1.25-1.57 THz): Design, Gaussian Modeling, and Measurements," *IEEE Transactions on Terahertz Science and Technology,* vol. 7, no. 1, pp. 1-11, 2016.
[77] B. Aqlan, M. Himdi, L. L. Coq, and H. Vettikalladi, "Sub-THz Circularly Polarized Horn Antenna Using Wire Electrical Discharge Machining for 6G Wireless Communications," *IEEE Access,* vol. 8, pp. 117245-117252, 2020.
[78] K. Konstantinidis *et al.*, "Low-THz Dielectric Lens Antenna With Integrated Waveguide Feed," *IEEE Transactions on Terahertz Science and Technology,* vol. 7, no. 5, pp. 572-581, 2017.
[79] N. Chudpooti, N. Duangrit, P. Akkaraekthalin, I. D. Robertson, and N. Somjit, "220-320 GHz Hemispherical Lens Antennas Using Digital Light Processed Photopolymers," *IEEE Access,* vol. 7, pp. 12283-12290, 2019.
[80] N. Llombart, G. Chattopadhyay, A. Skalare, and I. Mehdi, "Novel Terahertz Antenna Based on a Silicon Lens Fed by a Leaky Wave Enhanced Waveguide," *IEEE Transactions on Antennas and Propagation,* vol. 59, no. 6, pp. 2160-2168, 2011.
[81] D. R. Jackson *et al.*, "The fundamental physics of directive beaming at microwave and optical frequencies and the role of leaky waves," vol. 99, no. 10, pp. 1780-1805, 2011.
[82] A. Feresidis, K. Konstantinidis, and P. Gardner, "Fabry-Perot cavity antennas," in *Aperture Antennas for Millimeter and Sub-Millimeter Wave Applications*: Springer, 2018, pp. 221-241.
[83] R. J. E. o. R. Sauleau and M. Engineering, "Fabry–Perot Resonators," 2005.
[84] A. P. Feresidis and J. C. Vardaxoglou, "High gain planar antenna using optimised partially reflective surfaces," *IEE Proceedings - Microwaves, Antennas and Propagation,* vol. 148, no. 6, pp. 345-350, 2001.
[85] B. Aqlan, H. Vettikalladi, and M. A. S. Alkanhal, "Millimeter wave antenna with frequency selective surface (FSS) for 79 GHz automotive radar applications," *International Journal of Microwave and Wireless Technologies,* vol. 9, no. 2, pp. 281-290, 2017.
[86] W. Fuscaldo *et al.*, "Systematic design of THz leaky-wave antennas based on homogenized metasurfaces," vol. 66, no. 3, pp. 1169-1178, 2018.
[87] T. K. Nguyen, B. Q. Ta, and I. J. C. A. P. Park, "Design of a planar, high-gain, substrate-integrated Fabry–Perot cavity antenna at terahertz frequency," vol. 15, no. 9, pp. 1047-1053, 2015.
[88] K. Konstantinidis, A. P. Feresidis, Y. Tian, X. Shang, and M. J. Lancaster, "Micromachined terahertz Fabry–Perot cavity highly directive antennas," *IET Microwaves, Antennas & Propagation,* vol. 9, no. 13, pp. 1436-1443, 2015.
[89] A. Gomez-Torrent, U. Shah, and J. Oberhammer, "Compact Silicon-Micromachined Wideband 220–330-GHz Turnstile Orthomode Transducer," *IEEE Transactions on Terahertz Science and Technology,* vol. 9, no. 1, pp. 38-46, 2019.
[90] G. V. Trentini, "Partially reflecting sheet arrays," *IRE Transactions on Antennas and Propagation,* vol. 4, no. 4, pp. 666-671, 1956.
[91] D. R. Jackson, A. A. J. I. T. o. A. Oliner, and Propagation, "A leaky-wave analysis of the high-gain printed antenna configuration," vol. 36, no. 7, pp. 905-910, 1988.
[92] Y. Ge, K. P. Esselle, T. S. J. I. T. o. A. Bird, and Propagation, "The use of simple thin partially reflective surfaces with positive reflection phase gradients to design wideband, low-profile EBG resonator antennas," vol. 60, no. 2, pp. 743-750, 2011.

[93] S. S. Yao, Y. J. Cheng, M. M. Zhou, Y. F. Wu, Y. J. I. T. o. A. Fan, and Propagation, "D-band wideband air-filled plate array antenna with multistage impedance matching based on MEMS micromachining technology," vol. 68, no. 6, pp. 4502-4511, 2020.
[94] A. P. Feresidis, G. Goussetis, W. Shenhong, and J. C. Vardaxoglou, "Artificial magnetic conductor surfaces and their application to low-profile high-gain planar antennas," *IEEE Transactions on Antennas and Propagation,* vol. 53, no. 1, pp. 209-215, 2005.
[95] A. T. Almutawa, A. Hosseini, D. R. Jackson, F. J. I. T. o. A. Capolino, and Propagation, "Leaky-wave analysis of wideband planar Fabry–Pérot cavity antennas formed by a thick PRS," vol. 67, no. 8, pp. 5163-5175, 2019.
[96] A. P. Feresidis, J. J. I. P.-M. Vardaxoglou, Antennas, and Propagation, "High gain planar antenna using optimised partially reflective surfaces," vol. 148, no. 6, pp. 345-350, 2001.
[97] A. Foroozesh and L. Shafai, "Investigation Into the Effects of the Patch-Type FSS Superstrate on the High-Gain Cavity Resonance Antenna Design," *IEEE Transactions on Antennas and Propagation,* vol. 58, no. 2, pp. 258-270, 2010.
[98] L. Le Coq, N. Mézières, P. Leroy, and B. Fuchs, "Some Contributions for Antenna 3D Far Field Characterization at Terahertz," vol. 21, no. 4, p. 1438, 2021.
[99] N. Mézières, B. Fuchs, L. L. Coq, J. Lerat, R. Contreres, and G. L. Fur, "On the Application of Sparse Spherical Harmonic Expansion for Fast Antenna Far-Field Measurements," *IEEE Antennas and Wireless Propagation Letters,* vol. 19, no. 5, pp. 746-750, 2020.
[100] N. Mézières, B. Fuchs, L. L. Coq, J. M. Lerat, R. Contreres, and G. L. Fur, "On the Antenna Position to Improve the Radiation Pattern Characterization," *IEEE Transactions on Antennas and Propagation,* pp. 1-1, 2021.
[101] H. Yu, J. Yu, Y. Yao, X. Liu, and X. Chen, "Wideband circularly polarised horn antenna with large aspect ratio for terahertz applications," *Electronics Letters,* vol. 56, no. 1, pp. 11-13, 2020.
[102] B. Aqlan, M. Himdi, H. Vettikalladi, and L. Le-Coq, "A 300-GHz low-cost high-gain fully metallic Fabry–Perot cavity antenna for 6G terahertz wireless communications," *Scientific Reports,* vol. 11, no. 1, p. 7703, 2021/04/08 2021.
[103] Y. Shang, H. Yu, H. Fu, and W. M. Lim, "A 239–281 GHz CMOS Receiver With On-Chip Circular-Polarized Substrate Integrated Waveguide Antenna for Sub-Terahertz Imaging," *IEEE Transactions on Terahertz Science and Technology,* vol. 4, no. 6, pp. 686-695, 2014.
[104] D. Warmowska, K. A. Abdalmalak, L. E. G. Muñoz, and Z. Raida, "High-Gain, Circularly-Polarized THz Antenna With Proper Modeling of Structures With Thin Metallic Walls," *IEEE Access,* vol. 8, pp. 125223-125233, 2020.
[105] M. Beruete *et al.*, "Terahertz Corrugated and Bull's-Eye Antennas," *IEEE Transactions on Terahertz Science and Technology,* vol. 3, no. 6, pp. 740-747, 2013.
[106] H. d. Lu, X. Lv, Z. j. Gao, Y. J. M. Liu, and O. T. Letters, "Experimental radiation characteristics of micromachined terahertz low-profile corrugated horn antenna," vol. 57, no. 2, pp. 364-367, 2015.
[107] G. Wu, Y. Zeng, K. F. Chan, S. Qu, and C. H. Chan, "3-D Printed Circularly Polarized Modified Fresnel Lens Operating at Terahertz Frequencies," *IEEE Transactions on Antennas and Propagation,* vol. 67, no. 7, pp. 4429-4437, 2019.
[108] J. Pendry, L. Martin-Moreno, and F. J. s. Garcia-Vidal, "Mimicking surface plasmons with structured surfaces," vol. 305, no. 5685, pp. 847-848, 2004.
[109] A. P. Hibbins, B. R. Evans, and J. R. J. S. Sambles, "Experimental verification of designer surface plasmons," vol. 308, no. 5722, pp. 670-672, 2005.
[110] P. Nagpal, N. C. Lindquist, S.-H. Oh, and D. J. J. S. Norris, "Ultrasmooth patterned metals for plasmonics and metamaterials," vol. 325, no. 5940, pp. 594-597, 2009.

[111] L.-B. Yu *et al.*, "Physical origin of directional beaming emitted from a subwavelength slit," vol. 71, no. 4, p. 041405, 2005.
[112] F. Garcia-Vidal and L. J. P. R. B. Martin-Moreno, "Transmission and focusing of light in one-dimensional periodically nanostructured metals," vol. 66, no. 15, p. 155412, 2002.
[113] O. Mahboub *et al.*, "Optimization of bull's eye structures for transmission enhancement," vol. 18, no. 11, pp. 11292-11299, 2010.
[114] Y. J. Cheng *et al.*, "Substrate integrated waveguide (SIW) Rotman lens and its Ka-band multibeam array antenna applications," vol. 56, no. 8, pp. 2504-2513, 2008.
[115] A. Darvazehban, O. Manoochehri, M. A. Salari, P. Dehkhoda, A. J. I. T. o. M. T. Tavakoli, and Techniques, "Ultra-wideband scanning antenna array with Rotman lens," vol. 65, no. 9, pp. 3435-3442, 2017.
[116] O. Manoochehri, A. Darvazehban, M. A. Salari, A. Emadeddin, D. J. I. T. o. A. Erricolo, and Propagation, "A parallel plate ultrawideband multibeam microwave lens antenna," vol. 66, no. 9, pp. 4878-4883, 2018.
[117] M. Huang, S. Yang, F. Gao, R. Quarfoth, D. J. I. A. Sievenpiper, and W. P. Letters, "A 2-D multibeam half Maxwell fish-eye lens antenna using high impedance surfaces," vol. 13, pp. 365-368, 2014.
[118] R. K. Luneburg, *Mathematical theory of optics*. Univ of California Press, 1966.
[119] G. Peeler, H. J. I. T. o. A. Coleman, and Propagation, "Microwave stepped-index Luneberg lenses," vol. 6, no. 2, pp. 202-207, 1958.
[120] L. Xue, V. J. I. M. Fusco, Antennas, and Propagation, "24 GHz automotive radar planar Luneburg lens," vol. 1, no. 3, pp. 624-628, 2007.
[121] C. J. I. T. o. A. Walter and Propagation, "Surface-wave Luneberg lens antennas," vol. 8, no. 5, pp. 508-515, 1960.
[122] O. Quevedo-Teruel *et al.*, "Glide-symmetric fully metallic luneburg lens for 5G communications at K a-band," vol. 17, no. 9, pp. 1588-1592, 2018.
[123] D. M. Pozar, *Microwave engineering*. John wiley & sons, 2011.
[124] S. J. Orfanidis, "Electromagnetic waves and antennas."
[125] Zimmerman, "Luneburg Lens and Method of Constructing Same," *U. S.patent* Oct. 14, 1997 Art. no. 5 677 796.
[126] B. Fuchs, L. L. Coq, O. Lafond, S. Rondineau, and M. Himdi, "Design Optimization of Multishell Luneburg Lenses," *IEEE Transactions on Antennas and Propagation,* vol. 55, no. 2, pp. 283-289, 2007.
[127] H. Merlet, P. Le Bars, O. Lafond, and M. Himdi, "Manufacturing method of a dielectric material and its applications to millimeter-waves beam forming antenna systems," ed, 2011.
[128] "ABmm, http://www.abmillimetre.com/.".

Résumé

L'objectif principal de cette thèse est de développer et de fabriquer des antennes aux fréquences THz à fort gain, entièrement métalliques en utilisant différentes technologies de fabrication dans des bandes de fréquences autour des 300 GHz. La thèse couvre un large éventail de sujets liés aux conceptions et aux processus de fabrication des conceptions mentionnées. Six antennes sont construites en utilisant quatre technologies de fabrication distinctes : usinage par décharge électrique (EDM) (un prototype), usinage par découpe laser (trois prototypes), micro-usinage au silicium (un prototype) et fraisage CNC (un prototype) (un prototype).

À la fin de cette thèse, les antennes à lentille PPW Luneburg entièrement métalliques 2D fonctionnent comme formation de faisceaux pour les communications sans fil 6G dans les bandes WM-864 (220 - 330 GHz). Deux conceptions différentes ont été créées, qui fonctionnent toutes deux en mode TEM, sont à large bande et ont une faible perte. Le premier design porte sur la PPW Luneburg chargé de tiges métalliques cylindriques variables, a une bande passante plus large, le gain élevé vient de fait que l'antenne est entièrement métallique. La seconde est la lentille PPW Luneburg chargée de tiges métalliques cylindriques de taille uniforme.

Avec ces deux conceptions, plusieurs lentilles ont été conçues et simulées, parmi lesquelles deux configurations de 10,5 diamètres alimentées par un guide d'onde standard (WM-864), ont été choisies et intégrées dans des antennes multifaisceaux. Deux antennes multifaisceaux ont été conçues et simulées avec d'excellentes performances.

Au chapitre 1 :

Le contexte général du spectre térahertz est décrit, ainsi que ses utilisations et les possibilités émergentes du B5G. Sont présenté dans ce chapitre, les restrictions et les contraintes matérielles de la bande THz, la propagation et la génération des signaux.

Au chapitre 2 :

Un état de l'art sur différentes technologies de fabrication est présenté pour les antennes fabriquées dans la bande sous-térahertz. La plupart des structures discutées dans cette thèse sont basées sur des structures métalliques qui peuvent être remplacées les structures à substrat pour éviter les pertes diélectriques qui posent de gros problèmes dans la bande millimétrique et térahertz. Les antennes multifaisceaux passives basées sur des lentilles sont discutées en détail pour obtenir la formation de faisceau souhaitée dans le domaine RF sans utiliser de composants actifs. Les lentilles de Luneburg ont des performances plus stables avec une bande passante plus large et sont donc utilisés dans le développement de nombreux modèles présentés dans cette thèse. Comme notre objectif principal est les antennes à gain élevé, une comparaison entre les antennes existantes dans la littérature en termes de technologie de fabrication, de pertes de rayonnement, de fréquence de fonctionnement, de gain réalisé le plus élevé et de la structure du système pour évaluer sa complexité pour la fabrication et sa facilité d'utilisation pour la production de masse sont tous discutés.

Au chapitre 3 :

L'usinage par décharge électrique par coupe de fil est utilisé pour fabriquer une antenne cornet conique à polarisation circulaire dans un bloc de métal à 300 GHz. La polarisation circulaire (CP) a été obtenue en excitant deux modes orthogonaux à travers deux fentes croisées dans un disque polariseur circulaire excitant l'antenne cornet. Nous avons utilisé la technologie de forage mécanique pour un nouveau disque d'empreinte de la partie CP d'une épaisseur de 100 μm et 4 trous d'alignement des parties de l'ensemble de la structure. Nous avons ajouté un petit disque à la partie CP pour maintenir la fente croisée dans la position exacte (queue du gros disque) pour éviter la dégradation de la qualité de la polarisation circulaire. Une technique de gravure au laser a été utilisée pour créer une fente croisée de la partie CP dans l'antenne cornet aussi étroite que 100 μm. La partie guide d'ondes est fabriquée par technique d'électroérosion à fil dans un bloc de laiton car la bride de guide d'ondes (WM-864) n'était pas disponible à la première étape de nos travaux à l'IETR. L'antenne donne une bande passante

d'impédance mesurée de 60 GHz de 270 GHz à 330 GHz. La directivité mesurée de 18,3 dBic dans le sens large à 312 GHz. La bande passante AR mesurée à 3 dB de 7 GHz de 309 GHz à 316 GHz. Les diagrammes de rayonnement de l'antenne cornet conique Sub-THz CP fabriquée ont été mesurés et les résultats concordent bien avec les simulations. Ses hautes performances offrent une solution simple à faible coût pour plusieurs applications dans la bande sous-THz, y compris les communications radar ou 6G. L'épaisseur totale du prototype est de 5 mm. (cornet conique et polariseur CP), qui est une structure volumineuse en termes de longueur d'onde et difficile à intégrer avec d'autres composants actifs. Les travaux futurs pour ce prototype consistent à le remplacer par une structure à profil bas et plane.

- Au chapitre 4 :

Les défis rencontrés au chapitre 3 (structure volumineuse et la nécessité de fabriquer la partie guide d'onde) sont relevés et résolus. Une technologie de découpe laser à faible coût est appliquée pour la première fois sur du laiton métallique pour concevoir trois antennes planaires à cavité Fabry-Perot (FPC) à 300 GHz. Les trois antennes sont construites sur sept couches de laiton avec un profil bas de seulement 1,24 mm (c'est-à-dire l'épaisseur totale).

Le premier prototype est l'antenne FPC à polarisation linéaire constituée de sept couches métalliques ; une couche de masse, un élément cornet étagé intégré (trois couches), une couche de couplage, une couche de cavité et une couche de surface sélective de fréquence d'ouverture (FSS). La couche d'ouverture FSS agit comme une surface partiellement réfléchissante, contribuant à un rayonnement de faisceau directif. L'antenne FPC à polarisation linéaire a un coefficient de réflexion mesuré inférieur à - 10 dB de 282 à 304 GHz avec une bande passante de 22 GHz. Le gain maximal mesuré observé est de 17,7 dBi à 289 GHz, et le gain est supérieur à 14,4 dBi de 285 à 310 GHz. Le diagramme de rayonnement mesuré montre un diagramme hautement directif avec un niveau de polarisation croisée inférieur à - 25 dB sur toute la bande dans tous les plans de coupe, ce qui confirme les résultats de la simulation. Un écart de 5° entre le faisceau principal mesuré et simulé dans le plan de coupe azimutal

à partir de la direction latérale a été observé. C'est parce que nous avons découvert que l'une des brides du guide d'ondes qui a été utilisée a une petite inclinaison de 5°.

Le deuxième prototype est l'antenne FPC à polarisation circulaire (CP). L'antenne CP-FPC se compose de sept couches métalliques. Les six premières couches disposées de bas en haut, sont similaires au FPC polarisé linéairement. La septième couche fonctionnait comme un polariseur pour convertir les ondes LP en ondes CP. Le gain élevé et l'auto-génération de la polarisation circulaire sont réalisés en utilisant cette couche FSS en introduisant une ouverture périodique de forme hexagonale dans une fine couche métallique. La couche ouverture-FSS est utilisée pour exciter deux modes orthogonaux d'amplitude égale et en quadrature de phase, obtenant ainsi le rayonnement RHCP. Le prototype d'antenne CP-FPC atteint un gain RHCP maximal mesuré de 16,5 dBic à 292 GHz. L'antenne CP-FPC 300 GHz a été caractérisée à l'aide d'une chambre anéchoïque compacte à ondes millimétriques, obtenant des caractéristiques de diagrammes de rayonnement entre la fréquence de 285 à 315 GHz. L'antenne atteint une largeur de bande d'impédance mesurée de 281 à 305 GHz pour le coefficient de réflexion inférieur à -10 dB. La largeur de bande du rapport axial (AR) AR $\leq$ 3 dB est de 5,12 GHz de 292,8 à 297,92 GHz.

Le troisième prototype est une antenne à cavité résonnante à polarisation circulaire (CP-RCA), avec une nouvelle métasurface monocouche comme superstrat fonctionnant à 300 GHz. La cellule unitaire de la couche de métasurface métallique est constituée de grilles perforées d'ouvertures rayonnantes de forme hexagonale et octogonale. La couche de superstrat de métasurface agit comme un convertisseur de polarisation de linéaire à circulaire, qui fournit un rayonnement polarisé circulairement à gauche (LHCP). Le CP-RCA donne un gain LHCP mesuré de 16,2 dBic avec une directivité de 16,7 dBic à 302 GHz. Une bande passante AR mesurée à 3 dB d'environ 1,41 % (4,24 GHz) avec une fréquence centrale de 296 GHz est obtenue. Tous les prototypes ont été conçus avec la bride de guide d'ondes standard WM-864, qui contient des trous pour les broches et les vis d'alignement, permettant une connexion directe à la bride de guide d'ondes standard UG-387 sans aucun montage ou interface de test supplémentaire. Cette procédure de montage direct est plus facile que les configurations alternatives de

micro-usinage au silicium qui nécessitent la méthode d'alignement de liaison. Cette technologie est intéressante en termes de faible coût et de moindre complexité par rapport à la technologie de micro-usinage du silicium. Enfin, tous les prototypes ont un profil bas, un faible coût de fabrication, un gain élevé et une large bande passante de fonctionnement. de 2,6 λ_0×2,6 λ_0×1,24 λ_0, applicable aux futurs systèmes de communication sans fil térahertz 6G dans la bande sub-THz. La bande passante AR 3dB pour les deux prototypes à polarisation circulaire est inférieure à 5 GHz. Les travaux futurs pour ces prototypes consistent à les remplacer par des structures planes ondulées à profil bas.

- Au chapitre 5 :

Les défis rencontrés au chapitre 4 (c'est-à-dire la bande passante étroite 3dB-AR) sont relevés et résolus. Deux technologies différentes sont utilisées pour fabriquer une antenne œil de bœuf à polarisation circulaire (CP) à 300 GHz.

La première technologie est le micro-usinage du silicium qui est appliqué pour concevoir une antenne en œil de bœuf à polarisation circulaire avec un élément à fentes croisées à 300 GHz. Le prototype se compose de trois couches de silicium d'une épaisseur de 200 µm et de deux de 400 µm. Le guide d'ondes d'alimentation WM-864 est gravé dans la tranche inférieure. La fente croisée et les fentes à six anneaux sont gravées dans une plaquette d'épaisseur 200 µm. Après avoir pulvérisé de l'or, les trois tranches de silicium sont liées entre elles par thermocompression or-or. Nous avons gravé les plaquettes pour obtenir l'antenne en œil du tyran CP avec une dimension de 20 × 20 × 1 mm3. Le coefficient de réflexion mesuré de l'antenne est inférieur à -10 dB de 279,2 GHz à 314 GHz avec une bande passante de 34,8 GHz. Il y a un décalage entre les résultats de mesure et de simulation en raison de la tolérance de fabrication. Un gain maximal réalisé par LHCP simulé de 16,13 dBic est obtenu. L'efficacité totale est supérieure à 80 %, entre 295 et 325 GHz. L'AR simulé minimum à 290 GHz est de 0,675 dB, la bande passante AR à 3 dB de 21 GHz entre 287 GHz et 308 GHz étant de 7 %.

La deuxième technologie est un fraisage à commande numérique par ordinateur (CNC) qui est appliqué pour concevoir une antenne en œil de bœuf à polarisation circulaire avec un élément à fente en forme de double éventail à 300 GHz. Le prototype est fabriqué sur une couche d'une épaisseur de 400 μm. Le matériau utilisé était l'aluminium en raison de sa bonne conductivité et de ses propriétés mécaniques. Nous avons utilisé ce fraisage CNC avec l'élément à double fente en forme d'éventail en raison de la difficulté d'atteindre une épaisseur élevée de 1000 -μm en utilisant le micro-usinage du silicium et expansif. Les six ondulations périodiques concentriques de période p, de profondeur Dg et de largeur Wg sont similaires au prototype fabriqué par micro-usinage du silicium. Seulement deux différences entre les deux prototypes. Le premier est l'épaisseur totale (1000 μm et 400 μm) et le second est l'élément permettant de générer des caractéristiques de polarisation circulaire (fente croisée et fente en forme d'éventail double).

Le coefficient de réflexion mesuré de l'antenne est inférieur à -10 dB de 220 GHz à 330 GHz avec une bande passante de 110 GHz, ce qui est en bon accord avec les résultats de simulation. Un gain maximal réalisé par RHCP simulé de 16,37 dBic est atteint. L'efficacité totale est supérieure à 88 %, entre 260 et 360 GHz. L'AR simulé minimum à 300 GHz est de 0,12 dB avec la bande passante AR à 3 dB de 32,39 GHz

En raison de la construction du nouveau bâtiment du laboratoire IETR et du temps nécessaire pour déplacer les installations, peut-être en mai/juin 2022, nous n'avons pas la possibilité de mesurer le gain, le rapport axial et les diagrammes de rayonnement en champ lointain pour les deux prototypes.

- Au chapitre 6 :

Dans ce chapitre, la conception complète et la simulation de l'antenne à balayage de faisceau sous-THz ont été présentées. L'antenne est une antenne à lentille PPW Luneburg entièrement métallique excitée par un guide d'ondes standard. L'antenne est conçue à 300 GHz et fonctionne dans la bande WM-864 entre 220 GHz et 330 GHz. La lentille a un diamètre de 10,5 mm et est constituée de tiges métalliques. La permittivité est contrôlée par un degré de liberté : l'épaisseur du poteau métallique. Ce paramètre

change en fonction de la distance radiale au centre de la lentille et atteint les valeurs de permittivité requises par la loi de Lunebourg. La conception a été réalisée avec Matlab, CST. Principalement, la cellule unitaire a été analysée dans le solveur de mode propre de CST et l'antenne globale dans le solveur de domaine temporel de CST. Matlab a été utilisé pour calculer la cartographie entre les paramètres géométriques de la cellule unitaire et l'indice de réfraction effectif.

La simulation pleine onde de l'antenne à balayage de faisceau sous-THz a été réalisée en CST dans des configurations à alimentation unique et à alimentation multiple. Tout d'abord, les deux types d'alimentations (guide d'onde à double arête et guide d'onde standard WM-864) ont été étudiés à différents diamètres (6,5 λ_0 et 10,5λ_0), puis l'antenne à balayage de faisceau avec 37 alimentations.

Dans l'alimentation de guide d'ondes à double arête unique avec une configuration de 6,5 λ_0, l'antenne est adaptée dans la bande passante de fonctionnement ci-dessous à -8 dB entre 270 et 350 GHz. Les niveaux des lobes latéraux sont faibles, -15 dB en dessous du niveau maximal du faisceau principal. Le gain maximum varie approximativement de 17,3 dBi à 270 GHz à 20,5 dBi à 330 GHz. De plus, avec une configuration de 10,5 λ_0, l'antenne est adaptée dans la bande passante de fonctionnement ci-dessous à -8 dB entre 260 et 345 GHz. Les niveaux des lobes latéraux sont faibles, -14 dB en dessous du niveau maximal du faisceau principal. Le gain maximum varie approximativement de 20 dBi à 270 GHz à 22,8 dBi à 320 GHz.

Dans l'alimentation de guide d'ondes standard unique WM-864 avec une configuration de 6,5 λ_0, l'antenne est adaptée dans la bande passante de fonctionnement ci-dessous à -15 dB entre 250 et 350 GHz. Les niveaux des lobes secondaires sont bas, -17 dB en dessous du niveau maximal du faisceau principal. Le gain maximal varie approximativement de 20,3 dBi à 280 GHz à 21 dBi à 310 GHz. De plus, avec une configuration de 10,5 λ_0, l'antenne est adaptée dans la bande passante de fonctionnement ci-dessous à -10 dB entre 250 et 350 GHz. Les niveaux des lobes latéraux sont faibles, -14 dB en dessous du niveau maximum du faisceau principal exclu à 330 GHz est en dessous de -9 dB. Le gain maximum varie approximativement de 22,9 dBi à 290 GHz à 20,6 dB à 320 GHz, excluant à

330 GHz 17,7 dBi. L'antenne étant alimentée par des guides d'onde standards, il n'y a pas besoin de transition, ce qui évite d'introduire plus de pertes et de rendre plus difficile la fabrication de petite taille à 300 GHz.

L'antenne à balayage de faisceau sub-THz avec 37 sources de guide d'onde de 10,5 λ_0 de diamètre a été conçue à 300 GHz et simulée entre 250 GHz et 350 GHz en CST. Un angle de vue de ±65° a été couvert. Les résultats de la simulation montrent de très bonnes caractéristiques d'antenne. Le niveau d'adaptation est inférieur à -10 dB à l'exclusion des coefficients de réflexion pour les ports d'alimentation de bord. De même, le niveau d'isolation est de -20 dB. La symétrie des paramètres d'appariement et d'isolement a été vérifiée.

Les diagrammes de rayonnement du plan H confirment que la lentille PPW Luneburg entièrement métallique à alimentations multiples fonctionne parfaitement comme antenne à balayage de faisceau sur toute la bande passante de fonctionnement (250-320 GHz). Le gain maximum varie approximativement de 18 dB à 330 GHz à 22,6 dB à 290 GHz. Les faisceaux pointent dans des directions angulaires correctes avec un petit degré d'erreur au niveau des orifices d'alimentation bordés. Les niveaux des lobes latéraux sont de -16 dB sous le faisceau principal à 290 GHz. Le niveau de chevauchement des faisceaux est de 3 dB entre 250 et 310 GHz. La configuration à alimentation multiple de l'antenne à lentille de Luneburg donne d'excellents résultats.

Cependant, l'antenne à lentille PPW Luneburg avec des épaisseurs de poteaux métalliques variables nécessite une technologie de haute précision pour la fabrication afin d'imiter les valeurs de permittivité requises par la loi de Luneburg. Dans le chapitre suivant, une amélioration de l'antenne à lentille PPW Luneburg avec des épaisseurs de poteaux métalliques variables, résolvant ces problèmes, est développée.

- Au chapitre 7 :

Dans ce chapitre, la conception complète et les simulations de l'antenne à balayage de faisceau sous-THz chargée de poteaux métalliques uniformes ont été présentées. L'antenne à balayage de faisceau est

une antenne à lentille de Luneburg entièrement métallique excitée par 37 guides d'ondes standard (WM-864) et chargée par une éruption exponentielle à angle de 360° en tant qu'élément rayonnant. L'antenne est conçue à 300 GHz et fonctionne dans la bande WM864 entre 220 GHz et 330 GHz. La lentille a un diamètre de 10,5 mm et est constituée de tiges métalliques uniformes. La permittivité est contrôlée par un degré de liberté : l'espacement PPW de la plaque supérieure (c'est-à-dire l'entrefer). Ce paramètre, en fonction de la distance radiale au centre de la lentille, permet d'atteindre les valeurs de permittivité requises par la loi de Lunebourg.

La conception a été réalisée avec Matlab et CST. Principalement, la cellule unitaire a été analysée dans le solveur de mode propre de CST et l'antenne globale dans le solveur de domaine temporel de CST. Matlab a été utilisé pour calculer la cartographie entre les paramètres géométriques de la cellule unitaire et l'indice de réflexion effectif. La forme de la plaque métallique supérieure avec différents entrefers reproduit les valeurs de permittivité requises par la loi de Luneburg et les épaisseurs de poteaux métalliques uniformes de 100 um reposant sur la plaque métallique inférieure.

La simulation de l'antenne à balayage de faisceau sub-THz a été réalisée en CST. Tout d'abord, l'alimentation en guide d'onde standard unique a été étudiée, puis les alimentations multiples : 6, puis 37. Dans l'alimentation en guide d'onde standard unique WM-864 avec une configuration de 10,5 λ_0, l'antenne est adaptée dans la bande passante de fonctionnement inférieure à -10 dB entre 250- 320 GHz. Les niveaux des lobes secondaires sont bas, -13 dB en dessous du niveau maximal du faisceau principal. Le gain maximum varie approximativement de 20,7 dBi à 320 GHz à 23,2 dBi à 280 et 290 GHz.

L'antenne à balayage de faisceau chargée d'un poteau métallique uniforme utilisant 37 alimentations de guides d'ondes a été conçue à 300 GHz et simulée entre 250 GHz et 350 GHz en CST. Un angle de vue de ±65° a été couvert avec une direction exacte du faisceau et une faible perte de balayage. Les résultats de la simulation montrent de très bonnes caractéristiques d'antenne. Le niveau d'adaptation est inférieur à -10 dB à l'exclusion des coefficients de réflexion pour les ports d'alimentation de bord. De même, le niveau d'isolation est de -20 dB. La symétrie des paramètres d'appariement et d'isolement a été vérifiée.

Les diagrammes de rayonnement du plan H confirment que la lentille PPW Luneburg entièrement métallique à alimentations multiples avec des montants de taille uniforme fonctionne parfaitement comme antenne à balayage de faisceau sur toute la bande passante de fonctionnement (250-320 GHz). Le gain maximum varie approximativement de 18,2 dB à 320 GHz à 22,8 dB à 290 GHz. Les faisceaux pointent dans des directions angulaires correctes avec un petit degré d'erreur au niveau des orifices d'alimentation bordés. Les niveaux des lobes latéraux sont de -13 dB sous le faisceau principal. Le niveau de chevauchement des faisceaux est de 3 dB entre 250 et 320 GHz. La configuration à alimentation multiple de l'antenne à lentille de Luneburg donne d'excellents résultats.

En conclusion, l'antenne à lentille PPW chargée de performances de poste métallique uniformes est remarquable. Il est large bande, a plus de 20 % de bande passante, une faible perte et un grand angle de balayage, ±65°. De plus, l'antenne à balayage de faisceau sub-THz est entièrement en métal, de sorte qu'une faible perte et un rendement élevé sont atteints. Cependant, toujours, la fabrication de la plaque supérieure de la lentille présente différents entrefers plus difficiles avec une grande précision à 300 GHz.

L'antenne à lentille PPW entièrement métallique est un bon candidat en tant que formateur de faisceau quasi-optique pour les futures communications sans fil 6G à faisceaux multiples dans la bande sous-THz.

UNIVERSITÉ DE RENNES 1

Titre : Étude des antennes à ondes submillimétriques et des technologies associées

Mots clés : Communication sans fil 6G, polarisation circulaire (CP), antenne à gain élevé, faible coût, lentille de Lüneburg, structure métallique, antennes multifaisceaux (MBA), sub-terahertz (THz).

Résumé : Les activités présentées dans cette thèse portent sur l'étude et le développement d'antennes à ondes submillimétriques à gain élevé pour les communications sans fil à courte portée. Les prototypes proposés, basés sur une structure simplifiée et entièrement métallique, sont particulièrement adaptés aux systèmes de communication sans fil 6G nécessitant des antennes à faible coût avec de bonnes performances.

La première partie de la thèse porte sur le développement d'antennes à haut gain polarisées circulairement et linéairement basées sur différentes technologies. Six antennes ont été conçues et fabriquées démontrant le potentiel des prototypes pour la bande 300 GHz. Une large bande passante et un gain élevé des diagrammes de rayonnement sont obtenus.

Enfin, les implémentations et la conception d'antennes multifaisceaux (MBA) à large bande, à faible pertes et à large couverture sont proposées et étudiées. Les MBA sont basés sur des lentilles de Lüneburg à guide d'ondes à plaques parallèles (PPW) entièrement métalliques avec des structures périodiques. La première mise en œuvre consiste en des cylindres métalliques périodiques d'épaisseurs différentes. L'épaisseur du cylindre imite l'indice de réfraction équivalent de la loi de Lunebourg. La deuxième implémentation correspond à l'utilisation de cylindres métalliques de tailles uniformes. Les entrefers de la plaque supérieure PPW contrôlent l'indice de réfraction équivalent de la loi de Lunebourg. Les deux implémentations ont montré de bonnes performances avec une large couverture de ± 65 ° et de faibles pertes de balayage.

Title: Study of Submillimeter-wave Antennas and Associated Technologies

Keywords: 6G wireless communication, circularly polarized (CP), high gain antenna, low cost, Luneburg lens, metallic structure, multi-beam antennas (MBAs), sub-terahertz (THz).

Abstract: The activities presented in this Ph.D. focus on the study and development of high-gain submillimeter-wave antennas for short-range wireless communication. The proposed prototypes are based on a simplified structure and full metal, which is particularly suitable for 6G wireless communication systems requiring low-cost antennas with good performance.

The first part of the thesis deals with the development of circularly and linearly polarized high-gain antennas based on different technologies. Six antennas have been designed and manufactured demonstrating the potential of prototypes for the 300 GHz band.

Finally, the implementations and the design of wideband, low loss, and wide field-of-view based multi-beam antennas (MBAs) are proposed and studied. The MBAs are based on fully metallic parallel-plate waveguide (PPW) Luneburg lenses with periodic structures. The first implementation consists of a periodic cylindrical metallic post with different thicknesses. The post thickness mimics the equivalent refractive index of Luneburg law.

The second implementation consists of a uniform-size metallic post periodic. The air gaps of the PPW top plate control the equivalent refractive index of Luneburg law. Both implementations showed a good performance with a wide field-of-view of more than ±65°.